Fatigue Behavior and Life Estimations for Dissimilar Ultrasonic Welds in Lap-shear Specimens of Magnesium and Galvanized Steel Sheets

by

Teresa J. Franklin

A dissertation submitted in partial fulfillment
of the requirements for the degree of
Doctor of Philosophy
(Mechanical Engineering)
in the University of Michigan
2013

Doctoral Committee:

Professor Jwo Pan, Chair
Professor J. Wayne Jones
Associate Professor Wei Lu
Michael Santella, Oak Ridge National Lab
Professor Alan S. Wineman

Dedication

This thesis is dedicated to Noah Weatherwatch,

my grandmothers, Dr. Ruth Franklin and Dr. Lois Schneyer, and my fiancé, Eric Rinker.

Acknowledgements

I wish to express my sincere appreciation and gratitude to my advisor, Professor Jwo Pan, for his support, advice and guidance throughout my study. I would also like to thank my doctoral committee, Professor J. Wayne Jones, Professor Wei Lu, Professor Alan Wineman and Dr. Michael Santella from Oak Ridge National Lab.

Additionally, I would like to thank Dr. Santella and Dr. Tsung-Yu Pan for their support and inspiration as well as use of their materials and equipment for sample preparation. Their guidance and insightful discussions have been invaluable in the completion of this research.

I would like to thank Dr. Kamran Asim for guidance in experimental techniques and finite element modeling. I would like to thank my former office mates, Dr. Jaewon Lee and Dr. Kulthida Sripichai for their helpful suggestions with finite element methods. I would like to thank Katherine Avery, Seunghoon Hong and Wei-Jen Lai for their help and encouragement. I thank Albert Lee and Kevin Sun for their assistance with experimental work. I would like to thank Dr. Peter Friedman, Dr. Nia Harrison, and Rosa Nuño of Ford Motor Company for providing the opportunity to gain experience in forming research. I would like to thank and express well wishes to Dr. Yusuf Ali and Catherine Amodeo. Finally, I would like to thank my friends and family for their support and encouragement which has made this dissertation possible.

Table of Contents

Dedication ii

Acknowledgements iii

List of Figures viii

List of Tables xiii

List of Symbols xv

Abstract xviii

Chapter 1 Introduction.. 1

Chapter 2 Stress Intensity Factor Solutions for Welds in Lap-Shear Specimens of Dissimilar Sheet Materials with and without Kinked Cracks 4

2.1. Introduction 4

2.2. Analytical global stress intensity factor solutions for main cracks 8

2.3. Computational global stress intensity factor solutions for main cracks 13

2.4. Analytical local stress intensity factor solutions for kinked cracks 18

2.5. Computational local stress intensity factor solutions for finite kinked cracks... 20

2.6. Conclusions 26

References…….. 54

Chapter 3 Fatigue Behavior of Dissimilar Ultrasonic Welds in Lap-Shear Specimens of AZ31 and Steel Sheets............ 57
3.1. Introduction 57
3.2. Experiment 59
    3.2.1 Lap-shear specimen 59
    3.2.2 Quasi-static test of lap-shear specimen 62
    3.2.3 Fatigue test of lap-shear specimen 63
3.3. Failure modes of ultrasonic welds under cyclic loading conditions 64
    3.3.1. Failure mode under quasi-static (QS) loading conditions 66
        3.3.1.1 Failure mode under quasi-static (QS) loading conditions in 1.58 mm AZ31 and 1.5 mm HSLA steel 67
        3.3.1.2 Failure mode under quasi-static (QS) loading conditions in 1.58 mm AZ31 and 0.8 mm mild steel 67
    3.3.2 Failure mode under low-cycle (LC) loading conditions 68
        3.3.2.1 Failure mode under low-cycle (LC) loading conditions in 1.58 mm AZ31 and 1.5 mm HSLA steel 68
        3.3.2.2 Failure mode under low-cycle (LC) loading conditions in 1.58 mm AZ31 and 0.8 mm mild steel 69
    3.3.3 Failure mode under high-cycle (HC) loading conditions 70
        3.3.3.1 Failure mode under high-cycle (HC) loading conditions in 1.58 mm AZ31 and 1.5 mm HSLA steel 70
        3.3.3.2 Failure mode under high-cycle (HC) loading conditions in 1.58 mm AZ31 and 0.8 mm mild steel 72

3.4. Global and local stress intensity factor solutions 73

3.4.1 Theory …………………………………………………...................... 73

3.4.2 Finite Element Model ………………………………...................... 79

3.5. Fatigue life estimations 83

3.6. Discussion 87

3.7. Conclusions 88

References 117

Chapter 4 Investigations of Dissimilar Ultrasonic Spot Welds in Lap-Shear Specimens of AZ31 and Steel Sheets under Cyclic Loading 120

4.1. Introduction 120

4.2. Experiment 121

4.2.1 Lap-shear specimen 121

4.2.2 Quasi-static test of lap-shear specimen 123

4.2.3 Fatigue test of lap-shear specimen 124

4.3. Failure modes of ultrasonic spot welds under cyclic loading conditions 124

4.3.1 Failure mode under low-cycle (LC) loading conditions 126

4.3.2 Failure mode under high-cycle (HC) loading conditions …………....... 127

4.4. Global and local stress intensity factor solutions 128

4.4.1 Theory …………………………………………….………..................... 128

4.4.2 Finite Element Model ……………………………….…………….…...... 135

4.5. Fatigue life estimations 141

4.6. Discussion 144

4.7. Conclusions 146

References 172

Chapter 5 Conclusion 174

List of Figures

Figure 2.1. (a) A top view and (b) a bottom view of an ultrasonic welded lap-shear specimen which has been machined into a dog-bone shape. (c) A schematic of a lap-shear specimen. The applied force F is shown as the bold arrows. …………………………………………… 30

Figure 2.2. An optical micrographs of a failed weld at the fatigue life of 1.7×10^{3} cycles under a load range of 1.70 kN. …………………………………………………………………….. 31

Figure 2.3. (a) A schematic of the weld with the lap-shear loading condition. (b) A schematic of the left crack tip showing the normal stresses σ_{ui}, σ_{uo}, σ_{li} and σ_{lo} at the inner (*i*) and outer (*o*) surfaces of the upper (*u*) and lower (*l*) strips, respectively. ……………………………….…… 32

Figure 2.4. A schematic diagram of two semi-infinite solids of dissimilar materials with connection of the length w. The Cartesian $x-y$ coordinate system is shown. The shear forces per unit width, F/b, are applied along the x axis at $x=+\infty$ and $-\infty$ of the upper solid and lower solid, respectively. The normal forces per unit width, N/b, are applied along the y axis at $y=+\infty$ and $-\infty$ of the upper solid and lower solid, respectively. ………………...….. 33

Figure 2.5. (a) A schematic of a two-dimensional finite element model of a lap-shear specimen with the boundary and loading conditions. (b) A view of the finite element mesh for the idealized model showing the weld nugget and both pre-existing crack tips for a w/t ratio of 5.85, and (c) a close-up view of the finite element mesh near the right crack tip. …..…….. 34

Figure 2.6. The normalized effective stress intensity factor solutions as functions of w/t plotted in (a) linear and (b) logarithmic scales. …………………………………………………... 35

Figure 2.7. (a) The finite element mesh near the right main crack indicating the directions ahead of the crack tip $\theta=0$, and above the crack tip $\theta=-90$, as pointing horizontally and vertically from the main crack tip respectively. (b) A comparison between the actual material combination and the modified material combination with $\beta=0$ showing the normal stress in the $y-$direction ahead of the crack tip, (c) the shear stress ahead of the crack tip, (d) the normal stress in the $x-$direction vertically above the crack tip, and (e) the shear stress vertically above the crack tip. ……………………..……………………………………………………………..……….. 37

Figure 2.8. A schematic of a main crack and a kinked crack with the kink length a and the kink angle φ. ……………………………………………………………………………... 40

Figure 2.9. (a) A schematic of a two-dimensional finite elemental model of a lap-shear specimen with a kinked crack showing the boundary and loading conditions. (b) The finite element mesh

showing the pre-existing cracks and the kinked crack on the right hand side for $w/t = 5.85$ and $a/t = 0.1$, (c) a view of the finite element mesh near the kinked crack, and (d) a close-up view of the mesh refinement near the kinked crack tip. ……………………………………………41

Figure 2.10. The values of (a) $k_{\mathrm{I}}/(k_{\mathrm{I}})_0$, with linear axes, (b) $k_{\mathrm{I}}/(k_{\mathrm{I}})_0$, with logarithmic axes, (c) $|k_{\mathrm{II}}|/(k_{\mathrm{I}})_0$, with linear axes, (d) $|k_{\mathrm{II}}|/(k_{\mathrm{I}})_0$, with logarithmic axes, (e) $k_e/(k_{\mathrm{e}})_0$, with linear axes, and (f) $k_e/(k_{\mathrm{e}})_0$, with logarithmic axes, as functions of the normalized kink length a/t for the actual and modified material with $w/t = 5.85$ and $\varphi = -90°$. ……………..………… 43

Figure 2.11. (a) The values of $k_{\mathrm{I}}/(k_{\mathrm{I}})_0$ as functions of the normalized kink length a/t for $w/t = 0.5$, 1 and 5.85 and $\varphi = -90°$, and (b) an enlarged section showing the values near a kink crack of length zero. ……………………………………………………………….……… 49

Figure 2.12. The values of $|k_{\mathrm{II}}|/(k_{\mathrm{I}})_0$ as functions of the normalized kink length a/t for $w/t = 0.5$, 1 and 5.85 and $\varphi = -90°$. ……………………………………………………...… 51

Figure 2.13. (a) The values of $k_e/(k_{\mathrm{e}})_0$ as functions of the normalized kink length a/t for $w/t = 0.5$, 1 and 5.85 and $\varphi = -90°$, and (b) an enlarged section showing the values near a kink crack of length zero. ………………………………………………………………………. 52

Figure 3.1 (a) A top view of an ultrasonic welded lap-shear specimen prior to being machined into a dog-bone shaped specimen. (b) Face view and (c) side view of the sonotrode tip used in the ultrasonic welding. …………………………………………………………………..…. 94

Figure 3.2. (a) A top view and (b) a bottom view of an ultrasonic welded lap-shear specimen which has been machined into a dog-bone shape. …………………………..……….…. 95

Figure 3.3. A schematic of a lap-shear specimen with the loading directions shown as the bold arrows. …………………………………………………………………………..……. 96

Figure 3.4. An optical micrograph of the cross section of an ultrasonic welded joint in (a) 1.58 mm AZ31 and 1.5 mm HSLA steel and (b) 1.58 mm AZ31 and 0.8 mm mild steel prior to testing. ………………………………………………………………………....…..… 97

Figure 3.5. The experimental results of the fatigue tests of ultrasonic spot welds with a dog-bone profile in lap-shear specimens under cyclic loading conditions. ……………….…...….… 98

Figure 3.6. A top view of the weld in magnesium and thick steel after testing for (a) quasi-static load, (b) (low cycle) cyclic loading with 697 cycles under a load range of 1.93 kN, (c) (low cycle) cyclic loading with 2194 cycles under a load range of 1.66 kN, (d) (high cycle) cyclic loading with 8962 cycles under a load range of 1.19 kN. ……..…………….…………… 99
.

Figure 3.7. (a) A bottom view of the weld in magnesium and thin steel after testing for quasi-static load. A top view of the weld in magnesium and thin steel after testing for (b) (low cycle) cyclic loading with 2566 cycles under a load range of 1.57 kN and (c) (high cycle) cyclic loading with 80,821 cycles under a load range of 0.72 kN. ……………………………………….…… 100

Figure 3.8. Optical micrograph of a failed weld in 1.58 mm AZ31 and 1.5 mm HSLA steel under quasi-static loading conditions. ………………………………………………………..…….. 101

Figure 3.9. Optical micrographs of (a) the entire section and (b) an enlarged near the kinked crack of a partially failed thick steel weld at the fatigue life of 2.2×10^3 cycles under a load range of 1.43 kN. Optical micrographs of a failed thick steel welds (c) at the fatigue life of 1.7×10^3 cycles under a load range of 1.70 kN and (d) at the fatigue life of 3.3×10^3 cycles under a load range of 1.43 kN (low-cycle (LC) loading conditions). …………………………….……. 102

Figure 3.10. Optical micrograph of a failed thin steel weld at the fatigue life of 6.9×10^3 cycles under a load range of 1.16 kN (low-cycle (LC) loading conditions). ……………....……. 104

Figure 3.11. Optical micrographs of (a) the entire section and (b) an enlarged section near the kinked crack of a partially failed thick steel weld at the fatigue life of 5.46×10^4 cycles under a load range of 0.95 kN. (c) Optical micrograph of a fully failed weld at a fatigue life of 3.50×10^4 cycles under a load range of 0.99 kN (high-cycle (HC) loading conditions). ……..….…. 105

Figure 3.12. Optical micrographs of (a) a failed thin steel weld at a fatigue life of 1.53×10^4 cycles under a load range of 0.96 kN and (b) a failed thin steel weld at a fatigue life of 8.08×10^4 cycles under a load range of 0.72 kN (high-cycle (HC) loading conditions). ………....…. 107

Figure 3.13. (a) A schematic of the weld with the lap-shear loading condition. (b) A schematic of the left crack tip showing the normal stresses σ_{ui}, σ_{uo}, σ_{li} and σ_{lo} at the inner (*i*) and outer (*o*) surfaces of the upper (*u*) and lower (*l*) strips, respectively. ……………………....…... 108

Figure 3.14. A schematic of a main crack and a kinked crack with the kink length a and the kink angle φ. ……………………………..…………………………………………………….. 109

Figure 3.15. (a) A schematic of a two-dimensional finite element model of a lap-shear specimen with the boundary and loading conditions, (b) a view of the finite element mesh for the idealized showing the weld nugget and both pre-existing crack tips (c) a view of the finite element mesh for the weld geometry model showing the weld nugget and pre-existing crack tips and (d) a close-up view of the finite element mesh near the right crack tip. ……………………….……. 110

Figure 3.16. (a) A schematic of a two-dimensional finite element model of a lap-shear specimen showing a kinked crack on the right side of the weld and the boundary and loading conditions, and (b) a close-up view of the finite element mesh near the right kinked crack tip for $a/t = 0.3$. ……………………………………………………………………………………….. 112

Figure 3.17. The values of $k_{\mathrm{I}}/(k_{\mathrm{I}})_0$ for the kinked cracks emanating from the right pre-existing crack tips as functions of the normalized kink length a/t for $w/t = 5.85$ and $\varphi = -90°$ . . 113

Figure 3.18. The values of $|k_{II}|/(k_{\mathrm{I}})_0$ for the kinked cracks emanating from the right pre-existing crack tips as functions of the normalized kink length a/t for $w/t = 5.85$ and $\varphi = -90°$ . . 114

Figure 3.19. The experimental results and the fatigue life estimations based on the kinked fatigue crack growth models for three values of C and m. ………………………………….….. 115

Figure 3.20. The experimental results and the fatigue life estimation ranges based on the kinked fatigue crack growth models for ideal and weld geometry models. …………………….…...… 116

Figure 4.1. (a) A top view of an ultrasonic welded lap-shear specimen prior to testing. (b) Face view and (c) side view of the sonotrode tip used in the ultrasonic welding ……….…….... 150

Figure 4.2. (a) A schematic of a lap-shear specimen with a spot weld idealized as a circular cylinder, and (b) a top view of the weld nugget showing the orientation angle θ with respect to points A, B, C and D. ……………………………………………………………….…....….. 151

Figure 4.3. An optical micrograph of the cross section of an ultrasonic welded joint in 1.58 mm AZ31 and 1.5 mm HSLA steel. …………………………..…………………….…….….. 152

Figure 4.4. The experimental results of the fatigue tests of ultrasonic spot welds in lap-shear specimens under cyclic loading conditions. ……………………………….…………….…… 153

Figure 4.5. (a) A top view of the magnesium sheet, (b) a bottom view of the magnesium sheet and (c) a view of the steel sheet after quasi-static testing. (d) A top view of the magnesium sheet, (e) a bottom view of the magnesium sheet and (f) a view of the steel sheet after (low cycle) cyclic loading with 5.7×10^3 cycles under a load range of 3.20 kN. (g) A top view of the weld after (high cycle) cyclic loading with 3.08×10^4 cycles under a load range of 1.91 kN. The loading direction is shown schematically with arrows. …………..………………………. 154

Figure 4.6. Optical micrograph of a failed weld at the fatigue life of 9.5×10^3 cycles under a load range of 2.82 kN (low-cycle (LC) loading conditions). …………………………......… 155

Figure 4.7. Optical micrographs of (a) the entire section and (b) an enlarged near the kinked crack of a partially failed thick steel weld at the fatigue life of 1.6×10^4 cycles under a load range of 2.38 kN (low-cycle (LC) loading conditions). ……………………………….....……. 156

Figure 4.8. Optical micrograph of a failed weld at the fatigue life of 6.6×10^4 cycles under a load range of 2.02 kN (high-cycle (HC) loading conditions). ……………………….……… 157

Figure 4.9. (a) A schematic of the weld with the lap-shear loading condition. (b) A schematic of the left crack tip showing the normal stresses σ_{ui}, σ_{uo}, σ_{li} and σ_{lo} at the inner (*i*) and outer (*o*) surfaces of the upper (*u*) and lower (*l*) strips, respectively. …………………...…………. 158

Figure 4.10. A schematic of a main crack and a kinked crack with the kink depth d and the kink angle φ. ………………………………………..……………………………...…. 159

Figure 4.11. (a) A schematic of a three-dimensional finite element model featuring half of the lap-shear specimen with the boundary and loading conditions, (b) a view of the entire finite element mesh for the idealized model, and (c) a view of the half of the finite element mesh indicating the area shown in (d). (d) An enlarged view of the finite element mesh for the idealized model showing the main crack surfaces and main crack tips. (e) A view of the central portion of the finite element mesh for the weld geometry model showing the weld indentation. (f) An enlarged view of the finite element mesh near the weld for the weld geometry model. ……………………………………………………………………………………….. 160

Figure 4.12. The normalized K_1, K_2 and K_3 solutions as functions of θ for an idealized weld of 1.58 mm magnesium and 1.50 mm steel sheets based on the finite element analysis and the analytical solutions. …………………………….……………………………………… 164

Figure 4.13. The normalized K_1, K_2 and K_3 solutions as functions of θ for a lap-shear spot welded specimen of 1.58 mm magnesium and 1.50 mm steel sheets based on the finite element analysis of an ideal model and a model which follows the weld geometry. ……….…….. 165

Figure 4.14. (a) A schematic of a three-dimensional finite element model with an elliptical kinked crack of maximum depth, d, at point A with the boundary and loading conditions, (b) a view of half of the finite element mesh for the idealized model with a kinked crack, and (c) a view of the an enlarged section near the weld for the idealized model with a kinked crack of $d/t = 0.5$, with the welded area hidden. ……………………………………………….……… 166

Figure 4.15. The values of $k_{\mathrm{I}}/(k_{\mathrm{I}})_0$ for the semi-elliptical kinked cracks emanating from point A as functions of the normalized kink depth d/t for $\varphi = -90°$. ……………….……….…… 168

Figure 4.16. The values of $|k_{II}|/(k_{\mathrm{I}})_0$ for the semi-elliptical kinked cracks emanating from point A as functions of the normalized kink depth d/t for $\varphi = -90°$. ……………….……….…… 169

Figure 4.17. The experimental results and the fatigue life estimations based on the kinked fatigue crack growth models for three values of C and m. ……………………………….…….. 170

Figure 4.18. The experimental results and the fatigue life estimation ranges based on the kinked fatigue crack growth models for ideal and weld geometry models. ……………...……… 171

List of Tables

Table 2.1a: The normalized global stress intensity factor $\overline{K}_1$, $\overline{K}_2$ and $\overline{K}_{\mathrm{e}}$ solutions for the left crack tip at various normalized weld widths. ……………... 28

Table 2.1b: The normalized global stress intensity factor $\overline{K}_1$, $\overline{K}_2$ and $\overline{K}_{\mathrm{e}}$ solutions for the right crack tip at various normalized weld widths. …………... 28

Table 2.2: The normalized local stress intensity factor $k_{\mathrm{I}} / (k_{\mathrm{I}})_0$ solutions for $\varphi = -90°$, $w/t = 0.5$, 1, and 5.85. ……………………………………………………………….……… 29

Table 2.3: The normalized local stress intensity factor $|k_{\mathrm{II}}| / (k_{\mathrm{I}})_0$ solutions for $\varphi = -90°$, $w/t = 0.5$, 1, and 5.85. ……………………………………………………………….…...…. 29

Table 3.1. Dimensions of the lap-shear specimen …………………………….……….….. 91

Table 3.2. Mechanical properties of AZ31-H24 and steel ……….…………………..……. 91

Table 3.3a: The normalized computational global stress intensity factor $\overline{K_1}$ and $\overline{|K_2|}$ solutions for the right and left pre-existing crack tips for the thick steel welds. ……………………..…. 92

Table 3.3b: The normalized computational global stress intensity factor $\overline{K_1}$ and $\overline{|K_2|}$ solutions for the right and left pre-existing crack tips for the thin steel welds. ……………….….…. 92

Table 3.4a: The normalized local stress intensity factors $k_I / (k_{\mathrm{I}})_0$ and $k_{II} / (k_{\mathrm{I}})_0$ solutions for the right kinked crack with $w/t = 5.85$ and $\varphi = -90°$ for thick steel welds. …………………...... 93

Table 3.4b: The normalized local stress intensity factors $k_I/(k_{\mathrm{I}})_0$ and $k_{II}/(k_{\mathrm{I}})_0$ solutions for the right kinked crack with $w/t = 5.85$ and $\varphi = -90°$ for thin steel welds. …….……………… 93

Table 4.1. Dimensions of the lap-shear specimen ……………………………………... 148

Table 4.2. Mechanical properties of AZ31-H24 and steel ……………………………….. 148

Table 4.3. The normalized local stress intensity factors $k_I/(k_{\mathrm{I}})_0$ and $k_{II}/(k_{\mathrm{I}})_0$ solutions for several values of normalized kink depth d/t based on the semi-elliptical crack at point A of the three-dimensional finite element computational model with $\varphi = -90°$. ……….………..… 149

List of Symbols

a	kinked crack length
a_r	weld radius
a/t	ratio of kink length to sheet thickness
b	specimen reduced width (linear weld), specimen half width (spot weld)
c	half length along circumference of semi-elliptical kinked crack
c^{HH}, d^{HH}	complex-valued functions of φ, α and β
d	maximum kinked crack depth
d/c	aspect ratio of semi-elliptical kinked crack
d/t	ratio of kink depth to sheet thickness
C, m	Paris law material constants
E	Young's modulus
E'	effective Young's modulus under plane strain conditions
f_I, f_{II}	dimensionless geometric factor
F	resultant force
g	indentation width
G	shear modulus
k_I, k_{II}, k_{III}	local stress intensity factors
$\mathbf{K} = K_1 + iK_2$	complex stress intensity factor for an interface crack

$K_1,\ K_2, K_3$	global stress intensity factors
L	specimen coupon length
N	number of complete fatigue cycles
r	radius of reduced area
t_u	upper sheet thickness
t_l	lower sheet thickness
t'	effective thickness of the kinked crack
V	specimen overlap length
w	ultrasonic weld width
W	width of specimen in the grip section
w/t	ratio of the weld width to the thickness of the failing sheet
$\alpha\ ,\ \beta$	Dundurs' parameters
γ	empirical constant
$\delta = t_u/t_l$	thickness ratio
ε	bimaterial constant
$\eta = E'_u/E'_l$	modulus ratio
ν	Poisson's ratio
$\xi = G_u/G_l$	shear modulus ratio
σ	normal structural stress
σ^*	normal structural stress to satisfy the equilibrium, and continuity of the strain and strain gradient

τ	shear stress
φ	kink angle
ω	angular function of δ, α and β

Superscripts and Superscripts

u , l	upper and lower sheets of weld
i , o	inner and outer surfaces of the sheets
R , I	real, imaginary
CB , CtB	counter bending and central bending conditions
S , T	shear and tension conditions

Abstract

Fatigue behavior of dissimilar ultrasonic welds between magnesium alloy AZ31 and galvanized steel sheets is investigated experimentally, with stress intensity factor solutions and with a kinked crack growth life estimation model. First, stress intensity factor solutions for welds with various widths in lap-shear specimens with and without kinked cracks are obtained using finite element analyses. The analytical stress intensity factor solutions for lap-shear specimens based on the beam bending theory and the analytical solutions for two dissimilar semi-infinite solids with connection under plane strain conditions are reviewed. Results of the finite element analyses for global stress intensity factor solutions are compared with the analytical stress intensity factor solutions to identify transition weld widths for the analytical solutions.

Finite element analyses were also conducted for the ultrasonic welded lap-shear specimens of magnesium and steel sheets, but with a modified fictitious Poisson's ratio for the magnesium sheet such that the bimaterial constant is equal to zero. The results indicate that the crack-tip stresses directly ahead of the main crack tip are influenced by the oscillation of the interface crack-tip field. However, the crack-tip stresses directly above the main crack tips are weakly affected, and the oscillatory crack-tip stress distributions for both actual and modified material combinations are quite similar. The results suggest that the stress intensity factor solutions for a kinked crack with a vanishing kink length can be approximated by the available analytical solutions for fatigue life estimation.

Experimental fatigue results for dissimilar ultrasonic welds are presented for lap-shear specimens which have been machined into a dog-bone profile to approximate linear welds and specimens which have not been altered. Optical micrographs of the welds after testing were examined to understand the failure modes. Stress intensity factor solutions were obtained from finite element analyses of a plane strain model and a three-dimensional model. The global stress intensity factor solutions and the local stress intensity factor solutions for vanishing and finite kinked cracks were used for fatigue life estimations using a Paris law kinked crack growth model.

Chapter 1
Introduction

Reducing the weight of a vehicle is imperative to meeting the changing fuel economy standards and addressing environmental concerns while maintaining vehicle performance. One method to weight reduction is replacing traditional steel with a lighter alloy such as magnesium. This measure could result in significant weight savings; however certain strength components will still require a steel frame. Using high strength steel for components which need to endure more stress and magnesium alloys for lower stress components is one method for reducing weight while preserving crash safety. Therefore it is necessary to find a method to join these two metals and to study the resulting joint in detail. In this thesis, the fatigue behavior of ultrasonic welded lap-shear joints between steel and magnesium sheets is investigated. Each chapter covers a separate aspect of the fatigue behavior between the ultrasonic dissimilar welds. The chapters were prepared as individual papers. Therefore some concepts are repeated as necessary to facilitate comprehension for each chapter separately.

In Chapter 2, ultrasonic spot welds between magnesium and steel sheets have been machined into dog-bone profile to approximate a linear weld. This allows detailed study of the lap-shear weld while using two-dimensional finite element analyses and analytical solutions developed for plane strain. Chapter 2 represents a paper for investigating the global and local stress intensity factor solutions of plane strain ultrasonic welds in lap-shear specimens. The analytical stress intensity factor solutions for lap-shear specimens under plane strain conditions are reviewed based on the beam bending theory and solutions based on two dissimilar semi-infinite solids with connection. Finite element analyses of lap-shear specimens with several different weld widths were conducted to obtain global stress intensity factors. The stress intensity factors were compared to the analytical solutions to identify a transition weld width. Then finite element analyses were conducted for a modified fictitious material combination which maintained the ratio of shear moduli, but modified the Poisson's ratio for the magnesium sheet such that the bimaterial constant is equal to zero. The results show that while the crack-tip stresses directly ahead of the crack tip are affected by the oscillation of the interface crack-tip field, the stresses above the crack tip are quite similar for both material combinations. Stress intensity factor solutions for vanishing cracks are then obtained from computational results using the modified material combination for the main crack and existing analytical solutions. Finite element analyses for welded lap-shear specimens were conducted to find local stress intensity factor solutions for kinked cracks for three weld widths as functions of the kink length.

Chapter 3 represents a paper which builds on the concepts presented in Chapter 2 to compare experimental fatigue data with a kinked crack growth model for fatigue life estimation. First, experimental fatigue results of ultrasonic welds between magnesium and steel sheets which have been machined into a dog-bone profile are reviewed. Optical micrographs of the welds after testing are presented to observe the crack growth pattern of the fatigue failure. The lap-shear specimens were modeled with two different two-dimensional finite element plane strain models. The first model is idealized while the second model includes the sonotrode indentation which was created during welding. Stress intensity factor solutions for the main and kinked cracks were obtained from finite element analyses. The vanishing crack solution was obtained using existing analytical solutions with the modified material combination to find the global stress intensity factor solutions from the finite element analyses. A kinked crack growth model is adopted which uses the vanishing and finite kinked crack stress intensity factors, and Paris law constants from existing literature. The fatigue life estimation from the kinked crack growth model is compared with fatigue results.

In Chapter 4, fatigue of ultrasonic spot welds of magnesium and steel sheets in lap-shear specimens is investigated. In contrast to the prior chapters, the welds were tested without modification and finite element models were constructed in three-dimensions. First experimental fatigue results are reviewed. Two three-dimensional finite element models were constructed. The ideal model simply models the welds with a uniform thickness for the magnesium sheet. The weld geometry model accounts for the sontrode indentation which was created during welding. Then global stress intensity factor solutions were obtained from finite element analyses. Local stress intensity factor solutions were obtained for four kink lengths from the finite element analyses. The vanishing crack solution was found with existing analytical solutions and global stress intensity factors using a modified material combination as in Chapter 2. The experimental fatigue results are then compared with a fatigue estimation using a kinked crack growth model. The kinked crack growth model compares well with experimental results.

Chapter 2
Stress Intensity Factor Solutions for Welds in Lap-Shear Specimens of Dissimilar Sheet Materials with and without Kinked Cracks

2.1. Introduction

The advantage of solid state joining methods such as ultrasonic welding and friction stir welding is that melting is either avoided or minimized. Both solid state joining methods can be used to join dissimilar metals such as magnesium and steel sheets. Resistance spot welding of magnesium alloys is possible [1], but fusion welding tends to cause coarse grains and porosity in magnesium [2]. Researchers have been using ultrasonic welding or friction stir welding to join both similar and dissimilar materials. Similar joints between aluminum sheets have been made by many researchers, including Hetrick et al. [3], Jahn et al. [4], and Bakavos and Prangnell [5]. Jordan et al. [6] produced similar magnesium friction stir spot welds. Dissimilar welds have been produced most commonly between aluminum and steel sheets by researchers such as Gendo et al. [7], Liyanage et al. [8], and Watanabe et al. [9]. Dissimilar welds were also produced between magnesium and steel sheets by Santella et al. [10] Jana and Hovanski [11] and Uematsu et al. [12].

Due to the geometry of a lap joint, natural or pre-existing crack tips or notch tips are presented at the edges of the weld bead. Fatigue cracks usually are initiated from the natural crack tips or notch tips of lap joints. Welded components with lap joints are often subjected to cyclic loading conditions. Some researchers have investigated the fatigue behavior of solid state welds. This is an important and necessary step in order to develop life prediction and design tools for product development.

In this study, ultrasonic spot welded lap-shear specimens of steel and magnesium sheets were machined into a dog-bone profile. Certain ultrasonic welders are designed to produce seam welds such as those studied by Ueoka and Tsujino [13]. It is the hope that the results of this research would be applicable to welds produced with seam welders. The experimental results based on these dog-bone specimens can be analyzed by using two-dimensional plane strain finite element analyses and available analytical stress intensity factor solutions.

Fatigue models based on fracture mechanics rely on stress intensity factor solutions for the welds. Many researchers developed stress intensity factor solutions for similar and dissimilar welds in lap-shear specimens. For example, Sripichai et al. [14] developed stress intensity factor solutions for laser welds in lap-shear specimens based on the beam bending theory. Zhang [15, 16] developed stress intensity factor solutions for dissimilar welds in lap-shear specimens of different materials based on the J integral and the work of Suo and Hutchinson [17].

Figures 2.1(a) and 2.1(b) show the top and bottom views of an ultrasonic spot welded lap-shear specimen after being machined into the dog-bone shaped profile. Figure 2.1(c) shows a schematic of a lap-shear specimen with the loading direction represented by bold arrows. As shown in the figure, the specimen has a width W and overall length L for the upper and lower sheets. The specimen has the thickness t_u for the upper sheet and t_l for the lower sheet. The specimen has a reduced width b for the central portion, an overlap length V, and a transition radius r for the weld zone. The width of the sontrode tip indentation on the top surface of the upper sheet is denoted by g. The weld width w of the ultrasonic weld is defined as the distance between two crack tips as shown in Figure 2.1(c). Experimentally, the ultrasonic weld zone can be observed from failed specimens and is larger than the sontrode tip indentation on the top surface. For analytical and computational analyses presented in this paper, the sonotrode tip indentation will not be considered. The specimen has two spacers to align the applied force F, shown with bold arrows, along the weld interface. The weld zone is assumed to have the same elastic properties as the base metal. The dimensions of the specimens are W = 30 mm, L = 100 mm, b = 8 mm, V = 75 mm, w = 8.78 mm, g = 7 mm and r = 10 mm. The thickness t_u for the upper magnesium sheet is 1.58 mm and the thickness t_l for the lower steel sheet is 1.5 mm. Note that the upper and lower sheets used during the experiments have nearly the same thickness. Specimens with similar shapes were adopted by a number of researchers for the study of laser welded joints, for example, see Lee et al. [18], Asim et al. [19], Anand et al. [20], and Sripichai et al. [21]. The geometry of the specimen investigated here varies slightly from the specimen used in the finite element models. In the idealized model, the thickness of the magnesium sheet is taken to be 1.50 mm to provide a lap-shear specimen of equal thickness.

Figure 2.2 shows a micrograph of the cross section of a failed ultrasonic weld in a lap-shear specimen under the load range of 1.70 kN at the fatigue life of 1.7×10^3 cycles. The load is applied to the right on the upper right sheet and to the left on the lower left sheet as shown schematically with arrows. As shown in Figure 2.2, a fatigue crack is initiated near the main crack tip on the right side of the edge of the weld. The fatigue crack can be considered as a kinked crack with respect to the right main crack tip. All of the observed partially and fully failed ultrasonic welds displayed kink angles close to 90°.

As shown in Figure 2.2, the weld failed by the kinked crack emanating from the right main crack. In order to determine the fatigue life of the weld based on a kinked fatigue crack growth model, stress intensity factor solutions for kinked cracks with various lengths are needed.

Therefore, in this investigation, the local stress intensity factors for kinked cracks will be obtained by finite element analyses. He and Hutchinson [22] developed local stress intensity factor solutions for a small kinked crack growing from the bimaterial interface. However, for a material combination with a nonzero bimaterial constant, the local stress intensity factor solutions vary with the distance to the crack tip due to the stress oscillation which occurs at distances extremely close to the main crack tip. Therefore, finite element analyses will be used to investigate the asymptotic crack-tip fields of kinked cracks with vanishing lengths at different kink angles.

In this paper, the global stress intensity factor solutions for dissimilar welds in lap-shear specimens will first be investigated for various weld widths. Two-dimensional finite element models are developed to obtain the stress intensity factor solutions for selected weld widths under plane strain conditions. The computational stress intensity factor solutions are compared with both the global stress intensity factor solutions obtained from the beam bending theory and those found from the elasticity theory for two dissimilar semi-infinite solids with a connection as derived by Erdogan [23]. Based on the analytical stress intensity factor solutions obtained from the beam bending theory and the elasticity theory for two dissimilar semi-infinite solids with connection, the transition weld width is determined and compared with the computational solutions for the magnesium-steel material combination in this study.

Next, the solutions for the vanishing crack are obtained by comparing the crack-tip stresses in the finite element model of the current material combination with a modified dissimilar material model which has a similar shear modulus ratio, but a bimaterial constant equal to zero. The solution of He and Hutchinson [22] is then adopted for the vanishing crack using the modified material since the stress distributions of interest are quite similar. Then, finite element models for three weld widths are developed to obtain local stress intensity factor solutions for kinked cracks with various lengths. The global stress intensity factor solutions and local stress intensity factor solutions for vanishing and finite kinked cracks will then be used to estimate the fatigue lives of dissimilar ultrasonic welds in a separate study reported in the future.

2.2. Analytical global stress intensity factor solutions for main cracks

The asymptotic in-plane stress field around an interface crack tip is an oscillatory field that can be characterized by a complex stress intensity factor **K (**$= K_1 + iK_2,\ i = \sqrt{-1}$) (Rice and Sih [24]). The stresses σ_y and τ_{xy} at a small distance r ahead of the interface crack tip are characterized by **K** as

$$\sigma_y + i\tau_{xy} = \frac{K_1 + iK_2}{\sqrt{2\pi r}}\left(\frac{r}{t}\right)^{i\varepsilon} \tag{1}$$

Here, the bimaterial constant ε is defined as

$$\varepsilon = \frac{1}{2\pi}\ln\frac{\kappa_u / G_u + 1/G_l}{\kappa_l / G_l + 1/G_u} \tag{2}$$

where G_u represents the shear modulus of the upper sheet and G_l represents the shear modulus of the lower sheet. Here, κ_u and κ_l for the upper and lower sheets, respectively, are defined as

$$\kappa_u = 3 - 4\nu_u \tag{3}$$

and

$$\kappa_l = 3 - 4\nu_l \tag{4}$$

under plane strain conditions. Note that ν_u and ν_l represent the Poisson's ratios of the upper and lower sheets, respectively.

In Equation (1), t represents a characteristic length [25, 26]. In this investigation, t represents the upper sheet thickness t_u which is the smaller value of the thicknesses of the two sheets bonded together as in Suo and Hutchinson [17] and Zhang [25]. It should be noted that when the two materials are identical, $\varepsilon = 0$. In this case, K_1 and K_2 in Equation (1) for the interface crack become the conventional stress intensity factors K_I and K_{II}, respectively.

The dog-bone area of the lap-shear specimen shown in Figure 2.1 can be modeled as two sheets with connection under lap-shear loading conditions. Figure 2.3(a) shows a schematic for two sheets with connection. The width of the connection is w. The two beams are subject to a lap-shear load F/b.

The global stress intensity factor solutions, K_1 and K_2, are obtained by Zhang [25] as

$$\begin{aligned}
K_1 = {} & \frac{\cosh(\pi\varepsilon)\sqrt{t_u}}{2\sqrt{3(1+\eta)(1+4\eta\delta+6\eta\delta^2+3\eta\delta^3)(1+\tan^2\omega)}} \times \\
& \left\{ \left[\frac{(1+4\eta\delta+9\eta\delta^2+6\eta\delta^3)\tan\omega}{\sqrt{1+2\eta\delta(2+3\delta+2\delta^2)+\eta^2\delta^4}} - \sqrt{3} \right] \sigma_{ui} \right. \\
& - \left[\frac{(1+4\eta\delta+3\eta\delta^2)\tan\omega}{\sqrt{1+2\eta\delta(2+3\delta+2\delta^2)+\eta^2\delta^4}} + \sqrt{3} \right] \sigma_{uo} \\
& + \eta \left[\frac{\delta(1-2\eta\delta-3\eta\delta^2)\tan\omega}{\sqrt{1+2\eta\delta(2+3\delta+2\delta^2)+\eta^2\delta^4}} + \sqrt{3}(2+\delta) \right] \sigma_{li} \\
& \left. - \eta\delta \left[\frac{(1+4\eta\delta+3\eta\delta^2)\tan\omega}{\sqrt{1+2\eta\delta(2+3\delta+2\delta^2)+\eta^2\delta^4}} + \sqrt{3} \right] \sigma_{lo} \right\}
\end{aligned} \tag{5}$$

$$\begin{aligned}
K_2 = {} & \frac{\cosh(\pi\varepsilon)\sqrt{t_u}}{2\sqrt{3(1+\eta)(1+4\eta\delta+6\eta\delta^2+3\eta\delta^3)(1+\tan^2\omega)}} \times \\
& \left\{ \left[\frac{(1+4\eta\delta+9\eta\delta^2+6\eta\delta^3)}{\sqrt{1+2\eta\delta(2+3\delta+2\delta^2)+\eta^2\delta^4}} + \sqrt{3}\tan\omega \right] \sigma_{ui} \right.
\end{aligned}$$

$$-\left[\frac{(1+4\eta\delta+3\eta\delta^2)}{\sqrt{1+2\eta\delta(2+3\delta+2\delta^2)+\eta^2\delta^4}}-\sqrt{3}\tan\omega\right]\sigma_{uo}$$
$$+\eta\left[\frac{\delta(1-2\eta\delta-3\eta\delta^2)}{\sqrt{1+2\eta\delta(2+3\delta+2\delta^2)+\eta^2\delta^4}}-\sqrt{3}(2+\delta)\tan\omega\right]\sigma_{li}$$
$$\left.-\eta\delta\left[\frac{(1+4\eta\delta+3\eta\delta^2)}{\sqrt{1+2\eta\delta(2+3\delta+2\delta^2)+\eta^2\delta^4}}-\sqrt{3}\tan\omega\right]\sigma_{lo}\right\} \tag{6}$$

where the modulus ratio η is defined as

$$\eta = E'_u / E'_l \tag{7}$$

Here,

$$E'_u = E_u /(1-\nu_u^2) \tag{8}$$

and

$$E'_l = E_l /(1-\nu_l^2) \tag{9}$$

Here, E_u and E_l represent the Young's Moduli of the upper and lower sheets, respectively. The thickness ratio δ is defined as

$$\delta = t_u / t_l \tag{10}$$

where t_u and t_l are the upper and lower sheet thicknesses, respectively. Note that the expressions shown in Equations (5) and (6) are for welds joining sheets with $\delta \le 1$. For welds joining sheets with $\delta > 1$, one should rotate the strip model by an angle of 180º to represent the same physical system but with $\delta < 1$.

The values of the angular quantity ω in Equations (5) and (6) can be found in Suo and Hutchinson [17]. The angular quantity ω is a function of the thickness ratio δ and the Dundurs' parameters α and β which are defined as

$$\alpha = \frac{(\kappa_l + 1)G_u - (\kappa_u + 1)G_l}{(\kappa_l + 1)G_u + (\kappa_u + 1)G_l} \tag{11}$$

$$\beta = \frac{(\kappa_l - 1)G_u - (\kappa_u - 1)G_l}{(\kappa_l + 1)G_u + (\kappa_u + 1)G_l} \tag{12}$$

Recall that the lap-shear specimen is loaded with a force per unit width, F/b, applied to the lower left and upper right sheets along the interface as shown in Figure 2.3(a). Figure 2.3(b) shows the left part of the strip model near the crack tip with linearly distributed structural stresses based on the classical Kirchhoff plate theory based on the work of Zhang [25]. As shown in Figure 2.3(b), σ_{ui}, σ_{uo}, σ_{li} and σ_{lo} represent the normal stresses at the inner (*i*) and outer (*o*) surfaces of the upper (*u*) and lower (*l*) strips, respectively. Note also that the normal stresses σ^*_{ui}, σ^*_{uo}, σ^*_{li} and σ^*_{lo} can be derived from the normal structural stresses σ_{ui}, σ_{uo}, σ_{li} and σ_{lo} based on the equilibrium equations and the continuity conditions of the strain and the strain gradient along the bond line. The normal structural stresses σ_{ui}, σ_{uo}, σ_{li} and σ_{lo} which are marked in Figure 2.3(b) for the left crack tip are

$$\sigma_{uo,left} = 0 \tag{13}$$

$$\sigma_{ui,left} = 0 \tag{14}$$

$$\sigma_{li,left} = \frac{4F}{t_l b} \tag{15}$$

$$\sigma_{lo,left} = -\frac{2F}{t_l b} \tag{16}$$

The normal structural stresses σ_{ui}, σ_{uo}, σ_{li} and σ_{lo} for the right crack tip are

$$\sigma_{uo,right} = -\frac{2F}{t_u b} \tag{17}$$

$$\sigma_{ui,right} = \frac{4F}{t_u b} \tag{18}$$

$$\sigma_{li,right} = 0 \tag{19}$$

$$\sigma_{lo,right} = 0 \tag{20}$$

The values of the analytical global stress intensity factors, K_1 and K_2, for the left and right tips of the weld can be obtained from Equations (5) and (6) based on Equations (13)-(20).

When the weld width w becomes small compared to the upper thickness t_u, the stress intensity factor K_1 and K_2 solutions should approach to those for two dissimilar semi-infinite solids with connection under shear loading conditions as presented by Erdogan [23]. Figure 2.4 shows a schematic diagram of two dissimilar semi-infinite solids with connection of the length w under remote shear and normal loads. The Cartesian $x-y$ coordinate system is also shown. The shear forces per unit width, F/b, are applied along the x axis at $x=+\infty$ and $x=-\infty$ of the upper and lower solids, respectively. The normal forces per unit width, N/b, are applied along the y-axis at $y=+\infty$ and $y=-\infty$ of the two semi-infinite solids. Stress intensity factor K_1^E and K_2^E solutions of Erdogan [23] are in the form

$$\sigma_y + i\tau_{xy} = \frac{K_1^E + iK_2^E}{\sqrt{2\pi r}}\left(\frac{r}{w}\right)^{i\varepsilon} \tag{21}$$

where K_1^E and K_2^E are

$$K_1^E = \frac{\sqrt{2}}{\sqrt{\pi w}}\frac{N}{b}\cosh(\pi\varepsilon) \tag{22}$$

$$K_2^E = \frac{\sqrt{2}}{\sqrt{\pi w}}\frac{F}{b}\cosh(\pi\varepsilon) \tag{23}$$

For homogenous materials, $\varepsilon = 0$. The stress intensity factor solutions in Equations (22) and (23) can be simplified to $K_{\mathrm{I,TPI}}$ and $K_{\mathrm{II,TPI}}$, [14], based on the Westergaard stress function as in Tada et al. [27] as

$$K_{\mathrm{I,TPI}} = \frac{\sqrt{2}N}{b\sqrt{\pi w}} \tag{24}$$

and

$$K_{\mathrm{II,TPI}} = \frac{\sqrt{2}F}{b\sqrt{\pi w}} \tag{25}$$

2.3. Computational global stress intensity factor solutions for main cracks

Finite element analyses were carried out in order to obtain the global stress intensity factor solutions as functions of the weld width and to determine the ranges of the weld width where the two sets of the analytical solutions are applicable. Note that the upper and lower sheets used during the experiments have nearly the same thickness. The finite element models for this investigation will be idealized with the same thickness for both sheets. Figure 2.5(a) shows a schematic of a two-dimensional finite elemental model of a lap-shear specimen and the boundary conditions. The specimen has the same upper and lower sheet thickness $t\,(= t_u = t_l)$, length L, overlap length V, and weld width w. The $x-y$ coordinate system is shown in the figure. The left edge has a fixed displacement condition at the middle surface while the right edge has a concentrated force per unit width, F/b, applied at the middle surface in the $+x$ direction.

The two-dimensional plane strain finite elemental model has the sheet thickness $t = 1.5$ mm, length $L = 100$ mm and overlap length $V = 75$ mm. The width b, as shown in Figure 2.1(c), of the reduced section in the dog-bone area of the specimen used in the model is 8 mm. Note that the ratio of the weld width to the thickness is 5.85 for the specimens used in the experiments. The stress intensity factor solutions in Equations (5) and (6) should be applicable to this case, but will be validated in this investigation. The two-dimensional plane strain finite element model is used to obtain the stress intensity factor solutions and compared to the solutions in Equations (5) and (6). For future engineering applications, the weld width w is varied for the finite element model in order to investigate the effect of the weld width on the global stress intensity factor solutions. The displacements of the middle surface of the left edge in the x and y directions are constrained as shown in the Figure 2.5(a). Figures 2.5(b) and 2.5(c) show the central part of the finite element mesh and a detailed view of the mesh for $w/t = 5.85$ near the right main crack tip, respectively. The weld indentation in the upper sheet as shown in Figure 2.2 is not modeled in the finite element analyses. The effect of the weld indentation on the weld failure was investigated in Lee [28] and in Chapter 3 under quasi-static and cyclic loading conditions, respectively. The weld zone and the base metal are assumed to be linear elastic. The top AZ31-H24 sheet is modeled with the Young's modulus $E = 45$ GPa and the Poisson's ratio $\nu = 0.35$. The bottom high strength low alloy steel sheet is modeled with the Young's modulus $E = 206.3$ GPa and the Poisson's ratio $\nu = 0.3$. Second-order quarter point crack-tip elements with collapsed nodes were used to model the $1/\sqrt{r}$ singularity near the crack tip. Twelve width to thickness ratios, namely, $w/t = 0.0067$, 0.05, 0.125, 0.25, 0.5, 0.64, 1, 2, 3, 4, 5.85 and 6 were evaluated in this investigation. The commercial finite element program ABAQUS [29] was employed to perform the computation.

It should be noted that K_1^A and K_2^A of the complex stress intensity factor $\mathbf{K}^A$ $(= K_1^A + iK_2^A)$ obtained directly from ABAQUS are defined such that the stresses σ_y and τ_{xy} at a small distance r ahead of an interface crack tip are characterized by $\mathbf{K}^A$ as

$$\sigma_y + i\tau_{xy} = \frac{K_1^A + iK_2^A}{\sqrt{2\pi r}} r^{i\varepsilon} \tag{26}$$

The K_1 and K_2 solutions as defined in Equation (1) are related to the K_1^A and K_2^A solutions as defined in Equation (26) as

$$K_1 = K_1^A \cos(\varepsilon \ln t) - K_2^A \sin(\varepsilon \ln t) \tag{27}$$

$$K_2 = K_1^A \sin(\varepsilon \ln t) + K_2^A \cos(\varepsilon \ln t) \tag{28}$$

In this investigation, the computational K_1 and K_2 solutions for spot welds joining two sheets of dissimilar materials are obtained from Equations (27) and (28) with the K_1^A and K_2^A solutions obtained from ABAQUS [29].

The Erdogan stress intensity factor solutions [23] are also transformed into the form of Equation (1) as

$$K_1 = K_1^E \cos\left(\varepsilon \ln \frac{t}{w}\right) - K_2^E \sin\left(\varepsilon \ln \frac{t}{w}\right) \tag{29}$$

$$K_2 = K_1^E \sin\left(\varepsilon \ln \frac{t}{w}\right) + K_2^E \cos\left(\varepsilon \ln \frac{t}{w}\right) \tag{30}$$

Substituting Equations (22) and (23) into (29) and (30) gives

$$K_{1,E} = \frac{\sqrt{2}}{b\sqrt{\pi w}}\left(N \cos\left(\varepsilon \ln \frac{t}{w}\right) - F \sin\left(\varepsilon \ln \frac{t}{w}\right)\right)\cosh(\pi\varepsilon) \tag{31}$$

$$K_{2,E} = \frac{\sqrt{2}}{b\sqrt{\pi w}}\left(N \sin\left(\varepsilon \ln \frac{t}{w}\right) + F \cos\left(\varepsilon \ln \frac{t}{w}\right)\right)\cosh(\pi\varepsilon) \tag{32}$$

For lap-shear loading, $N = 0$. Therefore the stress intensity factor solutions can be simplified to

$$K_{1,E} = \frac{\sqrt{2}}{b\sqrt{\pi w}}\left(-F \sin\left(\varepsilon \ln \frac{t}{w}\right)\right)\cosh(\pi\varepsilon) \tag{33}$$

$$K_{2,E} = \frac{\sqrt{2}}{b\sqrt{\pi w}}\left(F\cos\left(\varepsilon \ln \frac{t}{w}\right)\right)\cosh(\pi\varepsilon) \tag{34}$$

The computational results are compared with the analytical results from the beam bending theory for large ratios of w/t in Equations (5) and (6) and the Erdogan solution [23] for the ratio of w/t approaching to zero in Equations (33) and (34). For the convenience of comparison of the solutions, the effective stress intensity factor K_e is defined as

$$K_e = \sqrt{K_1^2 + K_2^2} \tag{35}$$

Figure 2.6(a) and 2.6(b) show a comparison of the normalized effective stress intensity factor $\overline{K}_e$ solutions as functions of w/t obtained from the finite element analyses, Equations (5) and (6) based on the beam bending theory, and Equations (33) and (34) based on the Erdogan solution in linear and logarithmic scales, respectively. Note that the effective stress intensity factor solutions are normalized by the effective stress intensity factor solutions based on Equations (5) and (6) of the beam bending theory for the right crack tip.

As shown in Figures 2.6(a) and 2.6(b), for large ratios of w/t, the computational solutions agree well with the effective stress intensity factor of the beam bending theory in Equations (5) and (6). As the ratio w/t decreases, the computational solutions approach to that of Erdogan. It should be mentioned that although the left and the right side of the weld have different stress intensity factor solutions, as the weld width becomes sufficiently small, the solutions approach each other. A normalized transition weld width can be defined where the effective stress intensity factor $\overline{K}_e$ of the beam bending theory is equal to that of Erdogan. For the right tip, the normalized transition weld width occurs at $w/t = 0.209$. For the left tip, the normalized transition weld width occurs at $w/t = 1.216$. The transition does not occur at the same w/t ratio for the two crack tips. The normalized transition weld width is smaller for the right side with the higher effective stress intensity factor. It should be noted that the normalized transition weld width for dissimilar welds in lap-shear specimens depends on the particular combination of materials. Sripichai et al. [14] found the normalized transition weld width is 0.364 for similar welds in lap-shear specimens of equal thickness. Generally speaking, the transition is expected to be at a small normalized width ratio. Table 2.1 lists the normalized computational $\overline{K}_1$, $\overline{K}_2$ and $\overline{K}_e$ solutions as functions of w/t for future engineering applications. The $\overline{K}_1$ and $\overline{K}_2$ solutions are normalized by the analytical $|K_2|$ solution for the right crack tip in Equation (6). The $\overline{K}_e$ solutions are normalized by the effective stress intensity factor solutions based on Equations (5) and (6) for the right crack tip.

The near-tip stresses for main cracks are also examined in this section. Figure 2.7(a) shows a magnified view of the finite element model near the right crack tip for the lap-shear specimen with $w/t = 5.85$. The crack-tip stresses are obtained as functions of the radial distance to the tip, r, directly ahead of and above the crack tip.

A second finite element analysis is also carried out with a set of modified elastics constants of $E = 48.6\,\text{GPa}$ and $\nu = 0.458$ for the magnesium sheet and $E = 206.3\,\text{GPa}$ and $\nu = 0.3$ for the steel sheet. This set of material elastic constants gives the same ratio of the shear moduli, but the Poisson’s ratio of the magnesium sheet is modified to give $\beta = 0$ and consequently $\varepsilon = 0$. Here, the steel material constants are kept the same as in the actual material. It would be preferred to keep the actual material constants from the magnesium sheet. However, this results in a negative Poisson’s ratio for the steel. The crack-tip stresses ahead of and above the crack tip are compared for the solutions based on the two sets of material elastic constants.

Figures 2.7(b) and 2.7(c) show the normalized opening and shear stresses $\sigma_{22}/\overline{\sigma}$ and $\sigma_{12}/\overline{\sigma}$ as functions of the normalized radius r/t directly ahead of the crack tip. Here, the stresses are normalized by $\bar{\sigma}$ $(= F/(bt))$ which is the normalized applied stress. As shown in the figures, the normalized opening and shear stresses $\sigma_{22}/\bar{\sigma}$ and $\sigma_{12}/\bar{\sigma}$ directly ahead of the crack tip for the two sets of material elastic constants are different when the normalized radius decreases due to the oscillation of the stress near the crack tip for the actual material. For the modified material combination with $\beta = 0$ or $\varepsilon = 0$, the crack tip stresses follow the usual $1/\sqrt{r}$ singularity. Figures 2.7(d) and 2.7(e) show the normalized stresses $\sigma_{11}/\bar{\sigma}$ and $\sigma_{12}/\bar{\sigma}$ as functions of the normalized radius r/t above the crack tip for the two sets of material elastic constants. As shown in the figures, the dominant normalized opening stress $\sigma_{11}/\bar{\sigma}$ appears to follow the $1/\sqrt{r}$ singularity quite consistently for both sets of material elastic constants while the normalized shear stress $\sigma_{12}/\bar{\sigma}$ remains slightly influenced by the oscillation of the actual material with $\beta \neq 0$ or $\varepsilon \neq 0$. The crack-tip stress shown in Figures 2.7(b)-(c) indicate that the oscillations of the crack-tip stresses appear to be stronger directly ahead of the tip.

The crack-tip opening stresses above the crack tip in the vertical direction does not appear to be influenced by the oscillation as the crack-tip stresses directly ahead of the crack tip. Note that from the experimental observations, kinked cracks grew in the vertical direction above the crack tip. This suggests that the local stress intensity factor solutions for the modified material with $\beta = 0$ or $\varepsilon = 0$ may be used for the kink crack with the vanishing kink length.

2.4. Analytical local stress intensity factor solutions for kinked cracks

Figure 2.8 shows a schematic of a main crack and a kinked crack with the kink length a and the kink angle φ. Here, K_1 and K_2 represent the global stress intensity factor solutions for the main crack, and k_{I} and k_{II} represent the local stress intensity factor solutions for the kinked crack. Note that the arrows in the figure represent the positive values of the global and local stress intensity factors K_1, K_2, k_I and k_II.

For kinked cracks in dissimilar material, when the kink length approaches to 0, the k_I and k_II solutions can be expressed as functions of the kink angle φ, the Dundurs' parameters α and β, and the global K_1 and K_2 solutions for the main crack. The local stress intensity factors k_I and k_II are expressed in the complex form (He and Hutchinson [22]) as

$$k_I + ik_{II} = \left(c_R^{HH} + ic_I^{HH}\right)\left(K_1 + iK_2\right)a^{i\varepsilon} + \left(d_R^{HH} - id_I^{HH}\right)\left(K_1 - iK_2\right)a^{-i\varepsilon} \qquad (36)$$

where c_R^{HH}, c_I^{HH}, d_R^{HH} and d_I^{HH} are the real and imaginary part of the complex function c^{HH} and d^{HH}. Both c^{HH} and d^{HH} are complex functions of α, β and φ. Equation (36) indicates that k_I and k_II depend on the crack length a and bimaterial constant ε. The global stress intensity factors K_1 and K_2 are defined in the form as in Equation (26).

The functions c_R^{HH}, c_I^{HH}, d_R^{HH} and d_I^{HH} were tabulated in He and Hutchinson [30]. The values for c^{HH} and d^{HH} were interpolated from that report. As indicated in Equation (36), when the crack length approaches zero, the values for the local stress intensity factor solutions depend on the value of a when the bimaterial constant ε is nonzero. The dependence of the solutions on the crack length a presents a challenge to develop a fatigue life estimation method based on a fatigue crack growth model, even though the oscillation is in a region which is too small to be of concern. This challenge prevents the evaluation of the limit at the crack length of $a = 0$ in Equation (36).

However, for $\varepsilon = 0$, Equation (36) simplifies to

$$\left(k_I\right)_0 = \left(c_R^{HH} + d_R^{HH}\right)K_1 - \left(c_I^{HH} + d_I^{HH}\right)K_2 \qquad (37)$$

$$(k_{II})_0 = (c_I^{HH} - d_I^{HH})K_1 + (c_R^{HH} - d_R^{HH})K_2 \tag{38}$$

where $(k_I)_0$ and $(k_{II})_0$ represent the mode I and II stress intensity factor solution at the kink length a equal to zero. For cracks between similar materials, Equations (37) and (38) are reduced to those of Cotterell and Rice [31]. It should be noted that for $\varepsilon = 0$, the crack-tip stresses recover the traditional $1/\sqrt{r}$ singularity.

The local stress intensity factor solutions for kinked cracks with finite crack lengths in lap-shear specimens can be expressed as functions of the normalized kink length a/t as in [14] as

$$k_I(a) = f_I(a, w/t) \cdot (k_I)_0 \tag{39}$$

$$k_{II}(a) = f_{II}(a, w/t) \cdot (k_I)_0 \tag{40}$$

where f_{I} and f_{II} are geometric functions which depend on the crack length a, the weld width w and the sheet thickness t for the given material combinations. The local stress intensity factor solutions for idealized dissimilar welds in lap-shear specimens were obtained computationally and presented in the normalized form in for $w/t = 5.85$ to match the experimental specimen dimensions and for $w/t = 1$ and 0.5 for future engineering applications.

2.5. Computational local stress intensity factor solutions for finite kinked cracks

Sripichai et al. [14] obtained local stress intensity factor solutions for kink cracks of different kink lengths by two-dimensional plane strain finite element analyses for welds of similar material with $w/t = 0.5$, 1 and 2. In this investigation, two-dimensional plane strain finite element analyses were carried out for dissimilar welds to investigate the local stress intensity factor solutions for kinked cracks with different kink lengths for $w/t = 0.5$, 1 and 5.85. Fourteen normalized kink lengths, namely, $a/t = 0.00093$, 0.002, 0.005, 0.01, 0.025, 0.05, 0.075, 0.1, 0.2, 0.3, 0.4, 0.5, 0.6 and 0.7 are considered in this investigation. First, local stress intensity factor solutions are obtained computationally for $w/t = 5.85$ for the actual material combination and the modified material combination with $\beta = 0$ or $\varepsilon = 0$. These computational solutions are compared with each other and with the solutions for the vanishing crack length in Equations (37) and (38) for the modified material combination. Then, the local stress intensity factor solutions for kinked cracks for $w/t = 0.5$, 1 and 5.85 will be investigated.

Figure 2.9(a) again shows a schematic of a two-dimensional finite element model of a lap-shear specimen and the boundary conditions similar to those in Figure 2.5(a). The finite element models are developed for the weld widths of $w = 0.75$, 1.5 and 8.78 mm that correspond to $w/t = 0.5$, 1 and 5.85, respectively. For $w/t = 5.85$, the finite element analyses are carried out for both the actual and modified material combinations with the additional normalized kink length $a/t = 6.67\times10^{-6}$ for comparison as the crack length approaches zero. The width b of the central portion of the dog-bone area of the specimen is 8 mm. The length L of the upper and lower sheets and the overlap distance V remain unchanged as 100 mm and 75 mm, respectively. Both upper and lower sheets have the same thickness of 1.5 mm. The loading and boundary conditions of the specimen are the same as those for the finite element model shown in Figure 2.5(a). In Figure 2.9(a), a kinked crack is schematically shown to grow from the right crack tip into the upper magnesium sheet. Based on the micrograph in Figure 2.2, the value of the kink angle in this investigation is selected to be 90° (according to the sign convention in Figure 2.8, the kinked angle φ should be -90°). Figure 2.9(b) shows the finite element mesh near the right crack tip for $w/t = 5.85$ and $a/t = 0.1$. Figures 2.9(c) and 2.9(d) show a detailed view of the mesh near the right main crack and a detailed view of the mesh near the kinked crack tip, respectively.

Figures 2.10(a) and 2.10(b) show the values of $k_{\mathrm{I}}/(k_{\mathrm{I}})_0$ as functions of the normalized kink length a/t for $w/t = 5.85$ for the actual material and the modified material combinations with $\beta = 0$ in linear and logarithmic scales, respectively. Note that the value of $(k_{\mathrm{I}})_0$ used for normalization is based on the analytical K_1 and K_2 solutions in Equations (5) and (6) and Equation (37) for the modified material combination with $\beta = 0$ and the kink angle $\varphi = -90°$. Also shown in the figures is the analytic solution for the kinked crack with vanishing kink length in Equation (37) for the modified material combination. As shown in Figure 2.10(b) in the logarithmic scale, the computational local stress intensity factor solutions are similar for both materials. The kinked crack solution in Equation (36) for the actual material combination would decrease as the kinked crack length decreases and does not appear to reach a limit. However, the kinked crack solution shown in Figure 2.10(b) based on Equation (37) for the modified material combination is constant for all crack lengths. This vanishing kinked crack solution correlates well with the computational $k_{\mathrm{I}}/(k_{\mathrm{I}})_0$ solution for both the actual and modified materials.

Figures 2.10(c) and 2.10(d) show the values of $|k_{\mathrm{II}}|/(k_{\mathrm{I}})_0$ as functions of the normalized kink length for both material combinations in linear and logarithmic scales, respectively. First, it should be noted that the magnitude of the local shear stress intensity factor is much less than that of the local opening stress intensity factor. From Figure 2.10(c), it can be seen that the computational solutions for the actual material combination are different from those of the modified material combination for small kink lengths. The analytical vanishing kinked crack solution for the modified material combination correlate well to the computational solution for the modified material combination. In summary, for the local shear stress intensity factor solutions, the results for the modified material combination do not agree well with those for the actual material combination. Although Equation (38) can be used to accurately predict the solution for vanishing kinked crack for the modified material combination, it is only an approximation for the actual material combination. However, the shear contribution may not be important for a fatigue crack growth model, where the magnitude of the local shear stresses is much less than the magnitude of the local opening stresses.

Figures 2.10(e) and 2.10(f) show the computational $k_e/(k_\mathrm{e})_0$ along with the analytical vanishing kinked crack solution for the modified material combination in linear and logarithmic scales, respectively. Note that the value of $(k_e)_0$ used for normalization is based on the analytical K_1 and K_2 solutions in Equations (5) and (6) and Equations (37) and (38) for the modified material combination with $\beta = 0$ and the kink angle $\varphi = -90°$. These figures are remarkably similar to Figures 2.10(a) and 2.10(b) for $k_I/(k_\mathrm{I})_0$. It can be seen from Figure 2.10(f) that the stress intensity factor solution for the vanishing kinked crack in Equations (37) and (38) for the modified material combination agree with the computational solutions as the kink length decreases for the actual material combination. This is quite useful because a crack growth model needs to use the effective stress intensity factor k_e for the kink length equal to zero. Therefore, the analytical solution for the modified material combination can be used to obtain the local stress intensity factor solutions for the kink length equal to zero without impacting the accuracy of the fatigue crack growth model.

Figures 2.11(a) and 2.11(b) show the values of $k_\mathrm{I}/(k_\mathrm{I})_0$ as functions of the normalized kink length a/t for $w/t = 0.5$, 1 and 5.85 for the entire range and an enlarged section for small kinked cracks respectively. Note that the value of $(k_\mathrm{I})_0$ used for normalization is based on the analytical K_1 and K_2 solutions in Equations (5) and (6) and the kinked crack solution in Equation (37) for the modified material combination with $\beta = 0$ and the kink angle $\varphi = -90°$.

Figure 2.11(b) shows that, as the kink length approaches to 0, the value of $k_{\mathrm{I}}/(k_{\mathrm{I}})_0$ appears to approach to the local stress intensity factor solutions, shown as symbols at $a/t=0$, based on Equation (37) for the modified material combination and the computational K_1 and K_2 solutions for the main crack (without kinked cracks) for the modified material combination. The value of $k_{\mathrm{I}}/(k_{\mathrm{I}})_0$ increases monotonically as the kink length increases.

Figure 2.12 shows the values of $|k_{\mathrm{II}}|/(k_{\mathrm{I}})_0$ as functions of the normalized kink length a/t for $w/t=0.5$, 1 and 5.85. Note that the local stress intensity factor solutions k_{II} are negative as defined in Figure 2.8. Figure 2.12 shows that for $w/t=0.5$, 1 and 5.85, as the kink length approaches to 0, the value of $|k_{\mathrm{II}}|/(k_{\mathrm{I}})_0$ does not appears to follow the trend to approach to the local stress intensity factor solutions, shown as symbols at $a/t=0$. The local vanishing crack solutions shown are based on Equation (38) and the computational K_1 and K_2 solutions for the main crack for the modified material combination. It should be noted that the k_{I} local stress intensity factor solution which appears to be accurate is more dominant than the k_{II} local stress intensity factor solution. For $w/t=1$ and 5.85, as the kink length increases beyond the small kink length of $a/t=0.025$, the value of $|k_{\mathrm{II}}|/(k_{\mathrm{I}})_0$ decreases and appears to approach to 0 for a very large kink length.

As shown in Figure 2.12 for $w/t=0.5$, as the kink length increases, the value of $|k_{\mathrm{II}}|/(k_{\mathrm{I}})_0$ increases until it reaches the maximum value near the normalized kink length $a/t=0.2$. This is similar to the behavior of $|k_{\mathrm{II}}|/(k_{\mathrm{I}})_0$ for $w/t=0.5$ for similar welds [14]. As the kink length further increases, the value of $|k_{\mathrm{II}}|/(k_{\mathrm{I}})_0$ decreases and appears to approach to 0 for a very large kink length. It should be noted that the computational k_{I} and k_{II} solutions in Sripichai et al. [14]

and in this paper, can only indicate the trends of the local k_{I} and k_{II} solutions as the kink length approaches to 0.

Figures 2.13(a) and 2.13(b) shows the values of $k_e/(k_{\mathrm{e}})_0$ as functions of the normalized kink length a/t for $w/t = 0.5$, 1 and 5.85, for the entire range and an enlarged section for small kinked cracks respectively. Note that the value of $(k_e)_0$ used for normalization is based on the analytical K_1 and K_2 solutions in Equations (5) and (6) and Equations (37) and (38) for the modified material combination with $\beta = 0$ and the kink angle $\varphi = -90°$. Figure 2.13(a) appears very similar to Figure 2.11(a) which displays the values of $k_{\mathrm{I}}/(k_{\mathrm{I}})_0$. This is consistent with the kinked crack growing under dominant mode I loading conditions. Here, for a kinked crack of zero length, Figure 2.13(b) shows that the value of $k_e/(k_{\mathrm{e}})_0$ appears to approach the local stress intensity factor solutions, shown as symbols at $a/t = 0$, based on Equations (37) and (38) for the modified material combination and the computational K_1 and K_2 solutions for the main crack for the modified material combination. As the value of a/t increases, the value of $k_e/(k_{\mathrm{e}})_0$ increases monotonically, just as seen in Figure 2.11(a) for $k_{\mathrm{I}}/(k_{\mathrm{I}})_0$.

The solution shows that the k_{I} solutions for kinked cracks from the finite element analyses indeed show some trend to approach to the theoretical kinked crack solution at $a/t = 0$ for the modified material combination as the kink length decreases. The k_{II} solutions for kinked cracks from the finite element analyses do not approach to the theoretical kinked crack solution at $a/t = 0$ for the modified material combination as the kink length decreases. These normalized values of the local stress intensity factor solutions indicate that the kinked crack growth is under mixed mode I and II loading conditions. However, the kinked cracks are under dominant mode I loading conditions and the computational k_{e} solutions approach to that for the vanishing kinked crack solution for the modified material combination. Table 2.2 and 2.3 list the normalized local stress intensity factor k_I and k_II solutions, respectively, for $\varphi = -90°$, $w/t = 0.5$, 1 and 5.85 for future engineering applications. Note that at $a/t = 0$ the values for $k_\mathrm{I}/(k_\mathrm{I})_0$ are not 1, since the $(k_\mathrm{I})_0$ solutions used for normalization are obtained from the analytical K_1 and K_2 solutions based on the beam bending theory while the values being normalized are based on computational results.

2.6. Conclusions

First, global stress intensity factors for welds of various widths in lap-shear specimens of magnesium and steel sheets were obtained using finite element analyses and compared with two analytical solutions. The transition value is dependent on the weld width and the dissimilar materials used in the weld. Welded specimens of magnesium and steel sheets with a normalized width ratio, w/t, smaller than a transition value of 0.209 more closely follow analytical solutions based on semi-infinite solids with connection. Welds with a normalized width ratio, w/t, larger than a transition value of 1.216 more closely follow analytical solutions based on beam bending theory. The accuracy of the analytical solution based on beam bending improves as the weld width increases.

Next, welds in lap-shear specimens with kinked cracks of various lengths were modeled using finite element with both the actual material combination and a modified material combination such that the bimaterial constant was zero. Stresses directly ahead of and directly above the crack tip were compared for both material combinations. Ahead of the crack tip, the stresses were not similar due to the oscillation of the crack-tip stress field in the model with the actual material combination. However, above the crack tip, at a kink angle of $\varphi = -90$, the stresses were only weakly affected by the oscillation and stresses for both material combinations were quite similar. For large kink angles, the modified material combination may be substituted such that the bimaterial constant is zero, allowing use of existing analytical solutions to approximate the local stress intensity factors for a vanishing kinked crack of length $a = 0$.

Lastly, the local stress intensity factors for kinked cracks of finite length were obtained computationally and compared with vanishing crack solutions evaluated using the modified material. As the kink length decreases, the local k_{I} is shown to approach the solutions for a vanishing crack, while the local k_{II} solutions do not trend toward the solutions for a vanishing crack. The kinked cracks are under dominant mode I loading conditions. Therefore the k_{e} solutions, which are most important for fatigue estimations, are shown to approach the solutions for a vanishing crack as the kink length decreases. The global stress intensity factor solutions and the local stress intensity factor solutions for vanishing and finite kinked cracks can be adopted for fatigue life estimations in future research.

Table 2.1a: The normalized global stress intensity factor $\overline{K}_1$,$\overline{K}_2$ and $\overline{K}_e$ solutions for the left crack tip at various normalized weld widths.

w/t	0.0067	0.05	0.125	0.25	0.5	0.64
$\overline{K}_{1,\text{left}}$	-2.633	-0.726	-0.370	-0.187	-0.025	0.037
$\lvert\overline{K}_2\rvert_{\text{left}}$	6.378	2.296	1.365	0.864	0.510	0.425
$\overline{K}_{e,\text{left}}$	5.572	1.944	1.142	0.714	0.412	0.344

Table 2.1a continued

w/t	1	2	3	4	5.85	6
$\overline{K}_{1,\text{left}}$	0.161	0.328	0.355	0.358	0.358	0.358
$\lvert\overline{K}_2\rvert_{\text{left}}$	0.339	0.351	0.366	0.368	0.368	0.368
$\overline{K}_{e,\text{left}}$	0.303	0.388	0.412	0.414	0.415	0.415

Table 2.1b: The normalized global stress intensity factor $\overline{K}_1$,$\overline{K}_2$ and $\overline{K}_e$ solutions for the right crack tip at various normalized weld widths.

w/t	0.0067	0.05	0.125	0.25	0.5	0.64
$\overline{K}_{1,\text{right}}$	2.643	0.787	0.468	0.348	0.331	0.357
$\lvert\overline{K}_2\rvert_{\text{right}}$	6.412	2.540	1.746	1.390	1.193	1.152
$\overline{K}_{e,\text{right}}$	5.600	2.147	1.460	1.157	1.000	0.974

Table 2.1b continued

w/t	1	2	3	4	5.85	6
$\overline{K}_{1,\text{right}}$	0.454	0.666	0.719	0.728	0.729	0.729
$\lvert\overline{K}_2\rvert_{\text{right}}$	1.099	1.029	1.006	1.003	1.002	1.002
$\overline{K}_{e,\text{right}}$	0.960	0.990	0.999	1.001	1.001	1.001

Table 2.2: The normalized local stress intensity factor $k_{\mathrm{I}}/(k_{\mathrm{I}})_0$ solutions for $\varphi = -90°$, $w/t = 0.5$, 1, and 5.85.

	a/t	0	0.00093	0.002	0.005	0.01	0.025	0.05	0.075
$k_{\mathrm{I}}/(k_{\mathrm{I}})_0$	$w/t = 0.5$	1.001	1.006	1.029	1.066	1.108	1.201	1.328	1.445
$k_{\mathrm{I}}/(k_{\mathrm{I}})_0$	$w/t = 1$	0.979	0.995	1.012	1.045	1.079	1.162	1.279	1.389
$k_{\mathrm{I}}/(k_{\mathrm{I}})_0$	$w/t = 5.85$	0.999	1.049	1.058	1.078	1.106	1.178	1.287	1.393

Table 2.2 continued

	a/t	0.1	0.2	0.3	0.4	0.5	0.6	0.7
$k_{\mathrm{I}}/(k_{\mathrm{I}})_0$	$w/t = 0.5$	1.558	2.038	2.637	3.483	4.783	6.975	11.191
$k_{\mathrm{I}}/(k_{\mathrm{I}})_0$	$w/t = 1$	1.499	1.982	2.596	3.461	4.775	6.975	11.193
$k_{\mathrm{I}}/(k_{\mathrm{I}})_0$	$w/t = 5.85$	1.500	1.973	2.586	3.448	4.761	6.957	11.169

Table 2.3: The normalized local stress intensity factor $|k_{\mathrm{II}}|/(k_{\mathrm{I}})_0$ solutions for $\varphi = -90°$, $w/t = 0.5$, 1, and 5.85.

	a/t	0	0.00093	0.002	0.005	0.01	0.025	0.05	0.075
$|k_{\mathrm{II}}|/(k_{\mathrm{I}})_0$	$w/t = 0.5$	0.136	0.076	0.084	0.094	0.103	0.115	0.127	0.136
$|k_{\mathrm{II}}|/(k_{\mathrm{I}})_0$	$w/t = 1$	0.170	0.106	0.113	0.124	0.124	0.126	0.122	0.117
$|k_{\mathrm{II}}|/(k_{\mathrm{I}})_0$	$w/t = 5.85$	0.236	0.175	0.181	0.187	0.189	0.187	0.178	0.168

Table 2.3 continued

	a/t	0.1	0.2	0.3	0.4	0.5	0.6	0.7
$|k_{\mathrm{II}}|/(k_{\mathrm{I}})_0$	$w/t = 0.5$	0.144	0.158	0.147	0.119	0.084	0.051	0.024
$|k_{\mathrm{II}}|/(k_{\mathrm{I}})_0$	$w/t = 1$	0.112	0.093	0.076	0.058	0.042	0.026	0.013
$|k_{\mathrm{II}}|/(k_{\mathrm{I}})_0$	$w/t = 5.85$	0.158	0.124	0.095	0.069	0.047	0.028	0.013

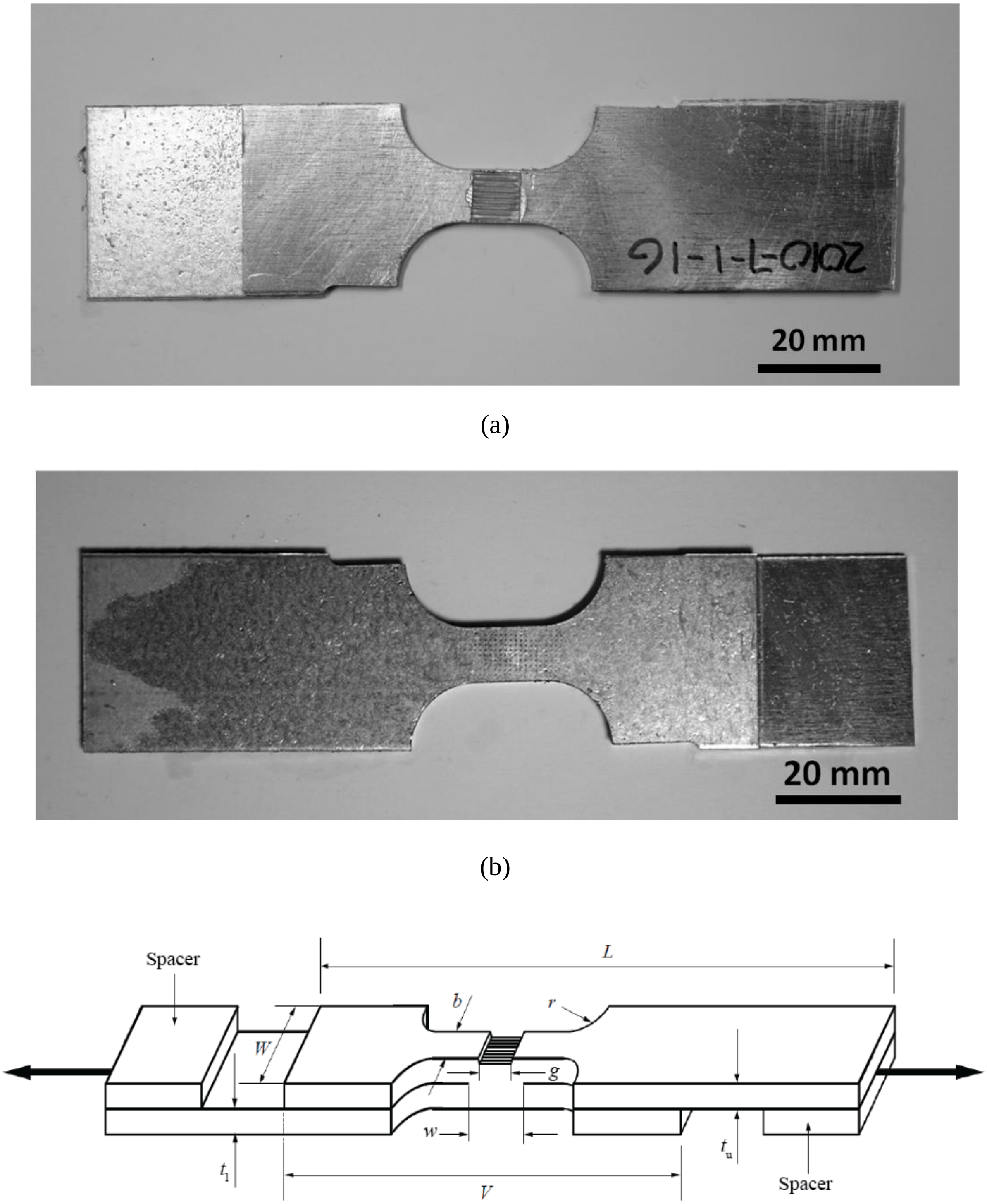

(a)

(b)

(c)

Figure 2.1. (a) A top view and (b) a bottom view of an ultrasonic welded lap-shear specimen which has been machined into a dog-bone shape. (c) A schematic of a lap-shear specimen. The applied force F is shown as the bold arrows.

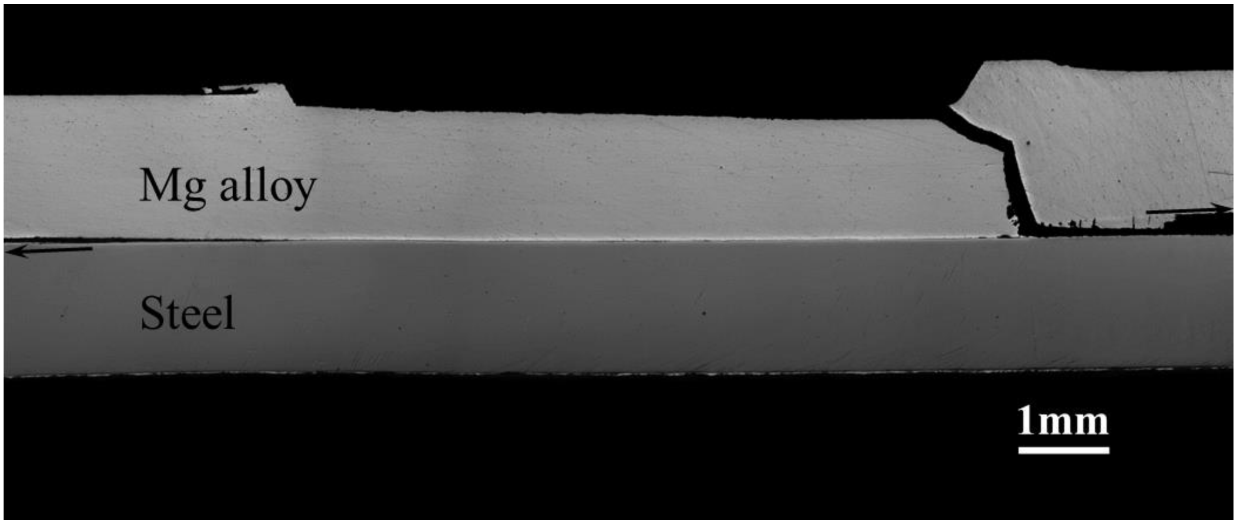

Figure 2.2. An optical micrographs of a failed weld at the fatigue life of 1.7×10^{3} cycles under a load range of 1.70 kN.

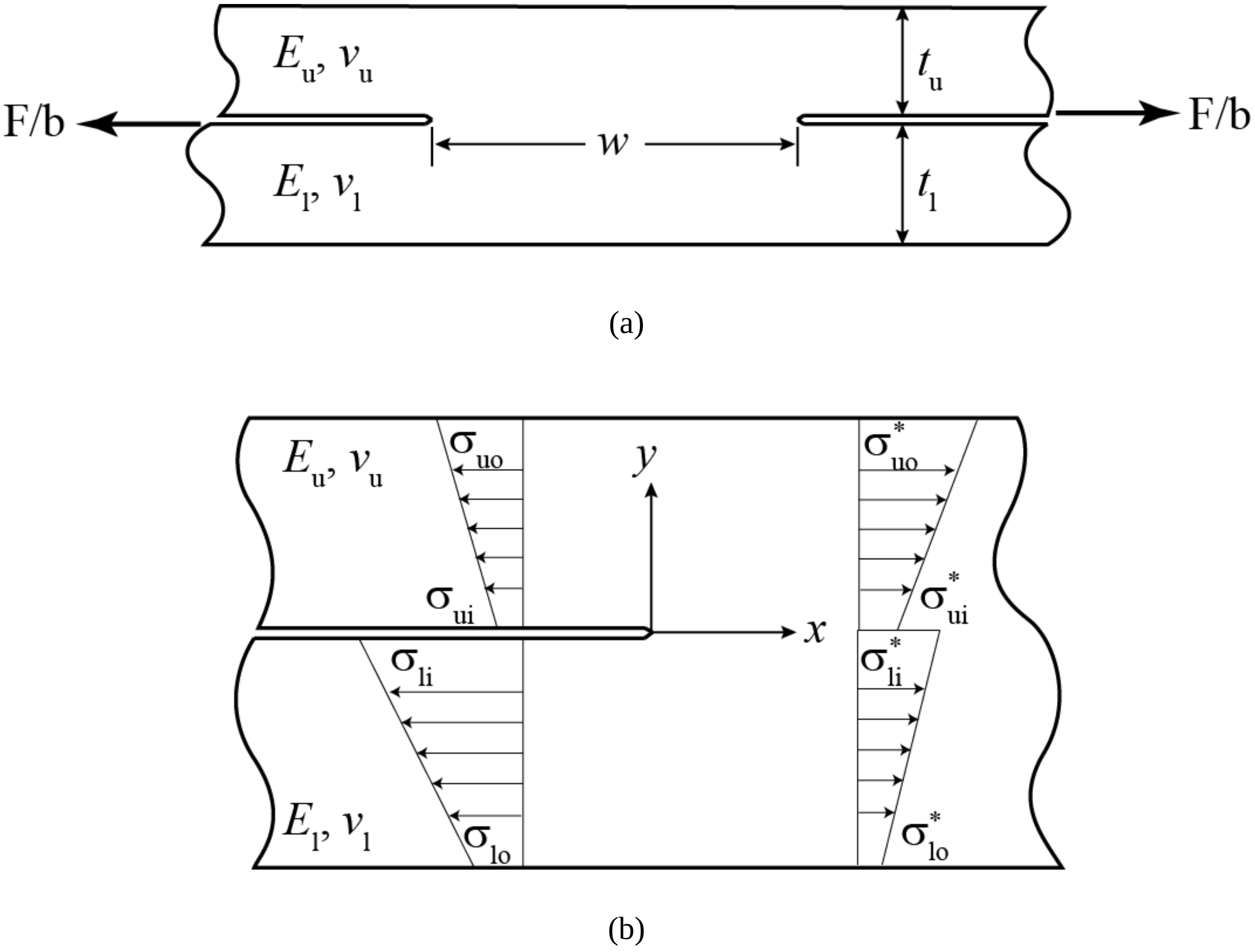

Figure 2.3. (a) A schematic of the weld with the lap-shear loading condition. (b) A schematic of the left crack tip showing the normal stresses σ_{ui}, σ_{uo}, σ_{li} and σ_{lo} at the inner (*i*) and outer (*o*) surfaces of the upper (*u*) and lower (*l*) strips, respectively.

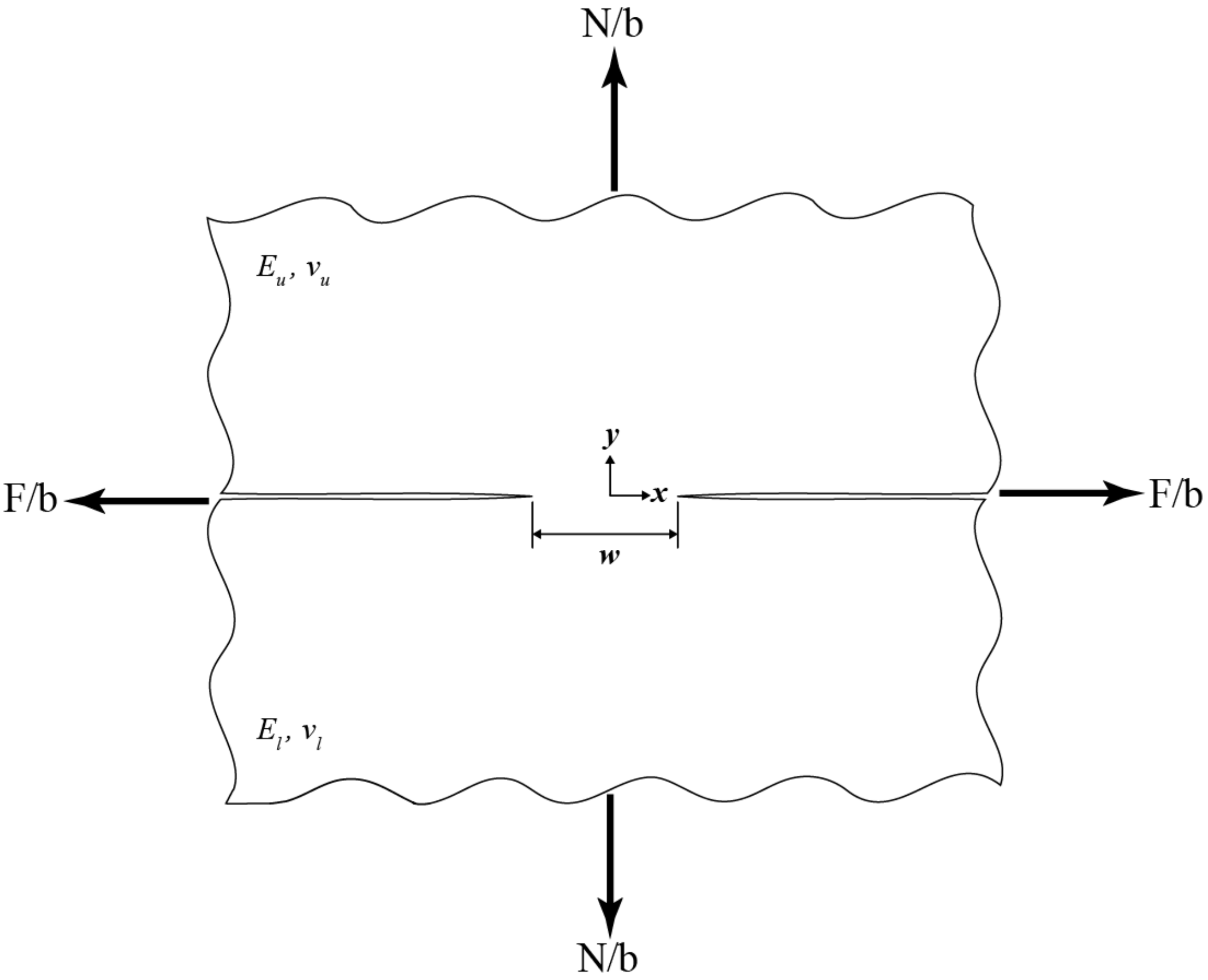

Figure 2.4. A schematic diagram of two semi-infinite solids of dissimilar materials with connection of the length w. The Cartesian $x-y$ coordinate system is shown. The shear forces per unit width, F/b, are applied along the x axis at $x=+\infty$ and $-\infty$ of the upper solid and lower solid, respectively. The normal forces per unit width, N/b, are applied along the y axis at $y=+\infty$ and $-\infty$ of the upper solid and lower solid, respectively.

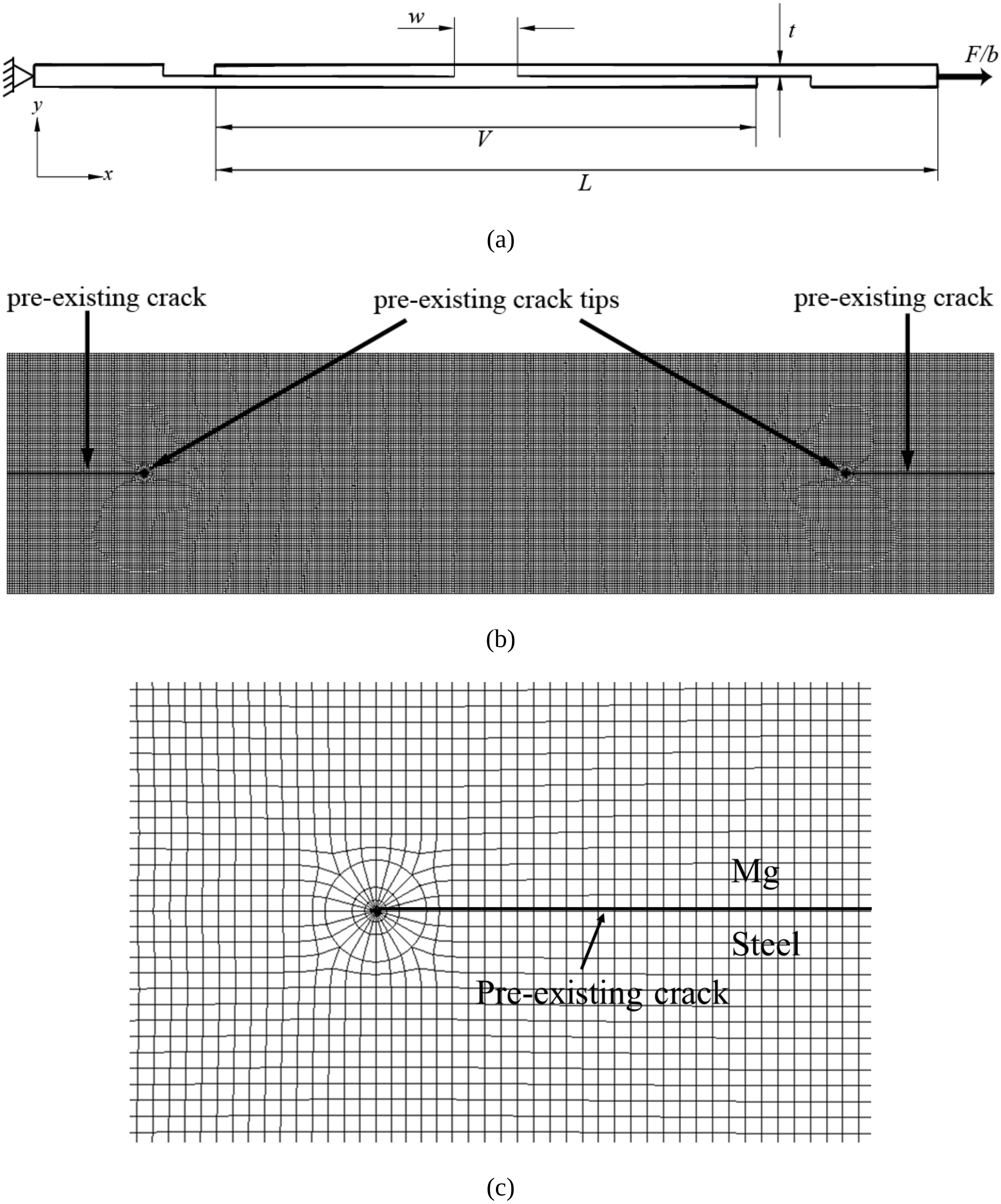

Figure 2.5. (a) A schematic of a two-dimensional finite element model of a lap-shear specimen with the boundary and loading conditions. (b) A view of the finite element mesh for the idealized model showing the weld nugget and both pre-existing crack tips for a w/t ratio of 5.85, and (c) a close-up view of the finite element mesh near the right crack tip.

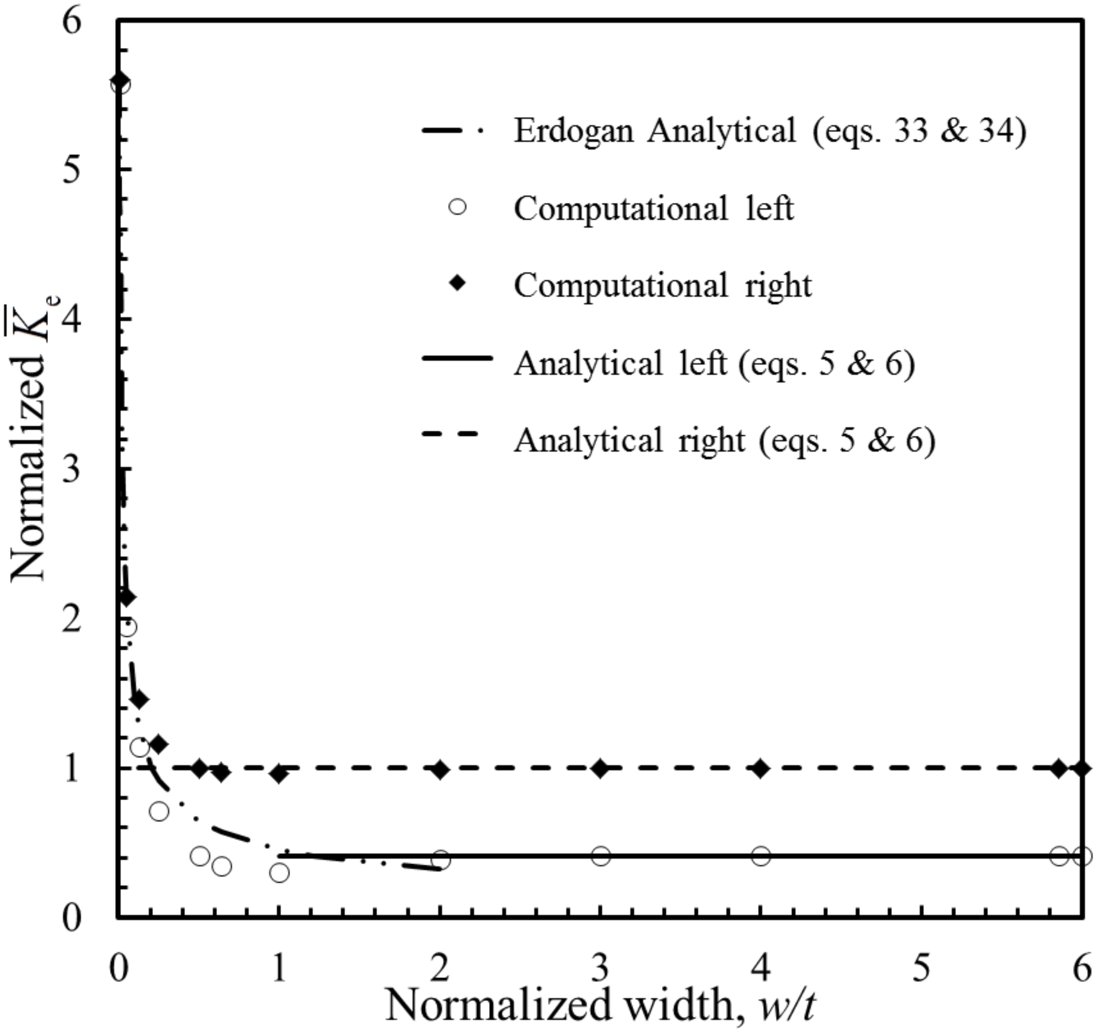
Erdogan Analytical (eqs. 33 & 34)
Computational left
Computational right
Analytical left (eqs. 5 & 6)
Analytical right (eqs. 5 & 6)
Normalized $\overline{K}_e$
Normalized width, w/t
0
1
2
3
4
5
6
0
1
2
3
4
5
6

(a)

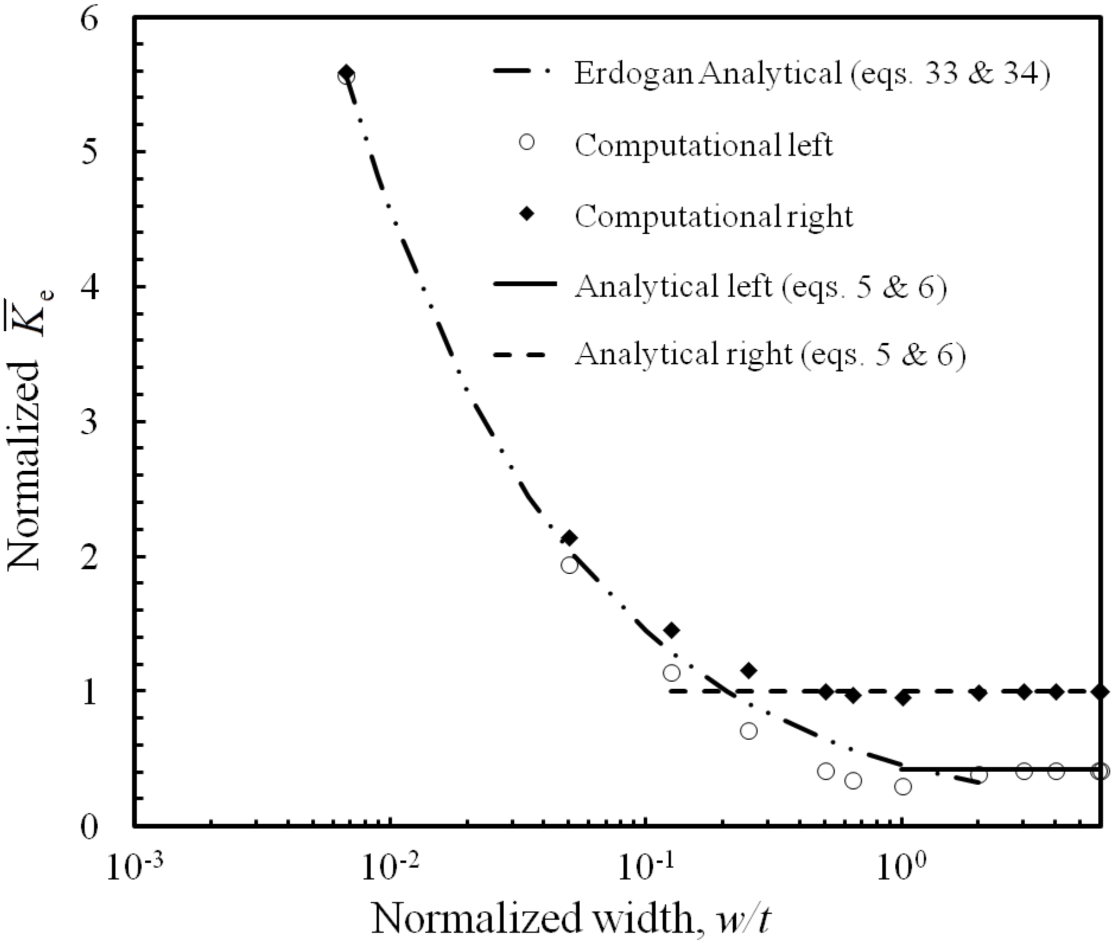

(b)

Figure 2.6. The normalized effective stress intensity factor solutions as functions of w/t plotted in (a) linear and (b) logarithmic scales.

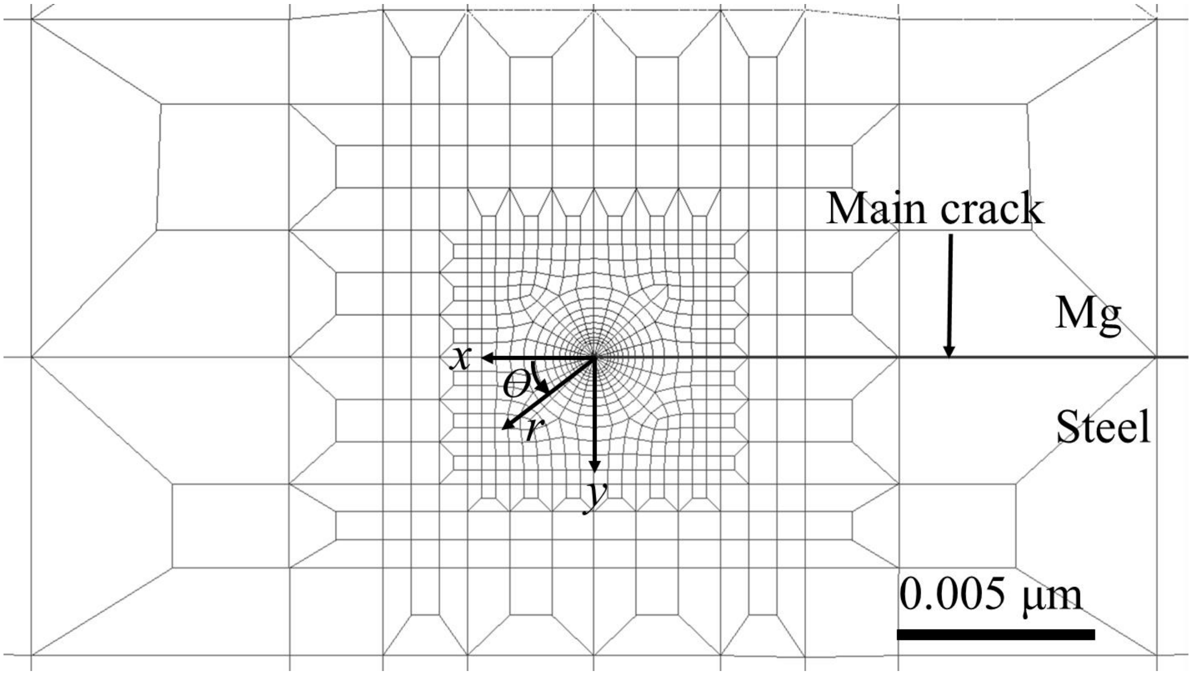
Main crack
Mg
Steel
x
y
θ
r
0.005 μm

(a)

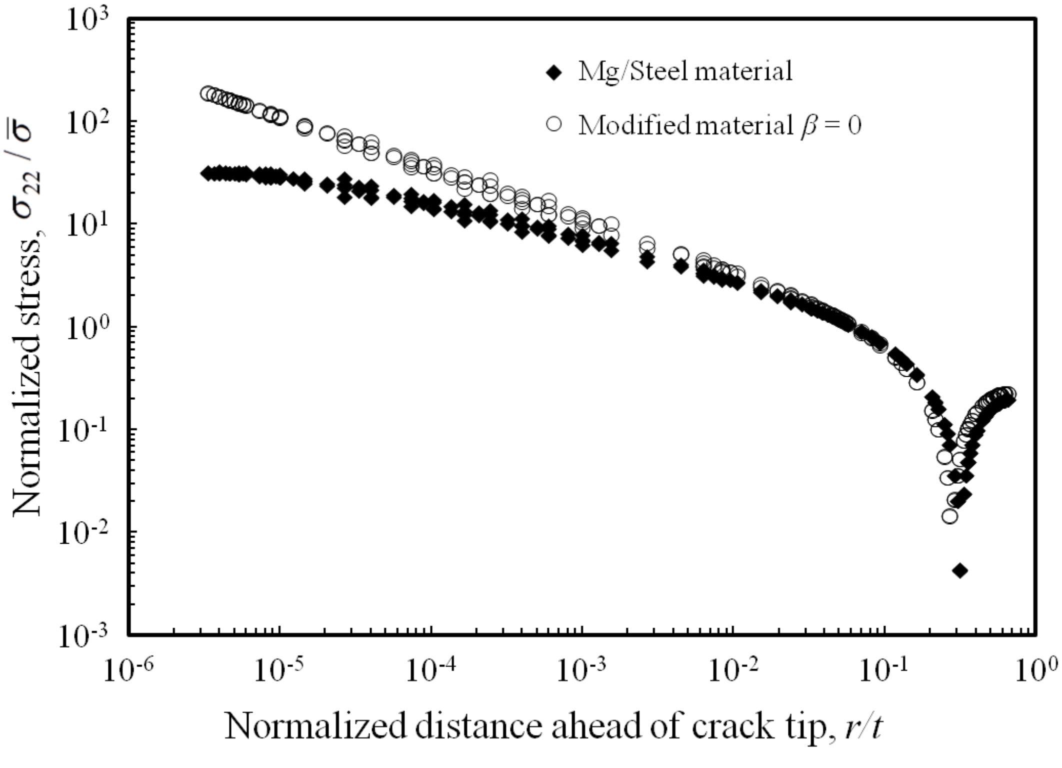
Mg/Steel material
Modified material β = 0
Normalized stress, $\sigma_{22} / \overline{\sigma}$
Normalized distance ahead of crack tip, r/t
10^{3}
10^{2}
10^{1}
10^{0}
10^{-1}
10^{-2}
10^{-3}
10^{-6}
10^{-5}
10^{-4}
10^{-3}
10^{-2}
10^{-1}
10^{0}

(b)

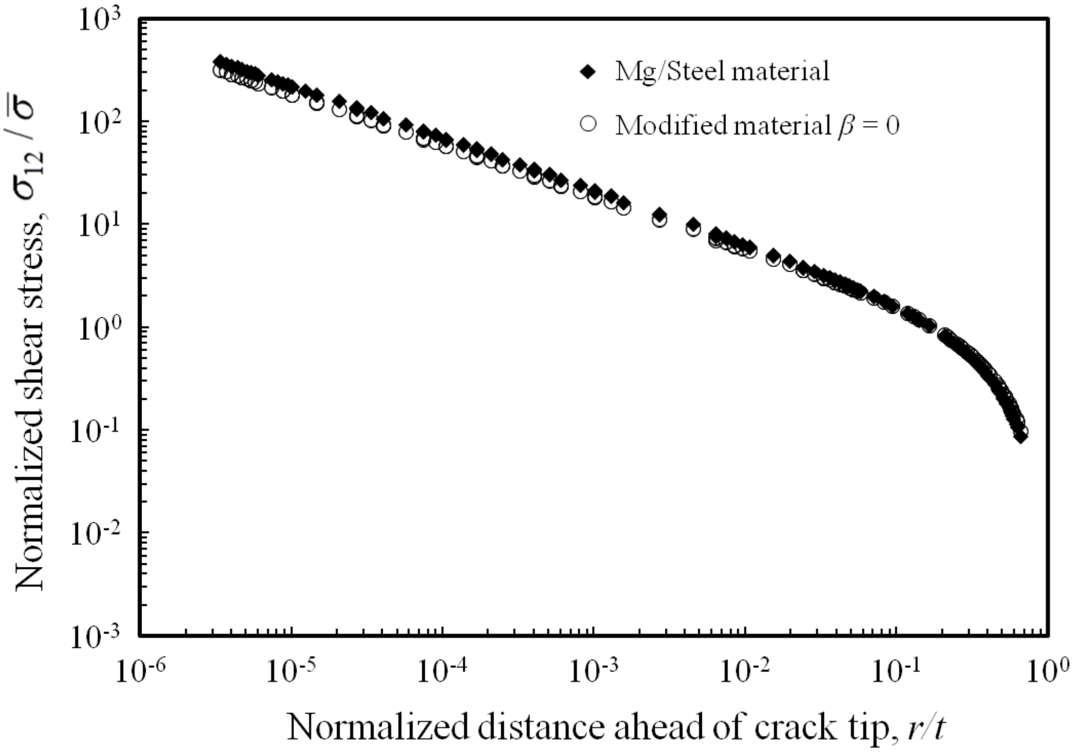
Normalized shear stress, $\sigma_{12} / \overline{\sigma}$
10^{3}
10^{2}
10^{1}
10^{0}
10^{-1}
10^{-2}
10^{-3}
10^{-6}
10^{-5}
10^{-4}
10^{-3}
10^{-2}
10^{-1}
10^{0}
◆ Mg/Steel material
○ Modified material $\beta = 0$
Normalized distance ahead of crack tip, r/t

(c)

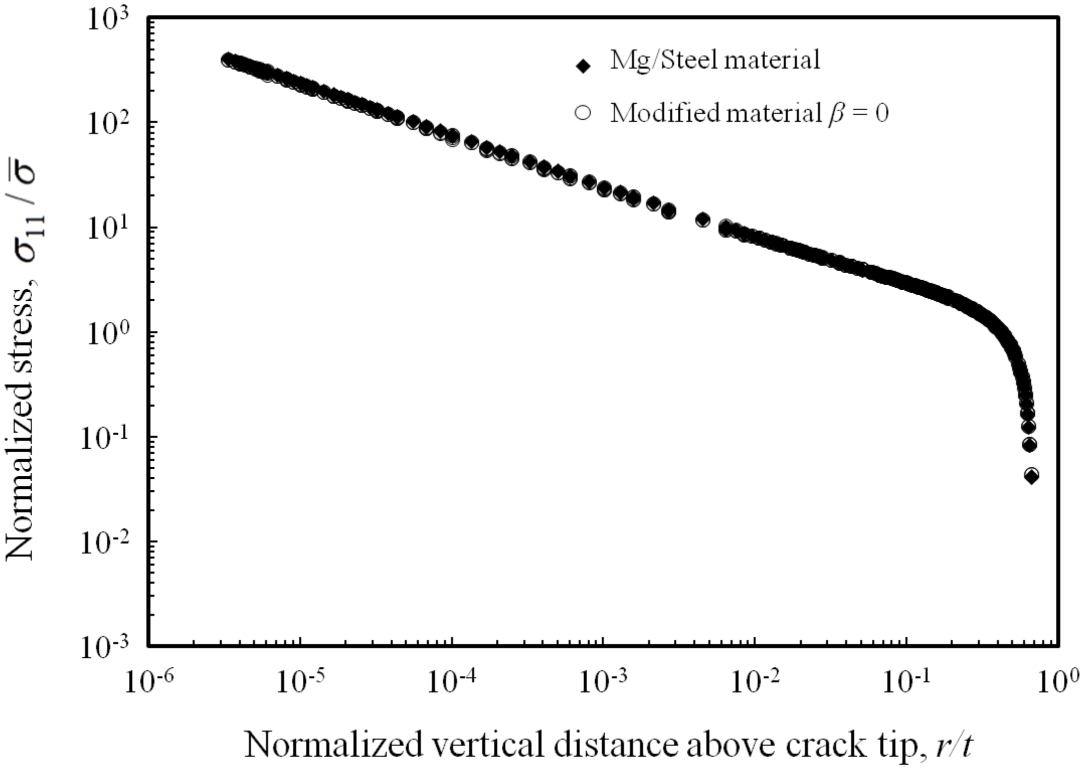
Normalized stress, $\sigma_{11} / \overline{\sigma}$
10^{3}
10^{2}
10^{1}
10^{0}
10^{-1}
10^{-2}
10^{-3}
10^{-6}
10^{-5}
10^{-4}
10^{-3}
10^{-2}
10^{-1}
10^{0}
◆ Mg/Steel material
○ Modified material $\beta = 0$
Normalized vertical distance above crack tip, r/t

(d)

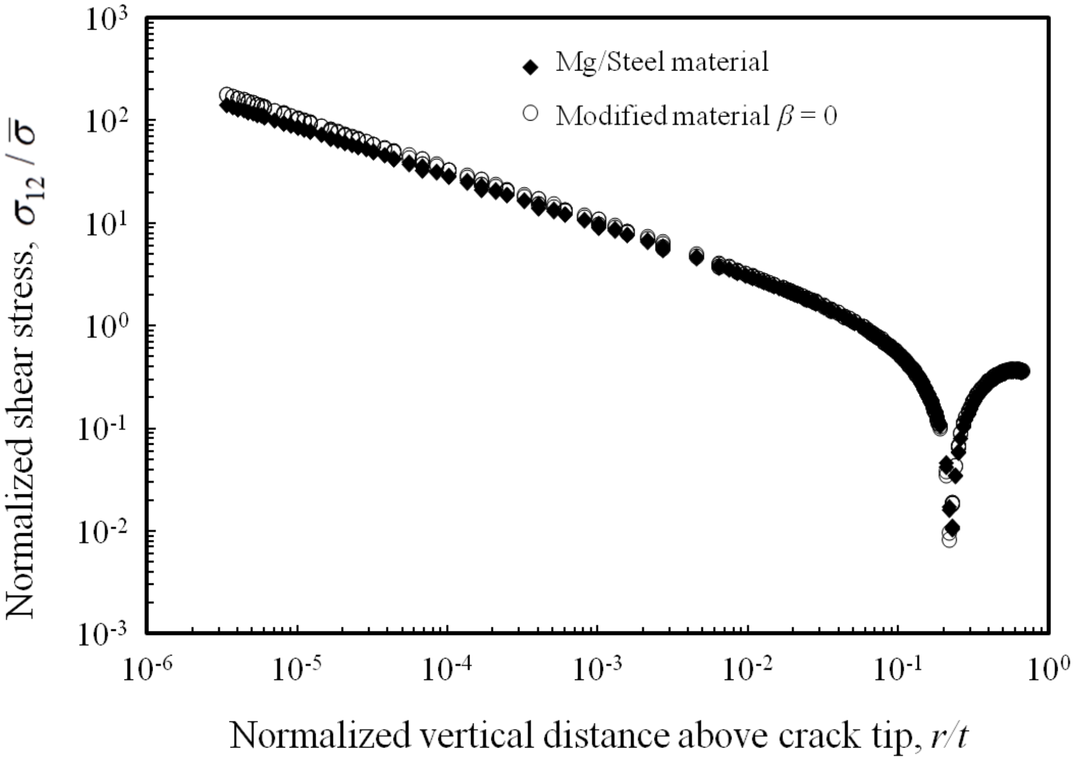

(e)

Figure 2.7. (a) The finite element mesh near the right main crack indicating the directions ahead of the crack tip $\theta = 0$, and above the crack tip $\theta = -90$, as pointing horizontally and vertically from the main crack tip respectively. (b) A comparison between the actual material combination and the modified material combination with $\beta = 0$ showing the normal stress in the $y-$direction ahead of the crack tip, (c) the shear stress ahead of the crack tip, (d) the normal stress in the $x-$direction vertically above the crack tip, and (e) the shear stress vertically above the crack tip.

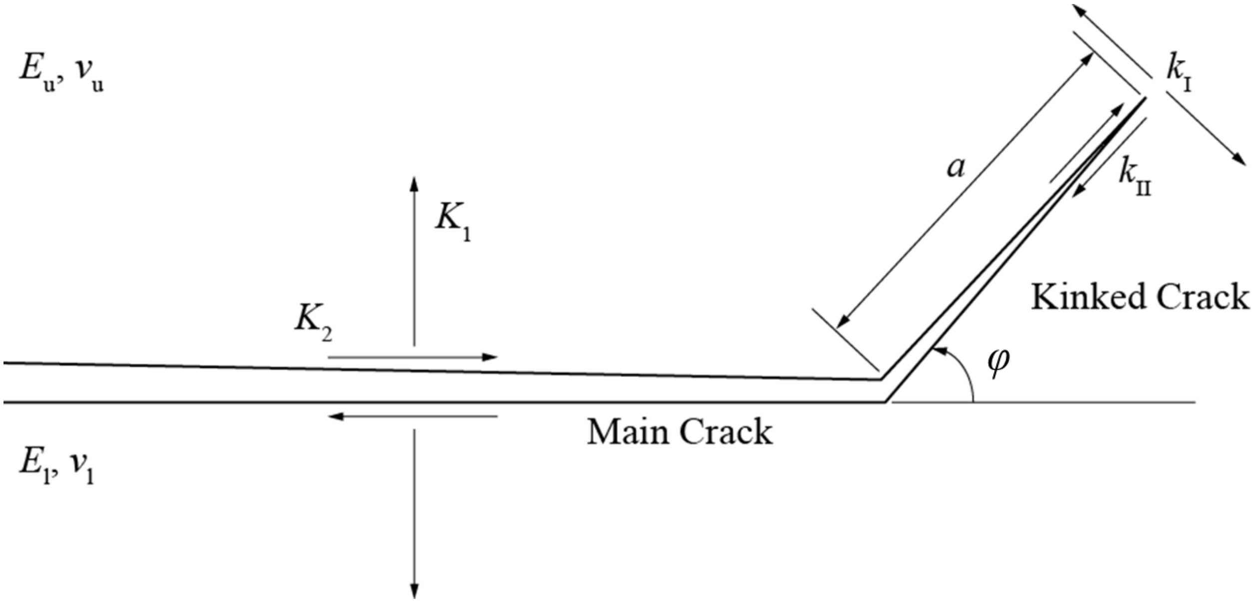

Figure 2.8. A schematic of a main crack and a kinked crack with the kink length a and the kink angle φ.

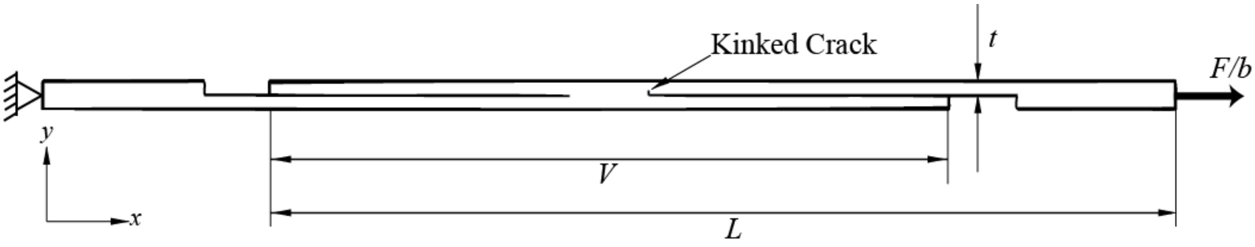
Kinked Crack
t
F/b
y
x
V
L

(a)

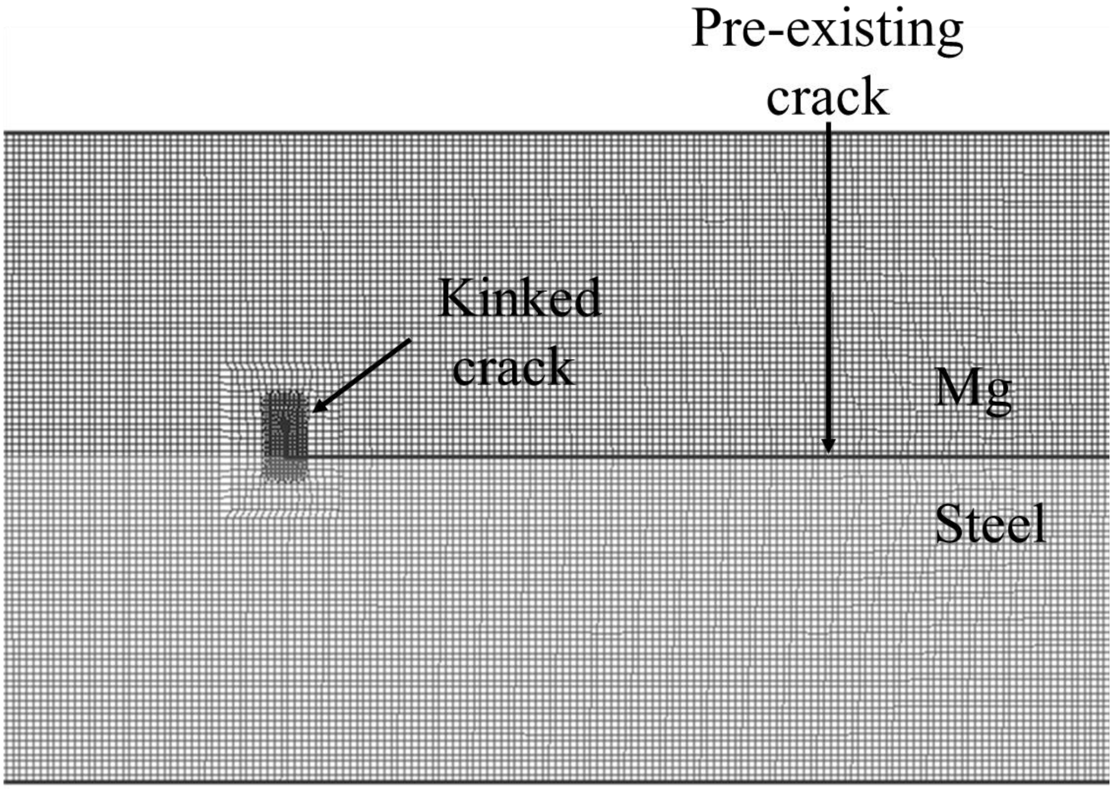
Pre-existing crack
Kinked crack
Mg
Steel

(b)

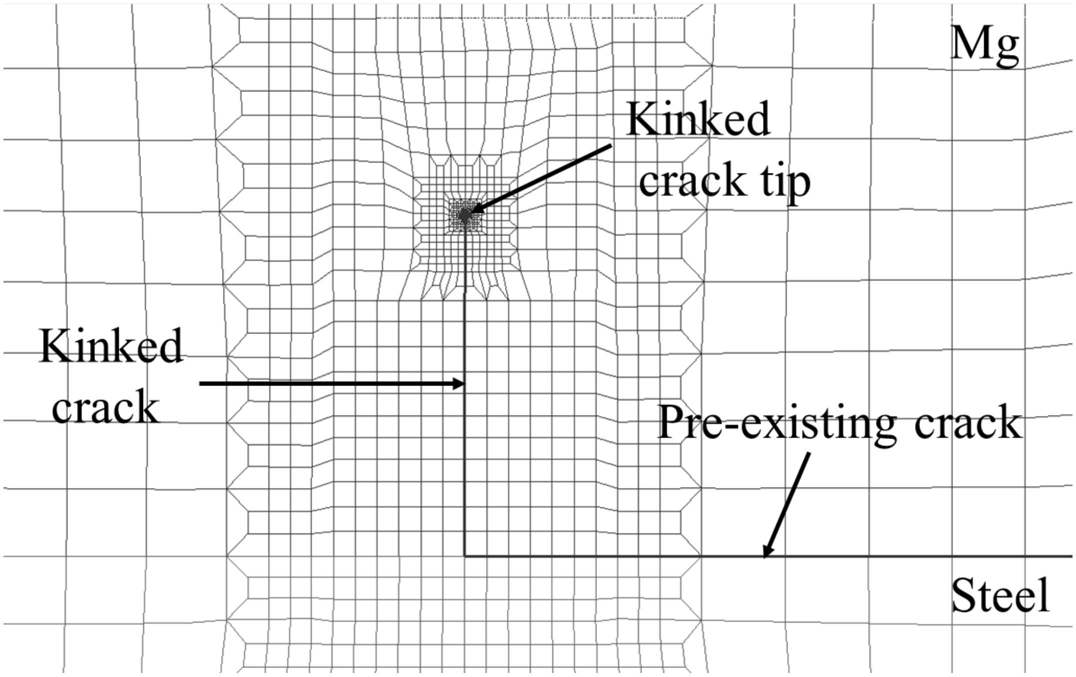

(c)

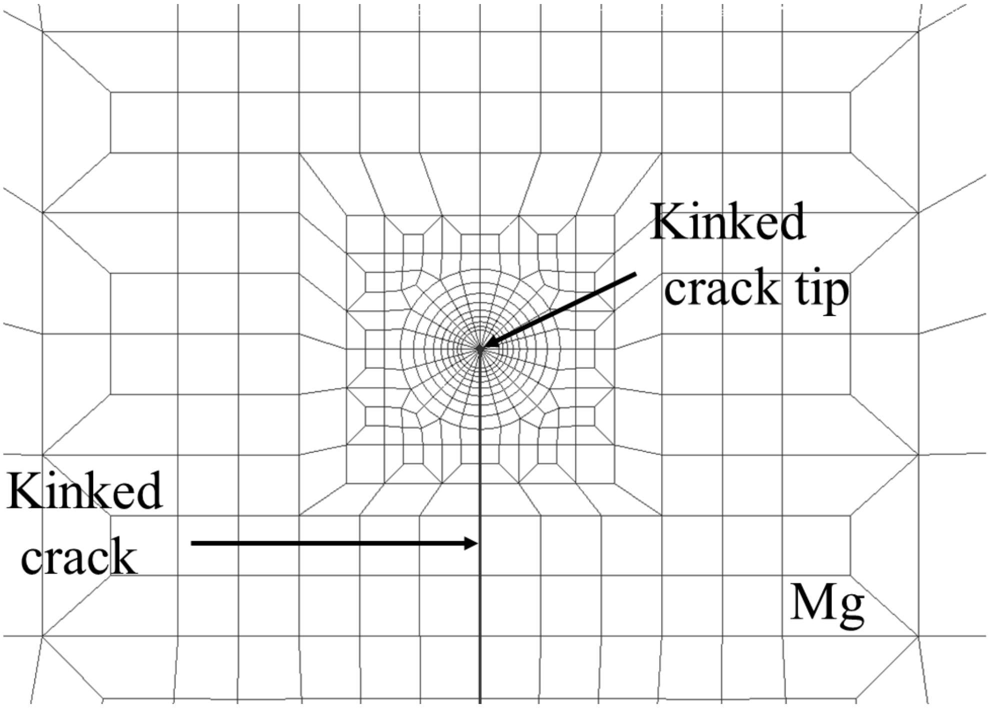

(d)

Figure 2.9. (a) A schematic of a two-dimensional finite elemental model of a lap-shear specimen with a kinked crack showing the boundary and loading conditions. (b) The finite element mesh showing the pre-existing cracks and the kinked crack on the right hand side for $w/t = 5.85$ and $a/t = 0.1$, (c) a view of the finite element mesh near the kinked crack, and (d) a close-up view of the mesh refinement near the kinked crack tip.

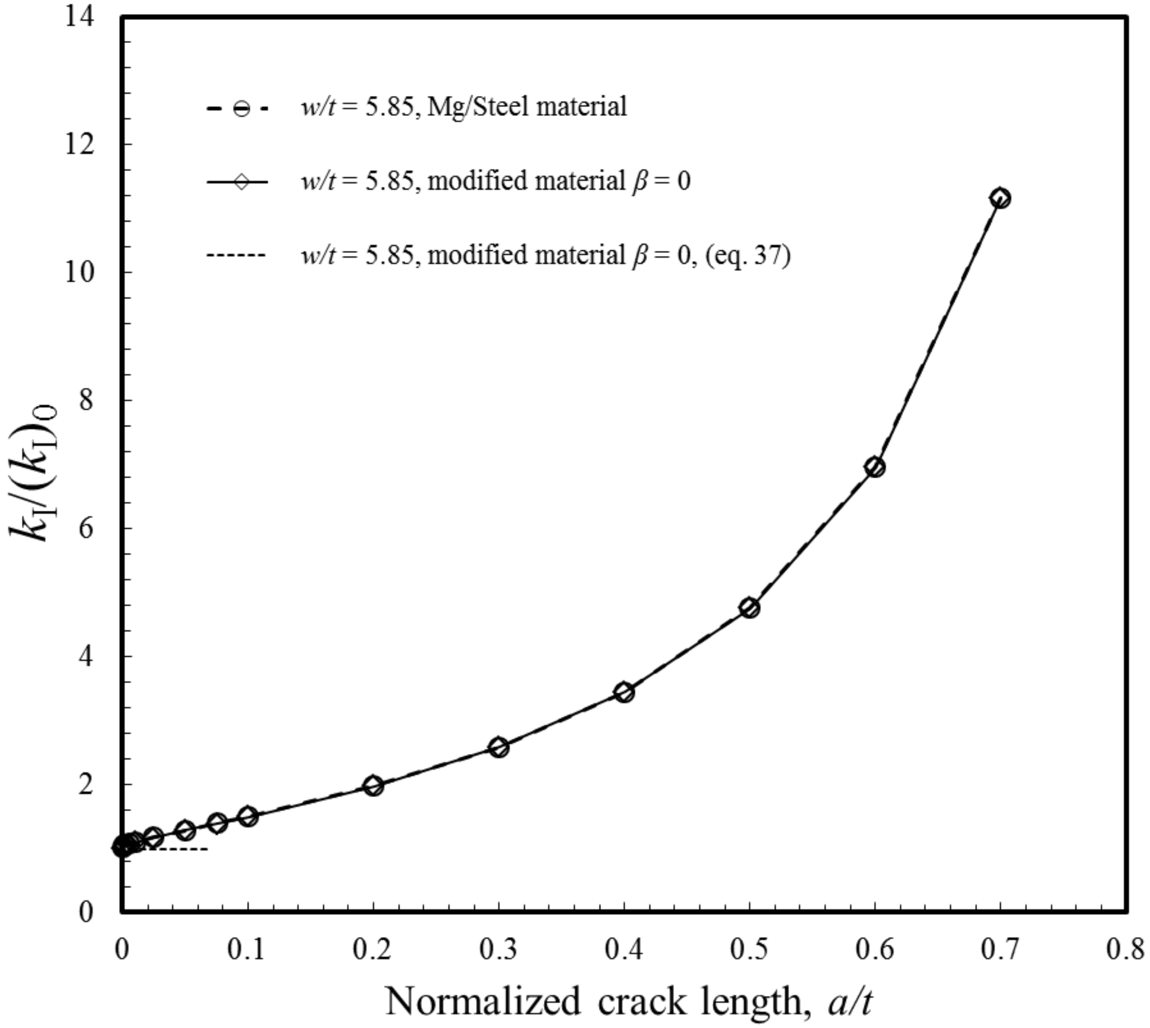
$k_I/(k_I)_0$
Normalized crack length, a/t
w/t = 5.85, Mg/Steel material
w/t = 5.85, modified material β = 0
w/t = 5.85, modified material β = 0, (eq. 37)
0
2
4
6
8
10
12
14
0
0.1
0.2
0.3
0.4
0.5
0.6
0.7
0.8

(a)

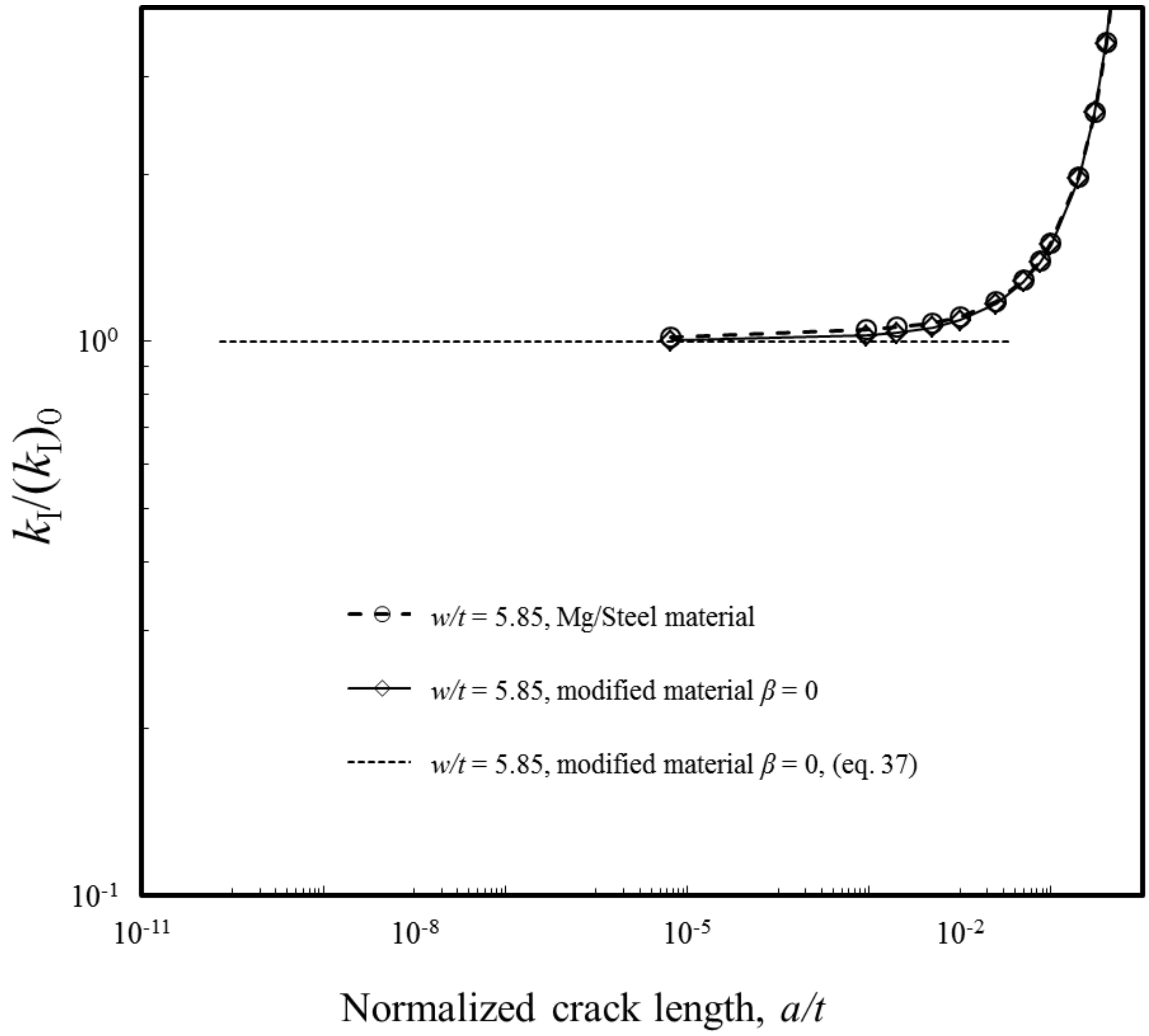
$k_I/(k_I)_0$
10^0
10^{-1}
10^{-11}
10^{-8}
10^{-5}
10^{-2}
Normalized crack length, a/t
w/t = 5.85, Mg/Steel material
w/t = 5.85, modified material β = 0
w/t = 5.85, modified material β = 0, (eq. 37)

(b)

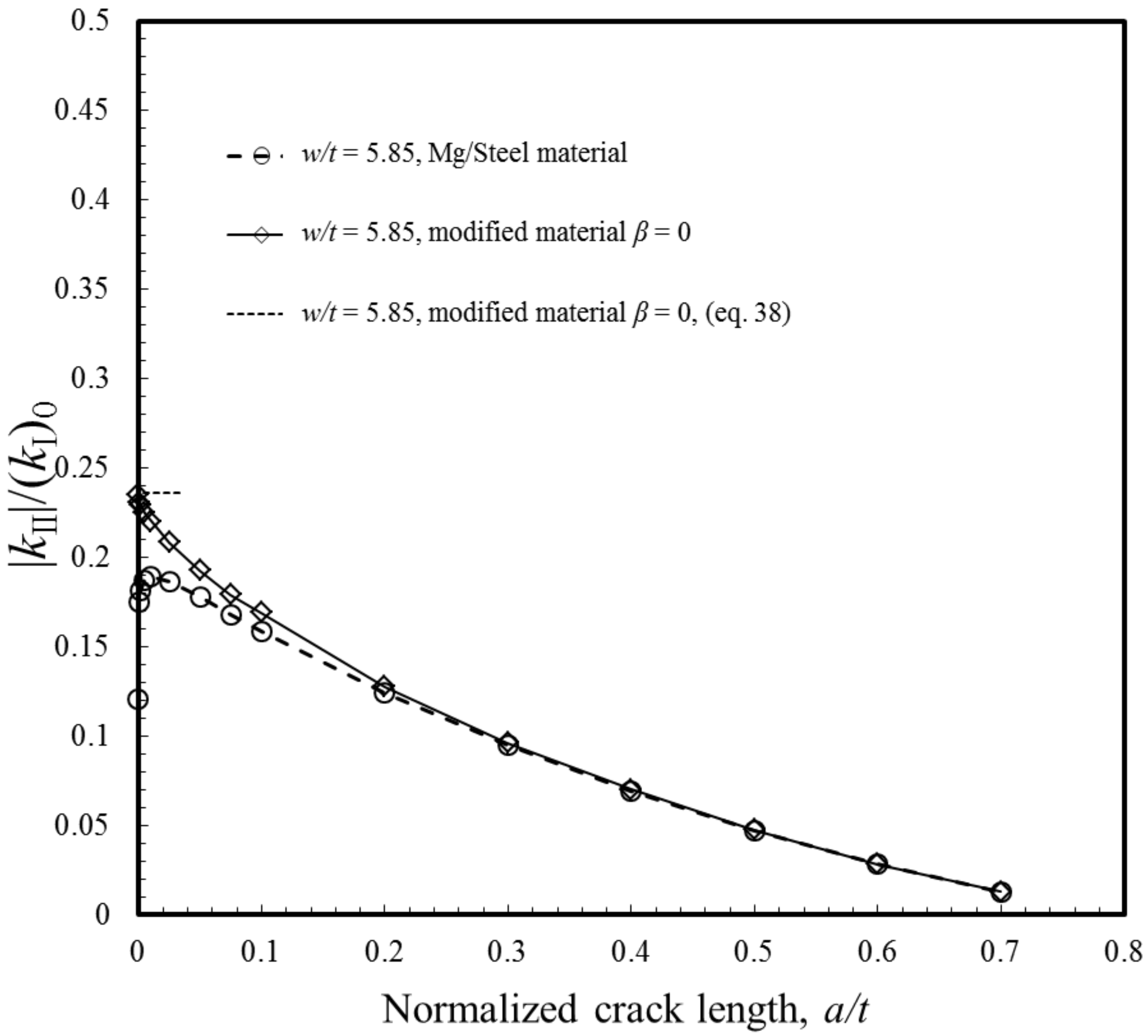

0.5
0.45
0.4
0.35
0.3
0.25
0.2
0.15
0.1
0.05
0
0
0.1
0.2
0.3
0.4
0.5
0.6
0.7
0.8
$|k_{\mathrm{II}}|/(k_{\mathrm{I}})_0$
Normalized crack length, a/t
w/t = 5.85, Mg/Steel material
w/t = 5.85, modified material β = 0
w/t = 5.85, modified material β = 0, (eq. 38)

(c)

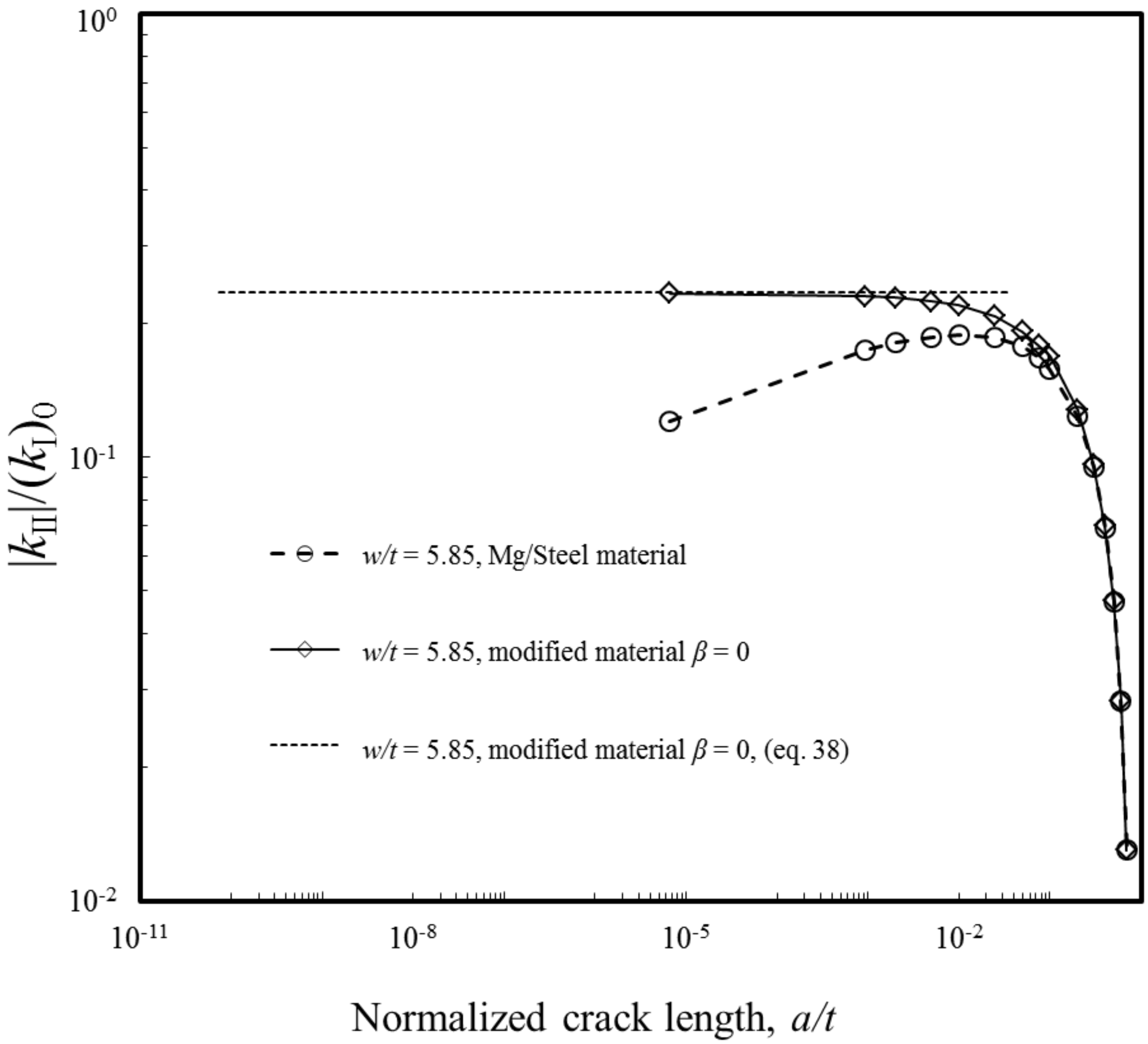

10^0
10^{-1}
10^{-2}
10^{-11}
10^{-8}
10^{-5}
10^{-2}
$|k_{II}|/(k_I)_0$
Normalized crack length, a/t
w/t = 5.85, Mg/Steel material
w/t = 5.85, modified material $\beta = 0$
w/t = 5.85, modified material $\beta = 0$, (eq. 38)

(d)

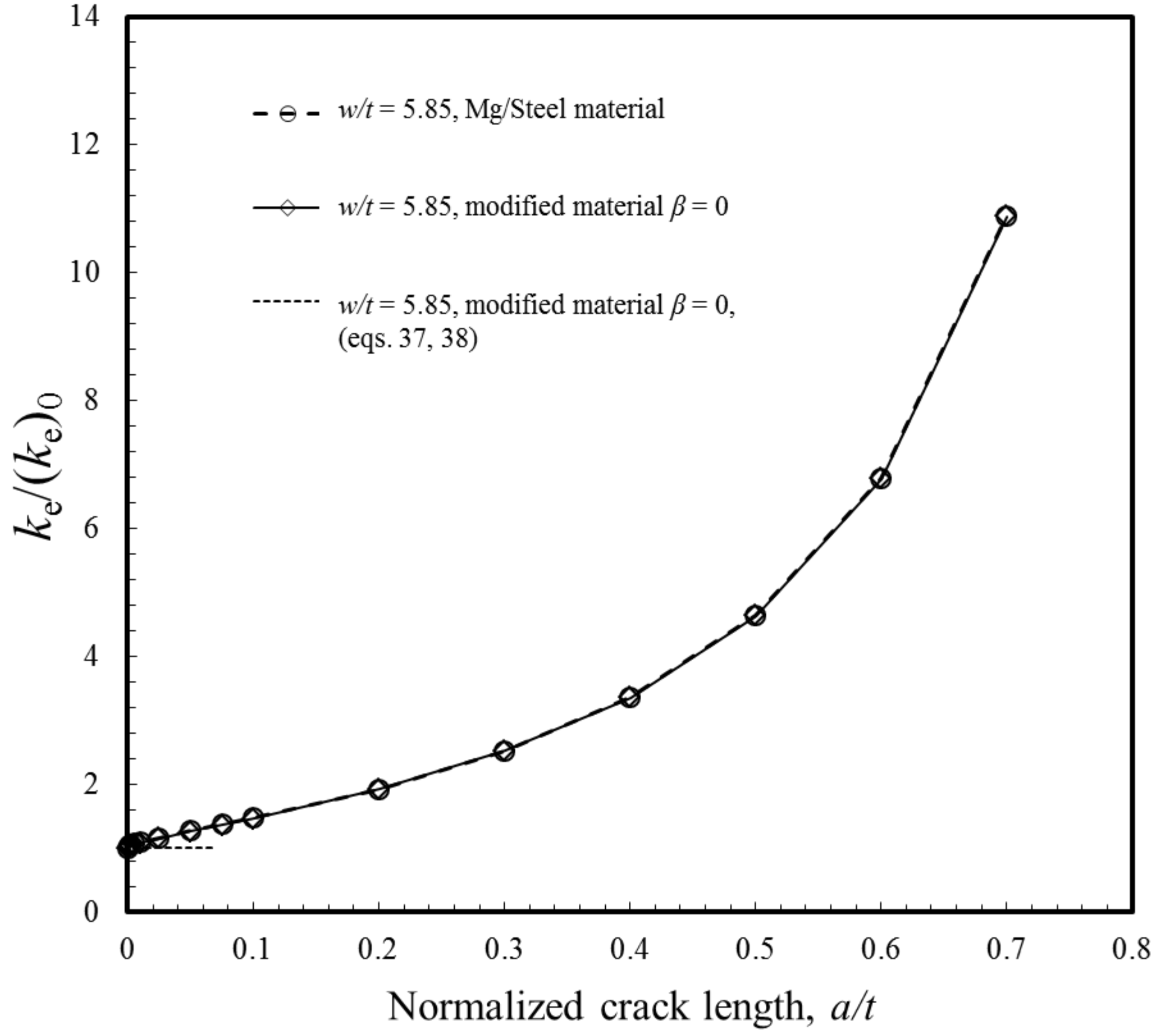

14
12
10
8
6
4
2
0
0
0.1
0.2
0.3
0.4
0.5
0.6
0.7
0.8
$k_e/(k_e)_0$
Normalized crack length, *a/t*
w/t = 5.85, Mg/Steel material
w/t = 5.85, modified material β = 0
w/t = 5.85, modified material β = 0, (eqs. 37, 38)

(e)

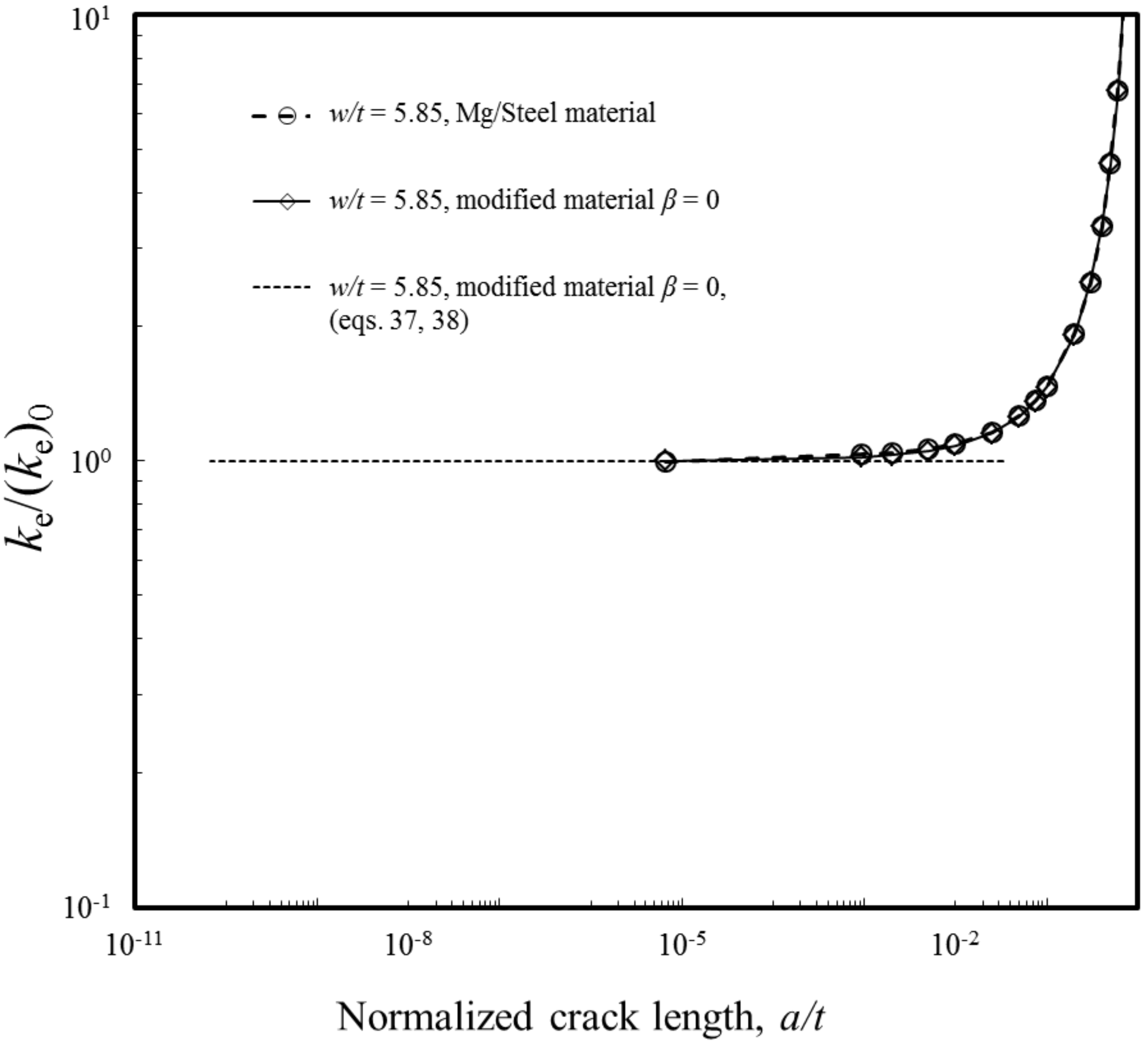

(f)

Figure 2.10. The values of (a) $k_{\mathrm{I}}/(k_{\mathrm{I}})_0$, with linear axes, (b) $k_{\mathrm{I}}/(k_{\mathrm{I}})_0$, with logarithmic axes, (c) $|k_{\mathrm{II}}|/(k_{\mathrm{I}})_0$, with linear axes, (d) $|k_{\mathrm{II}}|/(k_{\mathrm{I}})_0$, with logarithmic axes, (e) $k_e/(k_{\mathrm{e}})_0$, with linear axes, and (f) $k_e/(k_{\mathrm{e}})_0$, with logarithmic axes, as functions of the normalized kink length a/t for the actual and modified material with $w/t = 5.85$ and $\varphi = -90°$.

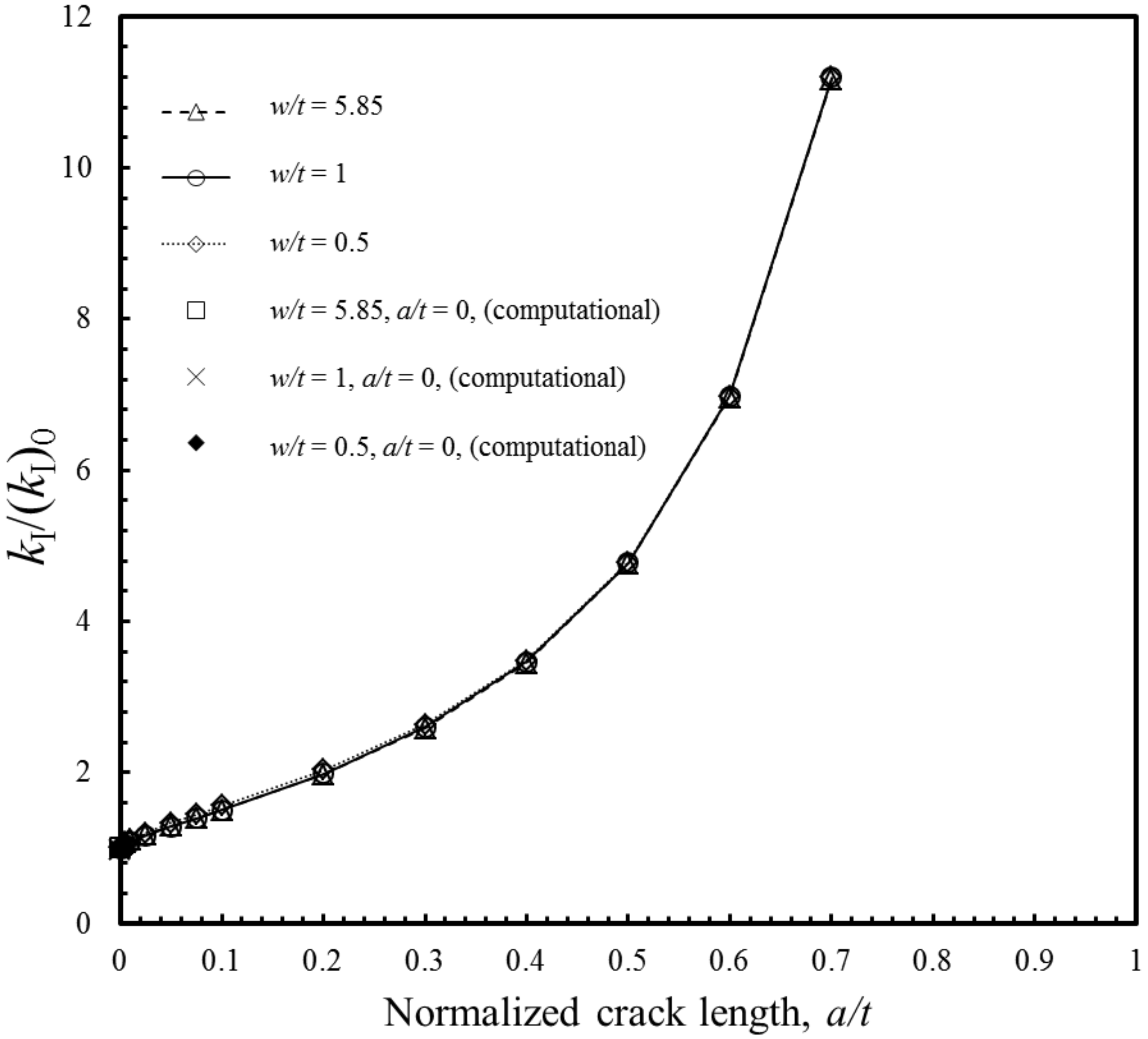
$k_I/(k_I)_0$
0
2
4
6
8
10
12
0
0.1
0.2
0.3
0.4
0.5
0.6
0.7
0.8
0.9
1
Normalized crack length, a/t
w/t = 5.85
w/t = 1
w/t = 0.5
w/t = 5.85, a/t = 0, (computational)
w/t = 1, a/t = 0, (computational)
w/t = 0.5, a/t = 0, (computational)

(a)

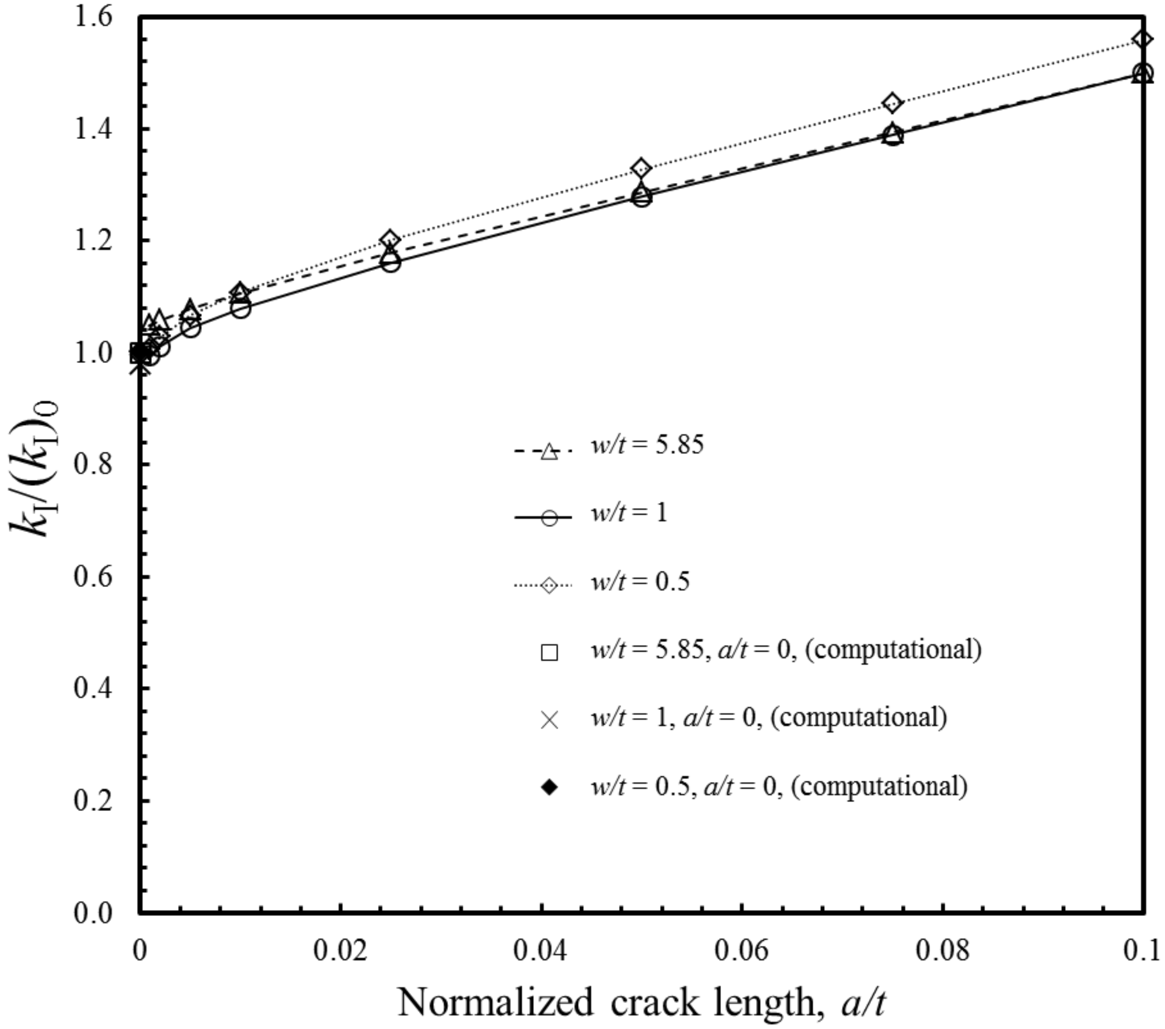

(b)

Figure 2.11. (a) The values of $k_\mathrm{I}/(k_\mathrm{I})_0$ as functions of the normalized kink length a/t for $w/t = 0.5$, 1 and 5.85 and $\varphi = -90°$, and (b) an enlarged section showing the values near a kink crack of length zero.

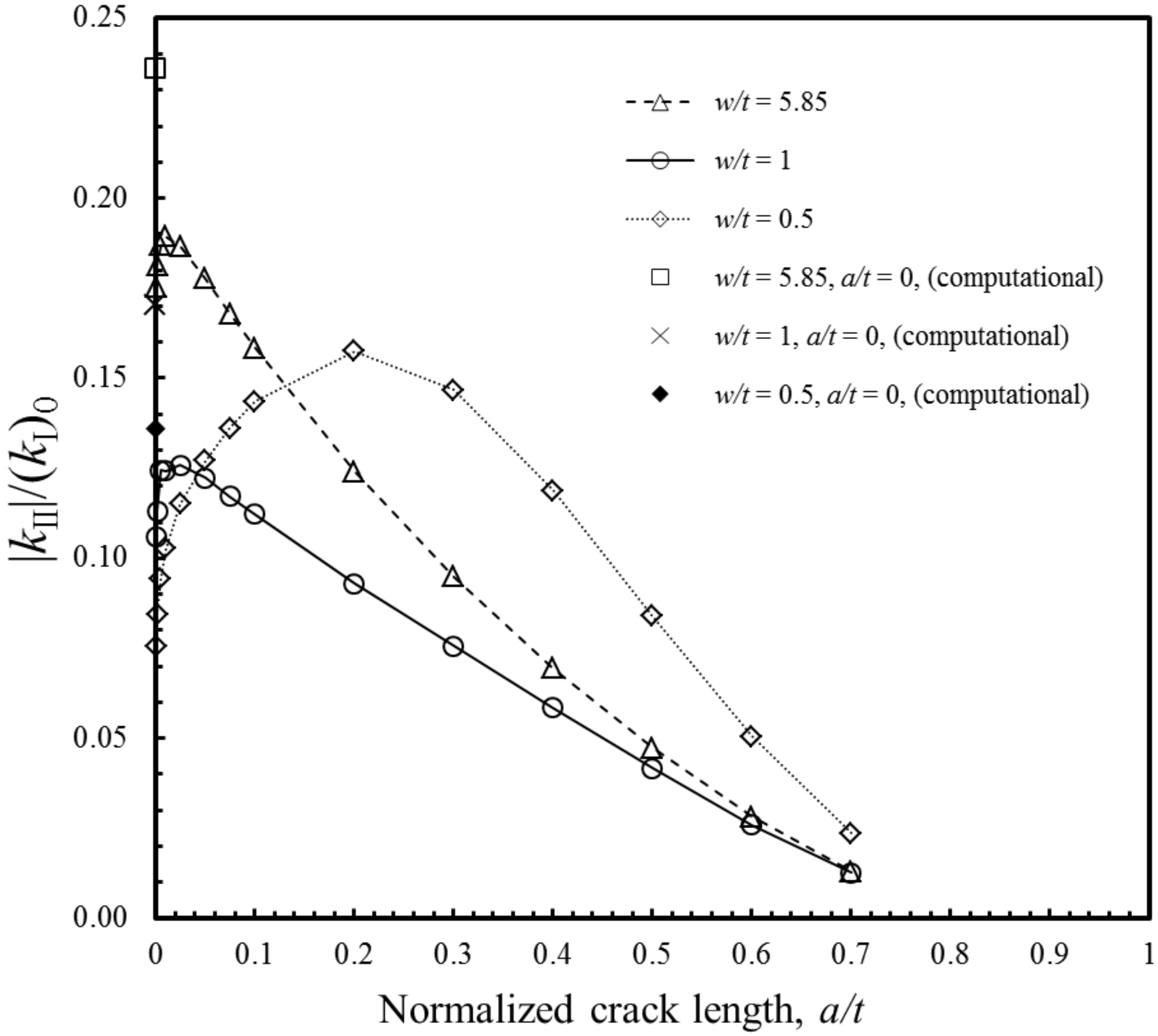

Figure 2.12. The values of $|k_{\mathrm{II}}|/(k_{\mathrm{I}})_0$ as functions of the normalized kink length a/t for $w/t = 0.5$, 1 and 5.85 and $\varphi = -90°$.

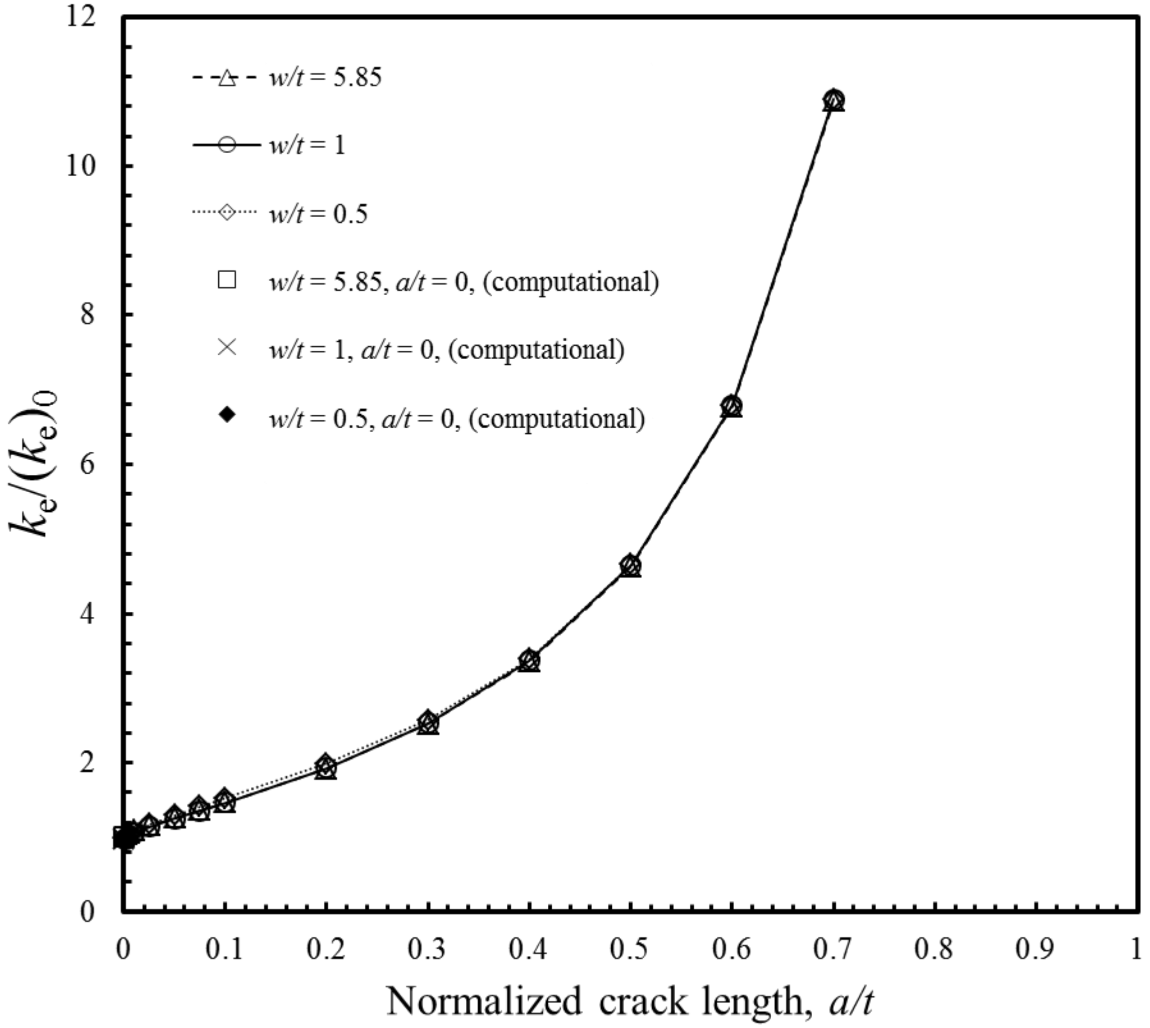
12
10
8
6
4
2
0
0
0.1
0.2
0.3
0.4
0.5
0.6
0.7
0.8
0.9
1
$k_e/(k_e)_0$
Normalized crack length, a/t
w/t = 5.85
w/t = 1
w/t = 0.5
w/t = 5.85, a/t = 0, (computational)
w/t = 1, a/t = 0, (computational)
w/t = 0.5, a/t = 0, (computational)

(a)

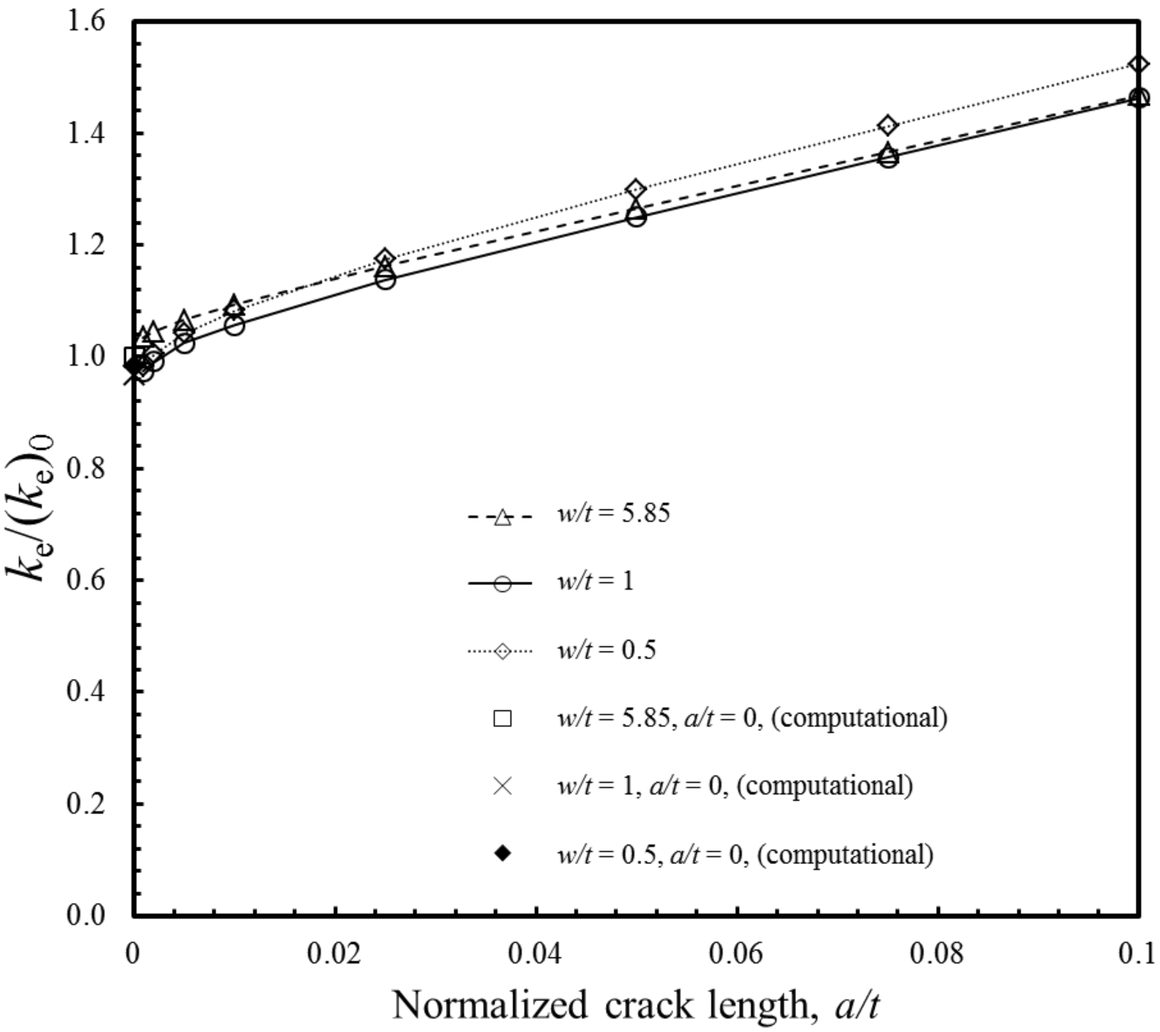

(b)

Figure 2.13. (a) The values of $k_e/(k_e)_0$ as functions of the normalized kink length a/t for $w/t = 0.5$, 1 and 5.85 and $\varphi = -90°$, and (b) an enlarged section showing the values near a kink crack of length zero.

Acknowledgements

This research was initially sponsored by the U.S. Department of Energy, Assistant Secretary for Energy Efficiency and Renewable Energy, Office of Vehicle Technologies, as part of the Lightweight Materials Program. Support of this work through a National Science Foundation Fellowship for TF is greatly appreciated.

References

[1] Lang B, Sun DQ, Xuan ZZ, Qin XF. Hot Cracking of Resistance Spot Welded Magnesium Alloy. ISIJ Int 2008;48(1):77-82.

[2]. Patel VK, Bhole SD, Chen DL, Ultrasonic spot welded AZ31 magnesium alloy: Microstructure, texture, and lap shear strength. Mater Sci Eng, A 2013;569:78-85.

[3] Hetrick E, Jahn R, Reatherford L, Skogsmo J, Ward SM, Wilkosz D, et al. Ultrasonic spot welding: A new tool for aluminum joining. Weld J 2005;84(2):26-30.

[4] Jahn R, Cooper R, Wilkosz D. The effect of anvil geometry and welding energy on microstructures in ultrasonic spot welds of AA6111-T4. Metall Mater Trans A 2007;38A:570-83.

[5] Bakavos D, Prangnell PB. Mechanisms of joint and microstructure formation in high power ultrasonic spot welding 6111 aluminium automotive sheet. Mater Sci Eng, A 2010;527:6320-34.

[6] Jordan JB, Horstemeyer MF, Daniewicz SR, Badarinarayan H, Grantham J. Fatigue characterization and modeling of friction stir spot welds in magnesium AZ31 alloy. J Eng Mater Technol 2010;132:041008-1-10.

[7] Gendo T, Nishiguchi K, Asakawa M, Tanioka S. Spot friction welding of aluminum to steel. SAE Technical Paper 2007-01-1703, Society of Automotive Engineers, Warrendale, PA.

[8] Liyanage T, Kilbourne J, Gerlich AP, North TH. Joint formation in dissimilar Al alloy/steel and Mg alloy/steel friction stir spot welds. Sci Technol Weld Joining 2009;14:500-8.

[9] Watanabe T, Sakuyama H, Yanagisawa A, Ultrasonic welding between mild steel sheet and Al–Mg alloy sheet. J Mater Process Technol 2009;209(15-16):5475-80.

[10] Santella M, Franklin T, Pan J, Pan T-Y, Brown E. Ultrasonic spot welding of AZ31B to galvanized mild steel. SAE Technical Paper 2010-01-0975, Society of Automotive Engineers, Warrendale, PA.

[11] Jana S, Hovanski Y. Fatigue behaviour of magnesium to steel dissimilar friction stir lap joints. Sci Technol Weld Joining 2012;17(2):141-5.

[12] Uematsu Y, Kakiuchi T, Tozaki Y, Kojin H. Comparative study of fatigue behaviour in dissimilar Al alloy/steel and Mg alloy/steel friction stir spot welds fabricated by scroll grooved tool without probe. Sci Technol Weld Joining 2012;17(5):348-56.

[13] Ueoka T, Tsujino J. Welding Characteristics of Aluminum and Copper Plate Specimens Welded by a 19 kHz Complex Vibration Ultrasonic Seam Welding System. Jpn J Appl Phys 2002;41:3237-42.

[14] Sripichai K, Asim K, Pan J. Stress intensity factor solutions for estimation of fatigue lives of laser welds in lap-shear specimens. Eng Fract Mech 2011;78:1424-40.

[15] Zhang S. Stress intensities at spot welds. Int J Fract 1997;88:167-85.

[16] Zhang S. Fracture mechanics solutions to spot welds. Int J Fract 2001;112:247-75.

[17] Suo Z, Hutchinson JW. Interface crack between two elastic layers. Int J Fract 1990;43:1-18.

[18] Lee J, Asim K, Pan J. Modeling of failure mode of laser welds in lap-shear specimens of HSLA steel sheets. Eng Fract Mech 2011;78:374-96.

[19] Asim K, Lee J, Pan J. Failure mode of laser welds in lap-shear specimens of high strength low alloy (HSLA) steel sheets. Fatigue Fract Eng Mater Struct 2011;35:219-237.

[20] Anand D, Chen DL, Bhole SD, Andreychuk P, Boudreau G. Fatigue behavior of tailor (laser)-welded blanks for automotive applications. Mater Sci Eng, A 2006;420:199-207.

[21] Sripichai K, Asim K, Jo WH, Pan J, Li M. Fatigue behavior of laser welds in lap-shear specimens of high strength low alloy (HSLA) steels. SAE Technical Paper No. 2009-01-0028, Society of Automotive Engineers, Warrendale, PA.

[22] He M-Y, Hutchinson JW. Kinking of a crack out of an interface. J Appl Mech 1989;56(2):270-8.

[23] Erdogan F. Stress distribution in a nonhomogeneous elastic plane with cracks. Trans ASME—J Appl Mech 1963;30(2):232-6.

[24] Rice JR, Sih GC. Plane problems of cracks in dissimilar media. J Appl Mech 1965;32:418-23.

[25] Zhang S. Stress intensities derived from stresses around a spot weld. Int J Fract 1999;99:239-257.

[26] Rice JR. Elastic fracture mechanics concepts for interfacial cracks. J Appl Mech 1988;55:98-103.

[27] Tada H, Paris PC, Irwin GR. The stress analysis of cracks handbook. 3rd edition. New York: ASME Press; 2000.

[28] Lee J. Simulations of similar and dissimilar weld joint failures and bearings for fatigue analyses [doctoral dissertation]. Ann Arbor, MI: University of Michigan; 2011.

[29] ABAQUS v6.10 User Manual. Providence, RI: SIMULIA; 2010.

[30] He M-Y, Hutchinson JW. Kinking of a crack out of an interface: tabulated solution coefficients. Harvard University Report MECH-113A. 1988.

[31] Cotterell B, Rice JR. Slightly curved or kinked cracks. Int J Fract 1980;16:155-69.

Chapter 3
Fatigue Behavior of Dissimilar Ultrasonic Welds in Lap-Shear Specimens of AZ31 and Steel Sheets

3.1. Introduction

Amid rising fuel efficiency standards, the automotive industry is seeking lightweight alternative materials such as aluminum or magnesium to replace steel where possible, reducing the overall weight of the vehicle. The goal is simple: lighter vehicles correlate to improved fuel economy. Using magnesium alloys, with a density 30% less than that of aluminum [1], could result in a significant reduction of the weight of a vehicle. However, replacing the entire structure with magnesium is unrealistic due to cost and certain strength requirements. One challenge to introducing more magnesium alloys into vehicle structures is joining magnesium components to the remaining steel structures. Joining magnesium alloys to steels is especially difficult due to the extreme difference in their melting temperatures and immiscibility of magnesium and iron [2].

The advantage of using ultrasonic welding or other solid state joining methods such as friction stir welding is that melting is either avoided or minimized. Both methods can be used to join dissimilar metals. Researchers have been using ultrasonic welding or friction stir welding to join both similar and dissimilar materials. Similar joints are mainly produced using sheets of aluminum or magnesium alloys. Similar joints in aluminum have been made by many researchers, including Hetrick et al. [3], Jahn et al. [4], and Bakavos and Prangnell [5]. Jordan et al. has produced similar magnesium friction stir spot welds [6]. Dissimilar welds have been produced most commonly in aluminum-steel by researchers Gendo et al. [7], Liyanage et al. [8], and Watanabee et al. [9]. Dissimilar welds were also produced in magnesium and steel by Santella et al. [2].

Some researchers have been investigating fatigue behavior of solid state welds. This is an important and necessary step in order to develop life prediction and design tools for product development. Tran and Pan [10] and Tran et al. [11-12] used a kinked fatigue crack growth model and the structural stress model for spot welds in lap-shear and cross tension specimens. Jordan et al. [6] modeled fatigue behavior in magnesium friction stir spot welds using a kinked fatigue crack growth model where the authors use an assumption that a three-dimensional crack maintains a constant stress intensity factor for all crack lengths, as used by Newman and Dowling [13].

In this study, ultrasonic spot welds on lap-shear specimens have been machined into a dog-bone profile to approximate an ultrasonic seam weld such as those studied by Ueoka and Tsujino [14]. This approach has been used in order to more thoroughly and accurately analyze experimental results using a two-dimensional finite element model and computational solutions which have been developed for plane strain. The kinked crack growth model is presented in Asim et al. [15] and Sripichai et al.[16]. Both studies correlate experimental fatigue behavior of laser welds of similar material with fatigue life prediction. Here, the same model will be used, except that these ultrasonic welds are of dissimilar materials. Dissimilar materials require a different approach to analytically calculating the global stress intensity factor solutions and obtaining a vanishing crack solution. Obtaining these stress intensity factor solutions will rely on solutions similar to those in Zhang [17] and Tran and Pan [18] for the global stress intensity factor solutions and He and Hutchinson [19] for a vanishing crack solution. The exact procedure for obtaining the stress intensity factors solutions is detailed in Chapter 2. Then the kinked crack growth model will be compared with experimental fatigue results.

3.2. Experiment

3.2.1 Lap-shear specimen

The lap-shear specimens were made by joining magnesium AZ31B-H24 sheets with a thickness of 1.58 mm to hot-dipped galvanized steel sheets. Two types of steel sheets were used to make two sets of lap-shear AZ31-steel welded specimens. The first type is a high strength low alloy (HSLA) steel sheet with a thickness of 1.50 mm. The second type is a mild steel sheet with a thickness of 0.8 mm. The magnesium and steel were cut into coupons of 30 mm × 100 mm. The lap-shear specimen was made by welding the magnesium and steel coupons with a weld centered in the 30 mm × 75 mm overlap area using an ultrasonic spot welder. The machine used for the ultrasonic spot welding was a Sonobond CLF 2500 single-transducer, wedge-reed ultrasonic welder. The sonotrode tip has a square face of 7 mm × 7 mm and the surface of the face had a grooved pattern on it described by Jahn et al [4]. The spot welding was done with a power of 1500 W, an impedance setting of 6 and a welding time of 1 s. The orientation of the sample was adjusted prior to welding so that the vibrations from the sonotrode tip were parallel to the surface of the sample and aligned with the short axis of the specimen. The pressure to the tip clamping mechanism was adjusted for a constant nominal pressure of 39 MPa on the material beneath the sonotrode tip. Figure 3.1(a) shows a lap-shear specimen with an ultrasonic weld. Figure 3.1(b) and 3.1(c) show the face and profile view of the sonotrode tip used in creating the welds. The microstructures of the sheets, the specimen preparation procedure and the processing conditions were detailed in Santella et al. [2].

The USW lap-shear specimens were machined into a dog-bone shaped profile using a CNC milling machine. The purpose of using a dog-bone shaped profile is to remove edge effects and approximate a two-dimensional weld. This allows for simplified modeling and fatigue prediction of the weld. Although it is documented by Wang and Pan [20] that a two-dimensional weld does not behave the same as the original spot weld, the work is still relevant because there are ultrasonic seam welders which produce a continuous linear weld. Figure 3.2(a) and 3.2(b) show the top and bottom views of an USW lap-shear specimen after being machined into the dog-bone shaped profile. The specimen geometry in general follows the guidelines of the ANSI/AWS B4.0:2007 standard for the mechanical testing of welds. The central portion of the dog-bone shaped specimens has a reduced width. The width and length of the uniform straight part of the section with the reduced width are 8 mm and 13.5 mm, respectively. The weld zone (crack tip to crack tip) has an average width of about 8.78 mm as measured from failed specimens. During fatigue testing, two spacers were used to align the fixture to avoid the initial realignment of the specimen due to the non-aligned grips under lap-shear loading conditions. Figure 3.3 shows a schematic of a lap-shear specimen with the loading direction represented by bold arrows. As shown in the figure, the specimen has a width W and overall length L for the upper and lower sheets. The specimen has the thickness t_u for the upper sheet and t_l for the lower sheet. The specimen has a reduced width b for the central portion, an overlap length V, a weld width w, an indentation width g and a transition radius r for the weld zone. The dimensions of the specimens are W = 30 mm, L = 100 mm, b = 8 mm, V = 75 mm, w = 8.78 mm, g = 7 mm and r = 10 mm. The thickness t_u for the upper sheet is 1.58 mm for the top magnesium sheet. The thickness t_l is 1.5 mm for the bottom HSLA steel sheet or 0.8 mm for the bottom mild steel sheet. Specimens with similar shapes were adopted by a number of researchers for the study of laser welded joints: for example, see, Lee et al. [21], Asim et al. [15], Anand et al. [22], and Sripichai et al. [16]. Lee also used the same geometry while studying quasi-static failure of ultrasonic welds [23]. The detailed dimensions of the lap-shear specimens are listed in Table 3.1.

Before testing, an ultrasonic welded specimen for each steel thickness was sectioned along the symmetry plane on the longitudinal axis and future loading direction of the specimen. The optical micrograph of the cross section can be seen in Figure 3.4(a) and 3.4(b) for the thick steel and thin steel welds respectively. Figure 3.4(a) shows an untested specimen of the ultrasonic weld with 1.58 mm AZ31 and 1.5 mm HSLA steel. The micrograph shows the indentation of the sonotrode tip into the magnesium sheet. The weld reaches just outside of the visible indented region. In Figure 3.4(a), it should be noted that the cross-section was taken near a ridge as opposed to a valley. A slight deviation between the angle of the ridges and the cutting angle explains the asymmetry of the top profile in the magnesium. The rest of the asymmetry, however, is not an artifact of sectioning. As observed by Santella et al. [2], during welding the magnesium and zinc reached a eutectic temperature where they liquefied. The pressure of the sonotrode tip along with the vibrations caused the layer to flow outward. This eutectic layer is discussed in detail in Santella et al. [24]. On the right side, a gap and a layer between the magnesium and steel sheets is clearly visible. On the left side, the gap between the magnesium and steel sheets is much smaller. The uneven distribution of the layer which has been displaced from the interface is most likely due to the vibrational modes associated with the sample sheets during welding. The third asymmetrical feature is the existing cracks within the welded region which can be seen on the right side and also just left of center in the magnesium sheet in the thick steel weld. These cracks are present in multiple sectioned USW lap-shear joints with this material combination. This is believed to be caused upon cooling after welding due to a mismatch in thermal expansion coefficients. These cracks do not appear in every micrograph. It is possible that the cracks are present at some locations in every specimen which are not always bisected by the sectioning plane. It is also possible that some welds have no internal cracks at all.

The micrograph of the untested weld with 1.58 mm AZ31 and 0.8 mm steel is shown in Figure 3.4(b). It also features a sonotrode tip indentation and a layer which was displaced from the interface on the right side. In this weld, internal cracks are not observed. Additional detail about the microstructure is discussed in Lee [23] and Santella et al. [2]. The magnesium and zinc in the displaced layer is thoroughly investigated in Santella et al. [24].

3.2.2 Quasi-static test of lap-shear specimen

Lap-shear specimens were first tested under quasi-static loading conditions by using an automated MTS testing machine equipped with a load cell and a built-in position sensor to track the movement of the cross-head. Spacers were not used during quasi-static tests. The load and displacement histories were simultaneously recorded during each test. The average failure or maximum load was about 2750 N for the weld with 1.5 mm HSLA steel. The average failure load was about 2350 N for the weld with 0.8 mm mild steel. The average failure load was used as the reference value to determine the applied load ranges for the fatigue tests. The weld with 1.5 mm HSLA steel failed through the magnesium sheet near the weld. In the weld with 0.8 mm mild steel, necking was observed, followed by failure of the steel sheet near the weld. A detailed study of the failure mechanism under quasi-static tests of the dog-boned ultrasonic welds in AZ31 and hot-dipped galvanized HSLA steel is reported by Lee [23].

The tested specimens were sectioned perpendicular to the welding direction and prepared for micrographic analyses. In the present study, a micrograph of the cross sections of a failed specimen under quasi-static loading conditions for the weld with 1.5 mm HSLA steel is presented for comparison with the failure mechanisms of the lap-shear specimens under cyclic loading conditions.

3.2.3 Fatigue test of lap-shear specimen

Lap-shear specimens were tested under cyclic loading conditions with an Instron servo-hydraulic fatigue testing machine using a load ratio of $R = 0.1$. A sinusoidal loading profile was chosen and the frequency was set at 10 Hz during the tests. The test was considered to be completed at the final separation of the welded sheets. A few tests were interrupted before the final separation to study the fatigue crack growth patterns. The number of life cycles to failure was recorded for different applied load ranges. A plot of the load range versus the fatigue life in a log-log scale is shown in Figure 3.5. The fatigue tests were also terminated when specimens were nearing one hundred thousand loading cycles without separation. These specimens were recorded as a runout and marked in the figure with an arrow. Some specimens that failed under cyclic loading conditions were sectioned perpendicular to the weld direction and prepared for micrographic analyses. The optical micrographs of the cross sections of the partially and fully failed specimens are presented in the following section.

3.3. Failure modes of ultrasonic welds under cyclic loading conditions

Ultrasonic welds in lap-shear specimens with a dog-bone profile were studied under cyclic loading conditions. The experimental observations indicate that the ultrasonic welds failed through the upper magnesium sheet on the right side under all cyclic conditions. All of the specimens show a crack originating at the pre-existing crack notch formed at the edge of the weld on the right side. The crack may grow along the interface briefly, but in all specimens before long, the crack kinks upward at roughly a 90° angle. Generally as the cyclic loading amplitude increased, the final rupture, where the crack kinks a second time, is larger. Under higher load ranges, the final rupture will connect the kinked crack with the corner of the indentation made by the sonotrode tip during welding. Under lower load ranges, the final rupture connects with the indentation at a location closer the surface or continues to the surface without connecting. Both of these crack growth patterns will be discussed in greater detail.

The overall nature of the crack growth pattern in the magnesium and thick steel specimens can be observed in Figure 3.6, which shows a top view of the weld for failed specimens. Figure 3.6(a) shows a top view of a quasi-static specimen which is included as a comparison. Figures 3.6(b)-(d) show the top surface which failed under cyclic loading with the maximum load set at 80%, 70%, and 50% respectively of the quasi-static failure load. All of the specimens failed through the loaded side of the magnesium sheet which is on the right side of the weld. From Figure 3.6, it can be seen that the two-dimensional approximation, which was created by milling a dog-bone profile, results in fractures which are nearly uniform through the reduced width of the sample. Some specimens, such as the one observed in Figure 3.6(c) exhibit non-uniform cross sections which fracture closer to the weld at the edges than in the center. Overall most specimens show a uniform fracture pattern across the reduced section. This knowledge give reassurance that the welds can be modeled using a two-dimensional finite element mesh. It also illustrates that prepared micrographs may or may not be representative of the entire fracture front. All micrographs have been sectioned along the center line where a plane strain assumption is valid, although there may be slight variation in the exact alignment. It can be observed in Figures 3.6(a)-(c) that the welds failed with the fracture connecting into the inside of the weld indentation. In contrast, Figure 3.6(d) shows a failed specimen tested under a lower load range with a fracture that appears to leave some material remaining on the right side of the weld indentation. These differences will be clearer in the sectioned micrographs.

The crack growth pattern in the magnesium and thin steel specimens can be observed in Figure 3.7. Figure 3.7(a) shows a bottom view of a weld after quasi-static testing. Under quasi-static load, the welds in 1.58 mm AZ31 and 0.8 mm mild steel fail through the mild steel sheet. It should be noted that this is the only loading condition for these specimens which results in failure of the steel. Figure 3.7(b) shows a top view of a failed weld after testing under cyclic loading with 2566 cycles and a load range of 1.57 kN. This specimen was tested at a maximum load set at 75% of the quasi-static failure load and failed under low-cycle fatigue. It can be seen that the weld failed through the magnesium sheet on the right side. The crack path can be seen to connect with the weld indentation. Figure 3.7(c) shows a weld which failed under high-cycle loading with 80,821 cycles under a load range of 0.72 kN. This specimen was tested at a maximum load set at 35% of the quasi-static failure load. Here it is observed that the failure occurs through the magnesium sheet on the right side of the weld, but the fatigue crack did not connect with the weld indentation. The magnesium on both sides of the weld still has excess magnesium material which was pushed from the indentation during welding, which shows the crack propagated nearly straight upward.

For the purpose of discussion in this paper, specimens will be divided into a low-cycle and high-cycle fatigue range. This is determined by the failure mode from the fatigue tests and is chosen for convenience. In actuality, the transition between low-cycle and high-cycle fatigue changes gradually as the load range is decreased. For this paper, the transition between low-cycle and high-cycle is set at roughly 8,000 cycles for both sets of specimens. The load range for the two sets of samples is slightly different. Welds with thick steel tested with a load range less than or equal to 1.3 kN, which lies between the specimens shown in Figures 3.6(c) and 3.6(d), will be referred to as high-cycle fatigue. Specimens with a load range greater than 1.3 kN will be referred to as low-cycle fatigue. Welds with thin steel tested at load ranges less or equal to 1.1 kN will be referred to as high-cycle fatigue. Welds with thin steel tested at a load range greater than 1.1 kN will be referred to as low-cycle fatigue. Note that the definitions of low-cycle and high cycle fatigue loading conditions in this study are only provided for convenient presentation. Both low-cycle and high-cycle fatigue crack growth patterns will be discussed further by looking at micrographs of the sectioned failed and partial failed specimens.

3.3.1. Failure mode under quasi-static (QS) loading conditions

Quasi-static results are included simply for comparison to cyclic loading. The quasi-static failure modes differ for the two sets of samples with different steel types. In the welds with 1.5 mm HSLA steel, the failure occurs through the magnesium leg on the right side of the weld. In the welds with 0.8 mm mild steel, the failure occurs through the mild steel leg on the left side of the weld.

3.3.1.1 Failure mode under quasi-static (QS) loading conditions in 1.58 mm AZ31 and 1.5 mm HSLA steel

Figure 3.8 shows an optical micrograph of the cross sections of a failed weld in lap-shear specimens under quasi-static loading conditions. The upper right and lower left sheets were the two load carrying sheets in these tests which is shown schematically with arrows. The weld and failed magnesium leg do not exactly fit together which is the result of a non-uniform failure surface through the width of the specimen and slightly different polishing depths. During the tests, the weld region and the non-load carrying leg rotated as the applied displacement increased. The angle of rotation continued to increase until failure. Upon failure a final value of 3.5° with respect to the line of loading was measured for quasi-static testing. The rotation is the consequence of non-uniform plastic deformation through the thickness of the load carrying sheet near the weld nugget. Under quasi-static loading, failure began in the right magnesium leg, where a crack propagates from the pre-existing crack tip. Failure occurred when the crack connects with the sonotrode tip indentation. A detailed investigation of the quasi-static failure mode is presented by Lee [23]. The welds failed through the upper right magnesium sheet which is also the case for all cyclic loading conditions.

3.3.1.2 Failure mode under quasi-static (QS) loading conditions in 1.58 mm AZ31 and 0.8 mm mild steel

The quasi-static failure of a 1.58 mm AZ31 and 0.8 mm mild steel weld is shown in Figure 3.7(a). Necking occurs on the lower left steel leg near the weld. This is the only condition which results in failure through the steel sheet of the specimen. No micrographs were prepared for this condition.

3.3.2 Failure mode under low-cycle (LC) loading conditions

Fatigue failure under low-cycle conditions was similar for welds with 1.5 mm HSLA steel or 0.8 mm mild steel. In both cases, failure occurred through the right magnesium leg. These are discussed next.

3.3.2.1 Failure mode under low-cycle (LC) loading conditions in 1.58 mm AZ31 and 1.5 mm HSLA steel

Figures 3.9(a)-3.9(d) show optical micrographs of the cross sections of partially and fully failed welds at low-cycle loading conditions. Figure 3.9(a) shows a partially failed weld at the fatigue life 2.2×10^3 cycles under a load range of 1.43 kN. Figure 3.9(b) shows an enlarged section near the kinked crack for the same weld. Figures 3.9(c) and 3.9(d) show a failed weld at the fatigue life of 1.7×10^3 cycles under a load range of 1.70 kN and one at 3.3×10^3 cycles under a load range of 1.43 kN. The upper right and lower left sheets were the two load carrying sheets in these tests which are shown schematically with arrows. The partially failed weld in Figures 3.9(a) and 3.9(b) was tested under the same load range as previous specimens; however, the test was interrupted between 65% and 85% of the expected cycle life. The partially failed weld allows observation of the crack growth pattern. In Figure 3.9(b), a crack can be seen kinking upward at an angle of 72° on the right side of the weld in the magnesium sheet. The kink angle is measured between the interface ahead of the crack and the kinked crack. At the point of kinking, this crack has already separated the dispersed layer from the steel. This can be observed by noting the absence of voids to the left of the kinked crack which are common in the dispersed layer.

As shown in Figure 3.9(c), the dominant failure mode for the specimens under low-cycle loading conditions appears to be a kinked crack growing upward and connecting with the weld indentation from the sonotrode tip. Figure 3.9(d) shows a failed weld at a slightly lower load range of 1.43 kN. Here it can be observed that the final fracture is slightly shorter than that seen in Figure 3.9(c). The crack growth pattern in 3.9(d) follows the same overall pattern, kinking upward at roughly 82° and connecting with the right lower corner of the weld indentation during the final fracture. The crack appears to kink a third time at the very end of its path, however, it should be remembered that the weld indentation is grooved and this micrograph was most likely sectioned at the edge of a ridge. That is, the crack most likely connected with the valley, so that the extra apparent kink in the path is an artifact of sectioning. This type of failure corresponds with low-cycle fatigue produced by testing with a load range greater than about 1.3 kN. The ultrasonic welds mainly fail from the through-thickness crack propagation of the upper right magnesium sheet under low-cycle loading conditions. The failure is most likely initiated from the pre-existing crack tips. The crack appears to grow from the pre-existing crack tips along the interface between the dispersed layer and the steel. As the crack reaches the end of the dispersed layer and the beginning of where the magnesium is bonded directly to steel, it kinks upward into the magnesium sheet, although there is variation in the exact kink location. A total of six specimens were tested to complete failure under these load ranges and they all exhibited the same failure mode.

3.3.2.2 Failure mode under low-cycle (LC) loading conditions in 1.58 mm AZ31 and 0.8 mm mild steel

Figure 3.10 displays an optical micrograph of a welded specimen in 1.58 mm AZ31 and 0.8 mm mild steel which failed under low-cycle loading conditions at a fatigue life of 6.9×10^3 cycles under a load range of 1.16 kN. The failure occurred in the right magnesium leg. The fatigue crack propagated from the notch created at the edge of the weld, kinking upward at an angle of 83°. The final rupture connected the kinked crack with the weld indentation. This failure mode is the same as that of the low-cycle thick steel welds. For specimens with thin steel, load ranges greater than about 1.1 kN result in low-cycle fatigue failure. Two specimens were tested to complete failure under these load ranges and they both exhibited the same failure mode.

3.3.3 Failure mode under high-cycle (HC) loading conditions

Specimens tested under high-cycle fatigue fail with a crack kinking upward into the magnesium from the notch formed at the right weld edge. The failure mode differs from that of low-cycle fatigue in that the final rupture does not connect with the corner of the weld indentation. Instead, the crack propagates further upward and connects with the side of the weld indentation or progresses to the right of the weld indentation without connecting. Additionally the location where the crack kinks upward from the interface is more likely to be within the dispersed layer.

3.3.3.1 Failure mode under high-cycle (HC) loading conditions in 1.58 mm AZ31 and 1.5 mm HSLA steel

Figures 3.11(a) and 3.11(b) show optical micrographs of the cross section of a partially failed weld at 5.46×10^4 cycles under a load range of 0.95 kN and an enlarged section near the kinked crack of the same specimen. Figure 3.11(c) shows a failed weld at the fatigue life of 3.50×10^4 cycles under a load range of 0.99 kN. In Figure 3.11(a), a kinked fatigue crack is visible near the right pre-existing crack tip. Figure 3.11(b) shows an enlarged section near the kinked crack from which several observations can be made. The crack appears to kink out of the interface at an angle of approximately 85°. As it grows it curves slightly so that it approaches 90° with respect to the weld interface. The crack appears to kink out from the interface from just within the dispersed layer, as can be observed by voids which persist in that region to the left of the kinked crack in Figure 3.11(b). After kinking, the crack propagates through the magnesium sheet. This weld was not tested until failure, but it appears the crack would emerge on the outside of the indented region.

Figure 3.11(c) shows an optical micrograph of a failed weld with slightly different crack growth patterns. The kinked crack in this specimen appears to kink at an angle of 90°. The crack grows upward as it propagates through the magnesium sheet. In this micrograph, the final failure is shown to kink at another angle of 90° and connect with the side wall of the sonotrode indentation.

The failure mode observed in Figures 3.11(a) and 3.11(c) is different from those observed under low-cycle loading conditions as discussed earlier. Note that for low-cycle fatigue, the crack generally proceeded along the interface past the dispersed layer before kinking. Under high-cycle fatigue, the crack has a tendency to kink upward from within the dispersed layer. This can be verified by comparing Figures 3.9(a) and 3.11(a) and observing that in the high-cycle fatigue case as seen in Figure 3.11(a), the crack appears to begin kinking from a position to the right of that in Figure 3.9(a), with respect to the weld indentation. Also note the angle of kinking is closer to 90° for high-cycle fatigue specimens. Lastly for the high-cycle fatigue case, the final fracture occurs outside the weld indentation, or connecting with the side wall of the weld indentation, which is in contrast to the crack growth pattern seen in the low-cycle fatigue specimens.

The dominant failure mode for the specimens under high-cycle loading appears to be through-thickness crack propagation in the upper right sheet with the crack emerging through the side of the weld indentation or outside the weld indentation. This type of failure mode corresponds to the applied load range equal to or less than about 1.3 kN for thick steel welds and a fatigue life greater than 8.0×10^3 cycles as indicated in Figure 3.5. In summary, the ultrasonic welds in lap-shear specimens tested under high-cycle conditions fail mainly due to the kinked fatigue crack emanating from the right pre-existing crack tip and propagating through the upper right sheet thickness connecting with the side, rather than the corner of the weld indentation. A total of five specimens were tested to complete failure under these load ranges and they exhibited the same failure mode.

3.3.3.2 Failure mode under high-cycle (HC) loading conditions in 1.58 mm AZ31 and 0.8 mm mild steel

Figures 3.12(a) shows an optical micrograph of the cross sections of a failed 0.8 mm steel weld at the fatigue life of 1.53×10^4 cycles under a load range of 0.96 kN. The fatigue crack initially kinks at an angle of 79°, and then curves slightly so that it propagates at an angle of 90° with respect to the interface. The fatigue crack then connects with the side wall of the sonotrode indentation during the final fracture. Figure 3.12(b) shows a failed weld at the fatigue life of 8.08×10^4 cycles under a load range of 0.72 kN. This specimen shows a slightly different crack pattern. The fatigue crack still kinks upward at an angle of approximately 93°. Instead of connecting with the sidewall of the sonotrode indentation, the crack propagates upward through the magnesium sheet without connecting.

For welds with mild steel, high-cycle fatigue corresponds to the applied load ranges less than 1.1 kN. In summary, the ultrasonic welds in lap-shear specimens tested under high-cycle conditions fail mainly due to the kinked fatigue crack emanating from the right pre-existing crack tip and propagating through the upper right sheet thickness connecting with the side, rather than the corner of the weld indentation, or continuing upward outside the indentation. A total of two specimens were tested to complete failure under these load ranges.

3.4. Global and local stress intensity factor solutions

3.4.1 Theory

Both the global stress intensity factor solutions and the local stress intensity factor solutions with a kinked crack are evaluated for the idealized two-dimensional ultrasonic weld. A simplified schematic of the two-dimensional weld is shown in Figure 3.13(a). The global stress intensity factor solutions of the pre-existing cracks are determined in order to explain the failure in the upper right magnesium sheet as observed experimentally and to validate the finite element model. The global stress intensity factor solutions are first found analytically using closed-form solutions developed by Zhang [17]. The stress intensity factor solutions were used by Tran and Pan [18] for a spot weld in a lap-shear specimen. They will be used here, with a simplification of the normal structural stresses, σ_{ui}, σ_{uo}, σ_{li} and σ_{lo}, which are defined in Figure 3.13(b) to represent a plane strain model of the weld with a dog-bone cross section in a lap-shear specimen.

The global stress intensity factor solutions, K_1 and K_2, are obtained by Zhang [17] as

$$
\begin{aligned}
K_1 = {} & \frac{\cosh(\pi\varepsilon)\sqrt{t_u}}{2\sqrt{3(1+\eta)(1+4\eta\delta+6\eta\delta^2+3\eta\delta^3)(1+\tan^2\omega)}} \times \\
& \left\{ \left[\frac{(1+4\eta\delta+9\eta\delta^2+6\eta\delta^3)\tan\omega}{\sqrt{1+2\eta\delta(2+3\delta+2\delta^2)+\eta^2\delta^4}} - \sqrt{3} \right] \sigma_{ui} \right. \\
& - \left[\frac{(1+4\eta\delta+3\eta\delta^2)\tan\omega}{\sqrt{1+2\eta\delta(2+3\delta+2\delta^2)+\eta^2\delta^4}} + \sqrt{3} \right] \sigma_{uo} \\
& + \eta \left[\frac{\delta(1-2\eta\delta-3\eta\delta^2)\tan\omega}{\sqrt{1+2\eta\delta(2+3\delta+2\delta^2)+\eta^2\delta^4}} + \sqrt{3}(2+\delta) \right] \sigma_{li} \\
& \left. - \eta\delta \left[\frac{(1+4\eta\delta+3\eta\delta^2)\tan\omega}{\sqrt{1+2\eta\delta(2+3\delta+2\delta^2)+\eta^2\delta^4}} + \sqrt{3} \right] \sigma_{lo} \right\} \qquad (1)
\end{aligned}
$$

$$
\begin{aligned}
K_2 = {} & \frac{\cosh(\pi\varepsilon)\sqrt{t_u}}{2\sqrt{3(1+\eta)(1+4\eta\delta+6\eta\delta^2+3\eta\delta^3)(1+\tan^2\omega)}} \times \\
& \left\{ \left[\frac{(1+4\eta\delta+9\eta\delta^2+6\eta\delta^3)}{\sqrt{1+2\eta\delta(2+3\delta+2\delta^2)+\eta^2\delta^4}} + \sqrt{3}\tan\omega \right] \sigma_{ui} \right. \\
& - \left[\frac{(1+4\eta\delta+3\eta\delta^2)}{\sqrt{1+2\eta\delta(2+3\delta+2\delta^2)+\eta^2\delta^4}} - \sqrt{3}\tan\omega \right] \sigma_{uo} \\
& + \eta \left[\frac{\delta(1-2\eta\delta-3\eta\delta^2)}{\sqrt{1+2\eta\delta(2+3\delta+2\delta^2)+\eta^2\delta^4}} - \sqrt{3}(2+\delta)\tan\omega \right] \sigma_{li} \\
& \left. - \eta\delta \left[\frac{(1+4\eta\delta+3\eta\delta^2)}{\sqrt{1+2\eta\delta(2+3\delta+2\delta^2)+\eta^2\delta^4}} - \sqrt{3}\tan\omega \right] \sigma_{lo} \right\}
\end{aligned}
\qquad (2)
$$

where the stresses σ_y and τ_{xy} at a small distance r ahead of the interface crack tip are characterized by **K** as

$$
\sigma_y + i\tau_{xy} = \frac{K_1 + iK_2}{\sqrt{2\pi r}} \left(\frac{r}{t} \right)^{i\varepsilon} \qquad (3)
$$

The modulus ratio η is defined as

$$
\eta = E'_u / E'_l \qquad (4)
$$

Here,

$$
E'_u = E_u / (1 - \nu_u^2) \qquad (5)
$$

and

$$
E'_l = E_l / (1 - \nu_l^2) \qquad (6)
$$

E_u and E_l represent the Young’s Moduli of the upper and lower sheets, respectively. The bimaterial constant ε is defined as

$$
\varepsilon = \frac{1}{2\pi} \ln \frac{\kappa_u / G_u + 1/G_l}{\kappa_l / G_l + 1/G_u} \qquad (7)
$$

where G_u represents the shear modulus of the upper sheet and G_l represents the shear modulus of the lower sheet. Here, κ_u and κ_l for the upper and lower sheets, respectively, are defined as

$$\kappa_u = 3 - 4\nu_u \tag{8}$$

and

$$\kappa_l = 3 - 4\nu_l \tag{9}$$

under plane strain conditions. The thickness ratio δ is defined as

$$\delta = t_u / t_l \tag{10}$$

where t_u and t_l are the upper and lower sheet thicknesses, respectively. Note that the expressions shown in Equations (1) and (2) are for welds joining sheets with $\delta \le 1$. For welds joining sheets with $\delta > 1$, one should rotate the strip model by an angle of 180º to represent the same physical system but with $\delta < 1$.

The values of the angular quantity ω in Equations (1) and (2) can be found in Suo and Hutchinson [25]. The angular quantity ω is a function of the thickness ratio δ and the Dundurs' parameters α and β which are defined as

$$\alpha = \frac{(\kappa_l + 1)G_u - (\kappa_u + 1)G_l}{(\kappa_l + 1)G_u + (\kappa_u + 1)G_l} \tag{11}$$

$$\beta = \frac{(\kappa_l - 1)G_u - (\kappa_u - 1)G_l}{(\kappa_l + 1)G_u + (\kappa_u + 1)G_l} \tag{12}$$

Recall that the lap-shear specimen is loaded with a force per unit width, F/b, to the lower left and upper right sheets along the interface as shown in Figure 3.13(a). Figure 3.13(b) shows the left part of the strip model near the crack tip with linearly distributed structural stresses based on the classical Kirchhoff plate theory based on the work of Zhang [17]. As shown in Figure 3.13(b), σ_{ui}, σ_{uo}, σ_{li} and σ_{lo} represent the normal stresses at the inner (*i*) and outer (*o*) surfaces of the upper (u) and lower (l) strips, respectively. Note also that the normal stresses σ_{ui}^*, σ_{uo}^*, σ_{li}^* and σ_{lo}^* can be derived from the normal structural stresses σ_{ui}, σ_{uo}, σ_{li} and σ_{lo} based on the equilibrium equations and the continuity conditions of the strain and the strain gradient along the bond line. The normal structural stresses σ_{ui}, σ_{uo}, σ_{li} and σ_{lo} which are marked in Figure 3.13(b) for the left crack tip are

$$\sigma_{uo,left} = 0 \tag{13}$$

$$\sigma_{ui,left} = 0 \tag{14}$$

$$\sigma_{li,left} = \frac{4F}{t_l b} \tag{15}$$

$$\sigma_{lo,left} = -\frac{2F}{t_l b} \tag{16}$$

The normal structural stresses σ_{ui}, σ_{uo}, σ_{li} and σ_{lo} for the right crack tip are

$$\sigma_{uo,right} = -\frac{2F}{t_u b} \tag{17}$$

$$\sigma_{ui,right} = \frac{4F}{t_u b} \tag{18}$$

$$\sigma_{li,right} = 0 \tag{19}$$

$$\sigma_{lo,right} = 0 \tag{20}$$

The values of the analytical global stress intensity factors, K_1 and K_2 for the left and right tips of the weld can be obtained from Equations (1) and (2) based on Equations (14)-(20).

Figure 3.14 shows a schematic of a main crack and a kinked crack with the kink length a and the kink angle φ. Here, K_1 and K_2 represent the global stress intensity factors for the main crack, and k_{I} and k_{II} represent the local stress intensity factors for the kinked crack. Note that the arrows in the figure represent the positive values of the global and local stress intensity factors K_1, K_2, k_{I} and k_{II}. When using Equation (2) with Equations (13)-(16), the value of K_2 should be multiplied by -1 to agree with the conventions in Figure 3.14.

For kinked cracks in dissimilar material, when the kink length approaches 0, the k_{I} and k_{II} solutions can be expressed as functions of the kink angle φ, the Dunders' parameters α and β, and the global K_1 and K_2 solutions for the main crack. The local stress intensity factors k_{I} and k_{II} are expressed in the complex form, from He and Hutchinson [19] as

$$k_I + ik_{II} = \left(c_R^{HH} + ic_I^{HH}\right)\left(K_1 + iK_2\right)a^{i\varepsilon} + \left(d_R^{HH} - id_I^{HH}\right)\left(K_1 - iK_2\right)a^{-i\varepsilon} \qquad (21)$$

where c_R^{HH}, c_I^{HH}, d_R^{HH} and d_I^{HH} are the real and imaginary part of the complex function c^{HH} and d^{HH}. Both c^{HH} and d^{HH} are complex functions of α, β and φ. Equation (21) indicates that k_{I} and k_{II} depend on the crack length a and bimaterial constant ε. The global stress intensity factors K_1 and K_2 are defined in the form as in $\sigma_y + i\tau_{xy} = \frac{K_1^A + iK_2^A}{\sqrt{2\pi r}} r^{i\varepsilon}$.

The functions c_R^{HH}, c_I^{HH}, d_R^{HH} and d_I^{HH} were tabulated by He and Hutchinson [26]. The values for c^{HH} and d^{HH} were interpolated from that report. As indicated in Equation (21), when the crack length approaches zero, the values for the local stress intensity factor solutions depend on the value of a when the bimaterial constant ε is nonzero. The dependence of the solutions on the crack length a presents a challenge to develop a fatigue life estimation strategy based on a fatigue crack growth model, even though the oscillation is in a region which is too small to be of concern. This challenge prevents the evaluation of the limit at the crack length of $a = 0$ in Equation (21).

Evaluating the local stress intensity factor at a crack length of $a = 0$ is necessary in order to use the kinked crack growth model for predicting fatigue life. As explained in Chapter 2, a modified material will be used to set β and ε equal to zero. The modified material chosen for this investigation has elastic constants $E = 48.6\,\text{GPa}$ and $\nu = 0.458$ for the magnesium sheet and $E = 206.3\,\text{GPa}$ and $\nu = 0.3$ for the steel sheet. This eliminates the dependence on the crack length for the vanishing crack. It can be considered a reasonable approximation since the oscillation begins at 0.01 mm which is slightly smaller than the grain size of 0.02 mm for the AZ31 in the weld as observed by Santella et al [2]. If the oscillation is not disregarded, there may be a small region of contact for very small kink lengths. This crack closure is calculated to at a distance of 10^{-14} mm from the main crack. This length scale is not relevant to the problem since at regions very close to the crack tip, there will be a region of plasticity. With the modified material, β and ε are equal to zero. With ε =0, Equation (21) simplifies to

$$(k_I)_0 = \left(c_R^{HH} + d_R^{HH}\right)K_1 - \left(c_I^{HH} + d_I^{HH}\right)K_2 \tag{22}$$

$$(k_{II})_0 = \left(c_I^{HH} - d_I^{HH}\right)K_1 + \left(c_R^{HH} - d_R^{HH}\right)K_2 \tag{23}$$

where $c^{HH} = c_R^{HH} + ic_I^{HH}$ and $d^{HH} = d_R^{HH} + id_I^{HH}$ as developed by He and Hutchinson [19]. For similar welds, Equations (22) and (23) simplifies to the solution presented by Cotterell and Rice [27]. It should be noted that for $\varepsilon = 0$, the crack tip stresses recover the traditional $1/\sqrt{r}$ singularity. The local stress intensity factor solutions for the vanishing crack can then be approximated using Equations (22) and (23) along with analytical or computational global stress intensity factor solutions obtained using the modified material. As noted in Chapter 2, this approximation is reasonable because of the similarities of the stresses observed in the real and modified material which is due to the low value of β for the real materials and the large kink angle of 90° (according to the sign convention in Figure 3.14, the kinked angle φ should be $-90°$).

The local stress intensity factor solutions for kinked cracks with finite crack lengths for ultrasonic welds in lap-shear specimens can be expressed as functions of the normalized kink length a/t as in [28] as

$$k_{\mathrm{I}}(a) = f_{\mathrm{I}} \cdot (k_{\mathrm{I}})_0 \tag{24}$$

$$k_{\mathrm{II}}(a) = f_{\mathrm{II}} \cdot (k_{\mathrm{I}})_0 \tag{25}$$

where f_{I} and f_{II} are geometric functions which depend on the geometric parameters of the ultrasonic welded lap-shear specimens such as the weld width w and the sheet thickness t. The local stress intensity factor solutions for idealized ultrasonic welds in lap-shear specimens were obtained computationally and presented in the normalized form in [28] for $w/t = 5.85$ to match the experimental specimen dimensions.

3.4.2 Finite Element Model

A finite element model was constructed to find the global and local stress intensity factors. The two-dimensional lap-shear model for the weld with thick steel is shown in Figure 3.15(a) with the boundary and loading conditions. The specimen has the upper sheet thickness t_u, lower sheet thickness t_l, the length L, the overlap length V, and the weld width w. The $x-y$ coordinate system is shown in the figure. The left edge has a fixed displacement condition at the middle surface while the right edge has a concentrated force per unit width, F/b, applied at the middle surface in the $+x$ direction. Here, F denotes the applied force and b denotes the width of the central portion of the specimen with the reduced width. The finite element model for the weld with thin steel is exactly the same, except the lower sheet thickness, t_l, is changed to 0.8 mm.

Finite element analyses have been conducted on both an idealized model and a model which follows the weld geometry for both steel thicknesses. The central portion of the mesh for the idealized model, showing the pre-existing cracks and the crack-tips, can be seen in Figure 3.15(b). For the idealized model, the weld indentation has been omitted. In the weld geometry model, the sonotrode indentation is modeled as shown in Figure 3.15(c). Both models are computed in plane-strain which means any curvature on the weld front remaining from the original spot weld has been assumed as straight and uniform through the cross section.

The two-dimensional plane-strain finite element model has the weld width $w = 8.78$ mm, length, $L = 100$ mm, and overlap length $V = 75$ mm. The thickness t_u for the upper sheet is 1.58 mm for the top magnesium sheet and the thickness t_l is 1.5 mm or 0.8 mm for the bottom HSLA or mild steel sheet respectively. The width b of the central portion of the specimen is taken as 8 mm to calculate the applied load per unit width for the finite element analyses. Figures 3.15(b) and 3.15(c) shows the central portion of the finite element model with the welded portion and both crack tip notches which have formed during welding. Figure 3.15(d) shows a close-up view of the finite element mesh near the right crack tip. Second-order quarter point crack-tip elements (CPE8R) with collapsed nodes were used to model the $1/\sqrt{r}$ singularity near the crack tip. Any change in the metal due to welding has been ignored. Both materials are assumed to be linear elastic. Steel is modeled with a Young’s modulus $E = 206.3$ GPa and a Poisson’s ratio $\nu = 0.3$. Magnesium (AZ31) is modeled with Young’s modulus $E = 45$ GPa and a Poisson’s ratio $\nu = 0.35$. These properties are listed in Table 3.2. Computations were performed using the commercial finite element software ABAQUS [29].

The normalized computational global stress intensity factor solutions for the two pre-existing crack tips are listed in Table 3.3a and 3.3b for the idealized and weld geometry models with 1.5 mm steel and 0.8 mm steel respectively. Note that the computational stress intensity factor solutions have been normalized by the analytical $|K_2|$ solution for the right side in Equation (2) using the thick steel model for both tables. The ratio of the analytical K_2 solutions for the thin and thick steel on the right side, $\frac{K_{2,thin}}{K_{2,thick}}$, is 0.962. The results of the finite element analysis show that the $\overline{K}_1$ and $|\overline{K}_2|$ solutions are higher for the right pre-existing crack tip compared to those for the left pre-existing crack tip for both the idealized and weld geometry model. These results can be used to explain the favorable condition for kinked fatigue crack propagation in the upper right sheet under all cyclic loading conditions.

As observed from the micrographs of partially failed specimens, kinked fatigue cracks are initiated from the pre-existing crack tips and propagate through the sheet thickness of the upper right sheet under cyclic loading conditions. From the micrographs of the failed specimens, the kinked crack angle was found to be between 72° and 93° for all the load ranges. Figure 3.16(a) shows a schematic of a two-dimensional finite element model of a lap-shear specimen with a single kinked crack growing into the magnesium sheet. The boundary and loading conditions of the specimen are the same as those for the finite element model shown in Figure 3.15(a). The kink angle in this investigation is selected to be 90° ($\varphi = -90^\circ$). Fourteen normalized kink lengths, namely, $a/t =$ 0.0009, 0.0019, 0.005, 0.01, 0.025, 0.05, 0.075, 0.1, 0.2, 0.3, 0.4, 0.5, 0.6, and 0.7 are considered in this investigation. Figure 3.16(b) shows a close-up view of the finite element mesh near the right kinked crack tip for $a/t = 0.3$.

Figure 3.17 shows the values of $k_{\mathrm{I}}/(k_{\mathrm{I}})_0$ for the kinked cracks emanating from the right pre-existing crack tips as functions of the normalized kink length a/t for $w/t = 5.85$ and $\varphi = -90°$ for both models. The values of $k_{\mathrm{I}}/(k_{\mathrm{I}})_0$ are also listed in Table 3.4a and 3.4b for the 1.5 mm steel welds and the 0.8 mm steel welds respectively. Note that the solutions are normalized by $(k_{\mathrm{I}})_0$ in Equation (22) with kink angle $\varphi = -90°$ and the analytical global stress intensity factor K_1 and K_2 solutions in Equations (1) and (2) based on equations from Zhang [17]. The material used for the $(k_{\mathrm{I}})_0$ solution has been modified to achieve $\beta = 0$ and allow the use of Equation (22) as discussed in Chapter 2. The $(k_{\mathrm{I}})_0$ solution for the thick steel model was used for normalizing both Table 3.4a and 3.4b. The ratio of the analytical $(k_{\mathrm{I}})_0$ solutions for the thin and thick steel, $\frac{(k_I)_{0,thin}}{(k_I)_{0,thick}}$, is 1.075. Figure 3.17 shows that the values of $k_{\mathrm{I}}/(k_{\mathrm{I}})_0$ increase monotonically with the kink length.

Figure 3.18 shows the values of $|k_{II}|/(k_{\mathrm{I}})_0$ for the kinked cracks emanating from the right pre-existing crack tips as functions of the normalized kink length a/t for $w/t = 5.85$ and $\varphi = -90°$ for the idealized and weld geometry models for welds with both 1.5 mm and 0.8 mm steel sheet. The values of $|k_{II}|/(k_{\mathrm{I}})_0$ are also listed in Table 3.4a and 3.4b for the welds with 1.5 mm steel and 0.8 mm steel respectively. The local stress intensity factor k_{II} solutions are negative based on the definitions shown in Figure 3.14. Figure 3.18 shows that the absolute values of $k_{II}/(k_I)_0$ for the idealized models decrease monotonically as the kink length increases for kinked cracks larger than $a/t =$ 0.01. The weld geometry models differ from the idealized models indicating that the sonotrode tip indentation has an effect on k_{II}. Figures 3.17 and 3.18

show that fatigue kinked crack growth is under mixed mode I and mode II loading conditions with mode I being the dominant mode. Table 3.4a and 3.4b lists the normalized local stress intensity factor k_{I} and k_{II} solutions with $w/t = 5.85$ and $\varphi = -90°$, for 1.5 mm steel and 0.8 mm steel respectively.

3.5. Fatigue life estimations

The fatigue life for the ultrasonic welds in lap-shear specimens with a dog-bone profile is calculated using a Paris law method for kinked cracks. To use the Paris law for fatigue estimation, the local stress intensity factor k_{I} and k_{II} solutions as functions of the normalized kink length a/t are obtained from linear interpolation between those obtained from the finite element analyses in Table 3.4a and 3.4b. The variations of the k_{I} and k_{II} solutions in the range of $0.7 < a/t < 1.0$ are assumed to be the same as those for $0.6 < a/t < 0.7$. The local and global stress intensity factor solutions obtained from the finite element analyses as expressed in Equations (24) and (25) and the experimentally observed kink angle of $90°$ are used in a kinked fatigue crack growth model. The k_{I} and k_{II} solutions for a vanishing crack, $a/t = 0$, are also required and are obtained using Equations (22) and (23) and K_1 and K_2 from the finite element computations with $\beta = 0$, as in Chapter 2. The Paris law is adopted to describe the propagation of the kinked fatigue cracks emanating from the pre-existing crack tips of ultrasonic welds in lap-shear specimens. The Paris law is given as

$$\frac{da}{dN} = C\left(\Delta k_{\mathrm{eq}}(a)\right)^m \tag{26}$$

where a is the kink length and N is the life or number of cycles. Noting that the experiments show crack propagation only through the magnesium sheet, the material constants C and m for

AZ31 are found in the literature. One complication of this study is that, while crack growth data is available for AZ31, the results vary by material, testing conditions and environment. The wide range of values for C and m for AZ31 can be observed from data in Choi et al.[30], Ochi et al.[31], Ishihara et al. [32], Morita et al.[33] and Tokaji et al.[34]. Tokaji et al. suggest that magnesium is particularly sensitive to the humidity level during fatigue. According to those results, magnesium samples tested in laboratory air, with a humidity of 50-70%, had shorter fatigue lives than samples tested in dry air. Additionally plots of crack propagation rates vs. stress intensity factor range revealed that the slope changes at $\Delta K = 3.5 - 4\,\mathrm{MPa}\sqrt{\mathrm{m}}$ [34]. The stress intensity factor range for this study is above $4\,\mathrm{MPa}\sqrt{\mathrm{m}}$ for all load ranges. The constants are therefore found from the upper stress intensity range for AZ31 using both the laboratory air and dry air in Tokaji et al.[34]. The constants are taken as $C = 1.86 \times 10^{-6}\ \dfrac{\mathrm{mm/cycle}}{(\mathrm{MPa}\sqrt{\mathrm{m}})^{m}}$ and $m = 2.8$ for laboratory air, and $C = 1.36 \times 10^{-7}\ \dfrac{\mathrm{mm/cycle}}{(\mathrm{MPa}\sqrt{\mathrm{m}})^{m}}$ and $m = 2.8$ for dry air [34]. Paris law constants are also taken from Ishihara et al. [32] as $C = 4.00 \times 10^{-7}\ \dfrac{\mathrm{mm/cycle}}{(\mathrm{MPa}\sqrt{\mathrm{m}})^{m}}$ and $m = 2.7$, where tests were conducted under laboratory air. In Equation (26), Δk_{eq} is the range of the equivalent stress intensity factor under mixed mode loading conditions. For the kinked fatigue crack growth model, the range of the equivalent stress intensity factor Δk_{eq} is given as

$$\Delta k_{\mathrm{eq}}(a) = \sqrt{\Delta k_{\mathrm{I}}(a)^{2} + \gamma \Delta k_{\mathrm{II}}(a)^{2}} \tag{27}$$

where γ is an empirical constant to account for the sensitivity of material to mode II loading conditions. The value of γ is taken as 1 here. The fatigue life N can be obtained numerically by integrating the Paris law in Equation (27) as

$$N=\frac{1}{C}\left[\int_{0}^{0.0009t'}\left[\Delta k_{eq}(a)\right]^{-m}da+\int_{0.0009t'}^{0.0019t'}\left[\Delta k_{eq}(a)\right]^{-m}da+\ldots+\int_{0.70t'}^{t'}\left[\Delta k_{eq}(a)\right]^{-m}da\right] \tag{28}$$

here 0, 0.0009, 0.0019, 0.005, 0.025, 0.05, …, and 0.70 represent the values of the normalized kink length a/t where the computational local stress intensity factor solutions are available and t' is the crack growth distance $\left(t'=t/\sin|\varphi|\right)$. For $\varphi=-90°$, $t'=t$.

In this investigation, a kinked crack emanating from the right pre-existing crack tips is modeled in the finite element analyses to represent the kinked crack in the ultrasonic weld as shown in the micrographs of partially failed specimens. As stated earlier, this kinked crack is modeled for 14 normalized kink lengths. The results of the local stress intensity factor solutions from the finite element analyses are input into Equations (27) and (28) to yield a prediction of the number of cycles to failure.

The stress intensity factor solutions are found for the ideal model and weld geometry model for both the 1.5 mm and 0.8 mm steel welds. The fatigue life is estimated based on those solutions, Equation (28) and the C and m constants obtained from Tokaji et al.[34] and Ishihara et al. [32].

Figure 3.19 shows the fatigue life estimations based on the kinked fatigue crack growth model in Equation (28) with the global and local stress intensity factor solutions from the finite element analyses. Twelve kinked crack growth models were computed. These represent weld geometry and ideal geometry for welds with both thick and thin steel for three values of C and m. The C and m from Ishihara et al.[32] and from the dry air and laboratory air in Tokaji et al. [34] were used. The kinked crack growth model fatigue life for the 1.5 mm steel welds and the 0.8 mm steel welds are within 2% of each other. Therefore these are consolidated, leaving the ideal geometry and weld geometry models with three values of C and m. The idealized models use a magnesium sheet of uniform thickness, while the weld geometry models include the weld indentation. All of the models have a magnesium sheet thickness of $t_u = 1.58$ mm. Stress intensity factor solutions from finite element analyses are found for each model. The vanishing crack is obtained using Equations (22) and (23) with the appropriate global stress intensity factor solutions from each finite element model. Then life estimations are found with the Paris law constants C and m from both Tokaji et al.[34] and Ishihara et al.[32]. In Figure 3.19, the models for ideal and weld geometry nearly overlap. This is not surprising since the local $k_{\mathrm{I}} / (k_{\mathrm{I}})_0$ shown in Figure 3.17, which is the dominate mode, is nearly the same for both ideal and weld geometry models. It can be observed, however, that the choice of C and m greatly influences the kinked crack growth model predictions. The shortest fatigue life prediction is based on the values for the laboratory air in Tokaji et al. [34], while the longest fatigue life prediction is based on the values for dry air. The values obtained from Ishihara et al. [32] in laboratory air fall between those obtained from Tokaji et al.[34]. While interesting to note the large change in predicted life depends on the choice of C and m, it is also distressing to the researcher since experimentally obtaining values for C and m would be preferable, but is typically not within the research scope.

The ranges of cycle life predictions are shown in Figure 3.20 for the ideal and weld geometry models. The fatigue life estimations based on the kinked fatigue crack growth model are mostly less than experimental results. The only exception is that for high load ranges, the life estimation range overlaps and exceeds the experimental results slightly. The life predictions are most accurate for low cycle fatigue. For high cycle fatigue, the kinked crack growth model under predicts the experimental fatigue life by about a decade.

3.6. Discussion

Estimations of the plastic zones size based on the linear elastic fracture mechanics were also carried out for different kinked fatigue crack lengths under various load ranges. Plastic zone sizes were determined using $2\sigma_o'$ with σ_o' as the initial cyclic yield strength of the base metal. The estimations of the plastic zone sizes vary from 3% to 10% of the sheet thickness as the kinked fatigue crack propagates from about 2% to 20% of the sheet thickness for a load range of 1.90 kN which represents the highest load range tested experimentally. The plastic zone sizes become 29% of the sheet thickness as the kinked fatigue crack length reaches 40% of the sheet thickness for load ranges of 1.90 kN in welds with thick steel. Similarly, specimens with thin steel had plastic zones that were 27% of the sheet thickness as the kinked fatigue crack length reached 40% of the sheet thickness for loads of 1.90 kN. This means that under high load ranges, the plastic zones extend about half of the remaining ligament of the sheet when reaching 40% of the sheet thickness. As the kink crack propagates, the plastic zone continues to increase in size. This can be used to explain the similarity of the final failure under low-cycle fatigue with that of quasi-static loading in thick steel welds. For high-cycle fatigue with load ranges between 0.7 kN and 1.3 kN in welds with thick steel, the plastic zone size ranges from less than a percent to roughly 4% while propagating from about 2% to 20% of the sheet thickness. For a load range of 1.3 kN, the plastic zone becomes 13% at a crack length of 40% of the sheet thickness. Plastic zone sizes for welds with thin steel follow similar trends. For high-cycle fatigue, this can be used to explain why the crack continued upward instead of connecting directly with the corner of the sonotrode tip indentation.

The fatigue life estimations based on the kinked crack growth models were less than those found experimentally. Underestimation of fatigue life has also been reported by Jordan et al.[6] in AZ31 welds.

It was shown that the Paris law constants, C and m, have a substantial impact on the fatigue life predictions for the kinked crack growth model. Environmental factors, such as humidity as well as material properties and heat treatment influence the values for C and m. The experiments necessary to obtain C and m for the base material were not conducted due to a shortage of research material and lack of equipment. If the C and m were obtained, it would not entirely solve the problem because the magnesium changes slightly during welding. The fatigue life estimations range from models based on constants in Tokaji et al. [34] for laboratory air resulting in lower life, to dry air resulting in higher life. Fatigue life estimations based on constants from Ishihara et al. [32] fall between those based on constants from Tokaji et al. [34]. Humidity measurements in the building where fatigue tests were conducted indicate that the relative humidity is 20-55% depending on the season. This is generally less than 50-70% as reported by Tokaji et al. [34]. Our environmental conditions should lie between the two extremes. Also interesting to note is that following the exact weld geometry did not change the kinked crack growth model appreciably.

3.7. Conclusions

In this paper, the fatigue behavior of dissimilar ultrasonic welds in lap-shear specimens of AZ31B-H24 and hot-dipped galvanized steel is investigated. The welded specimens were modified into a dog-bone profile before experimental fatigue testing. The fatigue life was also studied based on a kinked crack growth fatigue life estimation model. Optical micrographs of the ultrasonic welds before and after failure under quasi-static and cyclic loading conditions were examined. The micrographs showed that fatigue failure in all cases is through the upper right AZ31 load bearing leg. During quasi-static loading conditions, the failure began at the pre-existing crack tip and fractured upward, into the weld indentation for the welds with 1.5 mm steel. During quasi-static loading of welds with 0.8 mm mild steel, the failure occurred in the steel leg. For all cyclic loading in welds with either steel type, the weld fracture appears to be initiated from the right pre-existing crack tip, propagating and kinking at roughly 90°. Under low-cycle loading conditions, the weld failure appears to be initiated from the pre-existing crack tip and the specimens finally fail as the crack connects with the corner of the weld indentation in the AZ31 on the right side of the weld. Under high-cycle loading conditions, the weld failure appears to be initiated from the pre-existing crack tip and the specimens finally fail from the kinked fatigue crack propagating through the upper right load carrying sheets, with the final fracture connecting with the side wall of the weld indentation, or outside the indentation. Finite element analyses of the ultrasonic welded lap-shear specimens for an idealized weld and model representing the welded geometry with consideration of the weld indentation were carried out to obtain the global and local stress intensity factor solutions for the main cracks and kinked cracks, respectively. The stress intensity factor solutions can be used to explain the crack growth on the right side of the weld for every cyclic load condition. A kinked fatigue crack growth model based on the global and local stress intensity factor solutions for finite kinked cracks obtained from the finite element analyses is adopted to estimate the number of fatigue cycles to failure for the ultrasonic welds. The fatigue life estimations based on the kinked fatigue crack growth model are nearly identical for welds with thick or thin steel. The inclusion of the weld indentation resulted in slightly lower fatigue life estimations than the idealized model. The kinked crack growth model is particularly sensitive to the parameters C and m. The kinked crack growth models using dry air parameters [34] were closest to the experimental fatigue results, but still underestimated the fatigue life for high cycle fatigue.

Table 3.1. Dimensions of the lap-shear specimen

Width of the grip section (W)	30 mm
Width of the central portion (b)	8.0 mm
Indentation width (g)	7 mm
Weld width (w)	8.78 mm
Length of each leg (L)	100 mm
Overlap length (V)	75 mm
Sheet thickness AZ31 (t_u)	1.58 mm
Sheet thickness steel, thick (t_l)	1.5 mm
Sheet thickness steel, thin (t_l)	0.8 mm
Radius (r)	10.0 mm

Table 3.2. Mechanical properties of AZ31-H24 and steel

	Elastic Modulus (GPa)	Poisson's ratio
AZ31-H24	45	0.35
Steel	206.3	0.3

Table 3.3a: The normalized computational global stress intensity factor $\overline{K_1}$ and $\overline{\lvert K_2 \rvert}$ solutions for the right and left pre-existing crack tips for the thick steel welds.

1.58 mm magnesium and 1.5 mm steel		$\overline{K_1}$	$\overline{\lvert K_2 \rvert}$
Model with weld geometry including sonotrode indentation	Right crack tip	0.731	1.024
	Left crack tip	0.335	0.373
Idealized model	Right crack tip	0.736	1.003
	Left crack tip	0.373	0.382

Table 3.3b: The normalized computational global stress intensity factor $\overline{K_1}$ and $\overline{\lvert K_2 \rvert}$ solutions for the right and left pre-existing crack tips for the thin steel welds.

1.58 mm magnesium and 0.8 mm steel		$\overline{K_1}$	$\overline{\lvert K_2 \rvert}$
Model with weld geometry including sonotrode indentation	Right crack tip	0.775	0.988
	Left crack tip	0.528	0.559
Idealized model	Right crack tip	0.760	0.975
	Left crack tip	0.547	0.558

Table 3.4a: The normalized local stress intensity factors $k_I/(k_I)_0$ and $k_{II}/(k_I)_0$ solutions for the right kinked crack with $w/t = 5.85$ and $\varphi = -90°$ for thick steel welds.

	Idealized Model		Weld Geometry Model	
a/t	$k_I/(k_I)_0$	$\lvert k_{II}\rvert/(k_{\mathrm{I}})_0$	$k_I/(k_I)_0$	$\lvert k_{II}\rvert/(k_{\mathrm{I}})_0$
0.0	1.015	0.237	1.002	0.238
0.0009	1.052	0.177	1.065	0.176
0.0019	1.061	0.183	1.075	0.182
0.005	1.082	0.189	1.098	0.188
0.01	1.110	0.191	1.127	0.192
0.025	1.183	0.189	1.205	0.192
0.05	1.292	0.180	1.320	0.187
0.075	1.398	0.170	1.432	0.182
0.1	1.507	0.160	1.547	0.178
0.2	1.983	0.125	2.045	0.169
0.3	2.598	0.095	2.681	0.171
0.4	3.465	0.070	3.558	0.179
0.5	4.784	0.047	4.875	0.184
0.6	6.992	0.028	7.059	0.170
0.7	11.226	0.013	11.252	0.125

Table 3.4b: The normalized local stress intensity factors $k_I/(k_I)_0$ and $k_{II}/(k_I)_0$ solutions for the right kinked crack with $w/t = 5.85$ and $\varphi = -90°$ for thin steel welds.

	Idealized Model		Weld Geometry Model	
a/t	$k_I/(k_I)_0$	$\lvert k_{II}\rvert/(k_{\mathrm{I}})_0$	$k_I/(k_I)_0$	$\lvert k_{II}\rvert/(k_{\mathrm{I}})_0$
0.0	0.982	0.243	0.989	0.238
0.0009	1.043	0.189	1.059	0.193
0.0019	1.051	0.195	1.067	0.199
0.005	1.072	0.200	1.089	0.205
0.01	1.101	0.201	1.119	0.206
0.025	1.175	0.197	1.197	0.204
0.05	1.287	0.186	1.314	0.197
0.075	1.394	0.175	1.427	0.190
0.1	1.504	0.165	1.543	0.185
0.2	1.982	0.127	2.043	0.172
0.3	2.598	0.097	2.679	0.172
0.4	3.465	0.070	3.558	0.179
0.5	4.784	0.047	4.875	0.184
0.6	6.992	0.028	7.059	0.170
0.7	11.228	0.013	11.252	0.125

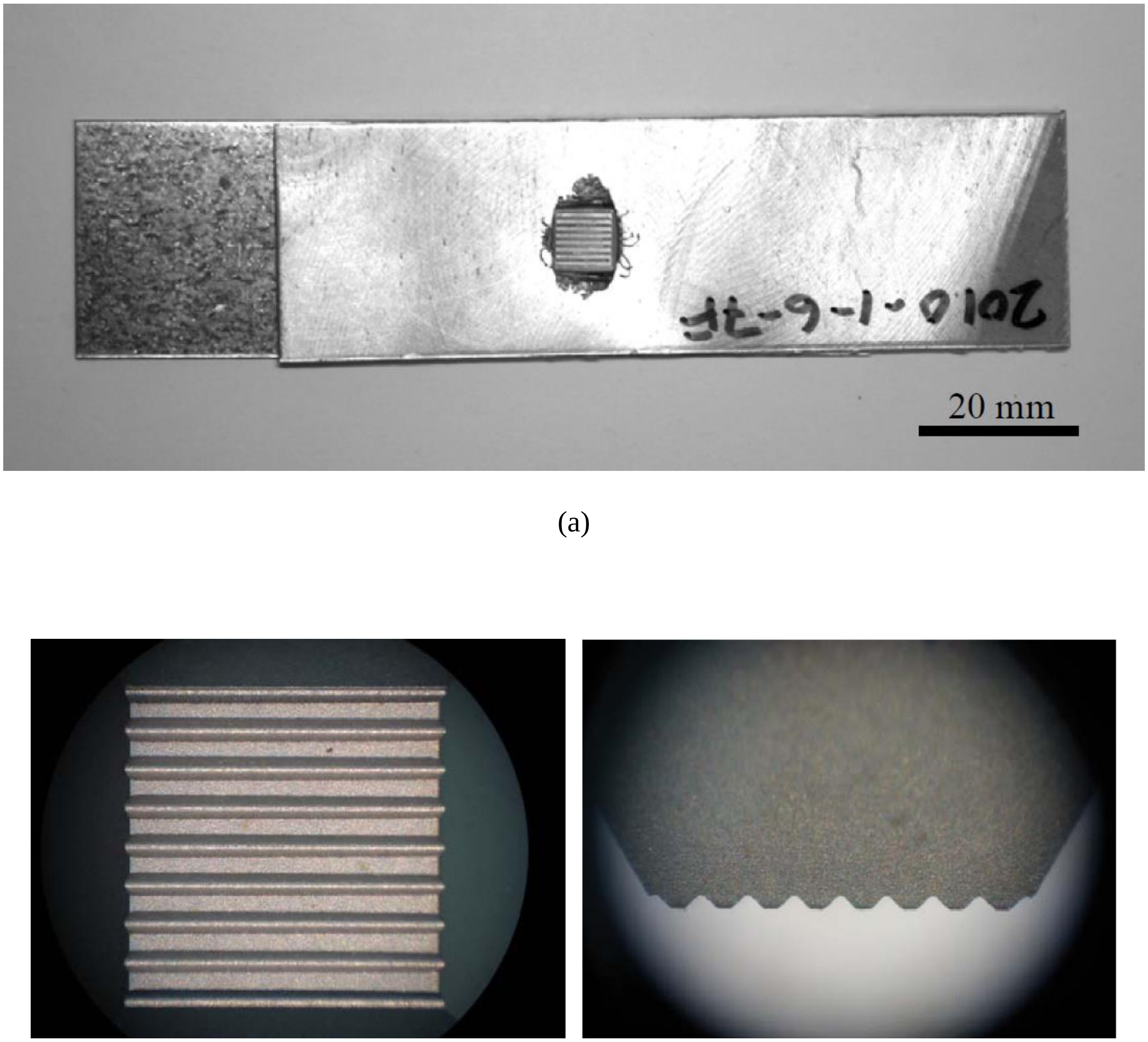

(a)

(b)

(c)

Figure 3.1 (a) A top view of an ultrasonic welded lap-shear specimen prior to being machined into a dog-bone shaped specimen. (b) Face view and (c) side view of the sonotrode tip used in the ultrasonic welding.

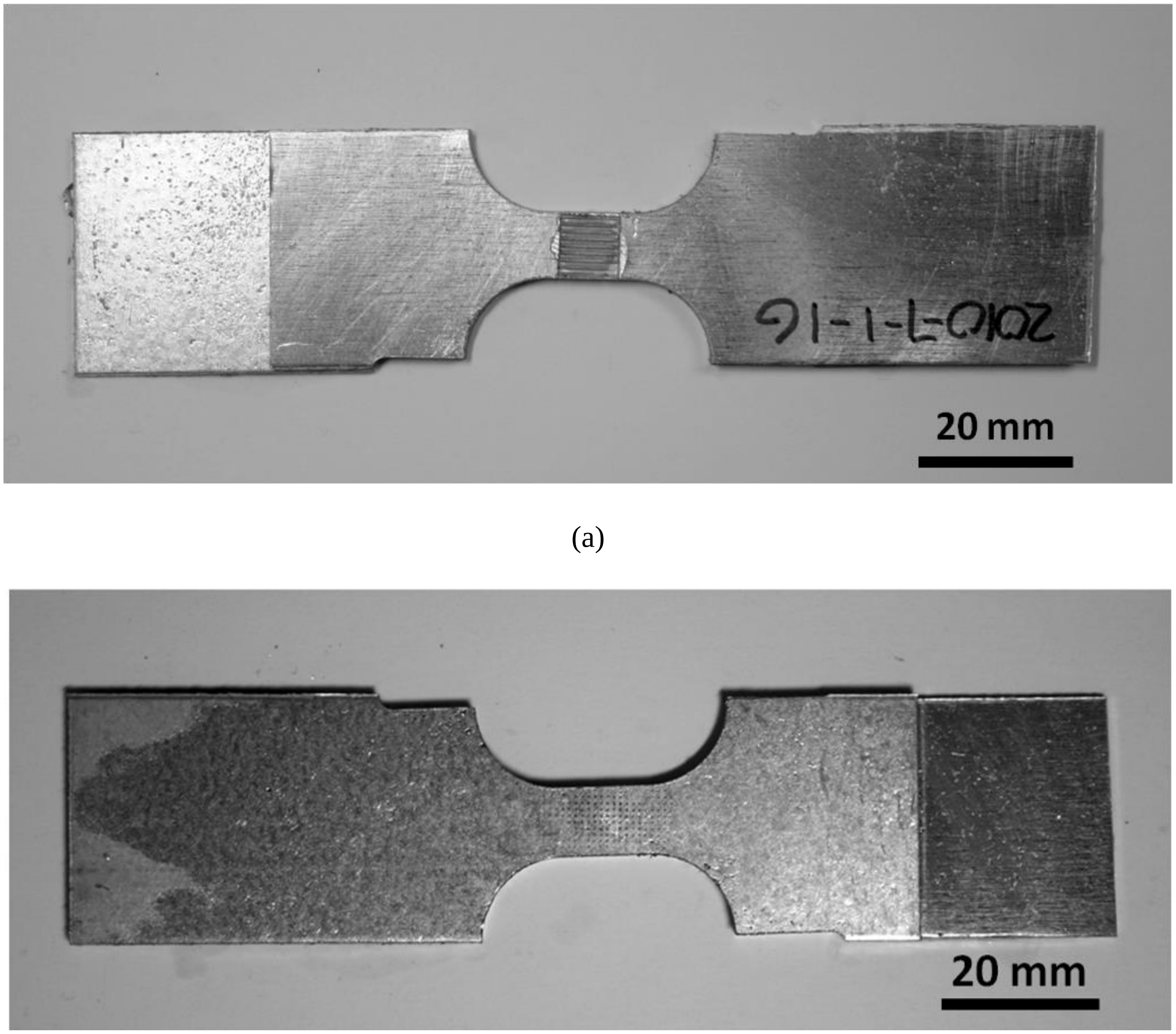

(a)

(b)

Figure 3.2. (a) A top view and (b) a bottom view of an ultrasonic welded lap-shear specimen which has been machined into a dog-bone shape.

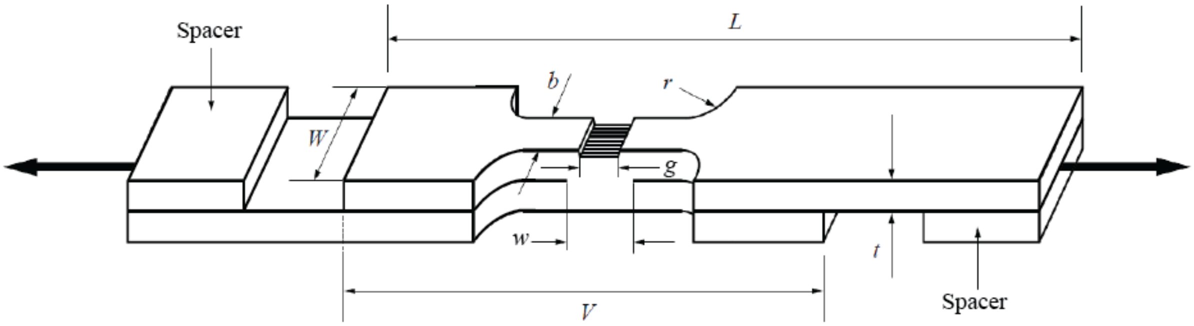

Figure 3.3. A schematic of a lap-shear specimen with the loading directions shown as the bold arrows.

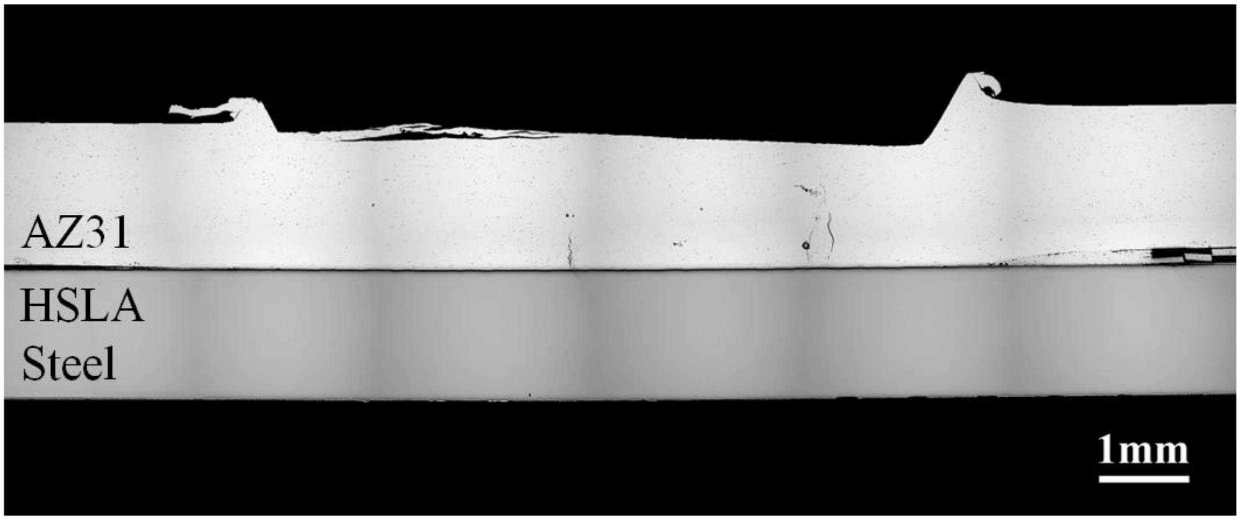

(a)

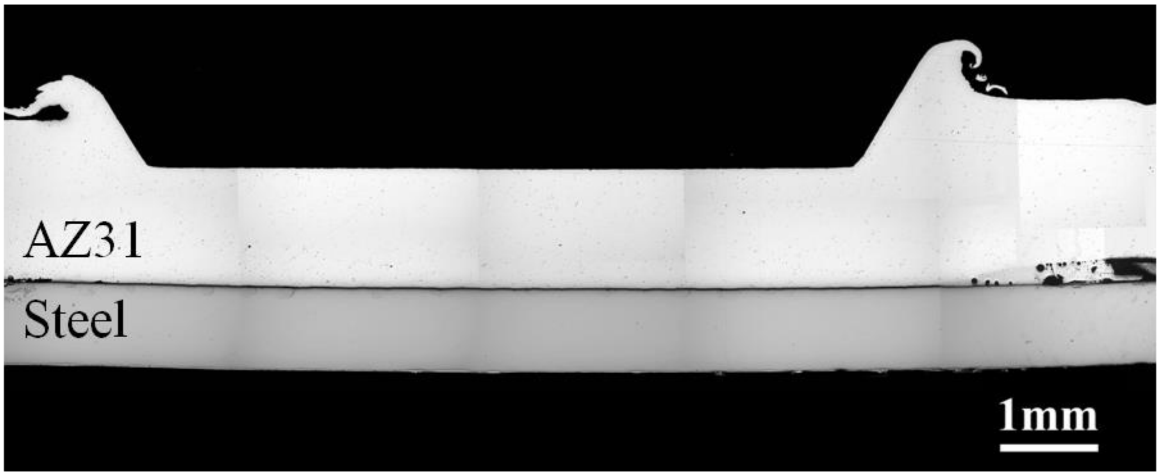

(b)

Figure 3.4. An optical micrograph of the cross section of an ultrasonic welded joint in (a) 1.58 mm AZ31 and 1.5 mm HSLA steel and (b) 1.58 mm AZ31 and 0.8 mm mild steel prior to testing.

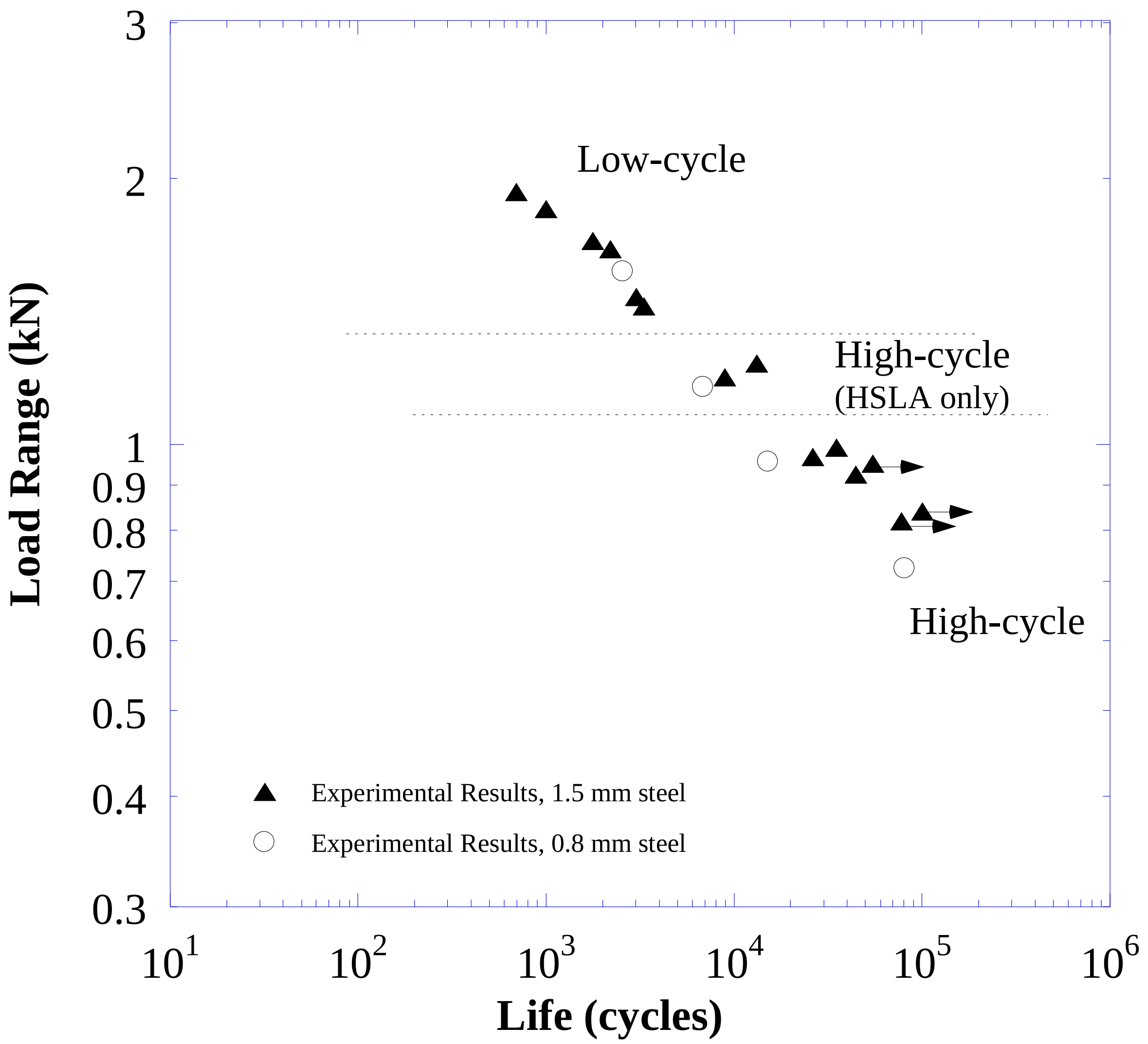

Figure 3.5. The experimental results of the fatigue tests of ultrasonic spot welds with a dog-bone profile in lap-shear specimens under cyclic loading conditions.

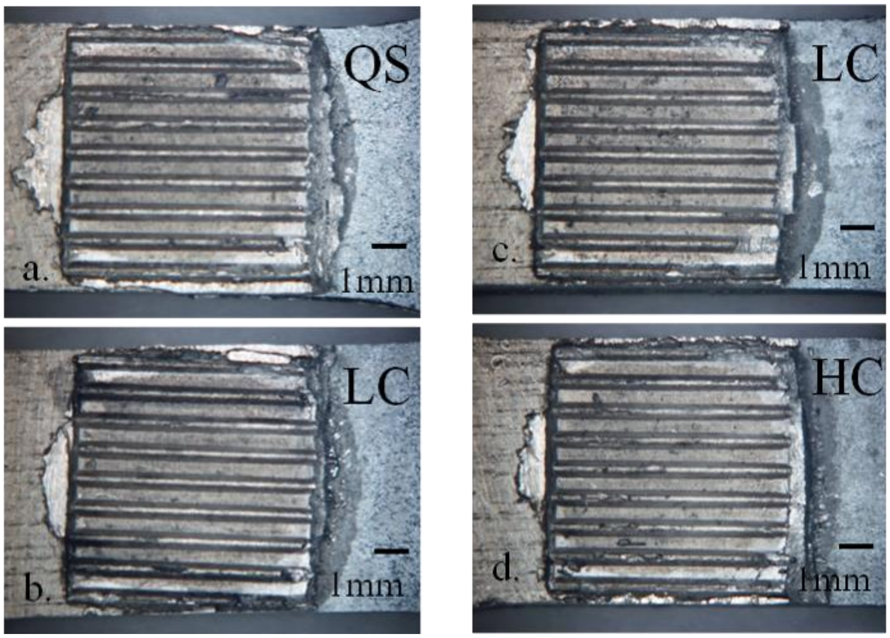

Figure 3.6. A top view of the weld in magnesium and thick steel after testing for (a) quasi-static load, (b) (low cycle) cyclic loading with 697 cycles under a load range of 1.93 kN, (c) (low cycle) cyclic loading with 2194 cycles under a load range of 1.66 kN, (d) (high cycle) cyclic loading with 8962 cycles under a load range of 1.19 kN.

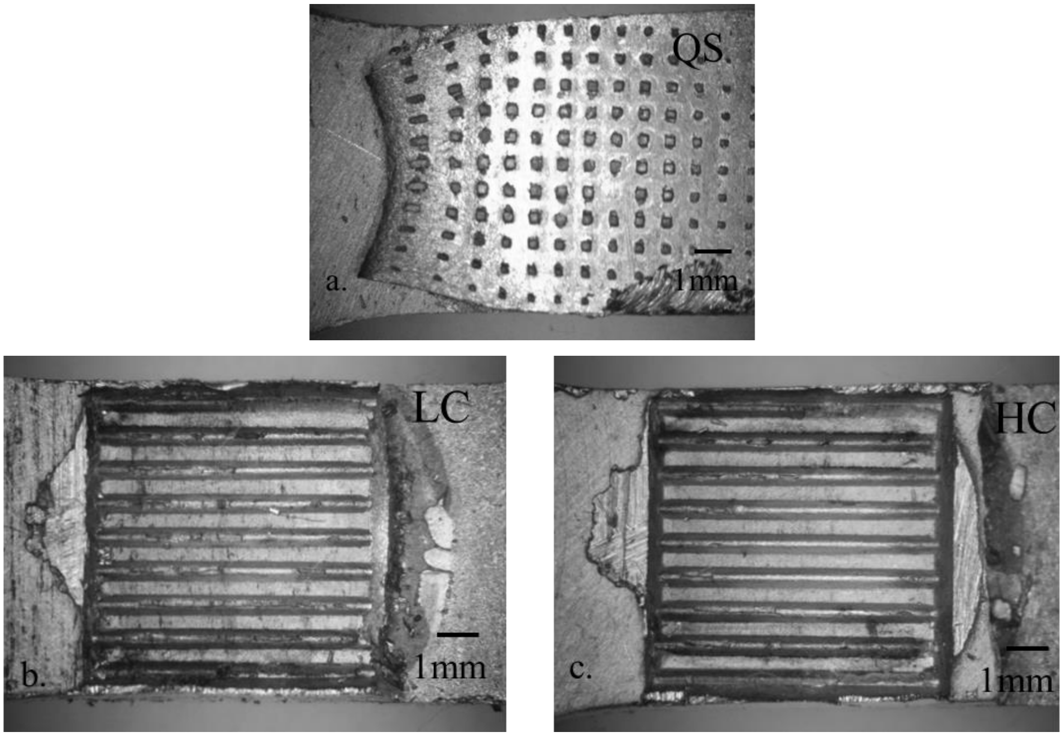

Figure 3.7. (a) A bottom view of the weld in magnesium and thin steel after testing for quasi-static load. A top view of the weld in magnesium and thin steel after testing for (b) (low cycle) cyclic loading with 2566 cycles under a load range of 1.57 kN and (c) (high cycle) cyclic loading with 80,821 cycles under a load range of 0.72 kN.

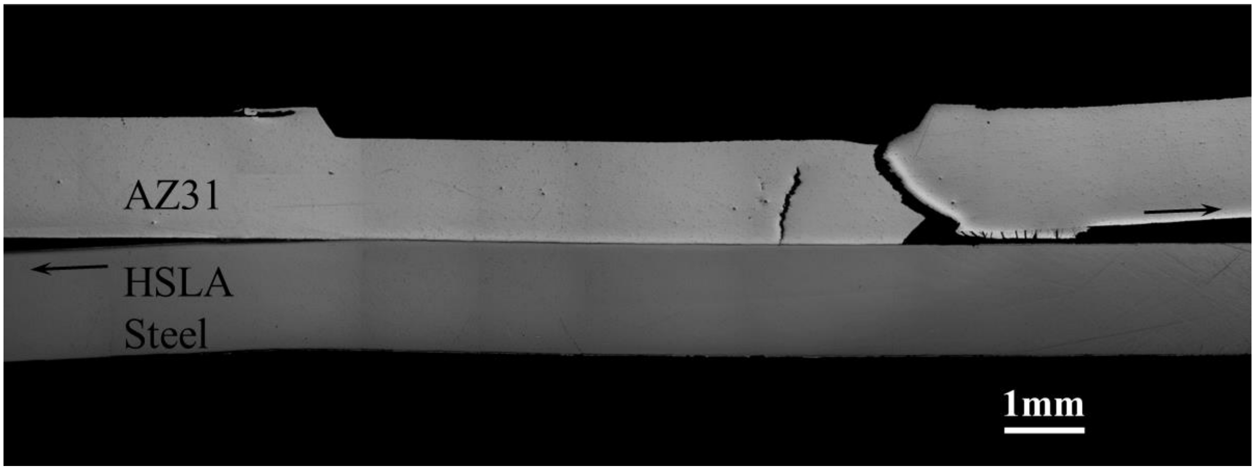

Figure 3.8. Optical micrograph of a failed weld in 1.58 mm AZ31 and 1.5 mm HSLA steel under quasi-static loading conditions.

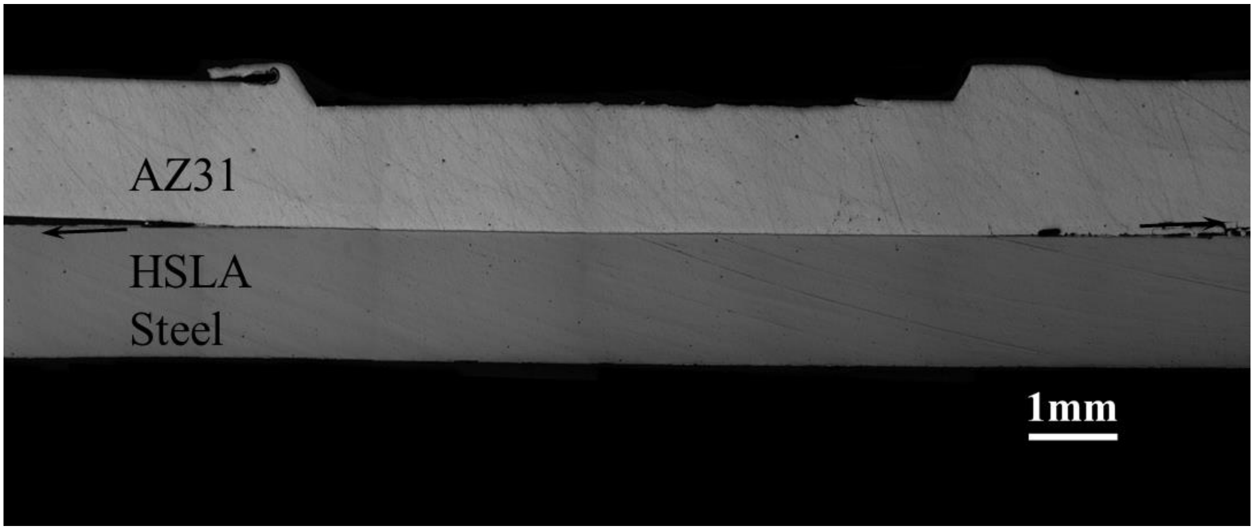

(a)

(b)

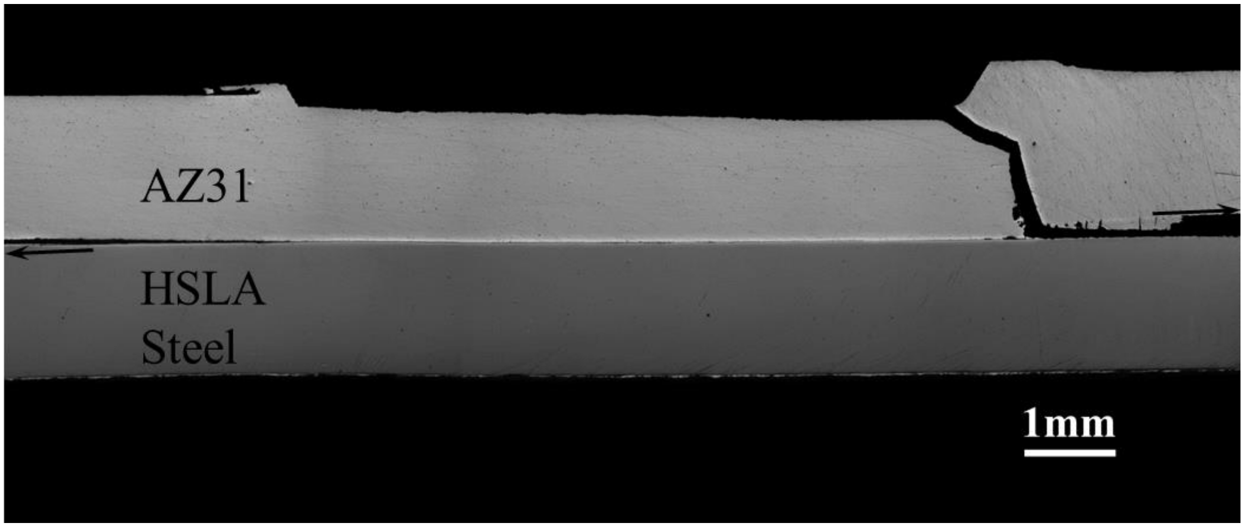

(c)

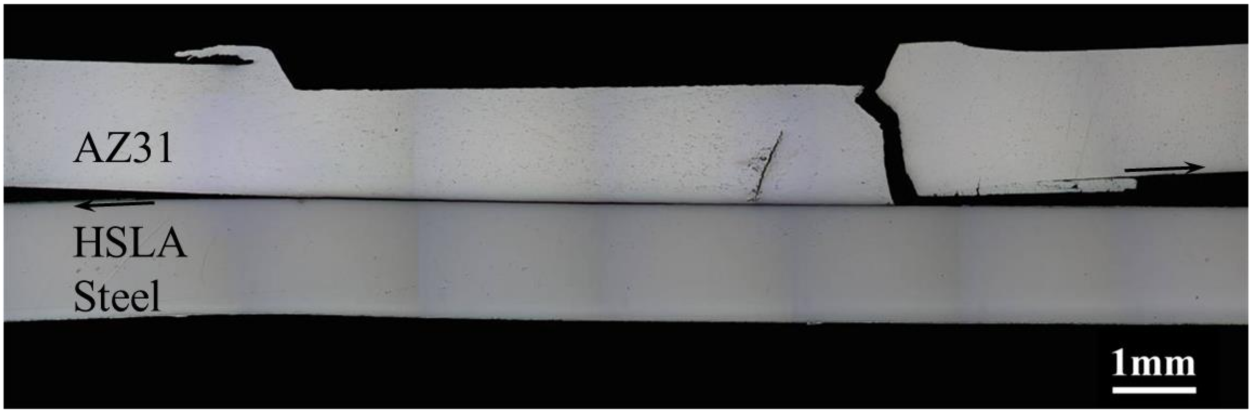

(d)

Figure 3.9. Optical micrographs of (a) the entire section and (b) an enlarged near the kinked crack of a partially failed thick steel weld at the fatigue life of 2.2×10^3 cycles under a load range of 1.43 kN. Optical micrographs of a failed thick steel welds (c) at the fatigue life of 1.7×10^3 cycles under a load range of 1.70 kN and (d) at the fatigue life of 3.3×10^3 cycles under a load range of 1.43 kN (low-cycle (LC) loading conditions).

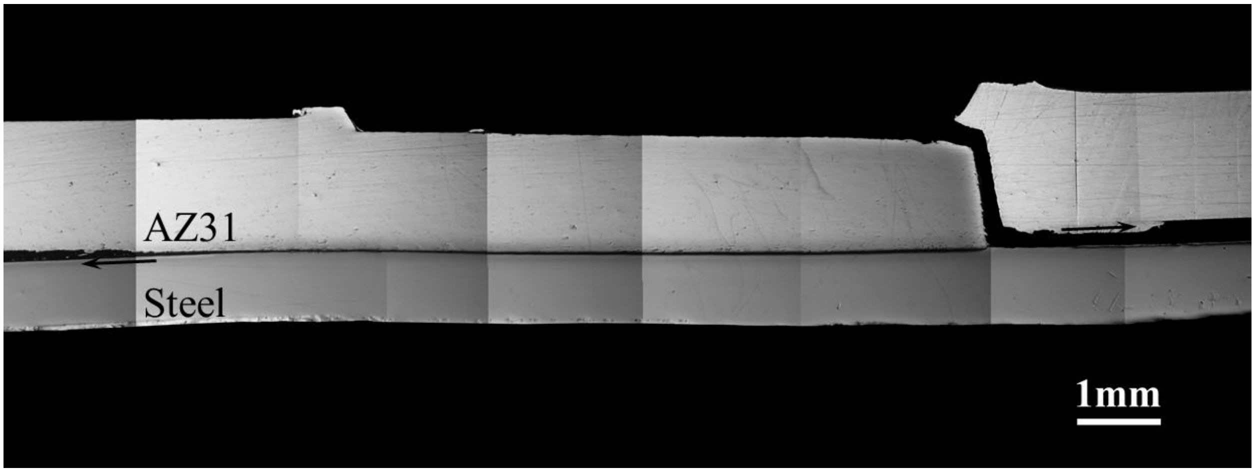

Figure 3.10. Optical micrograph of a failed thin steel weld at the fatigue life of 6.9×10^3 cycles under a load range of 1.16 kN (low-cycle (LC) loading conditions).

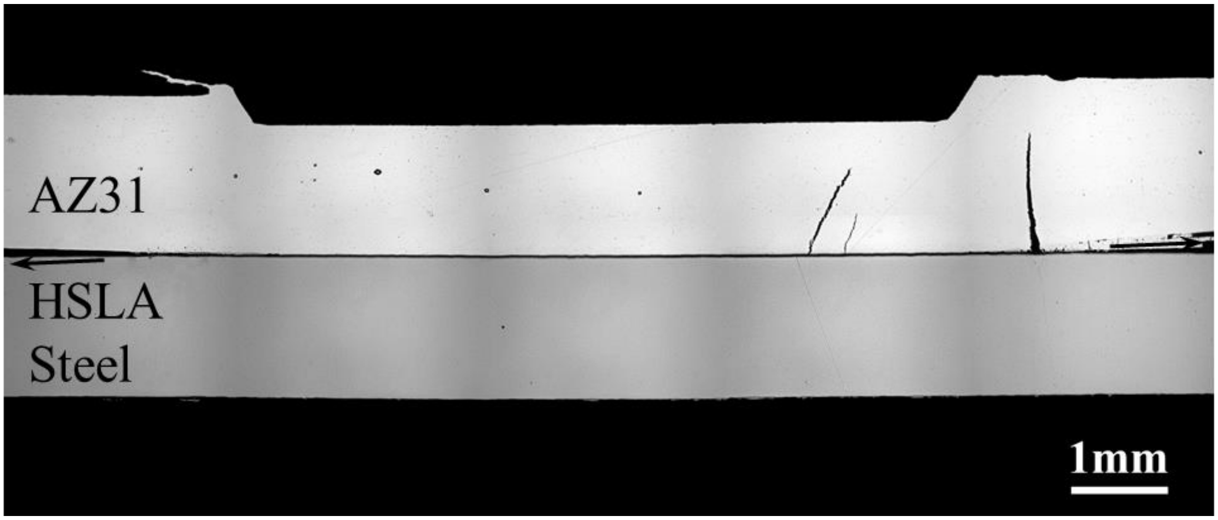

(a)

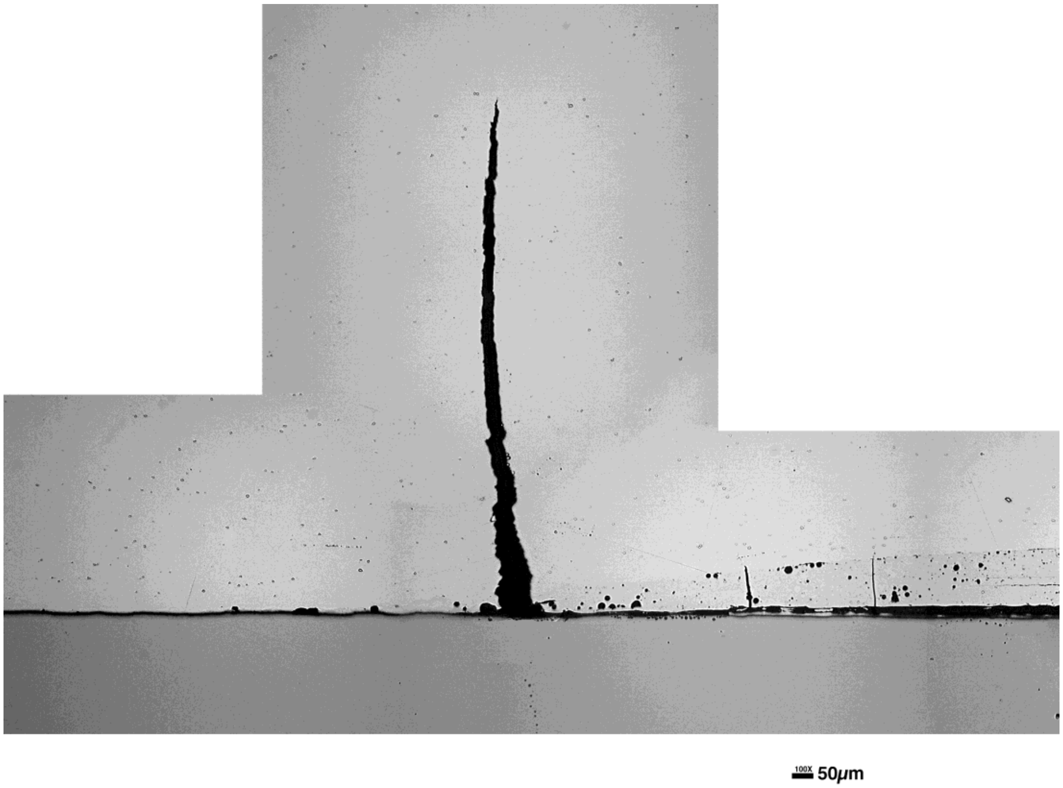

(b)

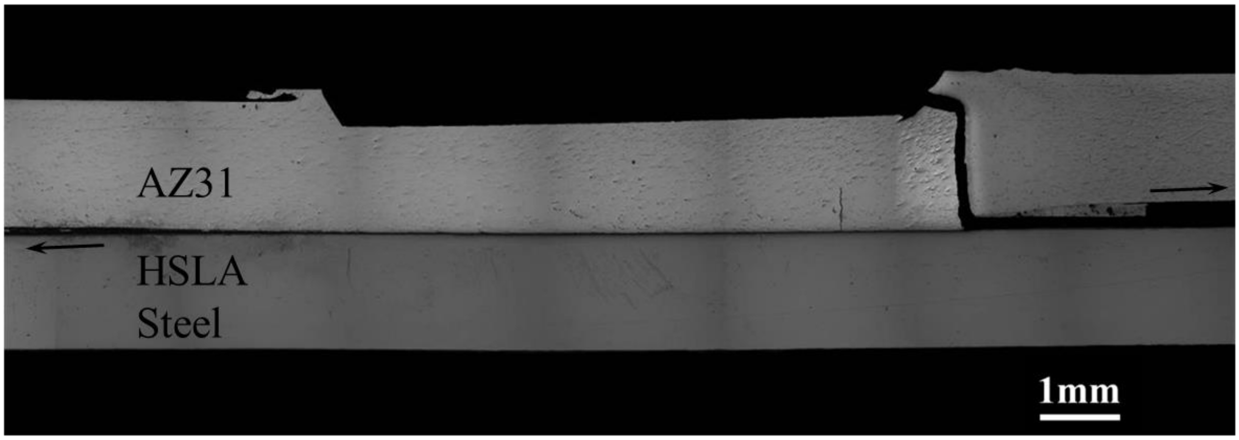

(c)

Figure 3.11. Optical micrographs of (a) the entire section and (b) an enlarged section near the kinked crack of a partially failed thick steel weld at the fatigue life of 5.46×10^4 cycles under a load range of 0.95 kN. (c) Optical micrograph of a fully failed weld at a fatigue life of 3.50×10^4 cycles under a load range of 0.99 kN (high-cycle (HC) loading conditions).

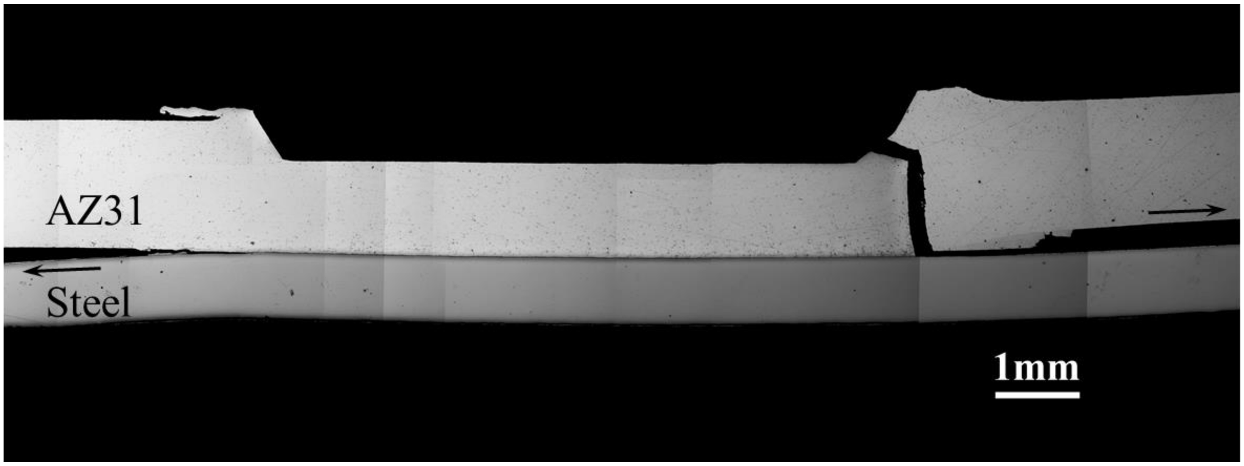

(a)

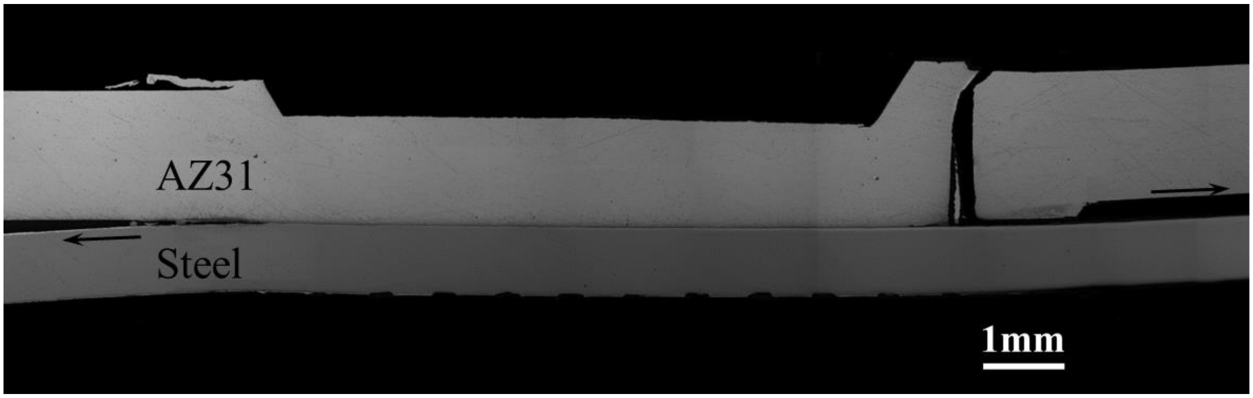

(b)

Figure 3.12. Optical micrographs of (a) a failed thin steel weld at a fatigue life of 1.53×10^4 cycles under a load range of 0.96 kN and (b) a failed thin steel weld at a fatigue life of 8.08×10^4 cycles under a load range of 0.72 kN (high-cycle (HC) loading conditions).

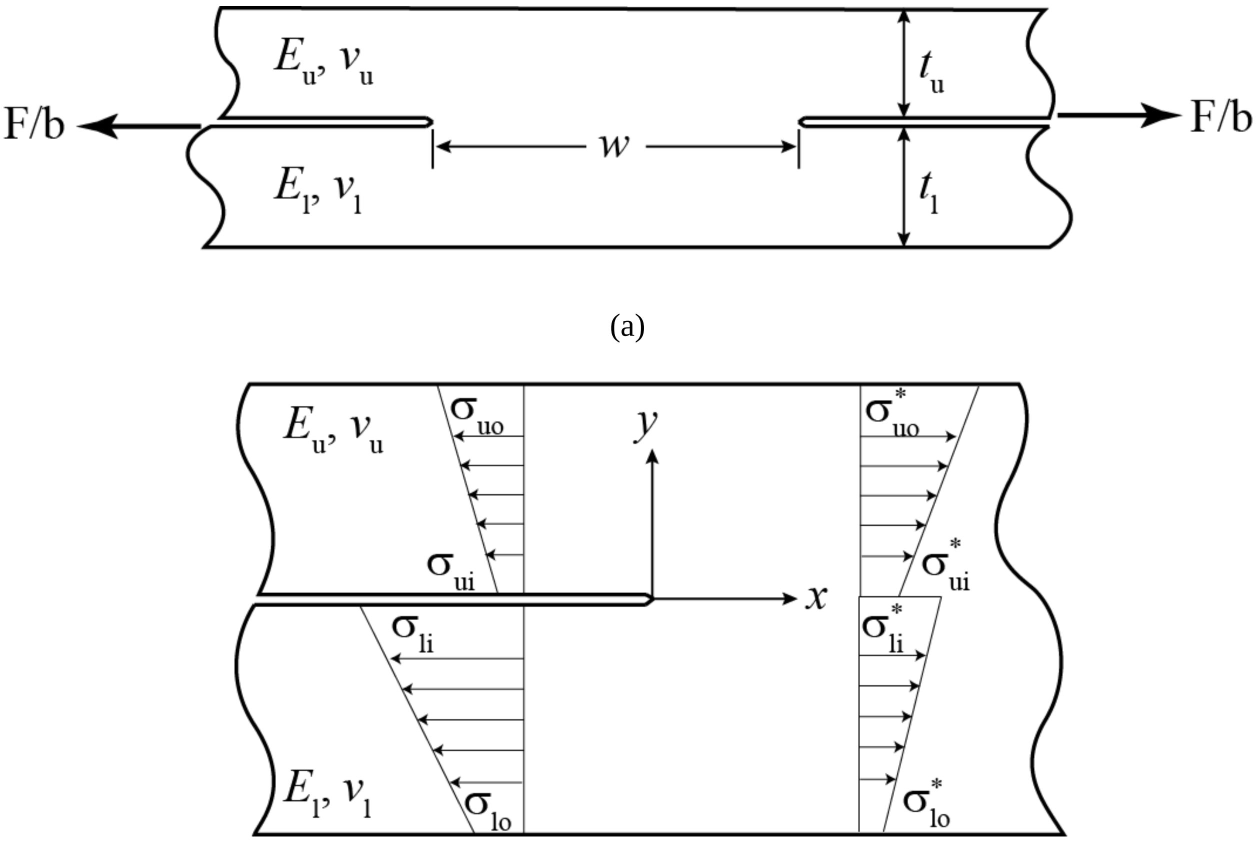

(a)

(b)

Figure 3.13. (a) A schematic of the weld with the lap-shear loading condition. (b) A schematic of the left crack tip showing the normal stresses σ_{ui}, σ_{uo}, σ_{li} and σ_{lo} at the inner (*i*) and outer (*o*) surfaces of the upper (*u*) and lower (*l*) strips, respectively.

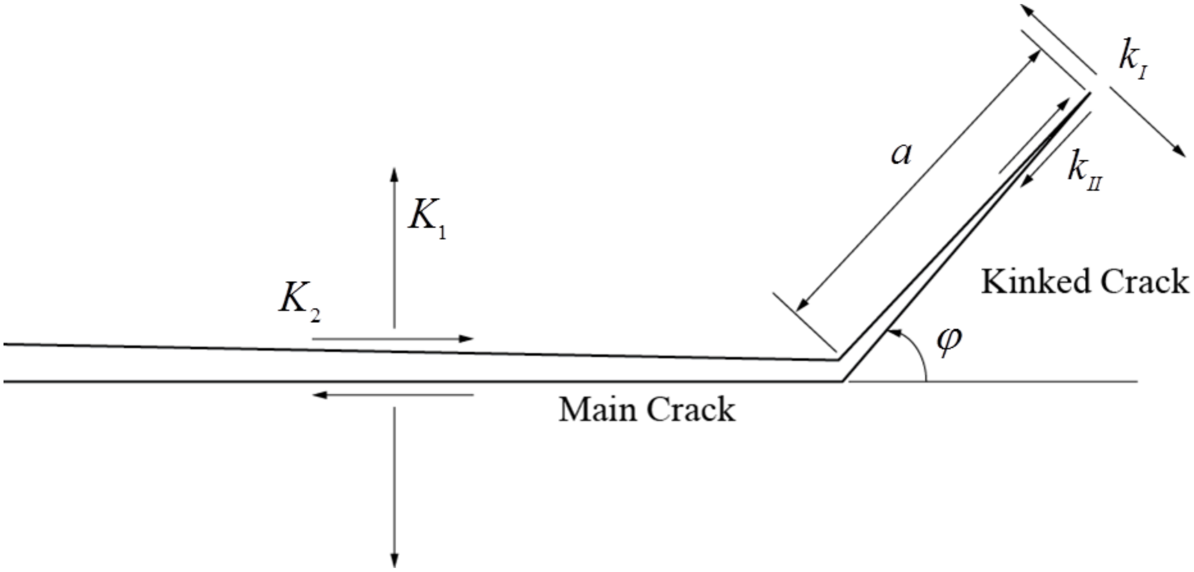

Figure 3.14. A schematic of a main crack and a kinked crack with the kink length a and the kink angle φ.

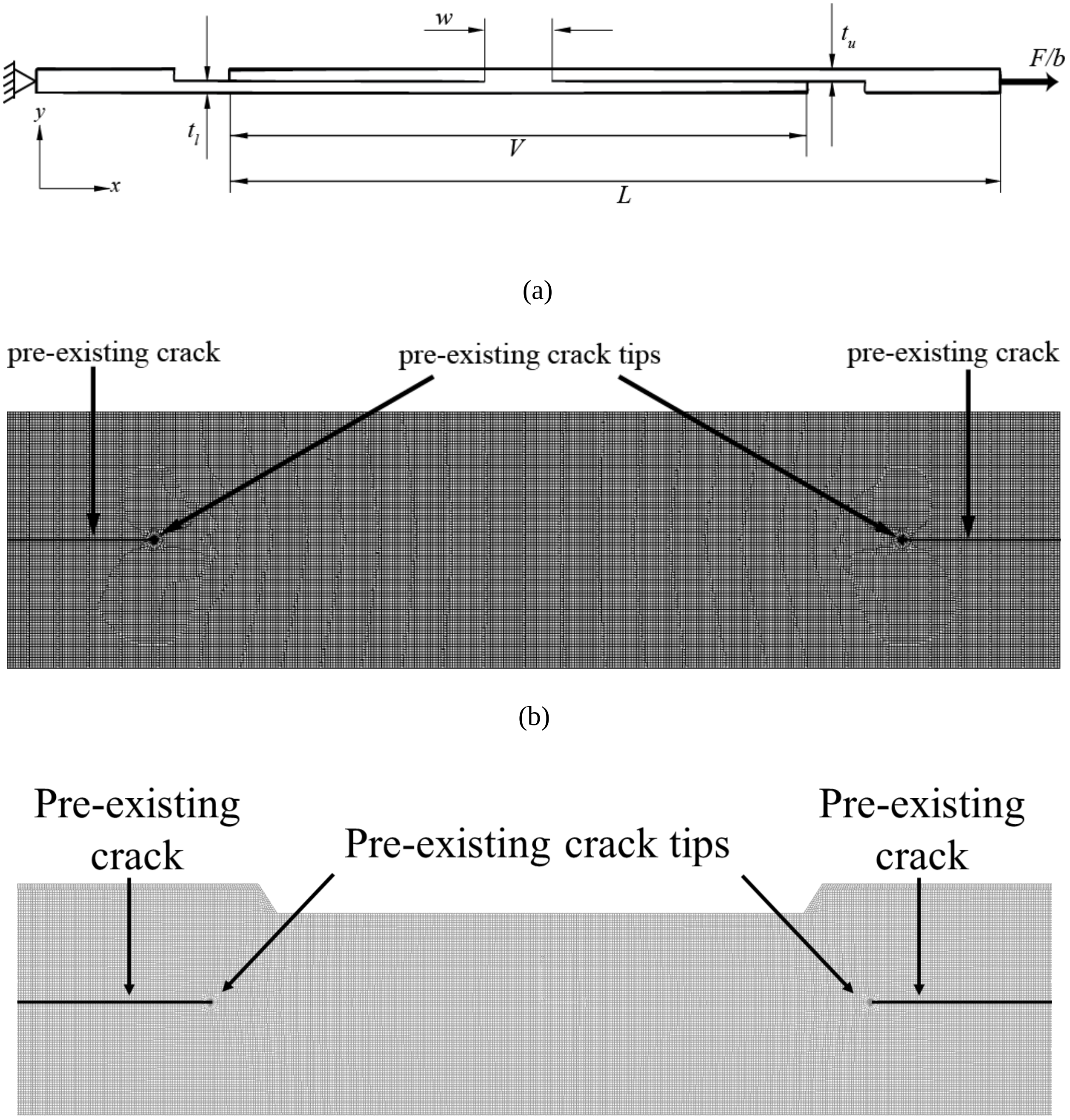
w
t_u
F/b
y
x
t_l
V
L
pre-existing crack
pre-existing crack tips
pre-existing crack
Pre-existing crack
Pre-existing crack tips
Pre-existing crack

(a)

(b)

(c)

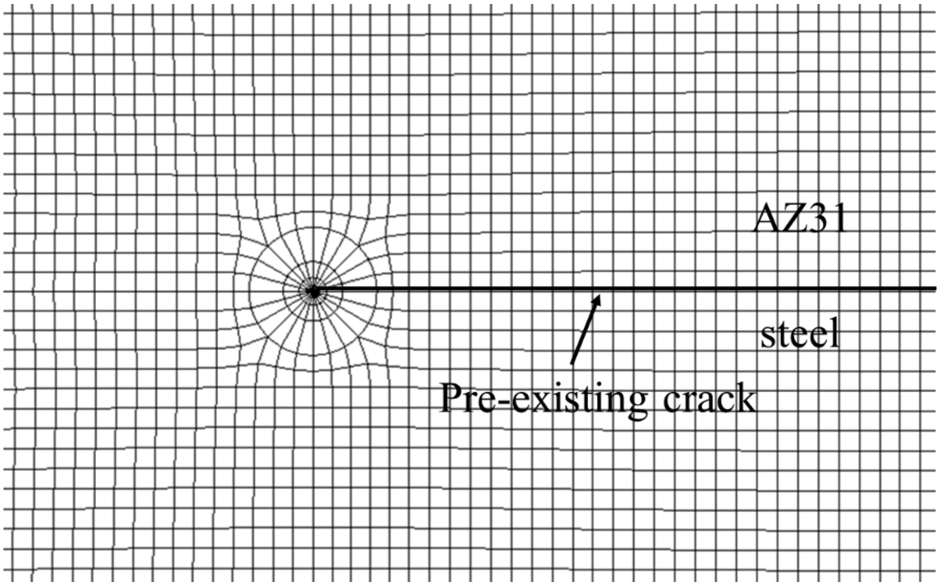

(d)

Figure 3.15. (a) A schematic of a two-dimensional finite element model of a lap-shear specimen with the boundary and loading conditions, (b) a view of the finite element mesh for the idealized showing the weld nugget and both pre-existing crack tips (c) a view of the finite element mesh for the weld geometry model showing the weld nugget and pre-existing crack tips and (d) a close-up view of the finite element mesh near the right crack tip.

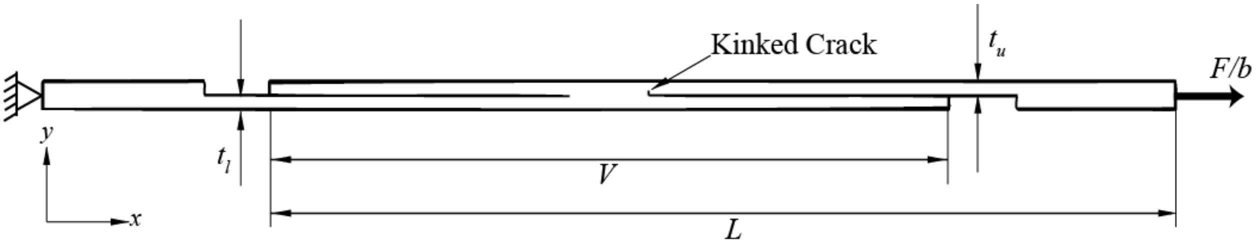

(a)

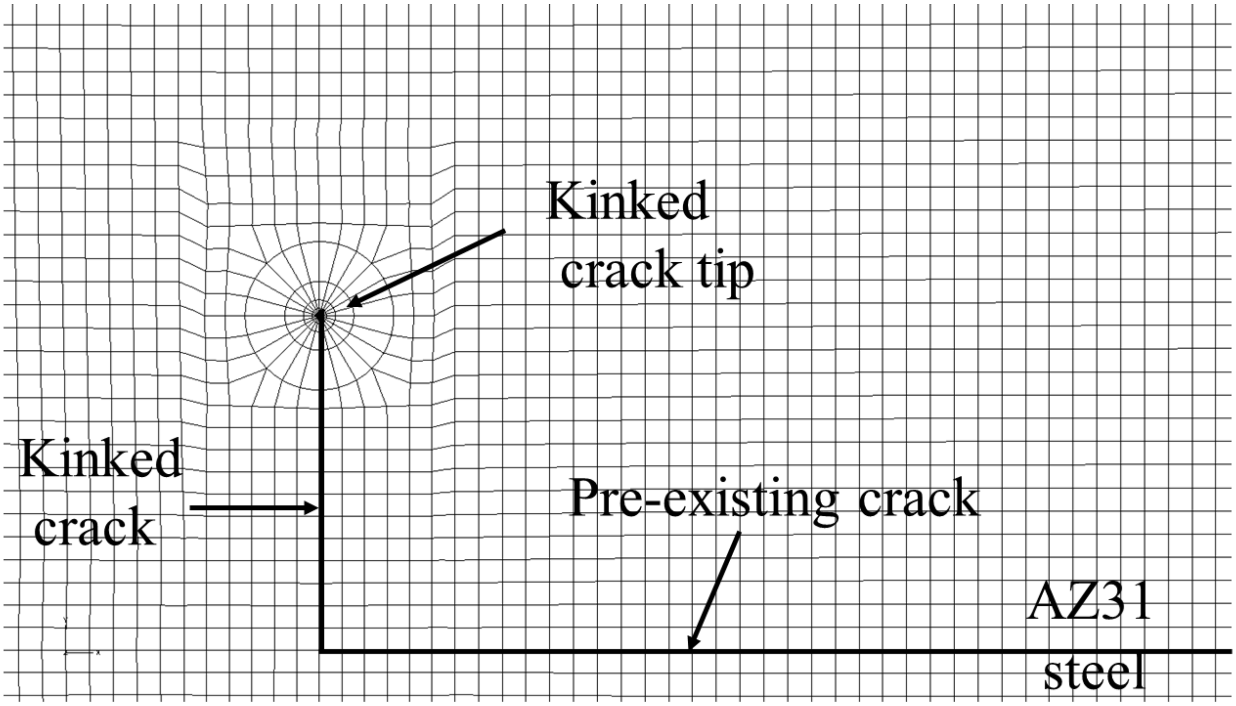

(b)

Figure 3.16. (a) A schematic of a two-dimensional finite element model of a lap-shear specimen showing a kinked crack on the right side of the weld and the boundary and loading conditions, and (b) a close-up view of the finite element mesh near the right kinked crack tip for $a/t = 0.3$.

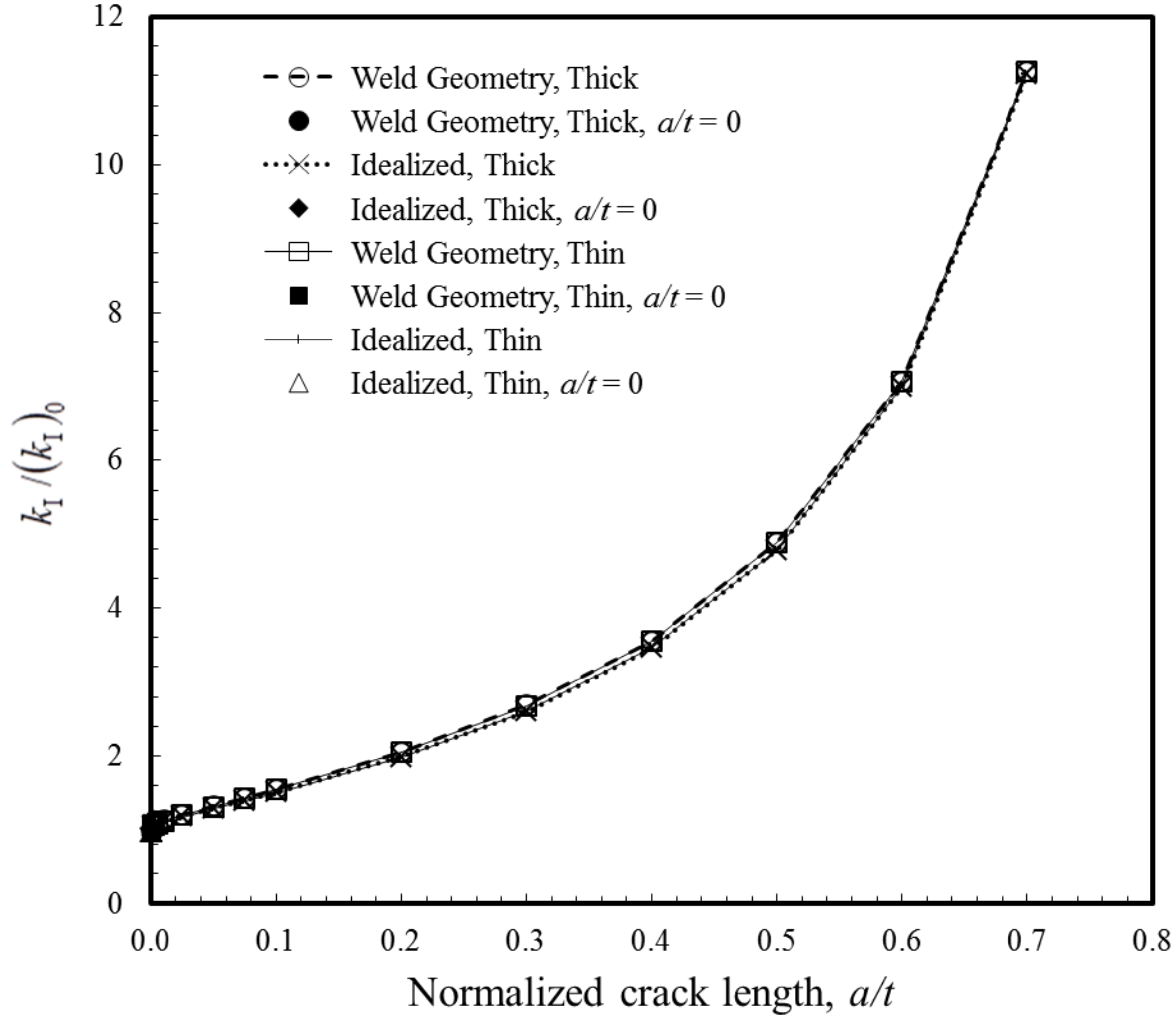

Figure 3.17. The values of $k_\mathrm{I}/(k_\mathrm{I})_0$ for the kinked cracks emanating from the right pre-existing crack tips as functions of the normalized kink length a/t for $w/t = 5.85$ and $\varphi = -90°$.

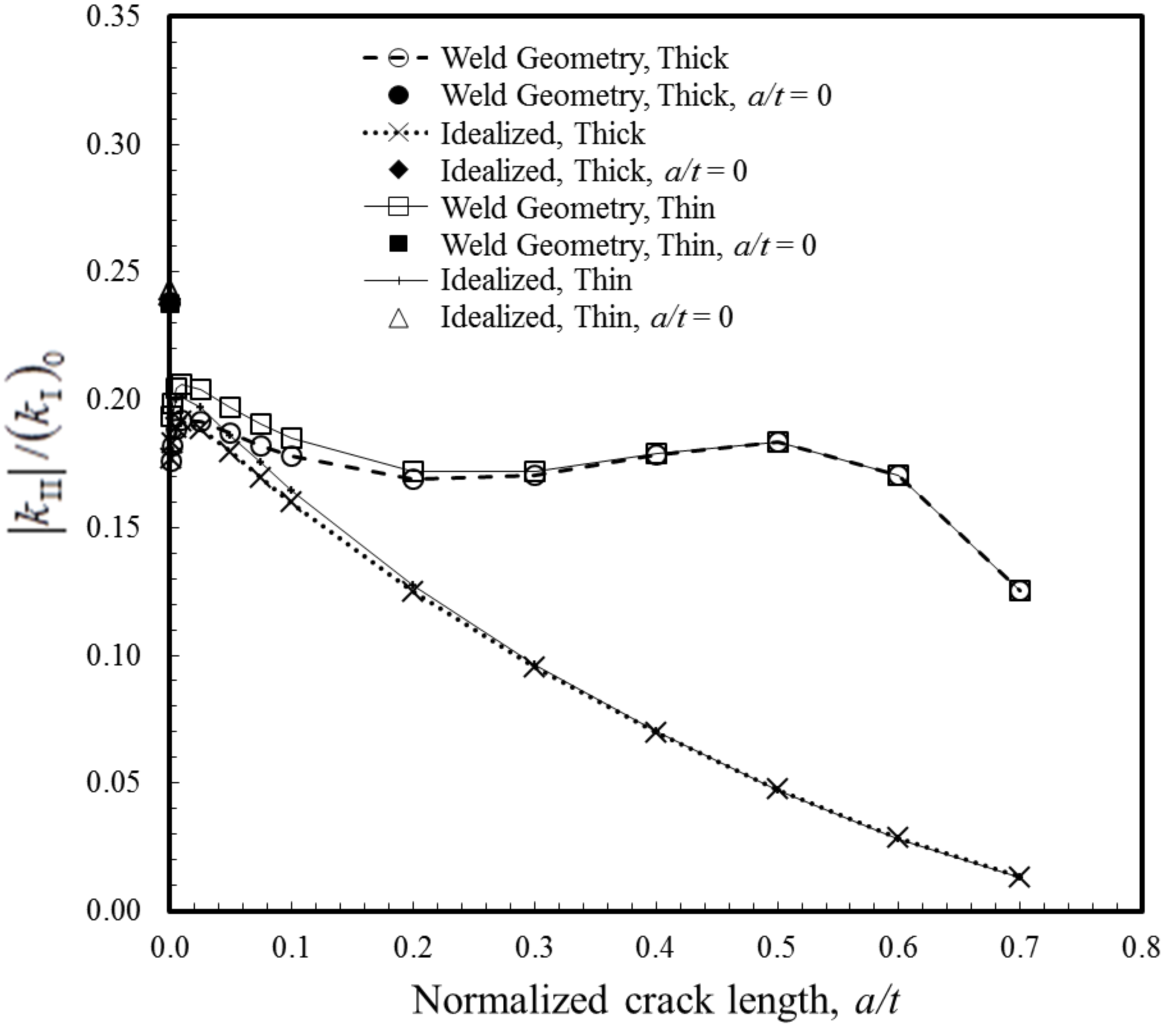

Figure 3.18. The values of $|k_{II}|/(k_{\mathrm{I}})_0$ for the kinked cracks emanating from the right pre-existing crack tips as functions of the normalized kink length a/t for $w/t = 5.85$ and $\varphi = -90°$.

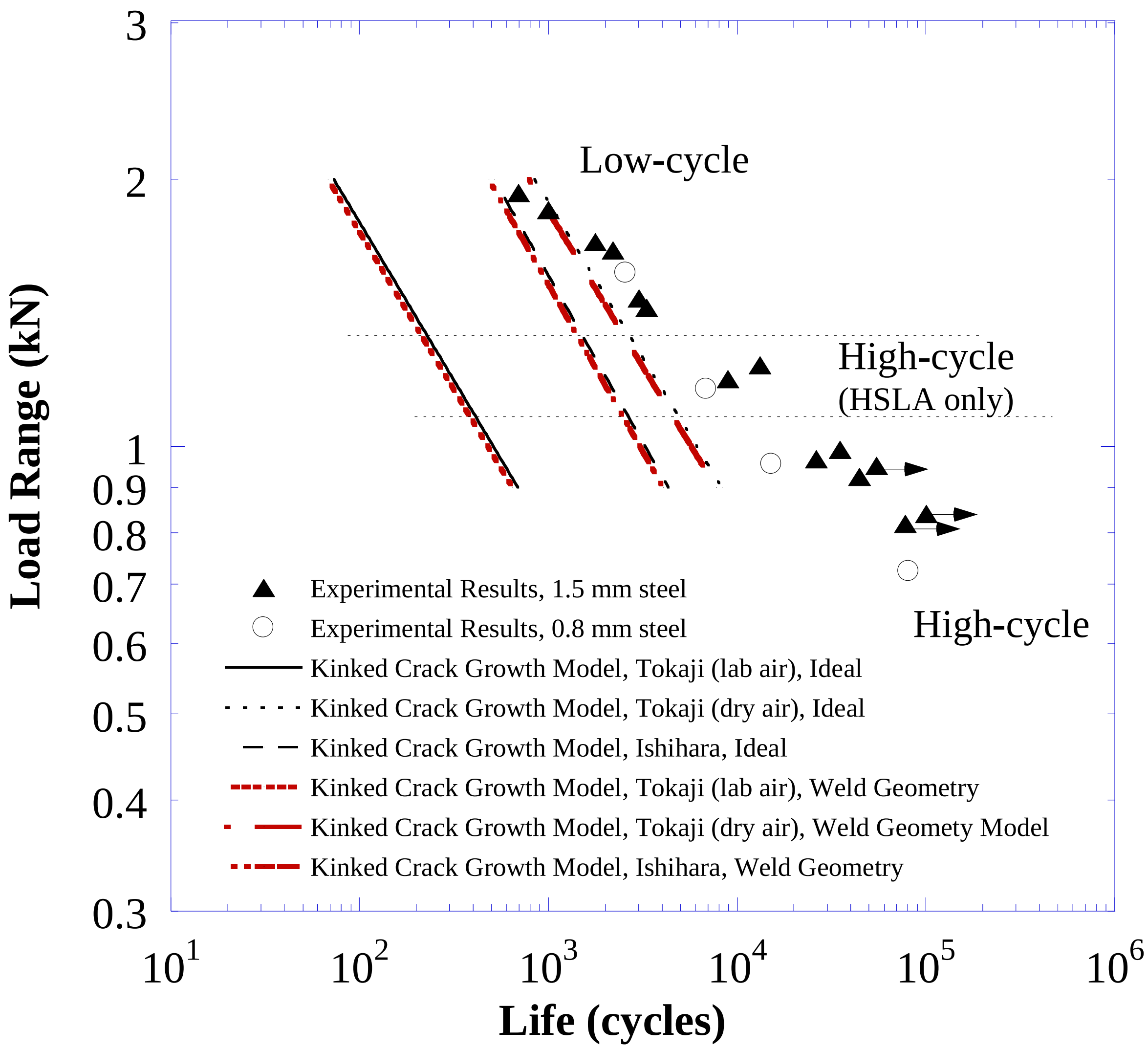

Figure 3.19. The experimental results and the fatigue life estimations based on the kinked fatigue crack growth models for three values of C and m.

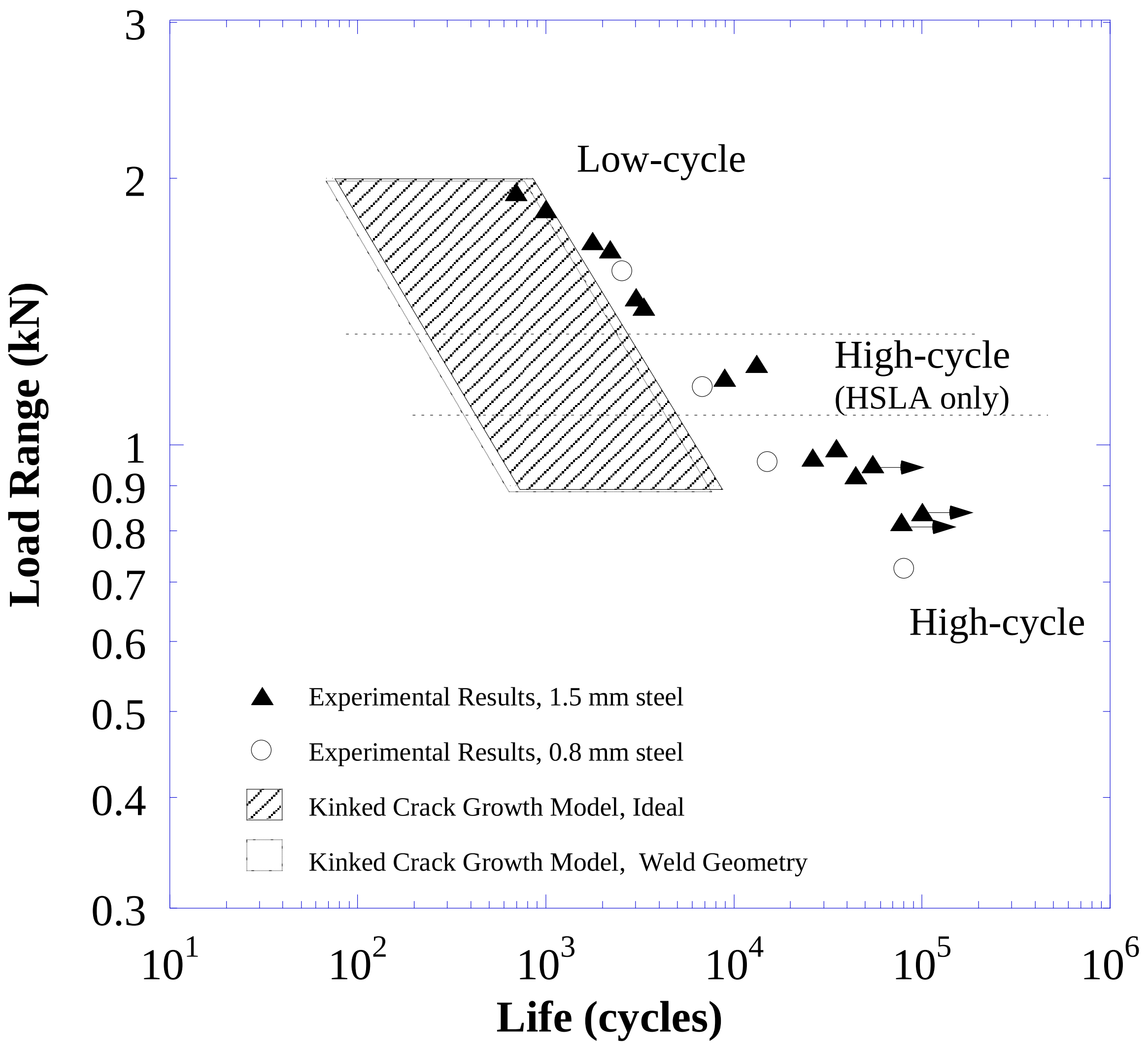

Figure 3.20. The experimental results and the fatigue life estimation ranges based on the kinked fatigue crack growth models for ideal and weld geometry models.

Acknowledgements

This research was initially sponsored by the U.S. Department of Energy, Assistant Secretary for Energy Efficiency and Renewable Energy, Office of Vehicle Technologies, as part of the Lightweight Materials Program. Support of this work through a National Science Foundation Fellowship for TF is greatly appreciated.

References

[1] Pollock T. Weight loss with magnesium alloys. Science 2010;328(5981):986-7.

[2] Santella M, Franklin T, Pan J, Pan T-Y, Brown E, Ultrasonic spot welding of AZ31B to galvanized mild steel. SAE Technical Paper 2010-01-0975, Society of Automotive Engineers, Warrendale, PA.

[3] Hetrick E, Jahn R, Reatherford L, Skogsmo J, Ward SM, Wilkosz D, et al. Ultrasonic spot welding: A new tool for aluminum joining. Weld J 2005;84(2):26-30.

[4] Jahn R, Cooper R, Wilkosz D. The effect of anvil geometry and welding energy on microstructures in ultrasonic spot welds of AA6111-T4. Metall Mater Trans A 2007;38A:570-83.

[5] Bakavos D, Prangnell PB. Mechanisms of joint and microstructure formation in high power ultrasonic spot welding 6111 aluminium automotive sheet. Mater Sci Eng, A 2010;527:6320-34.

[6] Jordan JB, Horstemeyer MF, Daniewicz SR, Badarinarayan H, Grantham J. Fatigue characterization and modeling of friction stir spot welds in magnesium AZ31 alloy. J Eng Mater Technol 2010;132:041008-1-10.

[7] Gendo T, Nishiguchi K, Asakawa M, Tanioka S. Spot friction welding of aluminum to steel. SAE Technical Paper 2007-01-1703, Society of Automotive Engineers, Warrendale, PA.

[8] Liyanage T, Kilbourne J, Gerlich AP, North TH. Joint formation in dissimilar Al alloy/steel and Mg alloy/steel friction stir spot welds. Sci Technol Weld Joining 2009;14:500-8.

[9] Watanabe T, Sakuyama H, Yanagisawa A, Ultrasonic welding between mild steel sheet and Al–Mg alloy sheet. J Mater Process Technol 2009;209(15-16):5475-80.

[10] Tran, V-X, Pan, J. Fatigue behavior of dissimilar spot friction welds in lap-shear and cross-tension specimens of aluminum and steel sheets. Int J Fatigue 2010;32:1167-79.

[11] Tran V-X, Pan J, Pan T. Fatigue behavior of spot friction welds in lap-shear and cross-tension specimens of dissimilar aluminum sheets. Int J Fatigue 2010;32:1022-41.

[12] Tran, V-X, Pan J, Pan T. Fatigue behavior of aluminum 5754-O and 6111-T4 spot friction welds in lap-shear specimens. Int J Fatigue 2008;30(12):2175-90.

[13] Newman J, Dowling, N. A Crack Growth Approach to Life Prediction of Spot-Welded Lap Joints. Fatigue Fract Eng Mater Struct 1998; 21: 1123–32.

[14] Ueoka T, Tsujino J. Welding Characteristics of Aluminum and Copper Plate Specimens Welded by a 19 kHz Complex Vibration Ultrasonic Seam Welding System. Jpn J Appl Phys 2002;41:3237-42.

[15] Asim K, Lee J, Pan J. Failure mode of laser welds in lap-shear specimens of high strength low alloy (HSLA) steel sheets. Fatigue Fract Eng Mater Struct 2011;35:219-237.

[16] Sripichai K, Asim K, Jo WH, Pan J, Li M. Fatigue behavior of laser welds in lap-shear specimens of high strength low alloy (HSLA) steels. SAE Technical Paper No. 2009-01-0028. Warrendale (PA): Society of Automotive Engineers; 2009.

[17] Zhang S. Stress intensities derived from stresses around a spot weld. Int J Fracture 1999;99:239-257.

[18] Tran V-X, Pan J. Analytical stress intensity factor solutions for resistance and friction stir spot welds in lap-shear specimens of different materials and thicknesses. Eng Fract Mech 2010;77(14):2611-39.

[19] He M-Y, Hutchinson JW. Kinking of a crack out of an interface. J Appl Mech 1989; 56(2): 270-278.

[20] Wang D-A, Pan J. A computational study of local stress intensity factor solutions for kinked cracks near spot welds in lap-shear specimens. Int J Solids Struct 2005;45:6277-98.

[21] Lee J, Asim K, Pan J. Modeling of failure mode of laser welds in lap-shear specimens of HSLA steel sheets. Eng Fract Mech 2011;78:374-96.

[22] Anand D, Chen DL, Bhole SD, Andreychuk P, Boudreau G. Fatigue behavior of tailor (laser)-welded blanks for automotive applications. Mater Sci Eng: A 2006;420:199-207.

[23] Lee J. Simulations of similar and dissimilar weld joint failures and bearings for fatigue analyses [doctoral dissertation]. Ann Arbor, MI: University of Michigan; 2011.

[24] Santella M, Brown E, Pozuelo M, Pan T-Y, Yang J-M. Details of Mg–Zn reactions in AZ31 to galvanised mild steel ultrasonic spot welds. Sci Technol of Weld Joi 2012; 17(3): 219-24.

[25] Suo Z, Hutchinson JW. Interface crack between two elastic layers. Int J Fract 1990;43:1-18.

[26] He M-Y, Hutchinson JW. Kinking of a crack out of an interface: tabulated solution coefficients. Harvard University Report MECH-113A. 1988.

[27] Cotterell B, Rice JR. Slightly curved or kinked cracks. Int J Fract 1980; 16: 155-69.

[28] Sripichai K, Asim K, Pan J. Stress intensity factor solutions for estimation of fatigue lives of laser welds in lap-shear specimens. Eng Fract Mech 2011; 78: 1424-40.

[29] ABAQUS v6.7 User Manual. Providence, RI: SIMULIA; 2007.

[30] Choi SS. Probabilistic Characteristics of fatigue behavior parameter of Paris-Erdogan law in Mg-Al-Zn alloy. The Korean Society of Mechanical Engineers 2011:375-381.

[31] Ochi Y, Masaki K, Hirasawa T, Wu X, Matsumura T, Takigawa Y, Higashi K. High cycle fatigue property and micro crack propagation behavior in extruded AZ31 magnesium alloys. Mater Trans 2006 47(4) 989-94.

[32] Ishihara S, McEvily AJ, Sato M, Taniguchi K, Goshima T. The effect of load ratio on fatigue life and crack propagationbehavior of an extruded magnesium alloy. Int J Fatigue 2009;31:1788-94.

[33] Morita S, Ohno, N, Tamai, F, Kawakami Y. Effect of grain size on fatigue crack propagation in extruded AZ31 magnesium alloys. Mater Sci Forum 2012;706-709:1233-6.

[34] Tokaji K, Nakajima M, Uematsu Y. Fatigue crack propagation and fracture mechanisms of wrought magnesium alloys in different environments. Int J Fatigue 2009; 31: 1137-43.

Chapter 4
Investigations of Dissimilar Ultrasonic Spot Welds in Lap-Shear Specimens of AZ31 and Steel Sheets under Cyclic Loading

4.1. Introduction

Replacing heavier metals in automobiles with magnesium is a great way to reduce vehicle weight. As the transportation industry is evolving toward better fuel efficiency and lower environmental impact, reducing weight by material substitution is becoming a priority. Therefore incorporating magnesium into traditional steel frames will require joining the two dissimilar materials. Many researchers are investigating all methods and aspects of joining magnesium and steel.

Santella et al.[1, 2] studied feasibility and metallurgical aspects of ultrasonic welding of a magnesium alloy (AZ31) to steel sheets. Jana et al. [3] studied friction stir welding of AZ31 to steel sheets. Additional research on dissimilar magnesium and steel friction stir lap joints is presented in Chen and Nakata [4], Wei et al.[5] and Schneider et al. [6]. Wahba and Katayama investigated laser welding of AZ31 to steel [7].

In this study, dissimilar ultrasonic spot welds between AZ31 and steel sheets in lap-shear specimens are investigated. The focus of this study is fatigue behavior of these dissimilar joints. Fatigue behavior is important for components intended for automotive application since welds will be subjected to cyclic loading conditions. Specimens were created and tested under cyclic loading with a load ratio of $R = 0.1$. The experimental results are reviewed and compared with analytical and computational solutions for stress intensity factors. The global stress intensity factor solutions were found analytically using equations obtained by Zhang [8]. This approach has also been used for spot welds in lap-shear specimens by Tran and Pan [9]. A three dimensional welded lap-shear finite element model was constructed. Global stress intensity factor results were obtained and compared with analytical results to validate the model. Then equations from He and Hutchinson [10] were used, with the modified material combination used in Chapter 2, to estimate the local stress intensity factor solutions for a vanishing crack. Local stress intensity factors for four maximum kink depths were obtained computationally. Then, a kinked crack growth model was adopted to estimate the fatigue life of the dissimilar spot welds in lap-shear specimens. The life estimations from the kinked crack growth model will be compared with the experimental fatigue results.

4.2. Experiment

4.2.1 Lap-shear specimen

The lap-shear specimens were made by joining magnesium AZ31B-H24 sheets with a thickness of 1.58 mm and 1.5 mm hot-dipped galvanized high strength low alloy (HSLA) steel sheets. The magnesium and steel were cut into coupons of 30 mm × 100 mm. The lap-shear specimen was made by welding the magnesium and steel coupons with a weld centered in the 30 mm × 75 mm overlap area using a Sonobond CLF 2500 single-transducer, wedge-reed ultrasonic welder. The spot welding was done with a power of 1500 W, an impedance setting of 6 and a welding time of 1 s. The orientation of the sample was adjusted prior to welding so that the vibrations from the sonotrode tip were parallel to the surface of the sample and aligned with the short axis of the specimen. The pressure to the tip clamping mechanism was adjusted for a constant nominal pressure of 39 MPa on the material beneath the sonotrode tip. Figure 4.1(a) shows a lap-shear specimen with an ultrasonic weld. Figures 4.1(b) and 4.1(c) show the face and profile view of the 7 mm × 7 mm sonotrode tip used in creating the welds. The microstructures of the sheets, the specimen preparation procedure and the processing conditions were explained in Santella et al. [1].

The lap-shear specimens were produced just as in Chapter 3. In this investigation, however, the lap-shear spot welded specimens were tested as-welded rather than machined into a dog-bone profile. During fatigue testing, two spacers were used to align the fixture to avoid the initial realignment of the specimen due to the non-aligned grips under lap-shear loading conditions. Figure 4.2(a) shows a schematic of a lap-shear specimen with the loading direction represented by bold arrows. The figure also shows the points A, B, C and D around the circumference of the weld. Figure 4.2(b) clearly illustrates the points A, B, C and D with respect to the angle θ around the weld. As shown in the figure, the specimen has a width $2b$ and overall length L for the upper and lower sheets. The specimen has the thickness t_u for the upper sheet and t_l for the lower sheet. The specimen has an overlap length V, a weld diameter $2a_r$, and an indentation width g. The dimensions of the specimens are $2b$ = 30 mm, L = 100 mm, V = 75 mm, $2a_r$ = 8.78 mm and g = 7 mm. The thickness t_u for the upper sheet is 1.58 mm for the top magnesium sheet. The thickness t_l is 1.5 mm for the bottom HSLA steel sheet. The detailed dimensions of the lap-shear specimens are listed in Table 4.1.

Before testing, an ultrasonic welded specimen was sectioned along the symmetry plane on the longitudinal axis. The optical micrograph of the cross section can be seen in Figure 4.3. The micrograph shows the indentation of the sonotrode tip into the magnesium sheet. The weld reaches just outside of the visible indented region. It should be noted that the cross-section was taken near a ridge as opposed to a valley of the impression left from the sonotrode tip. A slight deviation between the angle of the ridges and the cutting angle explains the asymmetry of the top profile in the magnesium. The rest of the asymmetry, however, is not an artifact of sectioning. As observed by Santella et al. [1], during welding the magnesium and zinc reached a eutectic temperature where they liquefied. The pressure of the sonotrode tip along with the vibrations caused the Mg-Zn eutectic layer to flow outward. This eutectic layer is discussed in detail in Santella et al. [2]. On the right side, a gap and a layer between the magnesium and steel sheets is visible. On the left side, the layer between two sheets is quite thin and the gap between the magnesium and steel sheets is much smaller. The uneven distribution of this dispersed layer is most likely due to the vibrational modes associated with the sample sheets during welding. The third asymmetrical feature is the existing cracks which can be seen on the right side and also just left of center in the magnesium sheet. These cracks are present in multiple sectioned USW lap-shear joints with this material combination. This is believed to be caused upon cooling after welding due to a mismatch in thermal expansion coefficients.

4.2.2 Quasi-static test of lap-shear specimen

Lap-shear specimens were first tested under quasi-static loading conditions by using an automated MTS testing machine equipped with a load cell and a built-in position sensor to track the movement of the cross-head. Spacers were not used during quasi-static tests. The load and displacement histories were simultaneously recorded during each test. The average failure or maximum load was about 4490 N. The average failure load was used as the reference value to determine the applied load ranges for the fatigue tests. The welds failed through the interface, leaving a small amount of magnesium material on the steel coupon.

4.2.3 Fatigue test of lap-shear specimen

Lap-shear specimens were tested under cyclic loading conditions with an Instron servo-hydraulic fatigue testing machine using a load ratio of $R = 0.1$. A sinusoidal loading profile was chosen and the frequency was set at 10 Hz during the tests. The test was considered to be completed at the final separation of the welded sheets. A few tests were interrupted before the final separation to study the fatigue crack growth patterns. A plot of the load range versus the fatigue life in a log-log scale is shown in Figure 4.4. Some specimens that failed under cyclic loading conditions were sectioned perpendicular to the weld direction and prepared for micrographic analyses. The optical micrographs of the cross sections of the partially and fully failed specimens are presented in the following section.

4.3. Failure modes of ultrasonic spot welds under cyclic loading conditions

Ultrasonic spot welds in lap-shear specimens were studied under cyclic loading conditions. For all specimens tested under cyclic loading, a kinked crack initiated in the magnesium sheet at the edge of the weld near point A in Figure 4.2(a). The kinked crack propagated at roughly a 90° angle through the magnesium sheet for all specimens. Then, the failures can be separated into two different failure modes depending on the applied load range. Under higher load ranges, the failed specimens exhibit a kinked crack near point A, but ultimately separate along the interface. Under lower load ranges, the kinked crack near point A continues to propagate transversely through the magnesium sheet, forming an eyebrow crack and then failing completely through the magnesium sheet on the right side of the weld. Both of these crack growth patterns will be discussed in greater detail.

The general nature of the crack growth pattern can be observed in Figures 4.5(a)-(g), which show views of the failed surfaces for quasi-static and two specimens tested under cyclic loading. Figure 4.5(a)-(c) shows a top view of a the magnesium sheet, the bottom view of the magnesium sheet, and the top view of the steel sheet of a specimen tested under quasi-static loading conditions respectively. The loading in each case is shown schematically with arrows. Figure 4.5(b) and 4.5(c) show that the quasi-static specimen failed through the interface, leaving a small amount of material on the steel sheet. Figure 4.5(b) shows some cracking on the underside of the magnesium coupon, however, a kinked crack at the edge of the weld is not observed.

Figures 4.5(d)-(f) shows a top view of a the magnesium sheet, the bottom view of the magnesium sheet, and the top view of the steel sheet, respectively, of a specimen tested at a maximum of 80% of the quasi-static failure load. This specimen was tested for 5.7×10^3 cycles under a load range of 3.20 kN. Similarly to the quasi-static specimen, this specimen failed through the welded interface, leaving some magnesium material on the steel sheet. Figures 4.5(d) and 4.5(e) show that the specimen had a kinked crack on the right side of the weld, near point A, growing completely through the thickness of the magnesium sheet. This feature is difficult to observe here and will be clearer in the sectioned micrographs.

Figure 4.5(g) shows a top view of a failed specimen tested at a maximum of 48% of the quasi-static failure load. This specimen had a fatigue life of 3.08×10^4 cycles under a load range of 1.91 kN. This weld failed by a kinked crack originating near point A on the right side and propagating upward and outward through the thickness and width of the magnesium sheet.

For the purpose of discussion in this paper, specimens will be divided into a low-cycle and high-cycle fatigue range. This is determined by the failure mode from the fatigue tests and is chosen only for convenience. In actuality, the transition between low-cycle and high-cycle fatigue changes gradually as the load range is decreased. For this paper, the transition between low-cycle and high-cycle is set at a load range of 2.1 kN which lies between the specimens shown in Figures 4.5(d)- (f) and 4.5(g). Welds tested at load ranges less or equal to 2.1 kN will be referred to as high-cycle fatigue. Note that the definitions of low-cycle and high cycle fatigue loading conditions in this study are only provided for convenient presentation. Both low-cycle and high-cycle fatigue crack growth patterns will be discussed further by looking at micrographs of the sectioned failed and partially failed specimens.

4.3.1 Failure mode under low-cycle (LC) loading conditions

Fatigue failure under low-cycle conditions is observed with an optical micrograph in Figure 4.6. Figure 4.6 shows an optical micrograph of a failed spot weld at a fatigue life of 9.5×10^3 cycles under a load range of 2.82 kN. The upper magnesium sheet is loaded on the right, while the lower steel sheet is loaded on the left as indicated schematically with arrows. The upper magnesium sheet, shows a kinked crack which propagated from the right side of the weld, upward through the thickness of the magnesium and into the indentation from the sonotrode tip. It should be noted that although the left and right side of the magnesium sheet appear completely separated in the sectioned view, the sheet is still intact at a small distance away from the weld, just as in Figures 4.5(d) and 4.5(e). On the left side of the weld, at point B, a kinked crack propagated into the weld at a shallow angle. On the left side, as the kinked crack advances from the main crack, it effectively reduces the load carrying area of the weld. Near the central portion of the weld, a third crack front propagated upward, possibly initiated at a pre-existing defect in the weld. The weld finally separated through the interface leaving residual magnesium material on the steel sheet. The specimens tested at this loading condition showed some variation as to the amount of magnesium left on the steel coupon, but all of the specimens displayed a kinked crack which propagated through the thickness of the magnesium on the right side near the weld before failure. Figure 4.7(a) shows a partially failed weld tested for 1.6×10^4 cycles under a load range of 2.38 kN. A box indicates the enlarged portion which is shown in Figure 4.7(b). In the enlarged section, the beginning of kinked cracks growing from the edge of the weld near point A can be seen. This shows that kinked crack initiation on the right side is one of the first observable features indicating fatigue failure is underway. In summary, specimens failing under low-cycle fatigue, with testing load ranges greater than 2.1 kN, display a kinked crack propagating at roughly a 90° angle and a final failure through the interface. A total of six specimens were tested to complete failure under these load ranges and they all exhibited the same failure mode.

4.3.2 Failure mode under high-cycle (HC) loading conditions

Specimens tested under high-cycle fatigue fail with a kinked crack forming on the right edge of weld and propagating upward through the thickness of the sheet. Then this crack grows transversely through the entire width of the magnesium sheet, separating the loaded magnesium leg from the rest of the weld. Figure 4.8 shows an optical micrograph of the cross section of a failed weld at the fatigue life of 6.6×10^4 cycles under a load range of 2.02 kN. The upper magnesium sheet is loaded on the right, while the lower steel sheet is loaded on the left as indicated schematically with arrows. The kinked crack, visible on the right side of the micrograph, appears to kink upward at an angle of 82° with respect to the weld interface. Unlike the specimens tested under low-cycle fatigue, the kinked crack in Figure 4.8 extends the entire width of the magnesium coupon. It also can be seen that the crack kinks upward through the dispersed layer, instead of propagating briefly along the interface before kinking. The dominant failure mode for the specimens under high-cycle loading appears to be a kinked crack propagation upward and then transversely through the upper right sheet. This type of failure mode corresponds to the applied load ranges equal to or less than about 2.1 kN. A total of four specimens were tested to complete failure under these load ranges and they exhibited the same failure mode.

4.4. Global and local stress intensity factor solutions

4.4.1 Theory

Global stress intensity factors can be found analytically and used to explain the crack growth pattern and validate the three-dimensional finite element model. The asymptotic in-plane stress field around an interface crack tip is an oscillatory field that can be characterized by a complex stress intensity factor **K (**$= K_1 + iK_2$, $i = \sqrt{-1}$) (Rice and Sih [11]). The stresses σ_y and τ_{xy} at a small distance r ahead of the interface crack tip are characterized by **K** as

$$\sigma_y + i\tau_{xy} = \frac{K_1 + iK_2}{\sqrt{2\pi r}}\left(\frac{r}{t}\right)^{i\varepsilon} \tag{1}$$

Here, the bimaterial constant ε is defined as

$$\varepsilon = \frac{1}{2\pi}\ln\frac{\kappa_u / G_u + 1/G_l}{\kappa_l / G_l + 1/G_u} \tag{2}$$

where G_u represents the shear modulus of the upper sheet and G_l represents the shear modulus of the lower sheet. Here, κ_u and κ_l for the upper and lower sheets, respectively, are defined as

$$\kappa_u = 3 - 4\nu_u \tag{3}$$

and

$$\kappa_l = 3 - 4\nu_l \tag{4}$$

under plane strain conditions. Note that ν_u and ν_l represent the Poisson's ratios of the upper and lower sheets, respectively.

In Equation (1), t represents a characteristic length [8, 12]. In this investigation, t represents the upper sheet thickness t_u which is the smaller value of the thicknesses of the two sheets bonded together as in Suo and Hutchinson [13] and Zhang [8]. It should be noted that when the two materials are identical, $\varepsilon = 0$. In this case, K_1 and K_2 in Equation (1) for the interface crack become the conventional stress intensity factors K_I and K_{II}, respectively.

The global stress intensity factor solutions, K_1 and K_2, are obtained by Zhang [8] as

$$
\begin{aligned}
K_1 = {} & \frac{\cosh(\pi\varepsilon)\sqrt{t_u}}{2\sqrt{3(1+\eta)(1+4\eta\delta+6\eta\delta^2+3\eta\delta^3)(1+\tan^2\omega)}} \times \\
& \left\{ \left[\frac{(1+4\eta\delta+9\eta\delta^2+6\eta\delta^3)\tan\omega}{\sqrt{1+2\eta\delta(2+3\delta+2\delta^2)+\eta^2\delta^4}} - \sqrt{3} \right] \sigma_{ui} \right. \\
& - \left[\frac{(1+4\eta\delta+3\eta\delta^2)\tan\omega}{\sqrt{1+2\eta\delta(2+3\delta+2\delta^2)+\eta^2\delta^4}} + \sqrt{3} \right] \sigma_{uo} \\
& + \eta \left[\frac{\delta(1-2\eta\delta-3\eta\delta^2)\tan\omega}{\sqrt{1+2\eta\delta(2+3\delta+2\delta^2)+\eta^2\delta^4}} + \sqrt{3}(2+\delta) \right] \sigma_{li} \\
& \left. - \eta\delta \left[\frac{(1+4\eta\delta+3\eta\delta^2)\tan\omega}{\sqrt{1+2\eta\delta(2+3\delta+2\delta^2)+\eta^2\delta^4}} + \sqrt{3} \right] \sigma_{lo} \right\} \qquad (5)
\end{aligned}
$$

$$
\begin{aligned}
K_2 = {} & \frac{\cosh(\pi\varepsilon)\sqrt{t_u}}{2\sqrt{3(1+\eta)(1+4\eta\delta+6\eta\delta^2+3\eta\delta^3)(1+\tan^2\omega)}} \times \\
& \left\{ \left[\frac{(1+4\eta\delta+9\eta\delta^2+6\eta\delta^3)}{\sqrt{1+2\eta\delta(2+3\delta+2\delta^2)+\eta^2\delta^4}} + \sqrt{3}\tan\omega \right] \sigma_{ui} \right.
\end{aligned}
$$

$$
\begin{aligned}
&-\left[\frac{(1+4\eta\delta+3\eta\delta^2)}{\sqrt{1+2\eta\delta(2+3\delta+2\delta^2)+\eta^2\delta^4}}-\sqrt{3}\tan\omega\right]\sigma_{uo}\\
&+\eta\left[\frac{\delta(1-2\eta\delta-3\eta\delta^2)}{\sqrt{1+2\eta\delta(2+3\delta+2\delta^2)+\eta^2\delta^4}}-\sqrt{3}(2+\delta)\tan\omega\right]\sigma_{li}\\
&-\eta\delta\left[\frac{(1+4\eta\delta+3\eta\delta^2)}{\sqrt{1+2\eta\delta(2+3\delta+2\delta^2)+\eta^2\delta^4}}-\sqrt{3}\tan\omega\right]\sigma_{lo}\Bigg\}
\end{aligned}
\tag{6}
$$

where the modulus ratio η is defined as

$$\eta = E'_u / E'_l \tag{7}$$

Here,

$$E'_u = E_u /(1-\nu_u^2) \tag{8}$$

and

$$E'_l = E_l /(1-\nu_l^2) \tag{9}$$

Here, E_u and E_l represent the Young's Moduli of the upper and lower sheets, respectively. The thickness ratio δ is defined as

$$\delta = t_u / t_l \tag{10}$$

where t_u and t_l are the upper and lower sheet thicknesses, respectively. Note that the expressions shown in Equations (5) and (6) are for welds joining sheets with $\delta \le 1$. For welds joining sheets with $\delta > 1$, one should rotate the strip model by an angle of 180º to represent the same physical system but with $\delta < 1$.

The values of the angular quantity ω in Equations (5) and (6) can be found in Suo and Hutchinson [13]. The angular quantity ω is a function of the thickness ratio δ and the Dundurs' parameters α and β which are defined as

$$\alpha = \frac{(\kappa_l + 1)G_u - (\kappa_u + 1)G_l}{(\kappa_l + 1)G_u + (\kappa_u + 1)G_l} \tag{11}$$

$$\beta = \frac{(\kappa_l - 1)G_u - (\kappa_u - 1)G_l}{(\kappa_l + 1)G_u + (\kappa_u + 1)G_l} \tag{12}$$

The K_3 solution can be obtained from Tran and Pan [9] as

$$K_3 = \sqrt{\frac{2}{(1+\xi)(1+\xi\delta)}}(\tau_u - \xi\tau_l)\sqrt{t_u} \tag{13}$$

where ξ is the shear modulus ratio defined as

$$\xi = G_u / G_l \tag{14}$$

Recall that the lap-shear specimen is loaded with a force, F , applied to the lower left and upper right sheets along the interface as shown in Figure 4.9(a). Figure 4.9(b) shows the left part of the strip model near the crack tip with linearly distributed structural stresses based on the classical Kirchhoff plate theory based on the work of Zhang [8]. As shown in Figure 4.9(b), σ_{ui}, σ_{uo}, σ_{li} and σ_{lo} represent the normal stresses at the inner (*i*) and outer (*o*) surfaces of the upper (*u*) and lower (*l*) strips, respectively. Note also that the normal stresses σ^*_{ui}, σ^*_{uo}, σ^*_{li} and σ^*_{lo} can be derived from the normal structural stresses σ_{ui}, σ_{uo}, σ_{li} and σ_{lo} based on the equilibrium equations and the continuity conditions of the strain and the strain gradient along the bond line. The normal structural stresses σ_{ui}, σ_{uo}, σ_{li} and σ_{lo} which are marked in Figure 4.9(b) were obtained from Tran and Pan [9]. Based on the superposition principle of the linear elasticity theory, the normal structural stresses σ_{ui}, σ_{uo}, σ_{li} and σ_{lo} for the spot weld under lap-shear loading conditions can be written as functions of σ^k_{CB}, σ^k_{CtB}, σ^k_S and σ^k_T ($k = u, l$) as

$$\sigma_{uo} = -\sigma^u_{CB} - \sigma^u_{CtB} + \sigma^u_S + \sigma^u_T \tag{15}$$

$$\sigma_{ui} = \sigma_{CB}^{u} + \sigma_{CtB}^{u} + \sigma_{S}^{u} + \sigma_{T}^{u} \tag{16}$$

$$\sigma_{li} = \sigma_{CB}^{l} - \sigma_{CtB}^{l} - \sigma_{S}^{l} + \sigma_{T}^{l} \tag{17}$$

$$\sigma_{lo} = -\sigma_{CB}^{l} + \sigma_{CtB}^{l} - \sigma_{S}^{l} + \sigma_{T}^{l} \tag{18}$$

The maximum stresses σ_{CB}^{k}, σ_{CtB}^{k}, σ_{S}^{k} and σ_{T}^{k} ($k = u, l$) along the nugget circumference $r = a_r$ under counter bending, central bending, shear and tension/compression loading conditions, respectively, are shown from Tran and Pan [9] as functions of the radius a_r of the spot weld (idealized as a rigid inclusion), the thicknesses t_k and the Poisson's ratios ν_k ($k = u, l$) of the upper (*u*) and lower (*l*) sheets, the half width b of the lap-shear specimen and the angular location θ as defined in Figure 4.2(b) as

$$\sigma_{CB}^{k} = \frac{-3F}{8bt_k X_k Y_k}\left[2b^2 X_k + 4Y_k (a_r^4 b^4 + b^8)\cos 2\theta\right] \tag{19}$$

$$\sigma_{CtB}^{k} = \frac{3F\cos\theta}{2\pi a_r t_k} \tag{20}$$

$$\sigma_{S}^{k} = \frac{F\cos\theta}{2\pi a_r t_k} \tag{21}$$

$$\sigma_{T}^{k} = \frac{F\left[3 - \nu_k + 2(1+\nu_k)\cos\theta\right]}{4bt_k(3 + 2\nu_k - \nu_k^2)} \tag{22}$$

where X_k and Y_k ($k = u, l$) are defined as

$$X_k = (-1+\nu_k)(a_r^4 + b^4)^2 - 4a_r^2 b^6 (1+\nu_k) \tag{23}$$

$$Y_k = a_r^2(-1+\nu_k) - b^2(1+\nu_k) \tag{24}$$

The shear stresses τ_u and τ_l in Equation (13) are obtained from Tran and Pan [9] as

$$\tau_u = -\frac{F\sin\theta}{2\pi a_r t_u} \tag{25}$$

$$\tau_l = \frac{F\sin\theta}{2\pi a_r t_l} \tag{26}$$

The values of the analytical global stress intensity factors, K_1, K_2 and K_3, for any angle around the circumference of the weld can be obtained from Equations (5), (6) and (13) based on Equations (15)-(26).

Figure 4.10 shows a schematic of a main crack and a kinked crack with the maximum kink depth d and the kink angle φ. Here, K_1, K_2 and K_3 represent the global stress intensity factors for the main crack, and k_{I}, k_{II} and k_{III} represent the local stress intensity factors for the kinked crack. Note that the arrows in the figure represent the positive values of the global and local stress intensity factors K_1, K_2, K_3, k_{I}, k_{II} and k_{III}.

For kinked cracks in dissimilar material, when the kink length approaches 0, the k_{I} and k_{II} solutions can be expressed as functions of the kink angle φ, the Dunders' parameters α and β, and the global K_1 and K_2 solutions for the main crack, just as in the two-dimensional case. The local stress intensity factors k_{I} and k_{II} are expressed in the complex form, from He and Hutchinson [10] as

$$k_I + ik_{II} = \left(c_R^{HH} + ic_I^{HH}\right)\left(K_1 + iK_2\right)d^{i\varepsilon} + \left(d_R^{HH} - id_I^{HH}\right)\left(K_1 - iK_2\right)d^{-i\varepsilon} \tag{27}$$

where c_R^{HH}, c_I^{HH}, d_R^{HH} and d_I^{HH} are the real and imaginary part of complex functions. Both $c^{HH} = c_R^{HH} + ic_I^{HH}$ and $d^{HH} = d_R^{HH} + id_I^{HH}$ from He and Hutchinson [10] are complex functions of α, β and φ. Equation (27) indicates that k_{I} and k_{II} depend on the crack depth d and bimaterial constant ε. The global stress intensity factors K_1 and K_2 are defined in the form as in $\sigma_y + i\tau_{xy} = \dfrac{K_1^A + iK_2^A}{\sqrt{2\pi r}} r^{i\varepsilon}$.

The functions c_R^{HH}, c_I^{HH}, d_R^{HH} and d_I^{HH} were tabulated by He and Hutchinson [14]. The values for c_R^{HH}, c_I^{HH}, d_R^{HH} and d_I^{HH} were interpolated from that report. As indicated in Equation (27), when the crack length approaches zero, the values for the local stress intensity factor solutions depend on the value of d when the bimaterial constant ε is nonzero. The dependence of the solutions on the crack depth d presents a challenge to develop a fatigue life estimation approach based on a fatigue crack growth model, even though the oscillation is in a region which is too small to be of concern. This challenge prevents the evaluation of the limit at the crack depth of $d = 0$ in Equation (27).

Evaluating the local stress intensity factor at a crack length of $d = 0$ is necessary in order to use the kinked crack growth model for predicting fatigue life. As explained in Chapter 2, a modified material will be used to set β and ε equal to zero. The modified material chosen for this investigation has elastics constants $E = 48.6\,\text{GPa}$ and $\nu = 0.458$ for the magnesium sheet and $E = 206.3\,\text{GPa}$ and $\nu = 0.3$ for the steel sheet. This ignores the oscillation and eliminates the dependence on the crack depth for the vanishing crack which was validated for the two-dimensional models in Chapter 2. With the modified material, β and ε are equal to zero. With $\varepsilon = 0$, Equation (27) simplifies to

$$(k_I)_0 = \left(c_R^{HH} + d_R^{HH}\right)K_1 - \left(c_I^{HH} + d_I^{HH}\right)K_2 \tag{28}$$

$$(k_{II})_0 = \left(c_I^{HH} - d_I^{HH}\right)K_1 + \left(c_R^{HH} - d_R^{HH}\right)K_2 \tag{29}$$

as developed by He and Hutchinson [10]. For similar welds, Equations (28) and (29) simplifies to the solution presented by Cotterell and Rice [15]. It should be noted that for $\varepsilon = 0$, the crack tip stresses recover the traditional $1/\sqrt{r}$ singularity. The local stress intensity factor solutions for the vanishing crack can then be approximated using Equations (28) and (29) along with analytical or computational global stress intensity factor solutions obtained using the modified material. As noted in Chapter 2, this approximation is reasonable because of the similarities of the stresses observed in the real and modified material which is due to the small value of β for the real materials and the large kink angle of 90° ($\varphi = -90°$).

The local stress intensity factor solutions for kinked cracks with finite crack lengths for ultrasonic welds in lap-shear specimens can be expressed as functions of the normalized maximum kink depth d/t as

$$k_{\mathrm{I}}(d) = f_{\mathrm{I}} \cdot (k_{\mathrm{I}})_0 \tag{30}$$

$$k_{\mathrm{II}}(d) = f_{\mathrm{II}} \cdot (k_{\mathrm{I}})_0 \tag{31}$$

where f_{I} and f_{II} are geometric functions which depend on the geometric parameters of the ultrasonic welded lap-shear specimens such as the weld radius a_r and the sheet thickness t. The local stress intensity factor solutions for idealized ultrasonic welds and welds featuring weld geometry in lap-shear specimens were obtained computationally and presented in the normalized form.

4.4.2 Finite Element Model

A finite element model was constructed in order to find the global and local stress intensity factor solutions. A schematic of the three-dimensional lap-shear model is shown in Figure 4.11(a) with the boundary and loading conditions. The spot-welded lap-shear specimen is symmetry about the longitudinal axis and therefore only half of the specimen is modeled. The specimen has upper sheet thickness t_u, lower sheet thickness t_l, the length L, the overlap length V, the half width b, and the weld diameter $2a_r$. The left edge has a fixed displacement condition along a line at the middle surface while the right edge has an applied uniform displacement along a line at the middle surface. The resultant force, F, is determined by adding the forces output at each node with the initial displacement condition.

Finite element analyses have been conducted on both an idealized model and a model which follows the weld geometry and includes the sonotrode tip indentation. The entire mesh for the idealized model is shown in Figure 4.11(b). The right half of the mesh is shown in Figure 4.11(c). The circled area is shown in an enlarged section in Figure 4.11(d). Here the main crack surfaces are indicated between the upper and lower sheets. The main crack tip is shown for $\theta = 0$ at point A. The main crack tip extends around the entire quarter circle. The shape of the weld in the experimental specimens can be seen in failed specimens in Figures 4.5(c) and 4.5(f). Although the welded area is the shape of a rounded square, the weld is simplified to a circle for the finite element models. The central portion for the weld geometry model is shown in Figure 4.11(e). The sonotrode tip indentation is modeled according to specimen geometry, but the ridges and valleys present on the actual specimens are omitted. Figure 4.11(f) shows the same enlarged region as in 11(d), but with the sonotrode tip indentation for the weld geometry model.

The three-dimensional finite element model has the weld diameter $2a_r = 8.78$ mm, length $L = 100$ mm, half width $b = 15$ mm and overlap length $V = 75$ mm. The thickness t_u for the upper sheet is 1.58 mm for the top magnesium sheet and the thickness t_l is 1.5 mm for the bottom HSLA steel sheet. Second-order quarter point crack-tip elements (C3D20R) with collapsed nodes were used to model the $1/\sqrt{r}$ singularity near the crack tip. The rest of the model was constructed mostly with second-order brick elements (C3D20R) although second-order wedge elements (C3D15) were used where necessary. Both materials are assumed to be linear elastic. Any change in the metal due to welding has been ignored. Steel is modeled with a Young's modulus $E = 206.3$ GPa and a Poisson's ratio $\nu = 0.3$. Magnesium (AZ31) is modeled with Young's modulus $E = 45$ GPa and a Poisson's ratio $\nu = 0.35$. These material parameters are listed in Table 4.2. Computations were performed using the commercial finite element software ABAQUS [16].

The normalized computational global stress intensity factor solutions and the analytical global stress intensity factors for an idealized model for the main crack tip for $0 \le \theta \le 180$ are graphed in Figure 4.12. The analytical solutions are found using Equations (5), (6) and (13). The stress intensity factors have been normalized by the maximum computational K_2 solution for the ideal geometry which is found at point A. There is some difference between analytical and computational stress intensity factor solutions. This is mostly due to the small ratio of half width to weld radius b/a_r. Due to the specimen geometry, $b/a_r = 3.4$. While developing mode I analytical solutions, Lin et al.[17] noted that the solutions deviate for $b/a_r < 5$. The stress intensity factor solutions for finite element models with larger values of b/a_r are closer to the analytical results.

The normalized computational global stress intensity factor solutions for both the ideal model and the weld geometry model are shown in Figure 4.13. The stress intensity factors have been normalized by the maximum computational K_2 solution for the ideal geometry which is found at point A. The K_1 and K_2 solutions are largest at $\theta = 0$ or point A. The most pronounced difference between the ideal and weld geometry models is that K_1 is larger at $\theta = 0$ or point A for the weld geometry model. These results can be used to explain the favorable condition for kinked fatigue crack propagation at point A as seen in the experimental results.

As observed from the micrographs of partially failed specimens, kinked fatigue cracks are initiated from the pre-existing main crack tip at point A and propagate through the sheet thickness of the upper right sheet under cyclic loading conditions. For low-cycle fatigue specimens, a kinked crack can also be observed propagating from point B. Since the stress intensity factors at point A are dominate, it is reasonable that the kinked crack at point B grew more slowly or after the crack at point A. The micrographs in Figures 4.7(a) and 4.7(b) show a partially failed specimen under low-cycle fatigue which has been tested up to 75% of the life cycles to failure of a fully failed specimen under similar loading conditions. The kinked crack emanating from point A, as seen in Figure 4.7(b), is still very small. This means the majority of the cycle life of a specimen is experienced as the kink crack grows from the main crack to the surface at point A. The fatigue models will follow the approach of Newman and Dowling [18] and account for fatigue life only until the kinked crack reaches the surface of the magnesium sheet. From the micrographs of the failed specimens, the kinked crack angles are observed to be near 90° for all the load ranges. With these observations, the computational model will focus on a three-dimensional model with a single kinked crack at a kink angle of 90° with a maximum depth at point A.

Figure 4.14(a) shows a schematic of a three-dimensional finite element model of a lap-shear specimen with a single kinked crack of depth d, growing into the magnesium sheet. The boundary and loading conditions of the specimen are the same as those for the finite element model shown in Figure 4.11(a). The kink angle in this investigation is selected to be 90°. The shape of the kinked crack is selected to be semi-elliptical with the aspect ratio $d/c = 0.4$ as used in Pan and Sheppard [19] and Wang and Pan [20], where c represents the half of the length of the semi-elliptical crack. Four normalized kink depths, namely, $d/t =$ 0.05, 0.2, 0.5, and 0.7 are considered in this investigation. Half of the finite element model with a kinked crack is shown in Figure 4.14(b). Figure 4.14(c) shows a close-up view of the finite element mesh near the semi-elliptical kinked crack for $d/t = 0.5$.

Figure 4.15 shows the values of $k_{\mathrm{I}}/(k_{\mathrm{I}})_0$ at $\theta = 0°$ for the kinked cracks emanating from point A as functions of the normalized maximum kink depth d/t for $\varphi = -90°$ for the idealized and weld geometry model. The values of $k_{\mathrm{I}}/(k_{\mathrm{I}})_0$ are also listed in Table 4.3. Note that the solutions are normalized by $(k_{\mathrm{I}})_0$ in Equation (28) with kink angle $\varphi = -90°$ and the computational global stress intensity factor K_1 and K_2 solutions based on the ideal geometry model. The material used for the $(k_{\mathrm{I}})_0$ solution has been modified to achieve $\beta = 0$ and allow the use of Equation (28) as discussed in Chapter 2. The value of $(k_{\mathrm{I}})_0$ is also displayed in Figure 4.15 at a maximum normalized crack depth of $d/t = 0$. This value is based on Equation (28) and computational stress intensity factor solutions for the main crack at point A. This has also been normalized by the value of $(k_{\mathrm{I}})_0$ based on the computational solutions for the ideal geometry model. The values of $k_{\mathrm{I}}/(k_{\mathrm{I}})_0$ are at a maximum near $d/t = 0.05$ for the weld geometry model or $d/t = 0.2$ for the ideal model and decrease modestly as the maximum kink depth is increased. This is in contrast to the behavior for similar material models in which the local model I stress intensity factor increases until a normalized depth of $d/t = 0.5$ and then decreases as seen in Wang and Pan [20]. Compared with the results from two-dimensional models in Chapter 3, the magnitude of change is much smaller, which is in agreement with the results shown by Wang and Pan [20].

Figure 4.16 shows the values of $|k_{II}|/(k_{\mathrm{I}})_0$ for the kinked cracks emanating the main crack at point A as functions of the normalized kink depth d/t for $\varphi = -90°$ for the idealized and weld geometry models for welds. The values of $|k_{II}|/(k_{\mathrm{I}})_0$ are also listed in Table 4.3. Note that the solutions are normalized by $(k_{\mathrm{I}})_0$ in Equation (28) and computational global stress intensity factor K_1 and K_2 solutions from the ideal geometry model. The local stress intensity factor k_{II} solutions are negative based on the definitions shown in Figure 4.10. Figure 4.16 shows that the absolute values of $k_{II}/(k_I)_0$ for the ideal and weld geometry models decrease as the kink length increases for kinked cracks for $0.05 \leq d/t \leq 0.5$. Both models show an increase in the absolute values of $k_{II}/(k_I)_0$ as the normalized depth is increased to 0.7. Overall both models show similar trends, with slightly higher $|k_{II}|/(k_{\mathrm{I}})_0$ values for the weld geometry model. The models for $d/t =$ 0.05 and $d/t =$ 0.2 had further mesh refinement in the area of the kinked crack. The values of $(k_{\mathrm{II}})_0$, at a depth of $d/t =$ 0.0, are also shown in the figure. These values are obtained with the use of Equation (29) and the results from the computational models. They are normalized by the $(k_{\mathrm{I}})_0$ solution which is obtained with Equation (28) and the comutational stress intensity factors from the ideal geometry model. The values of $|k_{II}|/(k_{\mathrm{I}})_0$ are small compared with the values of $k_{\mathrm{I}}/(k_{\mathrm{I}})_0$ as seen in Figure 4.15. The values of $|k_{II}|/(k_{\mathrm{I}})_0$ are similar in magnitude for the two-dimensional models in Chapter 2. The dissimilar lap-shear joint shows a steeper decline in the value of $|k_{II}|/(k_{\mathrm{I}})_0$ between $d/t =$ 0.2 and $d/t =$ 0.5 than is observed for lap-shear joints with similar material as studied by Wang and Pan [20] and Pan and Sheppard [19]. Figures 4.15 and 4.16 indicate that the fatigue kinked crack growth is under mixed mode I and II loading conditions with mode I being the dominant mode. Table 4.3 lists the normalized local stress intensity factor k_{I} and k_{II} solutions with $\varphi = -90°$ for both the ideal and weld geometry models.

4.5. Fatigue life estimations

The fatigue life for the ultrasonic spot welds in lap-shear specimens is calculated using a Paris law method for kinked cracks. To use the Paris law for fatigue estimation, the local stress intensity factor k_{I} and k_{II} solutions as functions of the normalized kink depth d/t are obtained from linear interpolation between those obtained from the finite element analyses in Table 4.3. The variations of the k_{I} and k_{II} solutions in the range of $0.7 < d/t < 1.0$ are assumed to be the same as those for $0.5 < d/t < 0.7$. The local finite kink crack and vanishing crack stress intensity factor solutions obtained from the finite element analyses as expressed in Equations (30) and (31) and the experimentally observed kink angle of $90°$ are used in a kinked fatigue crack growth model. The Paris law is adopted to describe the propagation of the kinked fatigue cracks emanating from the pre-existing crack tips of ultrasonic welds in lap-shear specimens. The Paris law is given as

$$\frac{d(d)}{dN} = C\left(\Delta k_{\mathrm{eq}}(d)\right)^{m} \tag{32}$$

where d is the kink depth and N is the life or number of cycles. Noting that the experiments show crack propagation only through the magnesium sheet, the material constants C and m for AZ31 are found in the literature. One complication of this study is that it is impossible to find material constants for magnesium which is exactly the same and tested under the same conditions as in this study. The wide range of values for C and m for AZ31 can be observed from data in Choi et al. [21], Ochi et al.[22], Ishihara et al. [23] Morita et al.[24] and Tokaji [25]. Tokaji et al. suggest that magnesium is particularly sensitive to the humidity level during fatigue. According to those results, magnesium samples tested in laboratory air, with a humidity of 50-70%, experienced a shorter fatigue life than samples tested in dry air. Additionally plots of crack propagation rates vs. stress intensity factor range reveal that the slope changes at

$\Delta K = 3.5 - 4\,\mathrm{MPa}\sqrt{\mathrm{m}}$ [25]. The stress intensity factor range for this study is above $4\,\mathrm{MPa}\sqrt{\mathrm{m}}$ for all load ranges. The constants are therefore found from the upper stress intensity range for AZ31 using both the laboratory air and dry air. The constants are taken as $C = 1.86 \times 10^{-6}$ $\frac{\mathrm{mm/cycle}}{(\mathrm{MPa}\sqrt{\mathrm{m}})^m}$ and $m = 2.8$ for laboratory air, and $C = 1.36 \times 10^{-7}$ $\frac{\mathrm{mm/cycle}}{(\mathrm{MPa}\sqrt{\mathrm{m}})^m}$ and $m = 2.8$ for dry air [25]. Paris law constants are also taken from Ishihara et al. [23] as $C = 4.00 \times 10^{-7}$ $\frac{\mathrm{mm/cycle}}{(\mathrm{MPa}\sqrt{\mathrm{m}})^m}$ and $m = 2.7$, where tests were conducted under laboratory air. In Equation (32), Δk_{eq} is the range of the equivalent stress intensity factor under mixed mode loading conditions. For the kinked fatigue crack growth model, the range of the equivalent stress intensity factor Δk_{eq} is given as

$$\Delta k_{\mathrm{eq}}(d) = \sqrt{\Delta k_{\mathrm{I}}(d)^2 + \gamma \Delta k_{\mathrm{II}}(d)^2} \tag{33}$$

where γ is an empirical constant to account for the sensitivity of material to mode II loading conditions. The value of γ is taken as 1 here. The fatigue life N can be obtained numerically by integrating the Paris law in Equation (32) as

$$N = \frac{1}{C}\left[\int_{0}^{0.05t'} \left[\Delta k_{eq}(d)\right]^{-m} d(d) + \int_{0.05t'}^{0.20t'} \left[\Delta k_{eq}(d)\right]^{-m} d(d) + \ldots + \int_{0.70t'}^{t'} \left[\Delta k_{eq}(d)\right]^{-m} d(d)\right] \tag{34}$$

here 0, 0.05, 0.20, 0.50 and 0.70 represent the values of the maximum normalized kink depth d/t where the computational local stress intensity factor solutions are available and t' is the crack growth distance $(t' = t/\sin|\varphi|)$. For $\varphi = -90°$, $t' = t$.

In this investigation, a kinked crack emanating from the right pre-existing crack tips is modeled in the finite element analyses to represent the kinked crack in the ultrasonic weld as shown in the micrographs of partially failed specimens. As stated earlier, this kinked crack is modeled for four normalized maximum kink depths. The results of the local stress intensity factor solutions from the finite element analyses are input into Equations (33) and (34) to yield a prediction of the number of cycles to failure. The stress intensity factor solutions are found for the ideal model and weld geometry model. The fatigue life is estimated based on those solutions, Equation (34) and the C and m constants for both laboratory and dry air as obtained from Tokaji et al.[25] and for laboratory air from Ishihara et al.[23]. In this kinked crack growth model, the growth period from $d/t = 0$ to $d/t = 1$ is modeled. This should account for most of the fatigue life. Although specimens tested under low-cycle fatigue conditions finally fail through the interface, after the kinked crack reaches the surface of the magnesium, most of the cycles have already occurred.

Figure 4.17 shows the fatigue life estimations based on the kinked fatigue crack growth model in Equation (34) with the global and local stress intensity factor solutions from the finite element analyses. Six kinked crack growth models were computed; weld geometry and ideal geometry models with three Paris law constants. The vanishing crack is computed using Equations (28) and (29) with the appropriate global stress intensity factor solutions from each finite element model. Then life estimations are found with the Paris law constants C and m from both Tokaji et al.[25] and Ishihara et al [23]. In Figure 4.17, the models for ideal geometry show slightly shorter fatigue life estimates than those for the weld geometry model. It can be observed, however, that the choice of C and m greatly influences the kinked crack growth model predictions. While interesting, this choice is also distressing to the researcher since experimentally obtaining values for C and m would be preferable, but is typically not within the research scope. Overall, the fatigue estimations for low-cycle fatigue correlate well with the experimental results. The fatigue estimations for high-cycle fatigue are slightly lower than experimental results.

When comparing low-cycle and high-cycle fatigue failure in Figures 4.6 and 4.8, it can be noted that the location of the kinked crack is closer to the weld for specimens tested under higher load ranges. Although there is some variation, this trend can be observed for all tested. The location of the kinked crack was measured for several failed specimens. Then the fatigue life estimations were adjusted to account for the change in weld radius using the analytical solution. The fatigue life estimation range based on the adjustment due to the variation in radius is shown in Figure 4.18. The kinked crack growth model for the ideal model predicts slightly lower fatigue life than the weld geometry model. Both models agree well with the experimental results for low-cycle fatigue. For high-cycle fatigue, the fatigue life estimations still show a slightly lower life than the experimental results. Generally, the experimental results and kinked crack growth model are well correlated.

4.6. Discussion

Stress intensity factor solutions in spot welds of lap-shear specimens have been studied by Wang and Pan [20] for similar materials. The stress intensity factor solutions found in that study can not be directly compared with those found in this study because the ratio of $b/a_r = 3.4$ in this study, while $b/a_r = 5.9$ in Wang and Pan [20]. As mentioned previously, according to work by Lin et al.[17], the mode I solutions for ratios of $b/a_r < 5$ are not well described by the analytical solutions. These two geometries therefore will have different stress intensity factor solutions even before dissimilar materials are introduced. To understand the influence, stress intensity factor solutions for similar spot welds were obtained from the finite element model with ideal geometry. In agreement with Wang and Pan [20], these results confirmed that the mode I stress intensity factor reached a maximum at $d/t = 0.5$. For dissimilar spot welds, the maximum mode I stress intensity factor is observed between $d/t = 0.05$ and $d/t = 0.2$. The mode I stress intensity factor were dominate in both dissimilar and similar welds in lap-shear specimens. It was also observed that as d/t increased, the dissimilar stress intensity factor solutions approached that of the stress intensity factor solutions for similar spot welds.

Also observed by Wang and Pan [20], mode I stress intensity factor solutions for a three dimensional spot weld are fairly constant as d/t increases, when compared to the solutions for a two dimensional plane strain model. The same statement can be made for dissimilar spot welds. The magnitude of $k_\mathrm{I}/(k_\mathrm{I})_0$ in Figure 4.15 decreases only slightly as d/t increases. In contrast, the magnesium of $k_\mathrm{I}/(k_\mathrm{I})_0$ in Figure 3.17 in Chapter 3 increases considerably as a/t increases. The fatigue crack growth model proposed by Newman and Dowling [18] use the assumption that the kinked crack stress intensity factors are fairly constant through the sheet thickness. The assumption seems to be reasonable for a spot weld, but would not be valid for a linear weld as studied in Chapter 3.

The fatigue predictions based on the kinked crack growth model for the three dimensional model correlate well the experimental results. The fatigue life estimation model agrees most closely with the experimental results for low-cycle fatigue. High-cycle fatigue is slightly under predicted when compared to the experimental results.

The Paris law constants, C and m, have a substantial impact on the fatigue life predictions for the kinked crack growth model. Environmental factors, such as humidity as well as material properties and heat treatment influence the values for C and m. The experiments necessary to obtain C and m for the base material were not conducted due to a shortage of research material and lack of equipment. If the C and m were obtained, it would not entirely solve the problem because the magnesium changes slightly during welding. The fatigue estimations range from laboratory air resulting in lower life, to dry air resulting in higher life. Humidity measurements in the building where fatigue tests were conducted indicate that the relative humidity is 20-55% depending on the season. This is generally less than 50-70% as reported by Tokaji [25]. Our environmental conditions should lie between the two extremes. The model which uses Paris law constants in laboratory air from Ishihara et al. [23] compares most closely with the experimental results. The adjustment which accounts for changes in kink location due to the load range improves the correlation with the experimental results for high-cycle fatigue.

4.7. Conclusions

Fatigue behavior of dissimilar ultrasonic spot welds between magnesium and steel sheets was investigated. The welds show a longer fatigue life than the welds which were machined into a dog-boned profile in Chapter 3. Two failure modes were observed. For higher load ranges, the welds first experienced a kinked fatigue crack which propagated through the loaded magnesium sheet. The spot welds also had a kinked crack growing from the left crack front at a shallow angle. The welds tested under low-cycle fatigue finally failed through the interface, leaving some magnesium material on the steel sheet. For lower load ranges, the welds fail from a kinked crack which grew on the right side through the magnesium sheet. After reaching the surface of the magnesium, the crack grew transversely through the magnesium sheet. The welds tested under high-cycle loading conditions finally failed from an eyebrow crack on the right side of the weld which propagated through the entire magnesium sheet.

Finite element analyses were conducted on two finite element models, an idealized model and a model which include the weld geometry. Stress intensity factor solutions were obtained for the main crack and a kinked crack at several depths. Stress intensity factor solutions for a vanishing crack were obtained from global stress intensity factors for a modified material and existing analytical solutions as in Chapter 2. The stress intensity factor solutions for the vanishing crack and kinked crack were used in a kinked crack growth fatigue life estimation model. The kinked crack growth model used three values of Paris law constants. This model outlines a range of fatigue life values expected at a given load range. The model has been adjusted to account for the change in the kink location for different load ranges which provides good agreement with experimental results.

Table 4.1. Dimensions of the lap-shear specimen

Width of the grip section $(2b)$	30 mm
Indentation width (g)	7 mm
Weld radius (a_r)	4.39 mm
Length of each leg (L)	100 mm
Overlap length (V)	75 mm
Sheet thickness AZ31 (t_u)	1.58 mm
Sheet thickness steel (t_l)	1.5 mm

Table 4.2. Mechanical properties of AZ31-H24 and steel

	Elastic Modulus (GPa)	Poisson's ratio
AZ31-H24	45	0.35
Steel	206.3	0.3

Table 4.3. The normalized local stress intensity factors $k_I/(k_I)_0$ and $k_{II}/(k_I)_0$ solutions for several values of normalized kink depth d/t based on the semi-elliptical crack at point A of the three-dimensional finite element computational model with $\varphi = -90°$. The values for vanishing crack have been obtained with the use of global stress intensity factors from the computational model and Equations (28) and (29). These values have been normalized by $(k_{\mathrm{I}})_0$ which is based on Equation (28) and computational solutions for the ideal geometry model at point A.

	Idealized Model		Weld Geometry Model	
d/t	$k_I/(k_{\mathrm{I}})_0$	$\lvert k_{II}\rvert/(k_{\mathrm{I}})_0$	$k_I/(k_I)_0$	$\lvert k_{II}\rvert/(k_{\mathrm{I}})_0$
0.0	1.000	0.264	1.049	0.286
0.05	1.068	0.271	1.108	0.322
0.2	1.073	0.252	1.076	0.274
0.5	1.009	0.058	0.988	0.095
0.7	0.774	0.120	0.749	0.145

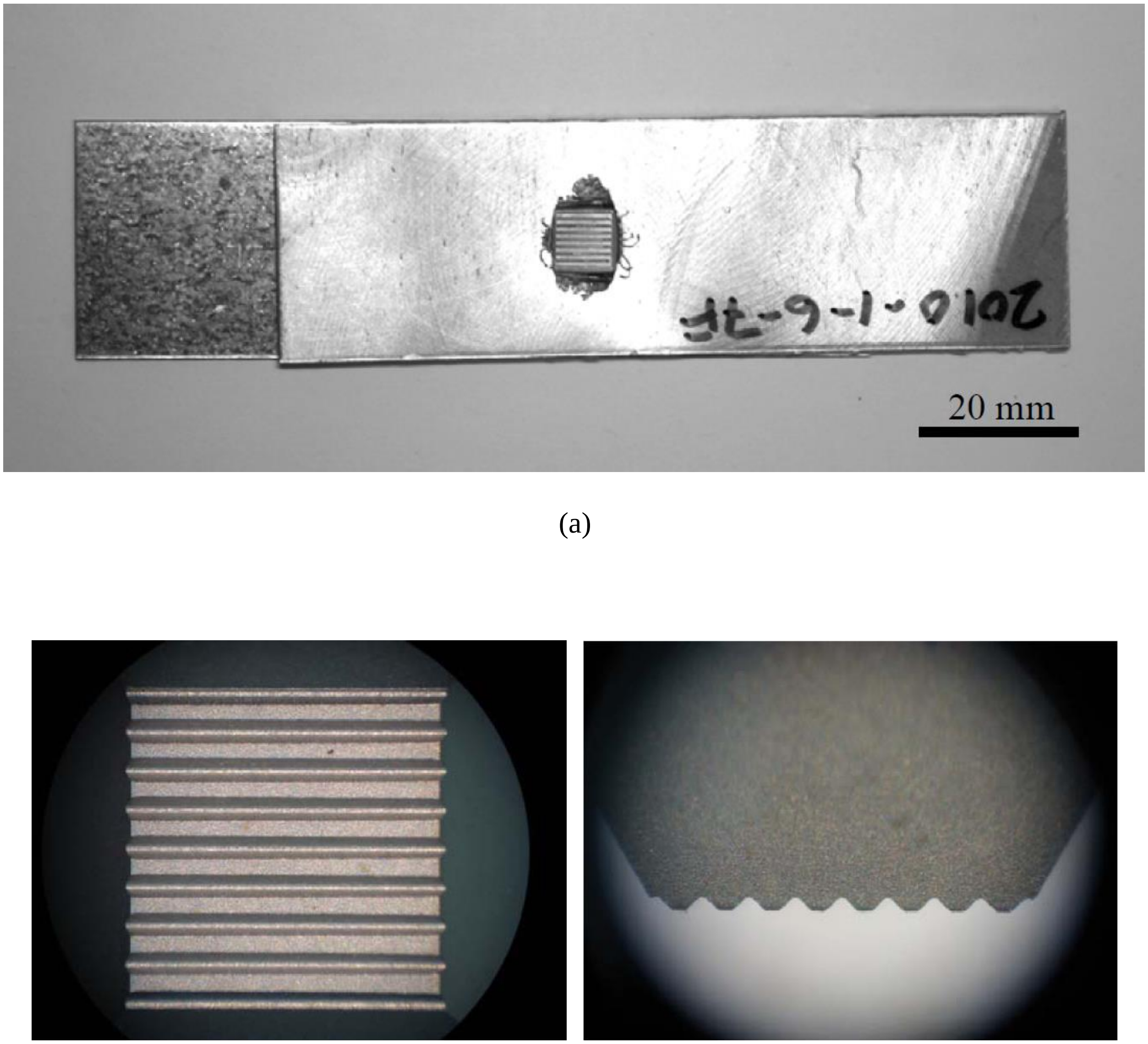

(a)

(b) (c)

Figure 4.1 (a) A top view of an ultrasonic welded lap-shear specimen prior to testing. (b) Face view and (c) side view of the sonotrode tip used in the ultrasonic welding.

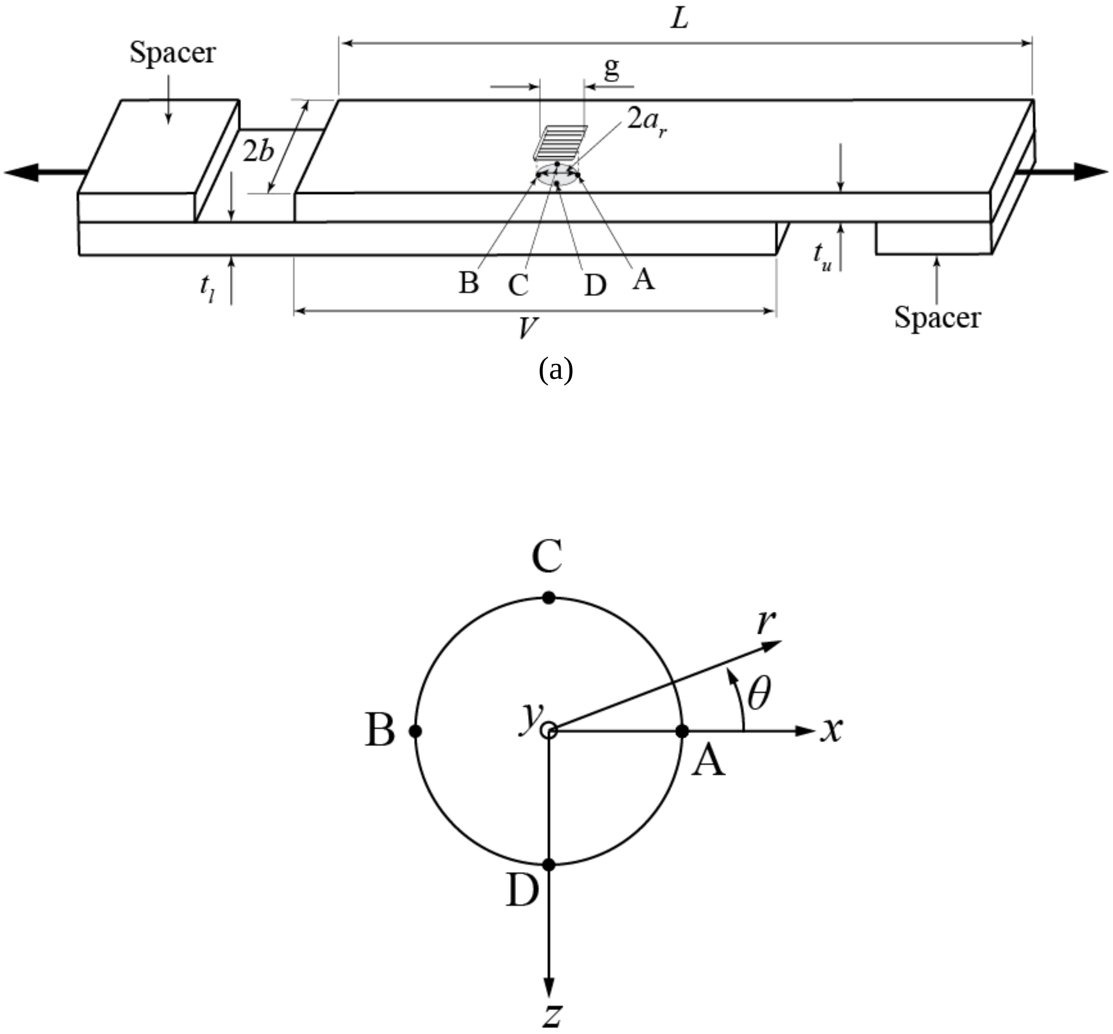

(a)

(b)

Figure 4.2. (a) A schematic of a lap-shear specimen with a spot weld idealized as a circular cylinder, and (b) a top view of the weld nugget showing the orientation angle θ with respect to points A, B, C and D. .

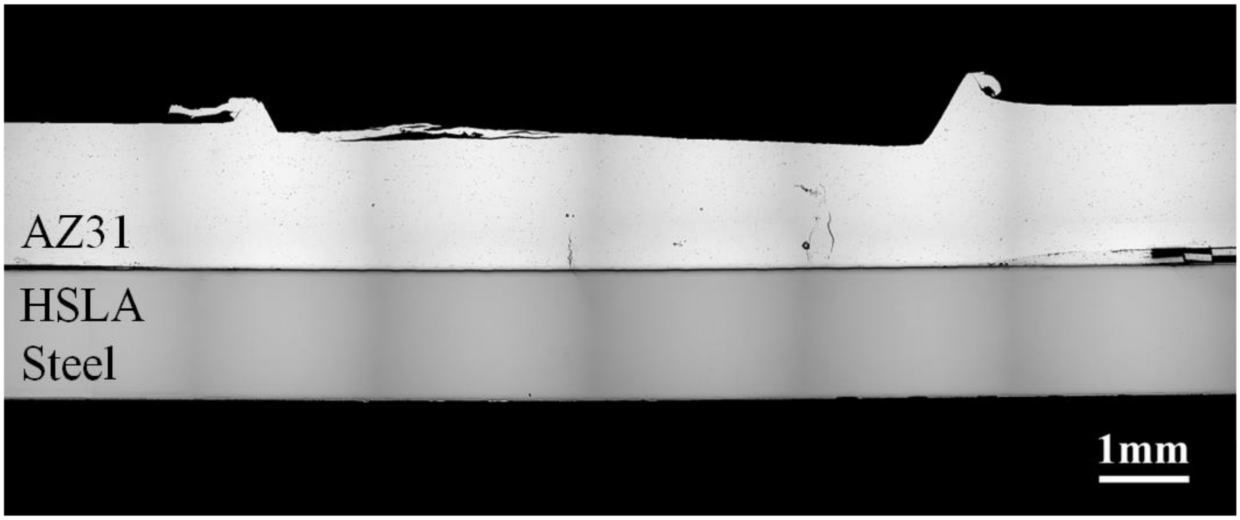

Figure 4.3. An optical micrograph of the cross section of an ultrasonic welded joint in 1.58 mm AZ31 and 1.5 mm HSLA steel.

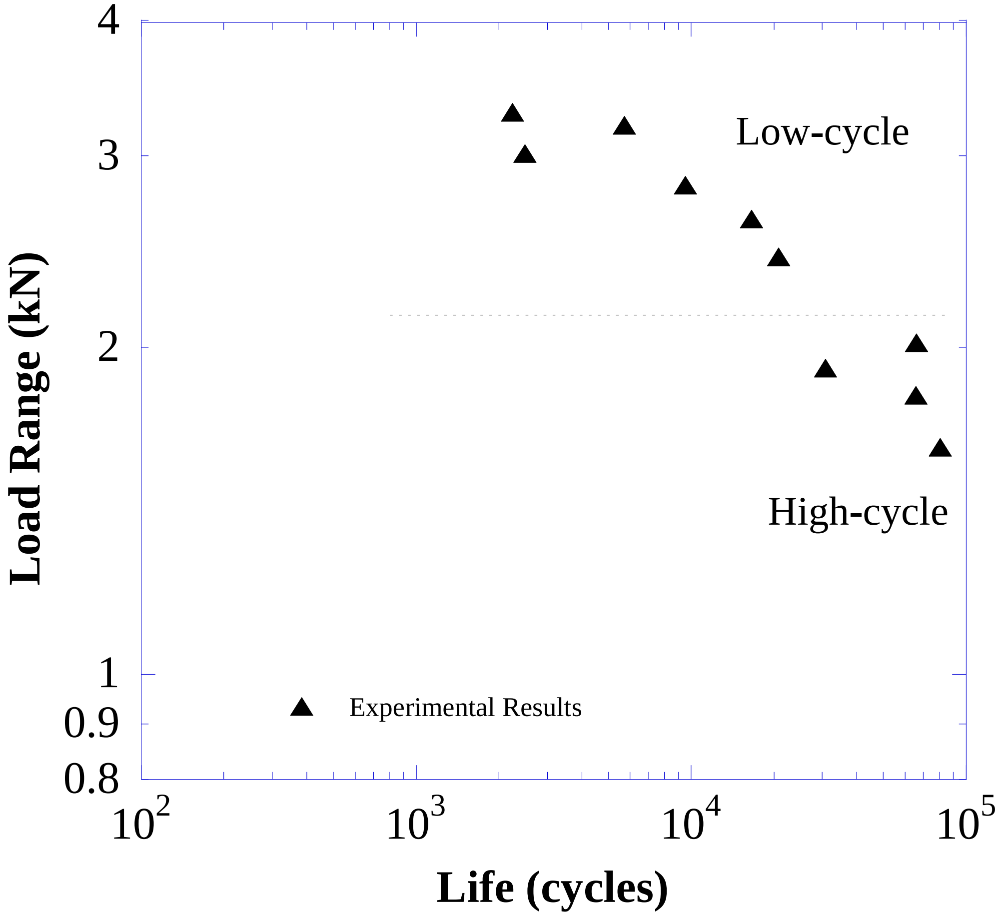

Figure 4.4. The experimental results of the fatigue tests of ultrasonic spot welds in lap-shear specimens under cyclic loading conditions.

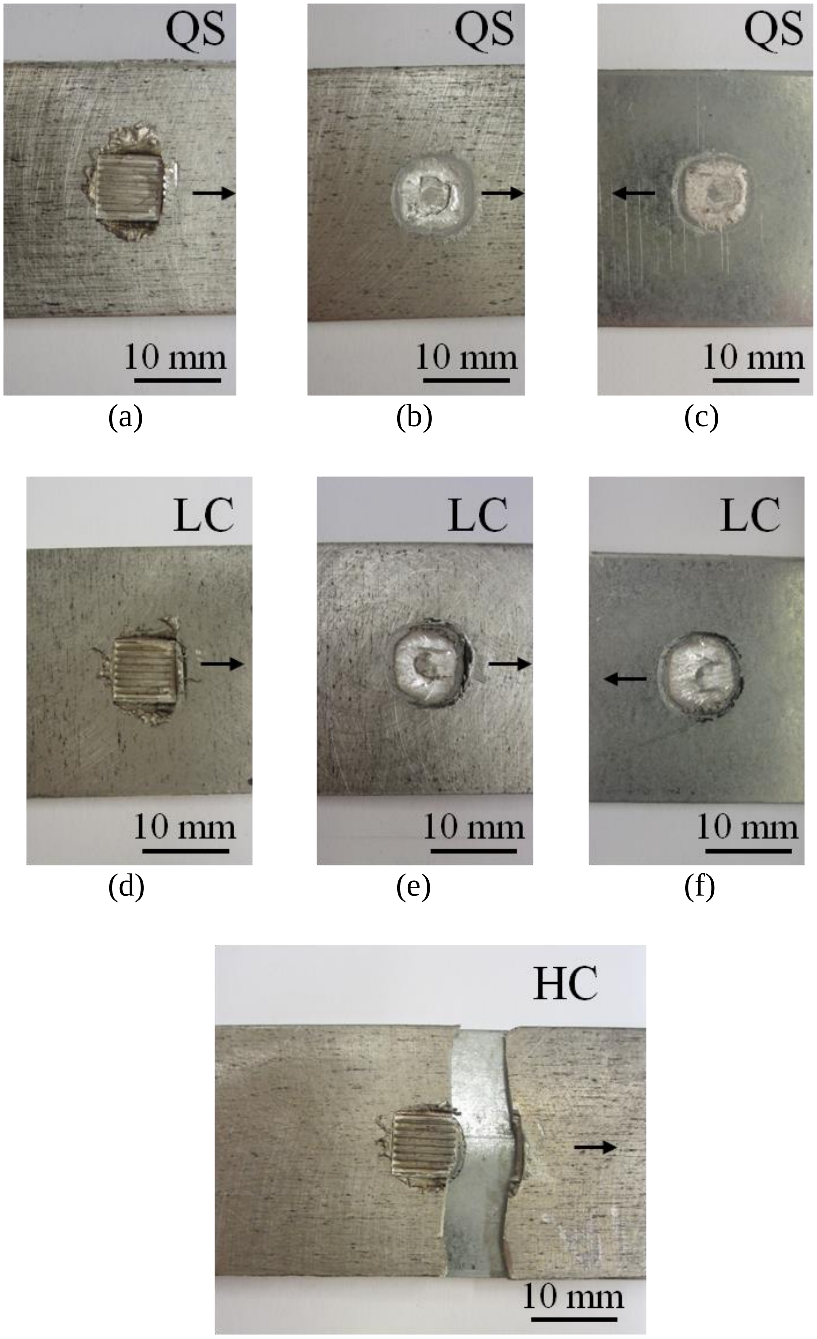

(a) (b) (c)

(d) (e) (f)

(g)

Figure 4.5. (a) A top view of the magnesium sheet, (b) a bottom view of the magnesium sheet and (c) a view of the steel sheet after quasi-static testing. (d) A top view of the magnesium sheet, (e) a bottom view of the magnesium sheet and (f) a view of the steel sheet after (low cycle) cyclic loading with 5.7×10^3 cycles under a load range of 3.20 kN. (g) A top view of the weld after (high cycle) cyclic loading with 3.08×10^4 cycles under a load range of 1.91 kN. The loading direction is shown schematically with arrows.

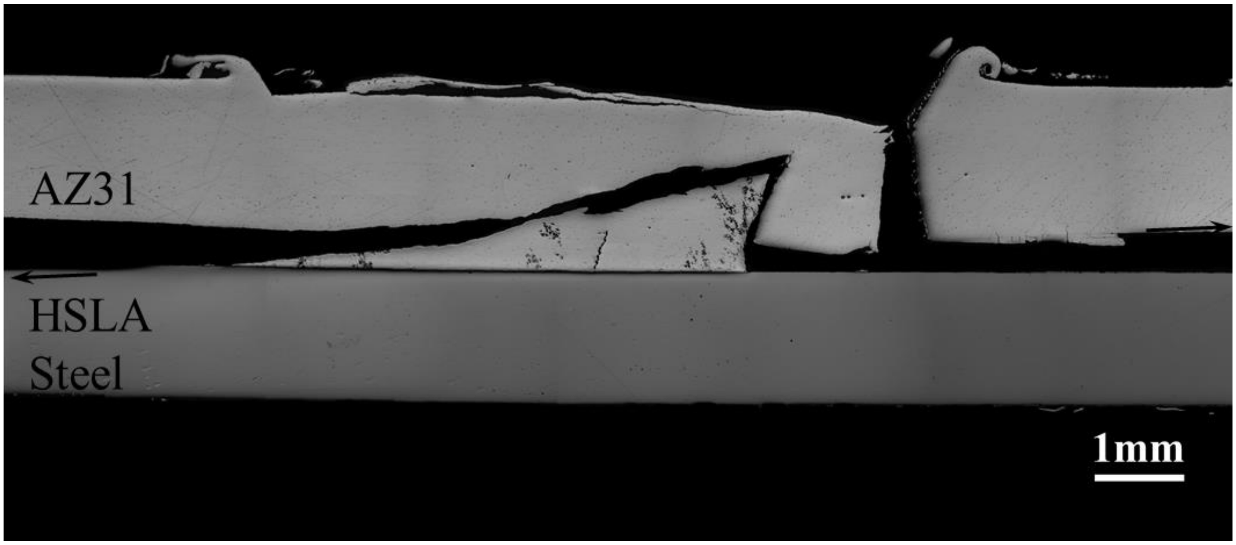

Figure 4.6. Optical micrograph of a failed weld at the fatigue life of 9.5×10^3 cycles under a load range of 2.82 kN (low-cycle (LC) loading conditions).

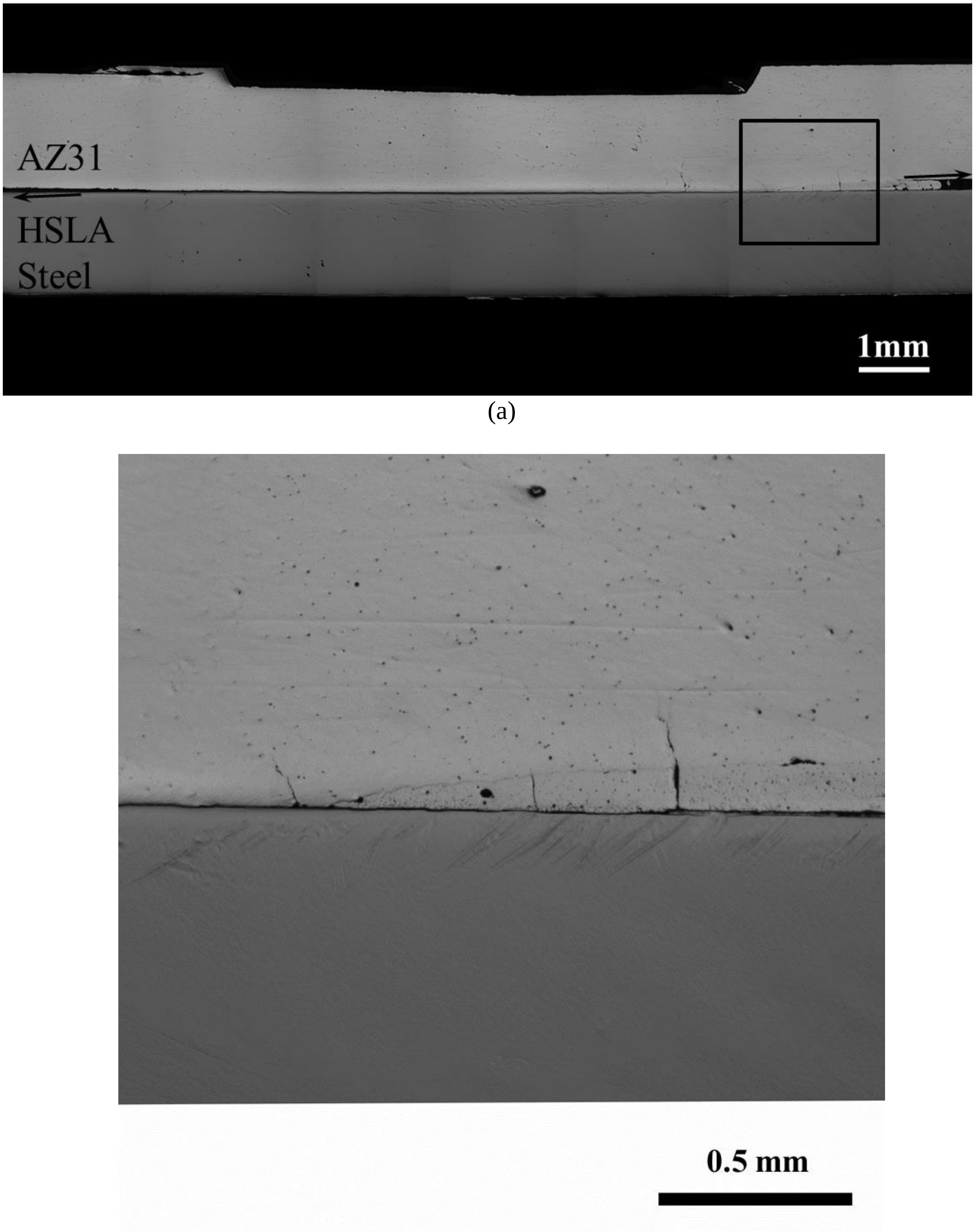

(a)

(b)

Figure 4.7. Optical micrographs of (a) the entire section and (b) an enlarged near the kinked crack of a partially failed thick steel weld at the fatigue life of 1.6×10^4 cycles under a load range of 2.38 kN (low-cycle (LC) loading conditions).

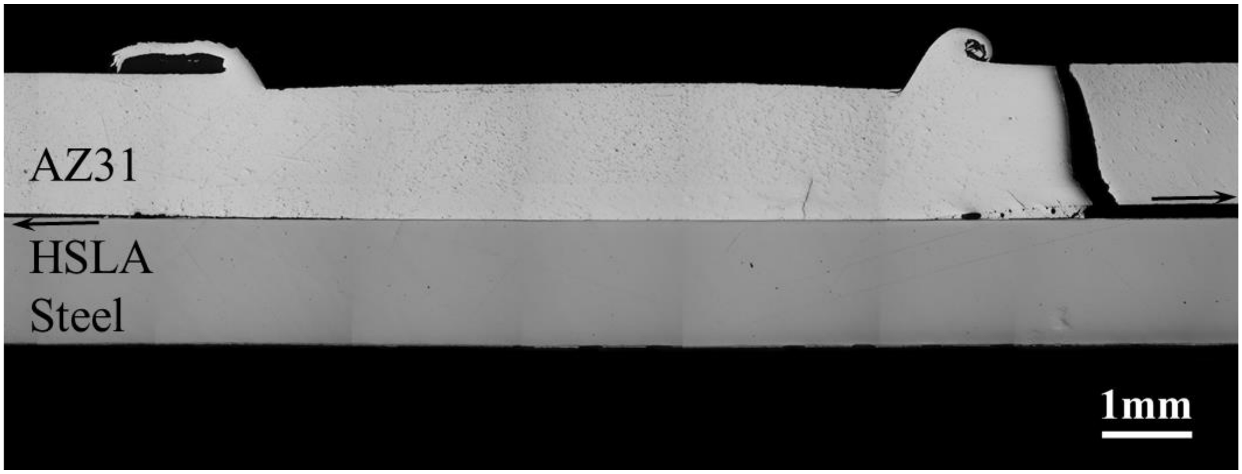

Figure 4.8. Optical micrograph of a failed weld at the fatigue life of 6.6×10^4 cycles under a load range of 2.02 kN (high-cycle (HC) loading conditions).

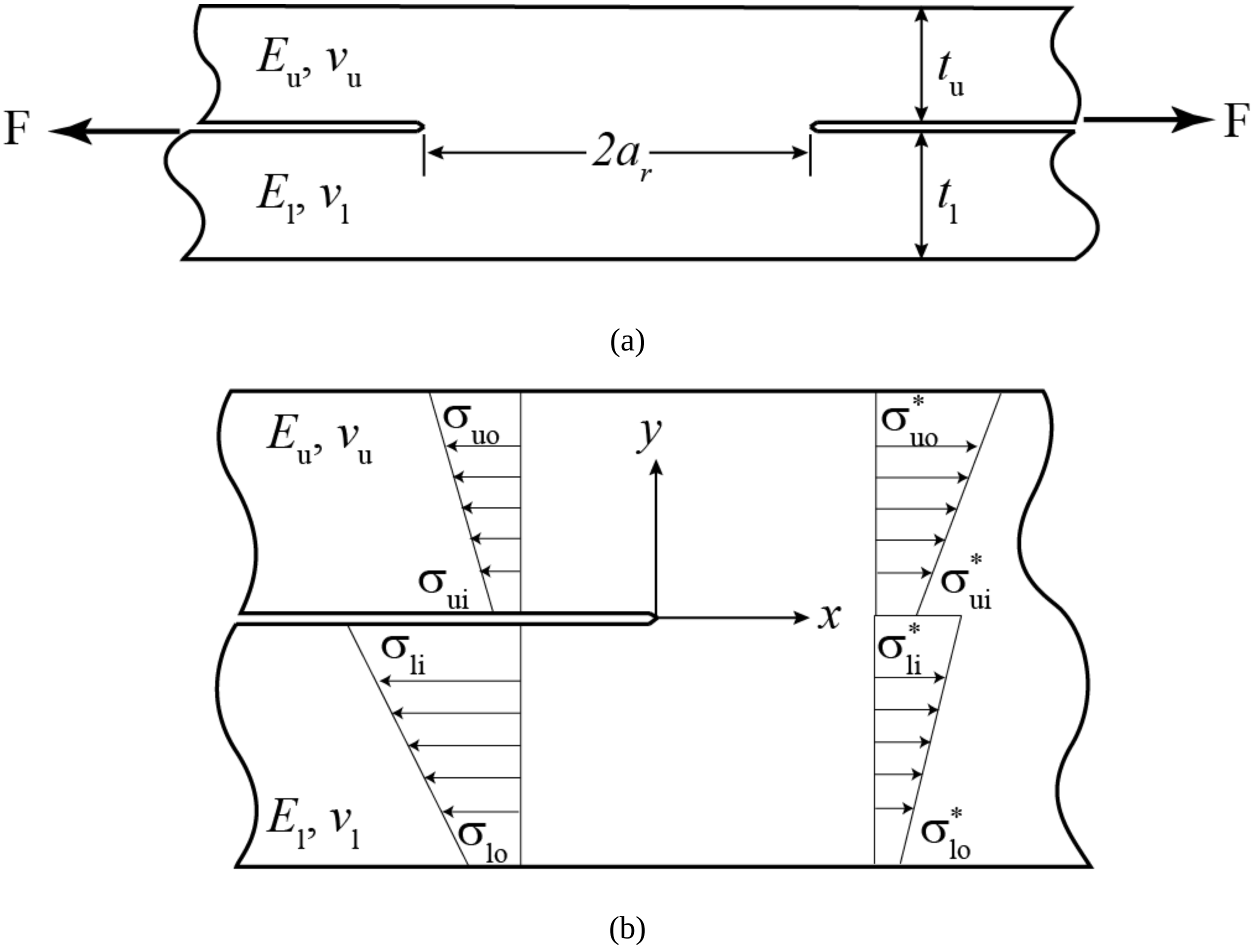

Figure 4.9. (a) A schematic of the weld with the lap-shear loading condition. (b) A schematic of the left crack tip showing the normal stresses σ_{ui}, σ_{uo}, σ_{li} and σ_{lo} at the inner (*i*) and outer (*o*) surfaces of the upper (*u*) and lower (*l*) strips, respectively.

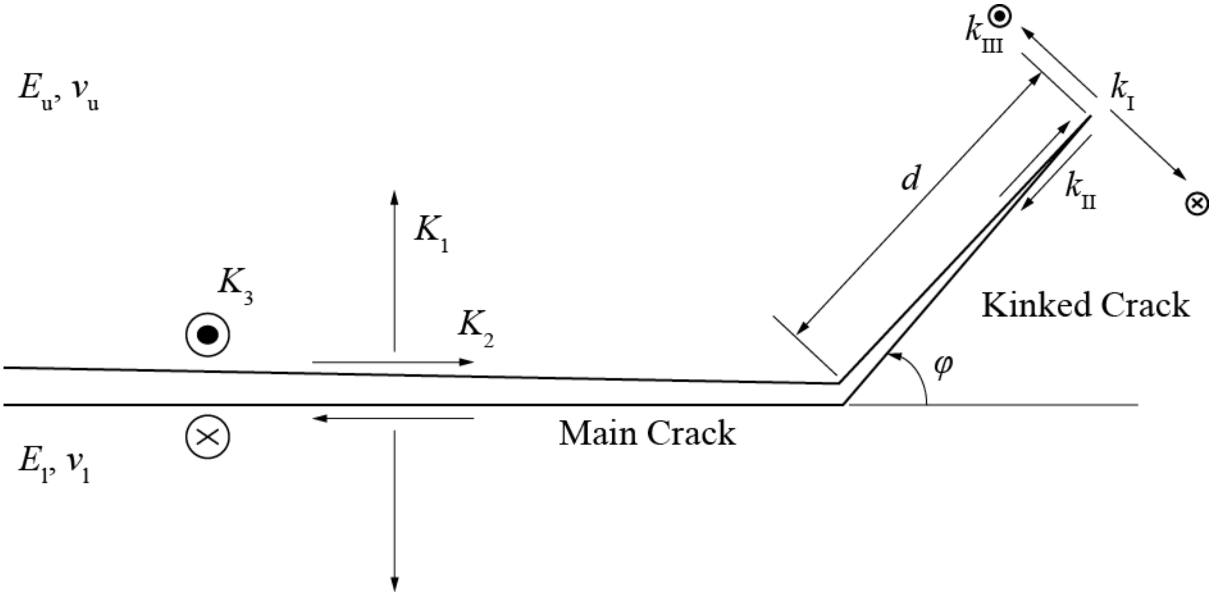

Figure 4.10. A schematic of a main crack and a kinked crack with the kink depth d and the kink angle φ.

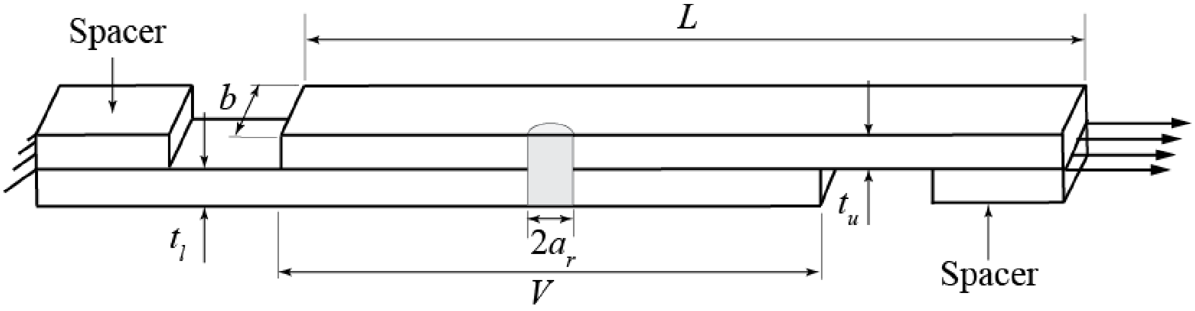

(a)

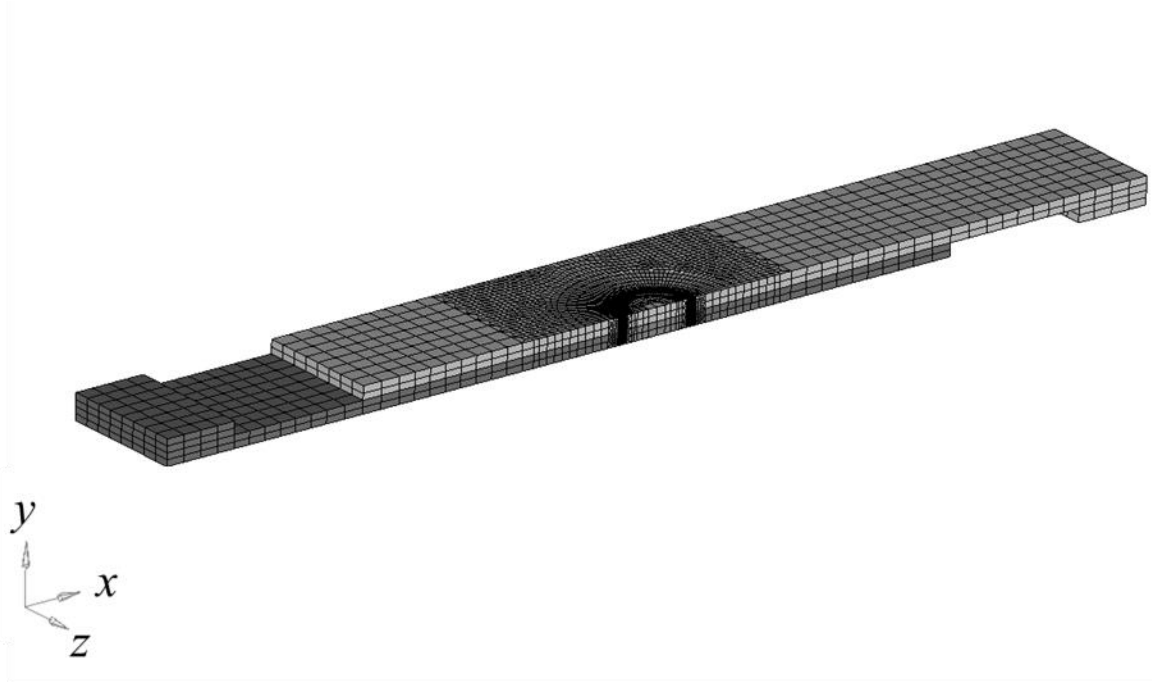

(b)

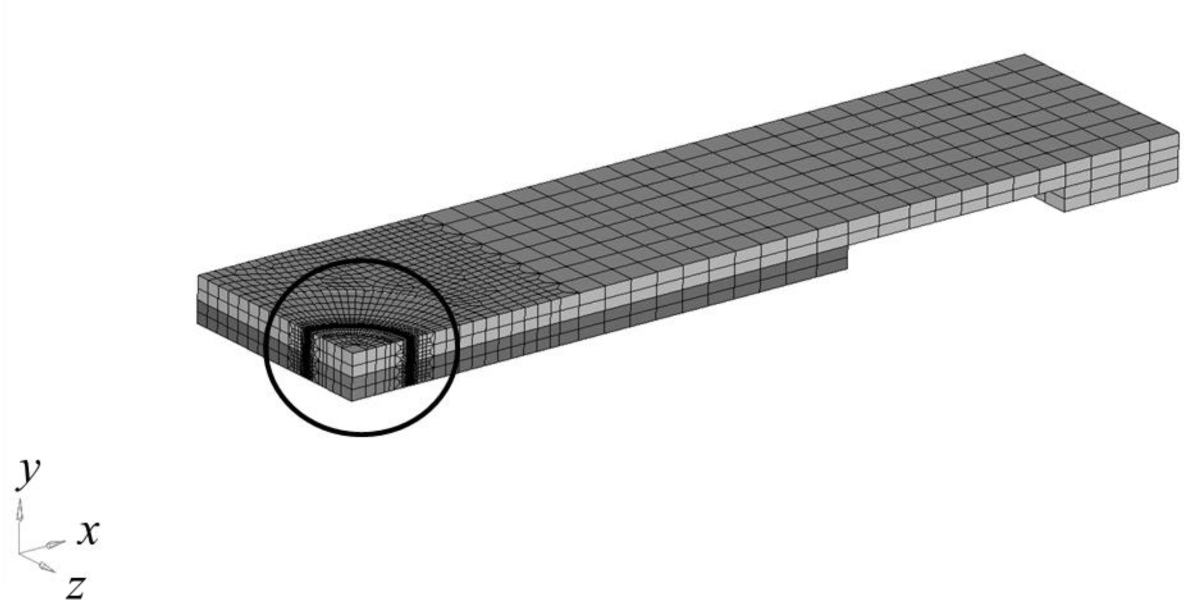
y
x
z

(c)

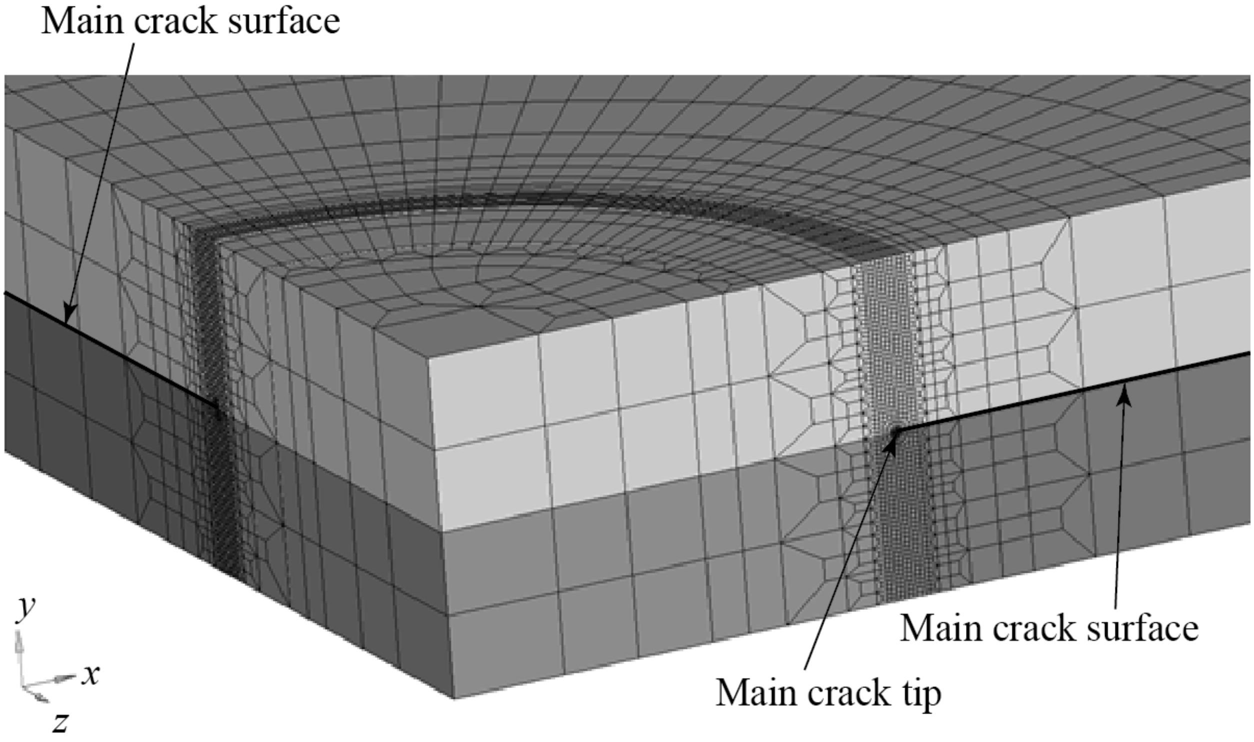
Main crack surface
y
x
z
Main crack tip
Main crack surface

(d)

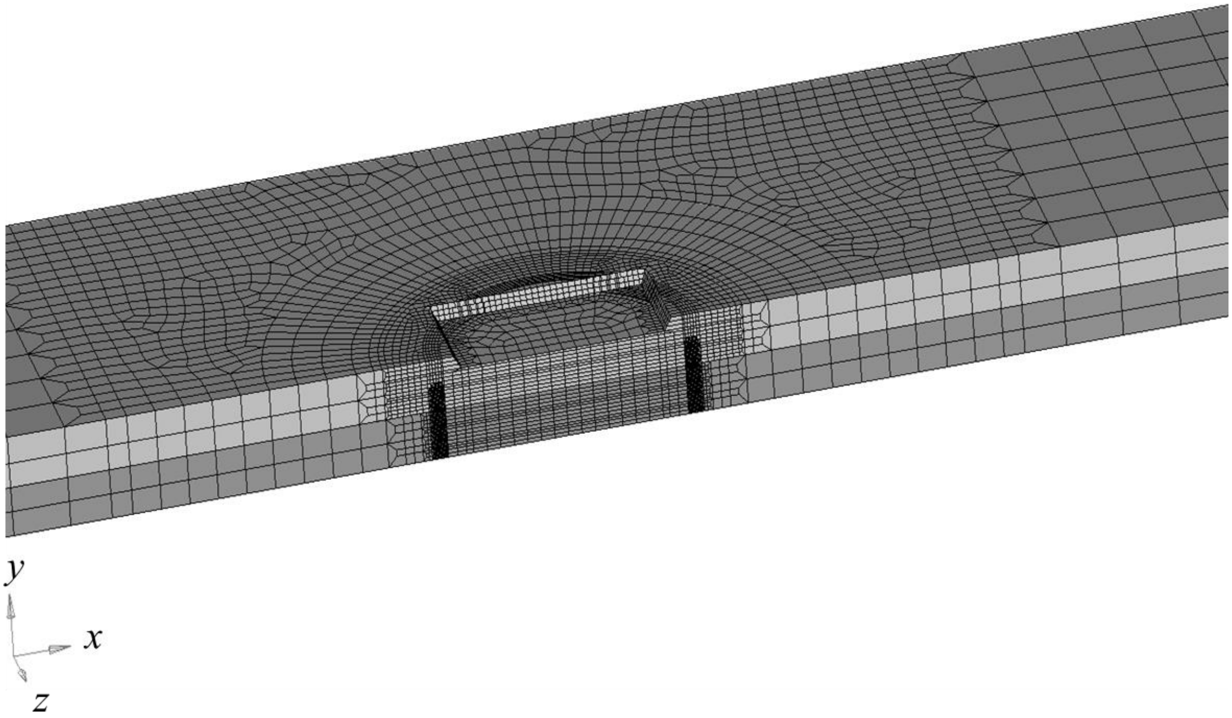

(e)

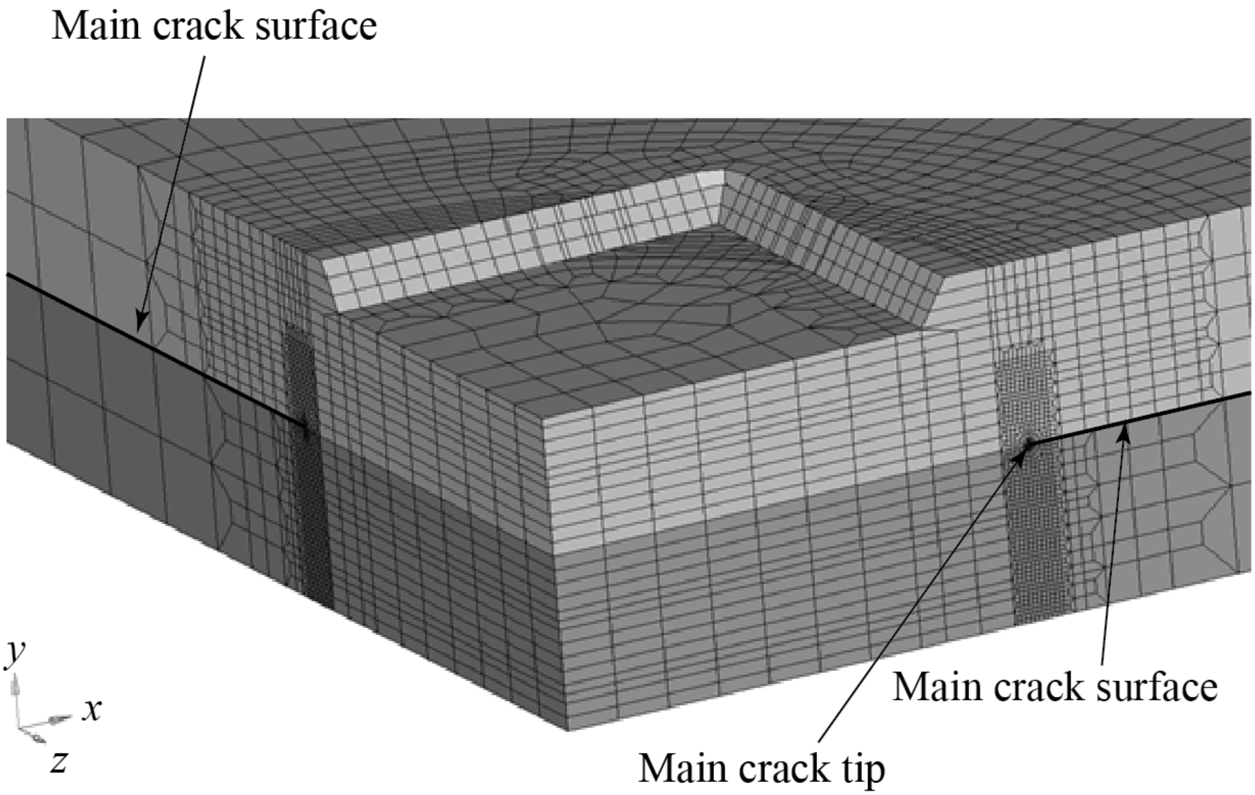

(f)

Figure 4.11. (a) A schematic of a three-dimensional finite element model featuring half of the lap-shear specimen with the boundary and loading conditions, (b) a view of the entire finite element mesh for the idealized model, and (c) a view of the half of the finite element mesh indicating the area shown in (d). (d) An enlarged view of the finite element mesh for the idealized model showing the main crack surfaces and main crack tips. (e) A view of the central portion of the finite element mesh for the weld geometry model showing the weld indentation. (f) An enlarged view of the finite element mesh near the weld for the weld geometry model.

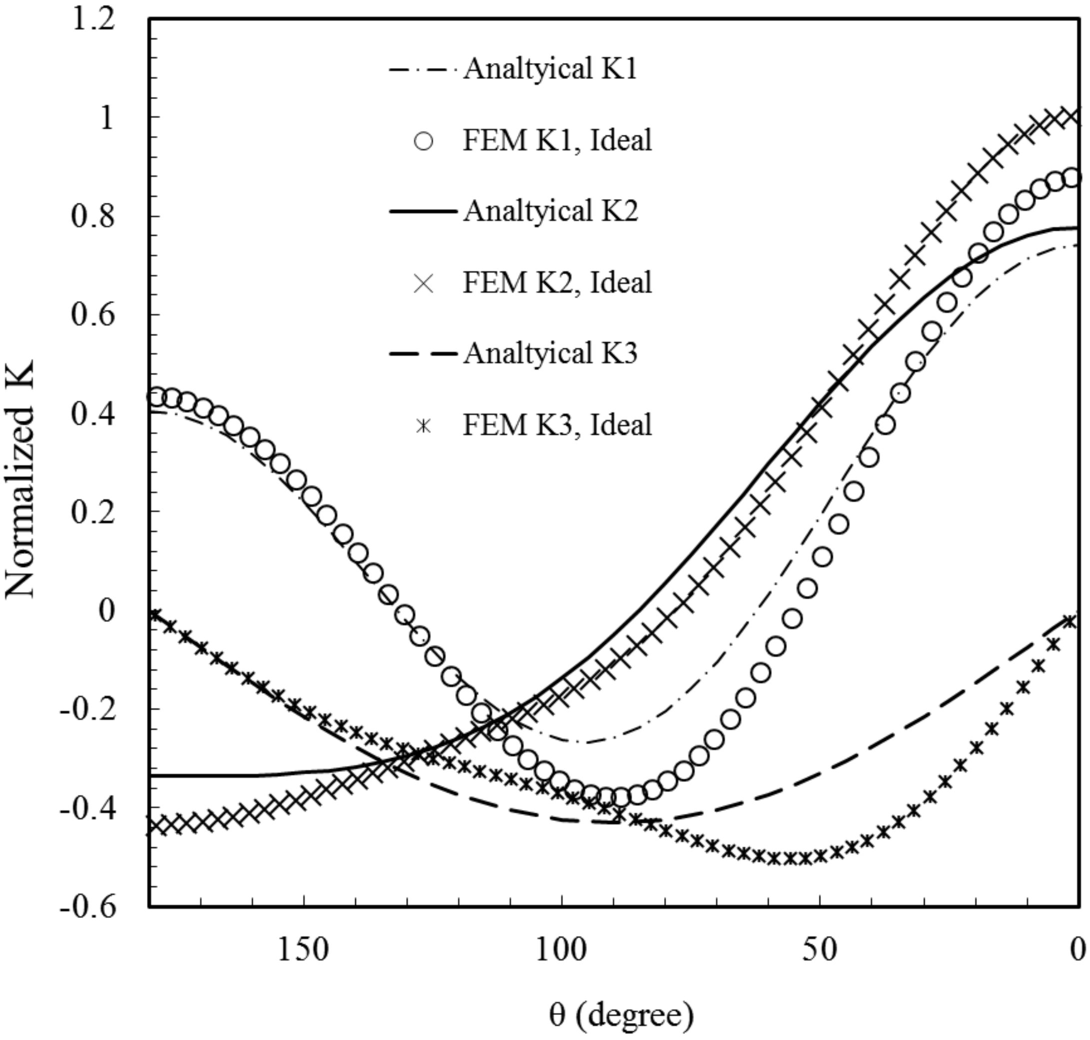

Figure 4.12. The normalized K_1, K_2 and K_3 solutions as functions of θ for an idealized weld of 1.58 mm magnesium and 1.50 mm steel sheets based on the finite element analysis and the analytical solutions.

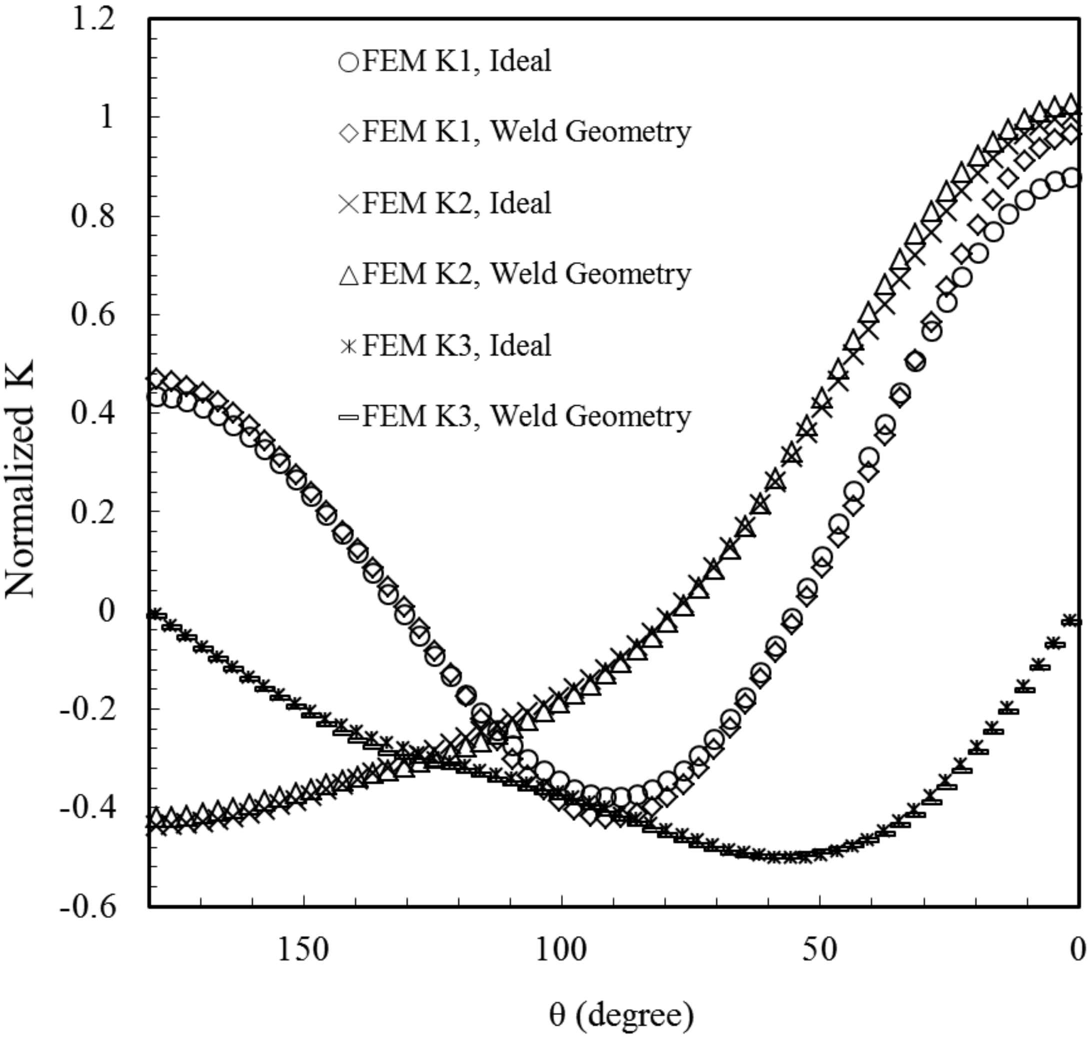

Figure 4.13. The normalized K_1, K_2 and K_3 solutions as functions of θ for a lap-shear spot welded specimen of 1.58 mm magnesium and 1.50 mm steel sheets based on the finite element analysis of an ideal model and a model which follows the weld geometry.

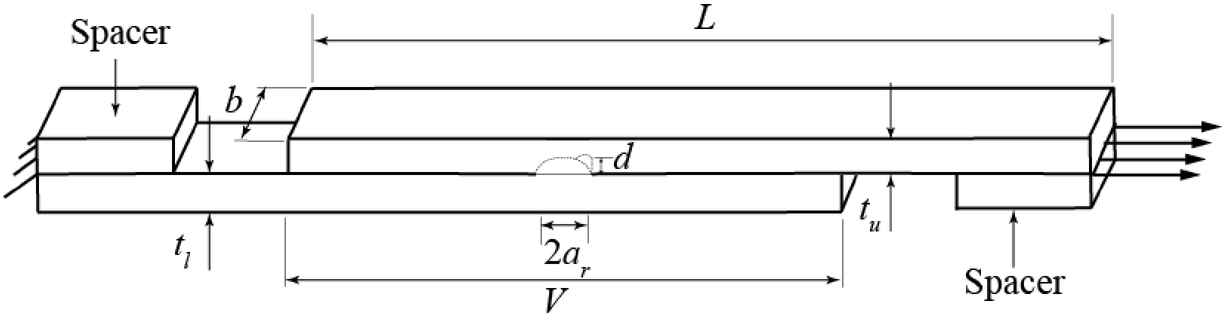

(a)

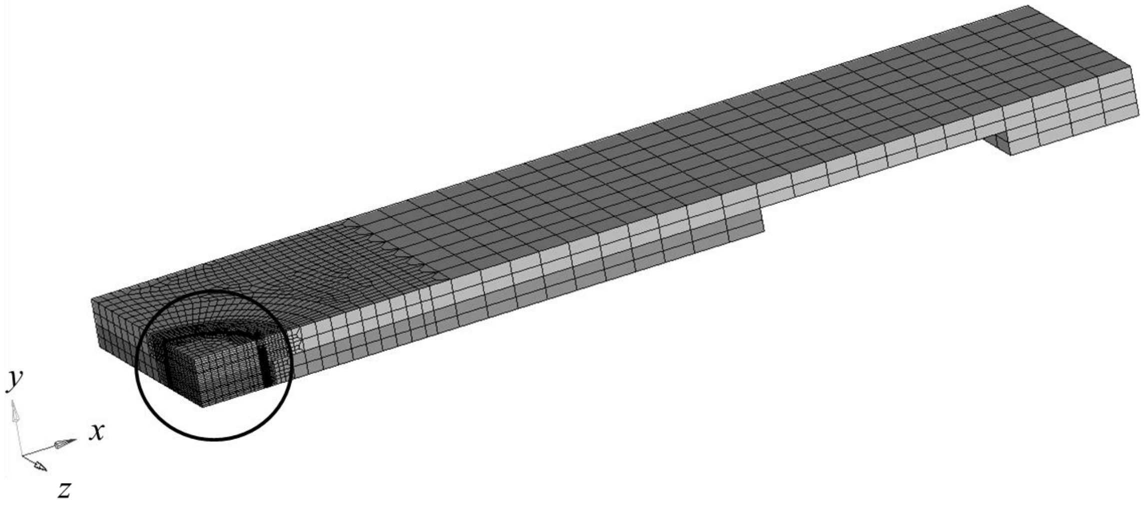

(b)

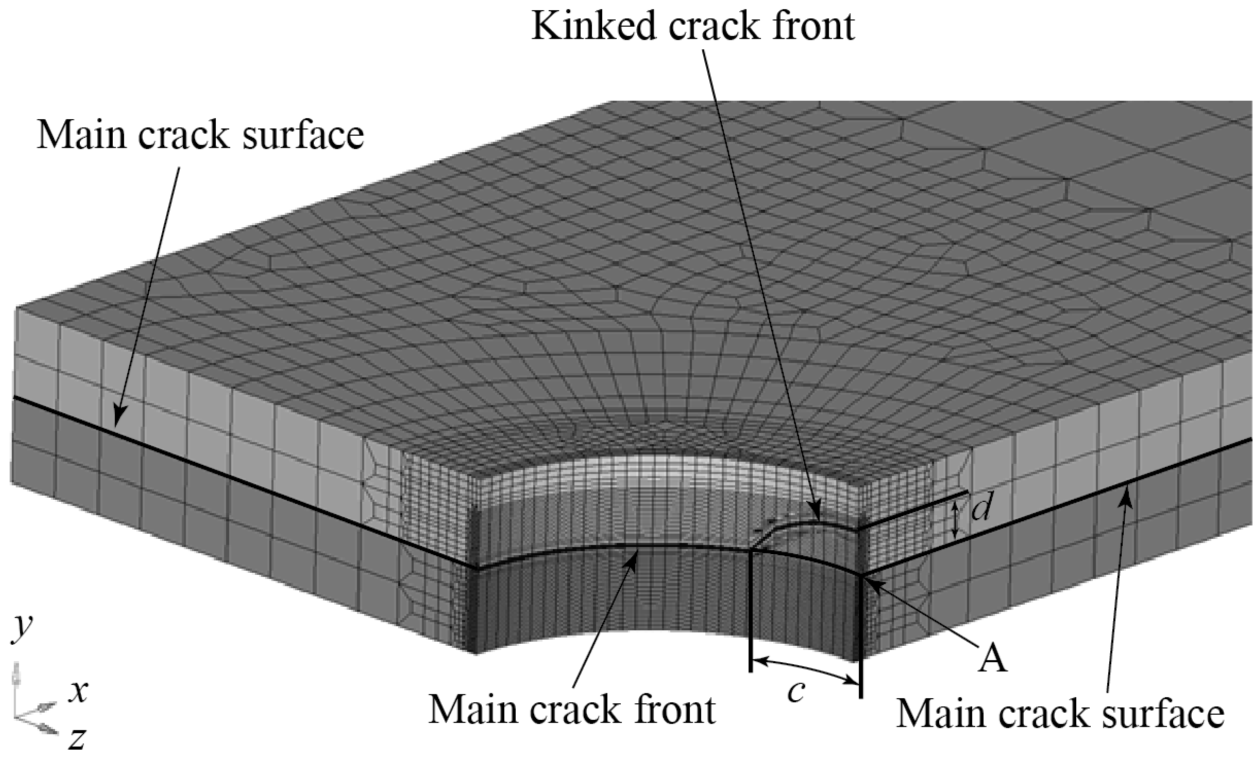

(c)

Figure 4.14. (a) A schematic of a three-dimensional finite element model with an elliptical kinked crack of maximum depth, d , at point A with the boundary and loading conditions, (b) a view of half of the finite element mesh for the idealized model with a kinked crack, and (c) a view of the an enlarged section near the weld for the idealized model with a kinked crack of $d/t = 0.5$, with the welded area hidden.

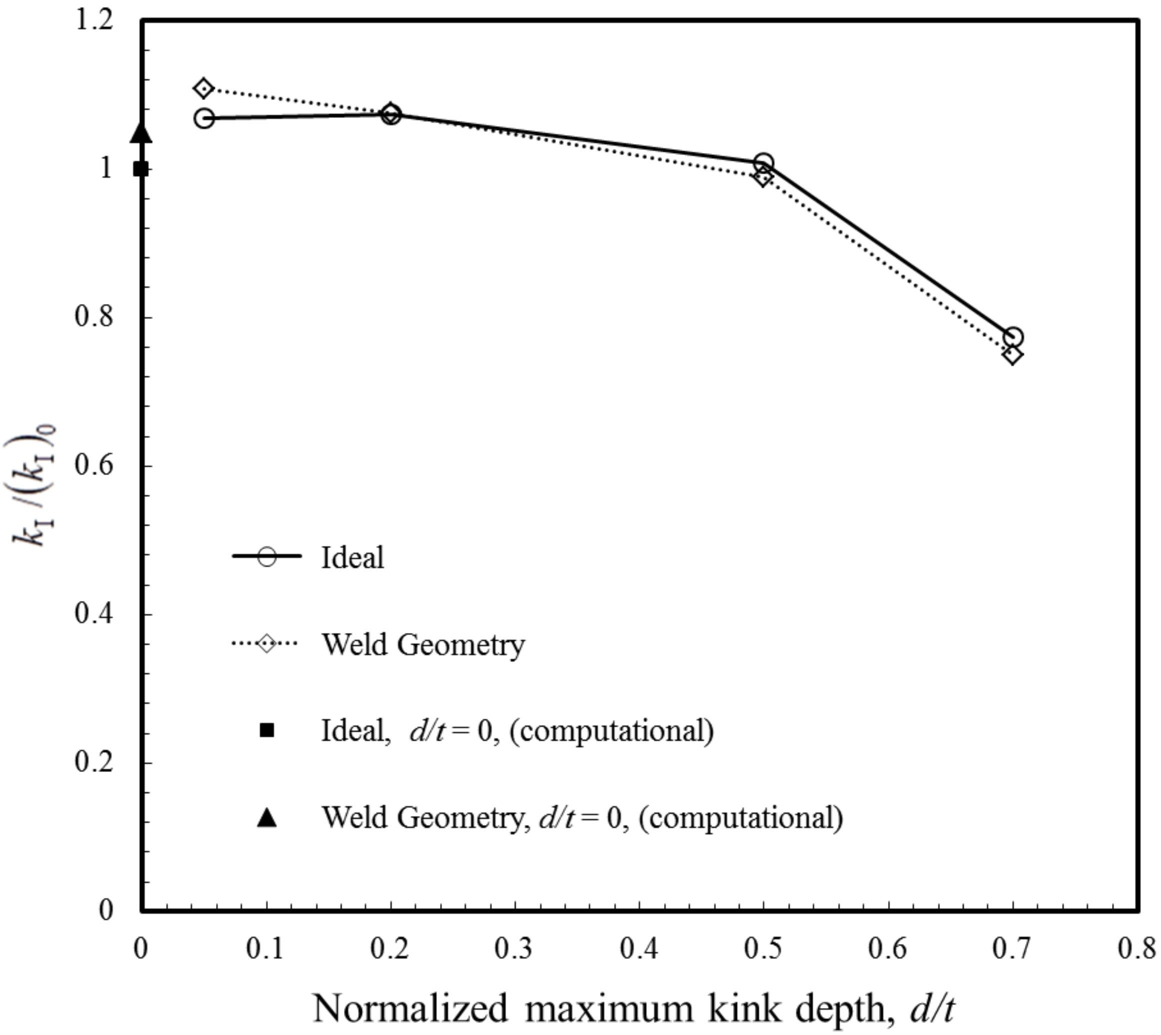

Figure 4.15. The values of $k_I/(k_I)_0$ for the semi-elliptical kinked cracks emanating from point A as functions of the normalized kink depth d/t for $\varphi = -90°$.

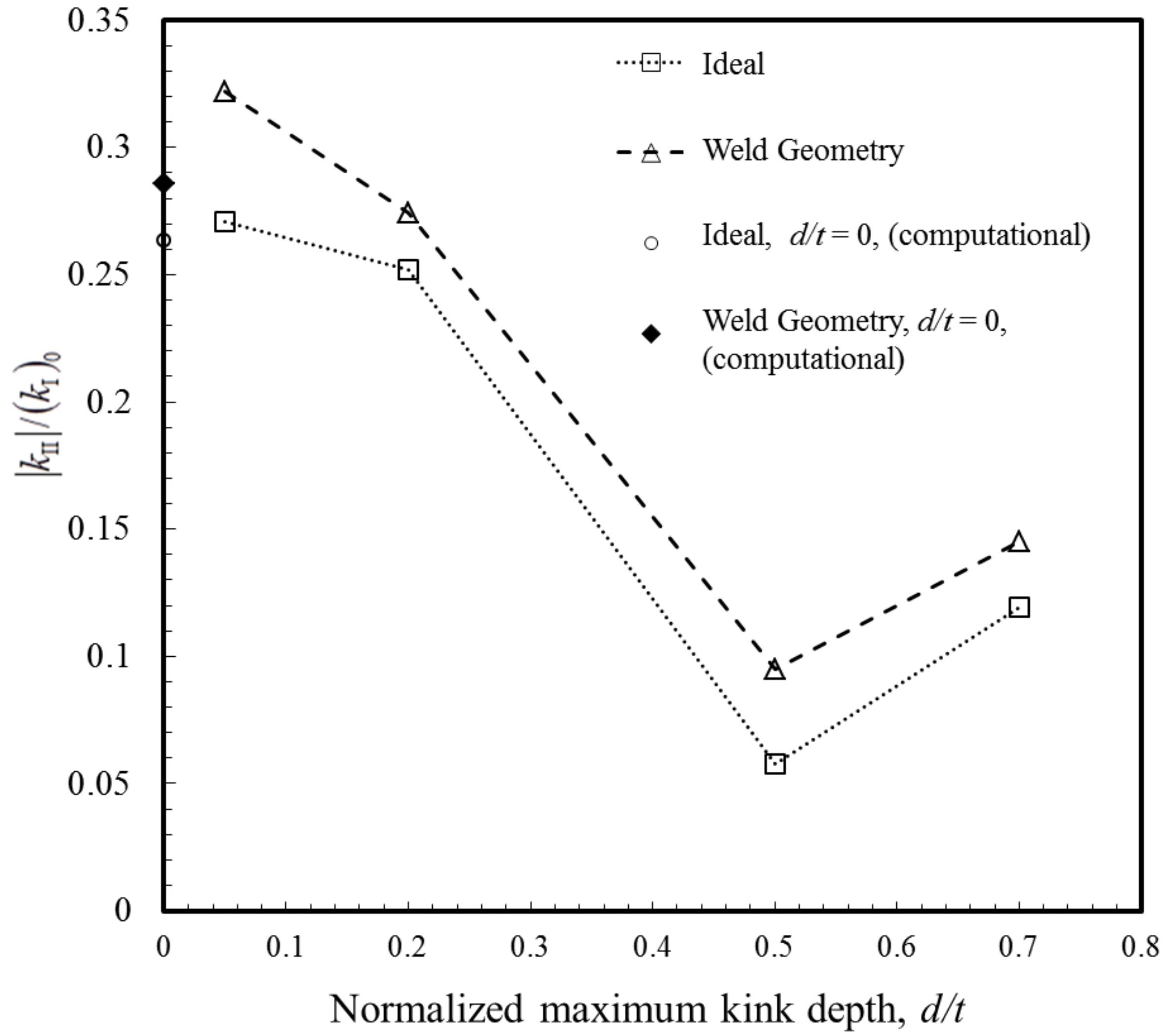

Figure 4.16. The values of $|k_{II}|/(k_{\mathrm{I}})_0$ for the semi-elliptical kinked cracks emanating from point A as functions of the normalized kink depth d/t for $\varphi = -90°$.

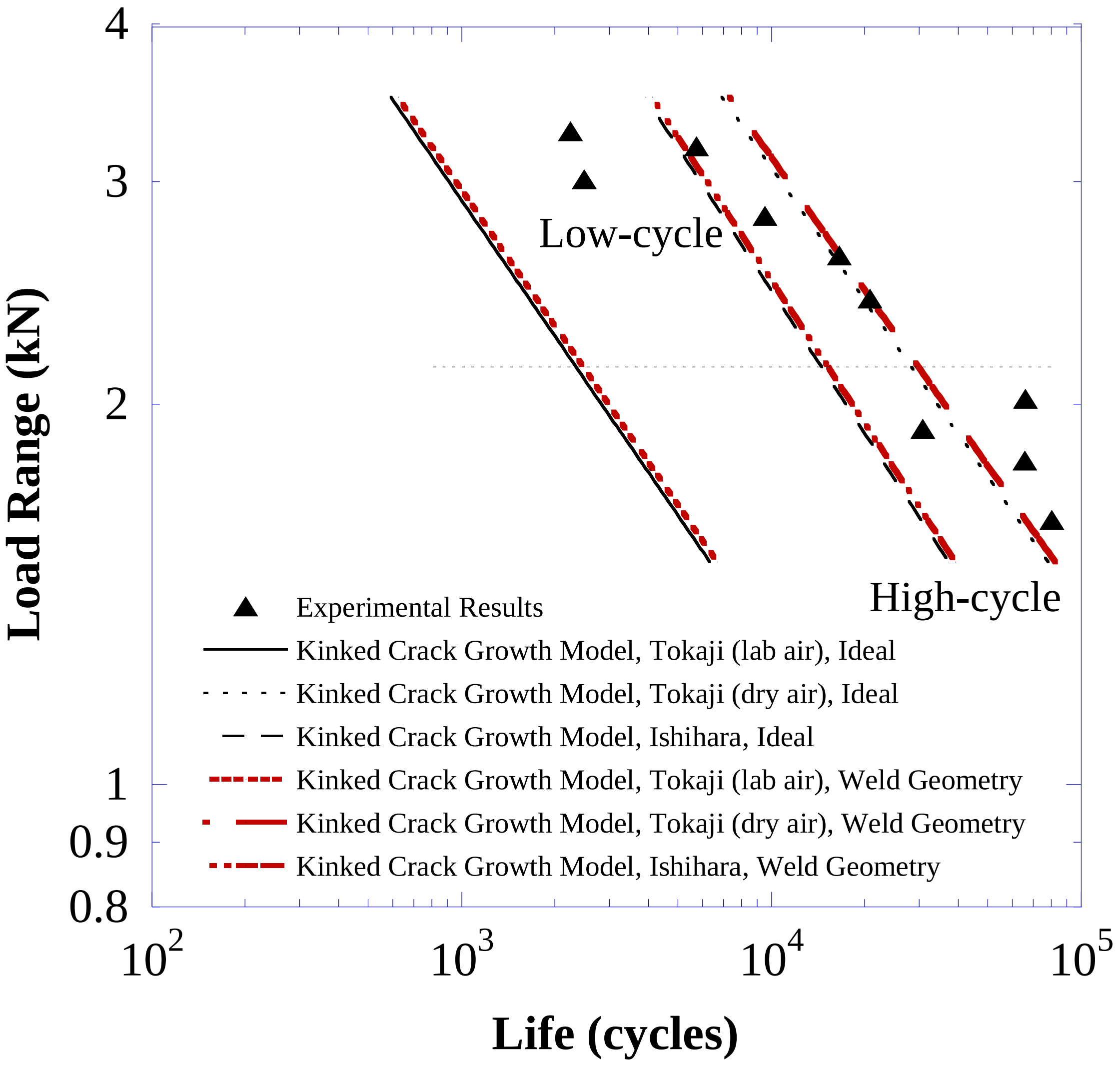

Figure 4.17. The experimental results and the fatigue life estimations based on the kinked fatigue crack growth models for three values of C and m.

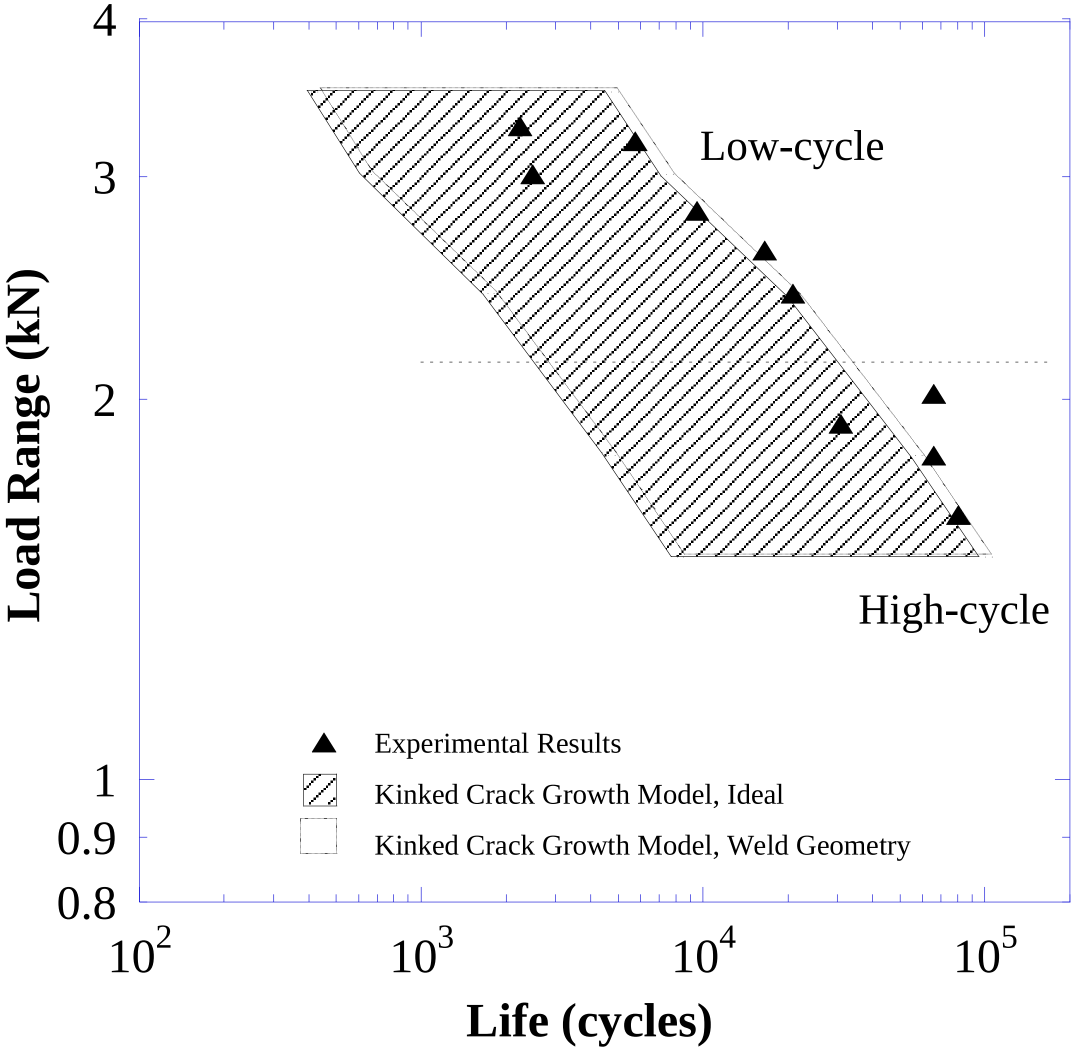

Figure 4.18. The experimental results and the fatigue life estimation ranges based on the kinked fatigue crack growth models for ideal and weld geometry models.

Acknowledgements

This research was initially sponsored by the U.S. Department of Energy, Assistant Secretary for Energy Efficiency and Renewable Energy, Office of Vehicle Technologies, as part of the Lightweight Materials Program. Support of this work through a National Science Foundation Fellowship for TF is greatly appreciated.

References

[1] Santella M, Franklin T, Pan J, Pan T-Y, Brown E, Ultrasonic spot welding of AZ31B to galvanized mild steel. SAE Technical Paper 2010-01-0975, Society of Automotive Engineers, Warrendale, PA.

[2] Santella M, Brown E, Pozuelo M, Pan T-Y, Yang J-M. Details of Mg–Zn reactions in AZ31 to galvanised mild steel ultrasonic spot welds. Sci Technol of Weld Joi 2012; 17(3): 219-24.

[3] Jana S, Hovanski Y, Grant GJ. Friction stir lap welding of magnesium alloy to steel: A Preliminary Investigation. Metall Mater Trans A 2010;41A:3173-82.

[4] Chen YC, Nakata K. Effect of tool geometry on microstructure and mechanical properties of friction stir lap welded magnesium alloy and steel. Mater Des 2009;30:3913-9.

[5] Wei Y, Li J, Xiong J, Huang F, Zhang F. Microstructures and mechanical properties of magnesium alloy and stainless steel weld-joint made by friction stir lap welding. Mater Des 2012;33:111-4.

[6] Schneider C, Weinberger T, Inoue J, Koseki T, Enzinger N. Characterisation of interface of steel/magnesium FSW. Sci Technol of Weld Joi 2011;16(1):100-6.

[7] Wahba M, Katayama S. Laser welding of AZ31B magnesium alloy to Zn-coated steel. Mater Des 2012;35:701-6.

[8] Zhang S. Stress intensities derived from stresses around a spot weld. Int J Fracture 1999;99:239-57.

[9] Tran V-X, Pan J. Analytical stress intensity factor solutions for resistance and friction stir spot welds in lap-shear specimens of different materials and thicknesses. Eng Fract Mech 2010;77(14):2611-39.

[10] He M-Y, Hutchinson JW. Kinking of a crack out of an interface. J Appl Mech 1989; 56(2): 270-8.

[11] Rice JR, Sih GC. Plane problems of cracks in dissimilar media. J Appl Mech 1965;32:418-23.

[12] Rice JR. Elastic fracture mechanics concepts for interfacial cracks. J Appl Mech 1988;55:98-103.

[13] Suo Z, Hutchinson JW. Interface crack between two elastic layers. Int J Fracture 1990;43:1-18.

[14] He M-Y, Hutchinson JW. Kinking of a crack out of an interface: tabulated solution coefficients. Harvard University Report MECH-113A. 1988.

[15] Cotterell B, Rice JR. Slightly curved or kinked cracks. Int J Fracture 1980; 16: 155-69.

[16] ABAQUS v6.7 User Manual. Providence, RI: SIMULIA; 2007.

[17] Lin P-C,Wang D-A, Pan J. Mode I stress intensity factor solutions for spot welds in lap-shear specimens. Int J Solids Struct 2007;44:1013-37.

[18] Newman J, Dowling, N. A Crack Growth Approach to Life Prediction of Spot-Welded Lap Joints. Fatigue Fract. Eng. Mater. Struct. 1998; 21: 1123–32.

[19] Pan N, Sheppard, SD. Stress intensity factors in spot welds. Eng Fract Mech. 2003; 70: 671–84.

[20] Wang D-A, Pan J. A computational study of local stress intensity factor solutions for kinked cracks near spot welds in lap-shear specimens. Int J Solids Struct 2005;45:6277-98.

[21] Choi SS. Probabilistic characteristics of fatigue behavior parameter of Paris-Erdogan law in Mg-Al-Zn alloy. The Korean Society of Mechanical Engineers, pp 375-381, 2011.

[22] Ochi Y, Masaki K, Hirasawa T, Wu X, Matsumura T, Takigawa Y, Higashi K. High cycle fatigue property and micro crack propagation behavior in extruded AZ31 magnesium alloys. Mater Trans 2006 47(4) 989-94.

[23] Ishihara S, McEvily AJ, Sato M, Taniguchi K, Goshima T. The effect of load ratio on fatigue life and crack propagation behavior of an extruded magnesium alloy. Int J Fatigue 2009;31:1788-94.

[24] Morita S, Ohno, N, Tamai, F, Kawakami Y. Effect of Grain Size on Fatigue Crack Propagation in Extruded AZ31 Magnesium Alloys. Mater Sci Forum 2012;706-709:1233-6.

[25] Tokaji K, Nakajima M, Uematsu Y. Fatigue crack propagation and fracture mechanisms of wrought magnesium alloys in different environments. Int J Fatigue 2009; 31: 1137-43.

Chapter 5
Conclusion

Stress intensity factor solutions and fatigue behavior of dissimilar ultrasonic welds between magnesium and steel sheets are investigated. In Chapter 2, analytical solutions for dissimilar plane strain joints are reviewed. Global stress intensity factor solutions for dissimilar welds of various widths in lap-shear specimens are obtained from a two-dimensional plane strain finite element model. The computational solutions are compared with two analytical solutions. The analytical solution based on structural stresses and beam bending theory is appropriate for magnesium and steel welds with a normalized width ratio, w/t, larger than a transition value of 1.216. The analytical solution for two dissimilar semi-infinite solids with connection under shear loading conditions is useful for welded specimens of magnesium and steel sheets with a normalized width ratio, w/t, smaller than a transition value of 0.209. Note that the transition value is dependent on both the weld width and the dissimilar materials used in the weld, so these transitions would not be applicable for other dissimilar materials.

The next part of Chapter 2 investigates local stress intensity factors for kinked cracks. Welds in lap-shear specimens with kinked cracks of various lengths were modeled using finite element with both the actual material combination and a modified material combination such that the bimaterial constant was zero. Stresses directly ahead of and directly above the crack tip were compared for both material combinations. Ahead of the crack tip, the stresses were not similar due to the oscillation of the crack-tip stress field in the model with the actual material combination. However, above the crack tip, at a kink angle of $\varphi = -90$, the stresses were only weakly affected by the oscillation and stresses for both material combinations were quite similar. For large kink angles, the modified material combination may be substituted such that the bimaterial constant is zero, allowing use of existing analytical solutions to approximate the local stress intensity factors for a vanishing kinked crack of length $a = 0$. The local stress intensity factors for kinked crack were compared with the vanishing crack solutions which were evaluated using the modified material. The k_{I} solution is shown to approach the solutions for a vanishing crack. While the k_{II} solutions do not approach the solutions for a vanishing crack, the magnitude of the k_{II} solutions is less than that of the k_{I} solutions. Therefore the k_{e} solutions, which are most important for fatigue estimations, are shown to approach the solutions for a vanishing crack as the kink length decreases.

In Chapters 3 and 4, the vanishing crack stress intensity factor solutions investigated in Chapter 2 are used to complete the set of local stress intensity factors, allowing the use of a fatigue estimation model. Fatigue behavior of ultrasonic welds in lap-shear specimens of magnesium and steel sheets were also investigated experimentally and with optical micrographs. In Chapter 3, the experimental lap-shear specimens were machined into a dog-bone profile to approximate a linear weld. Two types of steel were used for experiments in this chapter. For all cyclic loading in welds with either type of steel, the weld fracture appears to be initiated from the pre-existing crack which propagates and kinks upward at roughly 90°. Under low-cycle loading conditions, the weld failure appears to be initiated from the pre-existing crack tip and the specimens finally fail as the crack connects with the corner of the weld indentation in the magnesium on the right side of the weld. Under high-cycle loading conditions, the weld failure appears to be initiated from the pre-existing crack tip and the specimens finally fail from the kinked fatigue crack propagating through the upper right load carrying sheets, with the final fracture connecting with the side wall of the weld indentation, or outside the indentation. In Chapter 3, two-dimensional plane strain finite element models were constructed to obtain global stress intensity factor solutions and local stress intensity factor solutions for finite kinked cracks. The stress intensity solution for the vanishing crack was obtained using computational results for the global stress intensity factors using a modified material as detailed in Chapter 2.

In Chapter 4, fatigue behavior is investigated experimentally with dissimilar ultrasonic spot welds which have not been altered after welding. For higher load ranges, the welds first experienced a kinked fatigue crack which propagated through the loaded magnesium sheet and a shallow kinked crack growing from the left crack front. The welds tested under low-cycle fatigue finally failed through the interface, leaving some magnesium material on the steel sheet. For lower load ranges, the welds fail from a kinked crack which grew on the right side through the magnesium sheet. After reaching the surface of the magnesium, the crack grew transversely through the magnesium sheet. The welds tested under high-cycle loading conditions finally failed from an eyebrow crack on the right side of the weld which propagated through the entire magnesium sheet. For this chapter, three-dimensional finite element models were constructed to obtain global and local stress intensity factor solutions. The global stress intensity factor solutions and the local stress intensity factor solutions for vanishing and finite kinked cracks are used for fatigue life estimations with a kinked crack growth model. The fatigue estimations are compared with experimental fatigue results.

The three-dimensional spot welds in Chapter 4 had better correlation between the fatigue estimations and the experimental results than the plane strain models in Chapter 3. In Chapter 3, the fatigue estimation model tended to predict a slightly lower life than observed experimentally, particularly for high-cycle fatigue. The kinked crack growth model used three values of Paris law constants and was particularly sensitive to the parameters C and m. The model was not sensitive to the thickness of the steel in Chapter 3. It was also only mildly influenced by the modeling of the sonotrode indentation for both the plane strain and three-dimensional models. The kinked crack growth model and the experimental results were in good agreement for the three-dimensional study found in Chapter 4. The kinked crack model estimated cycles about 1 decade under the experimental result for the plane strain model in Chapter 3. It may be that even after machining the experimental specimens into a dog-bone shape, they did not behave exactly as if they were a linear weld. A tendency for the kinked crack to grow in a semi-elliptical pattern instead of a planer crack would contribute to a longer life.

In summary, existing analytical results for stress intensity factor solutions for dissimilar joints are reviewed in Chapter 2. A comparison of the stresses present in a lap-shear weld of modified material made it possible to use existing analytical solutions to obtain a vanishing crack solution. This vanishing crack solution is used in combination with global and local stress intensity factor solutions from finite element models for a two-dimensional plane strain model and a three-dimensional model. These stress intensity factor solutions are used in a kinked crack fatigue estimation model. The fatigue estimations for the plain strain model in Chapter 3 under predict the experimental results by roughly 1 decade while the estimations for the three-dimensional spot welds in Chapter 4 correlate well with experimental results.